Title

Thermal Energy Harvesting with Thermoelectrics for Self-powered Sensors: With Applications to Implantable Medical Devices, Body Sensor Networks and Aging in Place

Author

Chen, Alic

Publication Date

2011

Peer reviewed|Thesis/dissertation

Thermal Energy Harvesting with Thermoelectrics for Self-powered Sensors: With Applications to Implantable Medical Devices, Body Sensor Networks and Aging in Place

By

Alic Chen

A dissertation submitted in partial satisfaction of the

requirements for the degree of

Doctor of Philosophy

in

Engineering – Mechanical Engineering

in the

Graduate Division

of the

University of California, Berkeley

Committee in charge:

Professor Paul K. Wright, Chair
Professor James W. Evans
Professor David A. Dornfeld

Fall 2011

Thermal Energy Harvesting with Thermoelectrics for Self-powered Sensors: With Applications to Implantable Medical Devices, Body Sensor Networks and Aging in Place

Alic Chen

Abstract

Thermal Energy Harvesting with Thermoelectrics for Self-powered Sensors: With Applications to Implantable Medical Devices, Body Sensor Networks and Aging in Place

by

Alic Chen

Doctor of Philosophy in Engineering – Mechanical Engineering

University of California, Berkeley

Professor Paul K. Wright, Chair

This work examines the feasibility of applying thermoelectric generators as power sources for implantable applications. Thermoelectric design principles, manufacturing methods and novel materials are foundational aspects of the work.

Rapid advancements in the field of biomedical engineering has led to the vast number of implantable medical devices developed within the last few decades. As implantable medical devices provide more functionality, sufficient energy storage while maintaining compactness becomes challenging. The lifetime of implanted medical devices will often be much shorter than the expected lifespan of patients, adding risks and costs to the patient in the form of additional surgical procedures. A perpetual power source that extends the longevity of implantable devices still remains elusive. This presents opportunities for solid-state thermal energy harvesting with thermoelectric energy generators (TEGs) that scavenge waste heat, the most abundant source of energy from the body.

Thermoelectric energy generators (TEGs) provide solid-state energy by converting temperature differences into usable electricity. Since the fat in the human body provides thermal insulation, the largest temperature differences (typically 1-5 K) are found in the highest fat regions of the body. Bioheat transfer modeling shows that the optimal placement of TEGs for energy generation is in the abdomen under high convective conditions. Based on average 100 μW (at 1 V) input power requirements of implantable medical devices, thermoelectric and heat transfer design theories suggest a need for high aspect ratio thermoelectric elements in high density arrays to take advantage of the low temperature differences in the fat layer.

In order to maximize power output, traditional thermoelectric device designs must be abandoned and a planar TEG device design is proposed as an effective and scalable method for implantable medical applications. Dispenser printing was then shown as a scalable and repeatable manufacturing method for depositing thick-film thermoelectric materials in the fabrication of planar TEGs. The use of printed fabrication methods led to the development and synthesis of novel printable composite thermoelectric materials. The thermoelectric properties of the printed thermoelectric materials were analyzed and carefully characterized as a function of temperature. The maximum dimensionless figure of merit (ZT) at 302K for an n-type Bi_2Te_3-epoxy composite

was 0.18 when cured at 250°C, while the *ZT* of a p-type Sb_2Te_3-epoxy composite cured at 350°C was 0.34.

A 50-couple TEG prototype with 5 mm x 640 μm x 90 μm printed element dimensions was fabricated on a polyimide substrate with evaporated metal contacts. The prototype device produced a power output of 10.5 μW at 61.3 μA and 171.6 mV for a temperature difference of 20K resulting in a device areal power density of 75 $\mu W/cm^2$. The results of the work are promising and alternative methods to improve the performance of future devices are proposed. While the initial focus of this work was specific to the field of biomedical devices, the technologies that have been developed are applicable to other fields involving energy harvesting. The prospective impact of this work ultimately paves the path towards the advanced healthcare system of the future based on integrated autonomous wireless systems for the needs of "aging in place" or "aging at home" technologies.

Table of Contents

Acknowledgements

I am eternally grateful for all the encouragement, support and contributions I have received during my time at Berkeley. This work is dedicated all those who have impacted me both personally and professionally during my journey. I hope to personally thank every individual I am beholden to.

Although the list of individuals who I want to thank would immensely outnumber the pages in this work, I would like to particularly acknowledge the following people for their aide and inspirations:

Professor Paul Wright for his guidance and advice throughout my studies. He has not only acted as my mentor, but as my friend. His unwavering support and encouragement was instrumental to the success of this project. I am forever indebted to him for providing me the opportunity to be part of such an amazing community.

Professor Jim Evans acted as a co-advisor on this work, treating me as his own student. I am extremely thankful for all the support and direction he has provided since the inception of this project.

Alex Gorbach also acted a co-advisor and collaborator during my work at NIH. I am thankful for his insight and direction during our work together.

All of my past and present colleagues at BMI, BWRC, CITRIS and Berkeley. I have had the opportunity to work with extremely bright and talented individuals. Mike Koplow and Deepa Madan were both involved in this project from the beginning. As my predecessor, Mike was always a great motivator while constantly adding his unique sense of humor. I am glad to be able to call Mike both a colleague and a friend. Deepa's hard work and persistence helped build the foundation for this project. I am confident in her future success as she continues her graduate studies. This project culminated from the hard work of many students, and it goes without saying that it could not have succeeded without Alan Lee, Kevin Huang, Brian Mahlstedt, Jonathan Brown and Michael Nill. Each and every one of them contributed immensely to this project, and it has been an honor working with them. I look forward to watching their successes as they develop their careers.

My time as Berkeley would not have been the same without the professional and moral support of these next individuals. They have become close friends with whom I have built lasting relationships. Although Christine Ho and I sometimes jest in an adversarial manner, she has been an extremely caring friend who unselfishly provides support to all those around her. Andrew Waterbury has been equally supportive, albeit in his own taciturn manner. I am grateful for their kindness, support and friendship.

I cannot continue to thank my lab mates and colleagues enough. Ba Quan, Lindsay Miller, Peter Minor and Eli Leland have been extremely supportive and I will always cherish their friendships. At the risk of leaving someone out, I would also like to particularly thank Dan Chapman, Dan Steingart, Jay Keist, Joe Wang, Rei-Cheng Juang, Jack Ye, Chris Sherman, Andrew Pullin,

Michael Klein, Jessica Xu, Rich Winslow, Michael Mark, Mervin John, David Chen, Wei Min Liu, Kedar Hippalgaonkar, John Waldensen, Ryan Xie, Mike Siedel and Richard Xu among many others.

My girlfriend Valeria for her love, support and understanding. Words cannot express the heartfelt appreciation I have for her. She is the most caring person I know, and I am indebted to her.

I am forever grateful to my parents for their unfaltering love and support regardless of my choices and paths. It is impossible to describe the level of my appreciation for them. I would not be here today without the enormous amount of effort and sacrifice they have put forth. My mother's strict dedication to raising and caring for me at the expense of everything in her life cannot be stressed enough. My father has always been a rock, providing me with a sense of safety and stability when I need them most. I know I can never repay my parents for everything they have given me, but I hope to begin someday. They will always be my heroes.

Finally, I would like to thank my extended family for their love and confidence in me. Uncle Russell and Aunt Evelyn for always looking after me and loving me as their own. Jennifer, Richard, Chen and Jean for always being there for me. You are the siblings I never had. My grandfather for his constant advice and insight. And lastly, my grandmother, who always loved and cared for me more than, it seemed, anything in the world. I wish she could be here with us today.

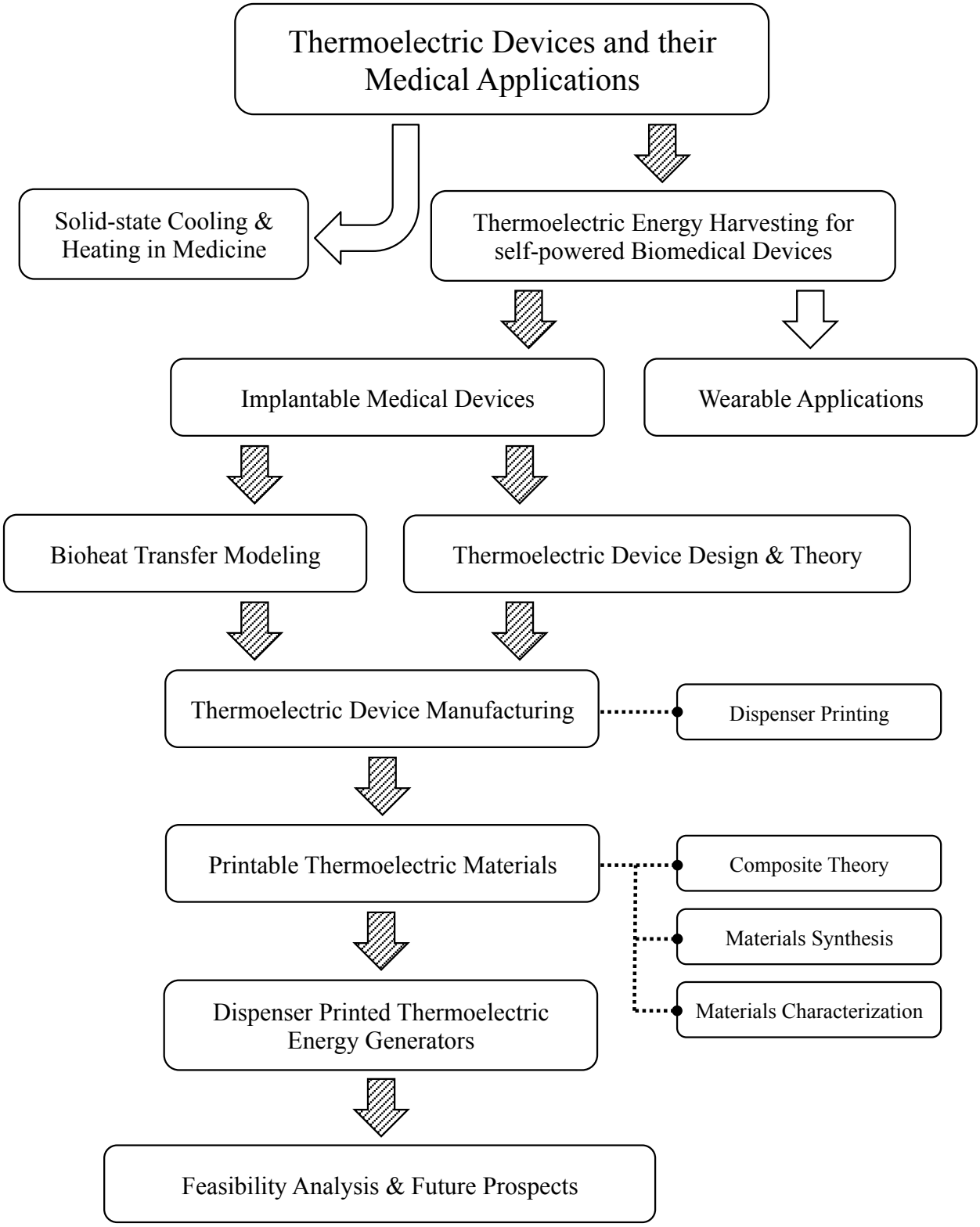
Thermoelectric Devices and their Medical Applications
Solid-state Cooling & Heating in Medicine
Thermoelectric Energy Harvesting for self-powered Biomedical Devices
Implantable Medical Devices
Wearable Applications
Bioheat Transfer Modeling
Thermoelectric Device Design & Theory
Thermoelectric Device Manufacturing
Dispenser Printing
Printable Thermoelectric Materials
Composite Theory
Materials Synthesis
Materials Characterization
Dispenser Printed Thermoelectric Energy Generators
Feasibility Analysis & Future Prospects

Chapter 1

Introduction to Thermoelectric Devices and their Medical Applications

1.1. Introduction

The development of the first implantable artificial pacemaker over half a century ago spurred the phenomenal growth in the field of biomedical engineering within the last few decades. Through the collaborative efforts between scientists, engineers and medical professionals, a large number of implantable medical devices are available today to treat a variety of symptoms. The success of their research can be exemplified by today's multibillion-dollar medical device industry [1]. Advancements in biomedical device technology have in large part traced the fast-paced electronics industry. The increasing medical needs of the aging population will inevitably expand because of longer life expectancies in the industrialized world [2]. These demands will only lead to more advanced and integrated medical devices that extend beyond the clinical environment and towards home healthcare systems. This is best exemplified by today's advanced pacemakers that include wireless communication for remote patient monitoring by physicians [3].

As implantable medical devices become exceedingly complex while maintaining compactness to reduce invasiveness, technical barriers arise from the perspective of energy storage. While the development of the mercury battery, and subsequently the lithium-iodide battery, galvanized the adoption of implantable devices, their limited energy and power densities are becoming conspicuous [4]. Barring any significant scientific progress in energy storage technologies, the lifetime of implanted medical devices will inevitably be much shorter than the expected lifespan of patients. Battery replacement adds risks and costs to the patient from seemingly unnecessary surgical procedures.

While the energy requirements of today's implantable medical devices are exceedingly lower (Figure 1.1) due to better engineering, a perpetual power source that extends the longevity of implantable devices still remains a formidable challenge for both engineers and scientists. Figure 1.1 suggests a need for a constant power source ranging from 10 μW to several mW. These challenges present opportunities for various energy harvesting techniques to be used in the human body. Figure 1.2 shows the available sources of energy for energy harvesting from the

body. These sources include biomechanical energy from kinetic movements of the joints [5], solar energy from external irradiation from the sun [6] and also vibrational energy from both cardiac muscle contractions [7], [8] and foot impact during movement [9]. While vibrational, biomechanical and solar energy can be converted to small amounts of power, thermal energy is the most abundant source of energy in the human body. The human body ultimately converts all caloric intakes into heat for maintaining its core body temperature.

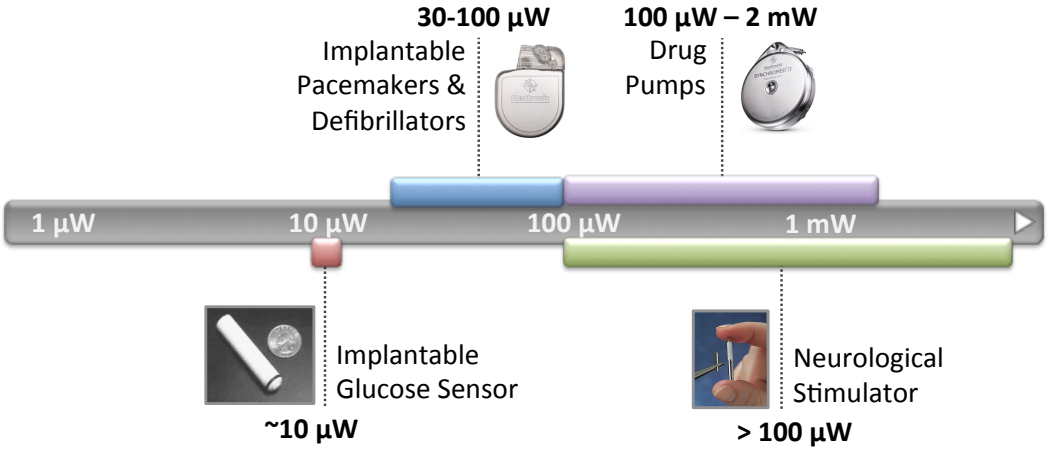

Figure 1.1. Typical power requirements of some implantable medical devices [10-12].

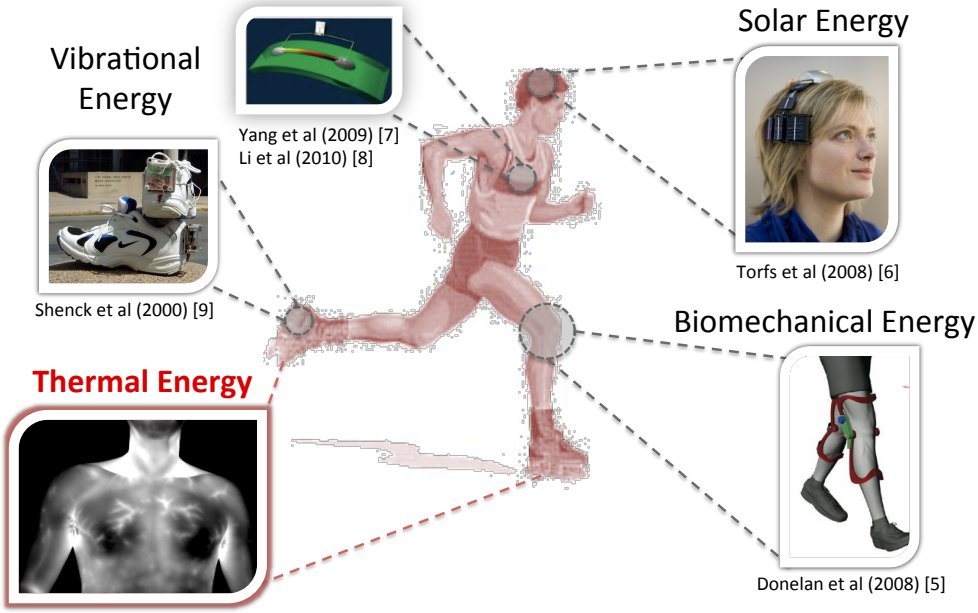

Figure 1.2. Sources of energy for energy harvesting in the human body [5-9].

The natural abundance of heat in the human body makes solid-state thermal energy harvesting with thermoelectric energy generators an excellent choice for energy harvesting in the body. By scavenging waste heat, thermoelectric generators might provide a perpetual solution to the ever-growing energy demands of implantable medical devices. This work aims to not only examine the feasibility of applying thermoelectric generators as power sources for implantable applications, but also present design principles, manufacturing methods and novel materials for

thermoelectric devices. While the focus of this work is specific to the field of biomedical devices, the technology that has been developed is applicable to other applications involving thermal energy harvesting. The goal of this work is to ultimately provide a technology platform that impacts the advancement of future autonomous healthcare technologies.

This chapter will begin by presenting the operating principles of thermoelectric devices, followed by a review of past and present uses of thermoelectric technologies in medicine.

1.2. Thermoelectric Operating Principles

In 1821, a German physicist named Thomas Johann Seebeck discovered that a compass needle could be deflected by a closed loop formed by two metals joined in two places, while maintaining a temperature difference between the junctions. This was due to the metals responding to the temperature difference, forming a current loop and a magnetic field. Since Seebeck did not recognize the presence of an electric current, he inaccurately named the phenomenon the thermomagnetic effect. This effect was later realized to be a result of an induced electrical potential from the temperature difference, leading to the coined term, "thermoelectricity". Today, this is known as the Seebeck effect. The measured output voltage is approximately proportional to the temperature difference between the two junctions. The proportionality constant is known as the Seebeck coefficient (α) and is often referred to as the thermoelectric power or thermopower. The Seebeck coefficient is a property of the materials and is influenced by its temperature and crystal structure. Metals typically have small Seebeck coefficients, while doped semiconductors have large Seebeck coefficients. The sign of the Seebeck coefficient determines the dominant charge carriers in transport of charge.

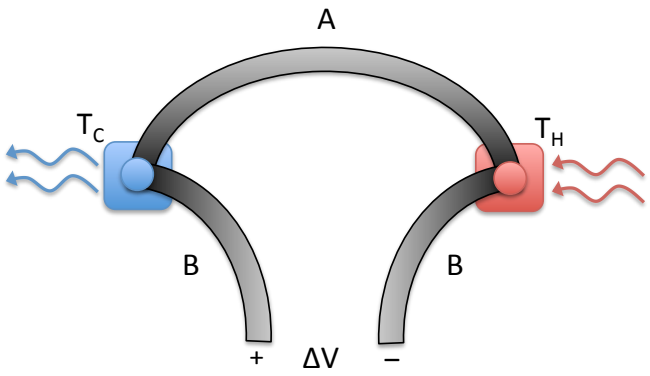

Figure 1.3. Schematic of a thermocouple demonstrating the Seebeck and Peltier effects. In the Seebeck effect, when two wires of different materials (A and B) are connected and a temperature difference (T_H and T_C) is maintained at the two junctions, a voltage potential (ΔV) can be measured across the wires. Conversely, when a ΔV is applied across the wires, a T_H and T_C can be formed across A and B.

It would be more than a decade after Seebeck's discovery (1834) before Jean Charles Athanase Peltier, a French physicist and watchmaker, found that an electrical current could produce heating or cooling at the junction of two dissimilar metals. A few years later, the German physicist Heinrich Lenz expanded on Peltier's discovery and found that by altering the direction

of current flow, heat could be either removed from a junction to freeze water into ice or heat could be generated to melt ice. The heat absorbed or created at the junction was proportional to the electrical current and was coined the Peltier coefficient.

Twenty years later, in 1851, William Thomson (later known as Lord Kelvin) issued a comprehensive explanation on the thermodynamic relationship between the Seebeck and Peltier effects. The Peltier coefficient is essentially the Seebeck coefficient multiplied by the absolute temperature. This thermodynamic derivation led Thomson to predict a third thermoelectric effect, known as the Thomson effect. The Thomson effect describes the rate of heat created or absorbed in a current-carrying metal or conductive material that is subjected to a temperature gradient. Together, these effects are known as the thermoelectric effects [13-15].

Perhaps the most prevalent application of the thermoelectric effect can be found in thermocouples for measuring temperatures. Because the Seebeck coefficients of many metals have been measured, the voltage measured between two metal junctions can be used to accurately calculate the temperature at the junction when calibrated. The discovery of Bi_2Te_3-based semiconductors as high performance thermoelectric materials in the 1950's opened opportunities for energy generation and refrigeration applications. Today, commercially available thermoelectric devices similar to one shown in Figure 1.4c can be purchased for a variety of applications. By using two ingot-shaped pellets (elements) of semiconductor-based materials to form a thermocouple, a device can be formed by placing pairs electrically in series and thermally in parallel. Scaling of thermocouples into devices allows for enhanced Seebeck and Peltier effects that open up applications such as thermal energy generation and refrigeration.

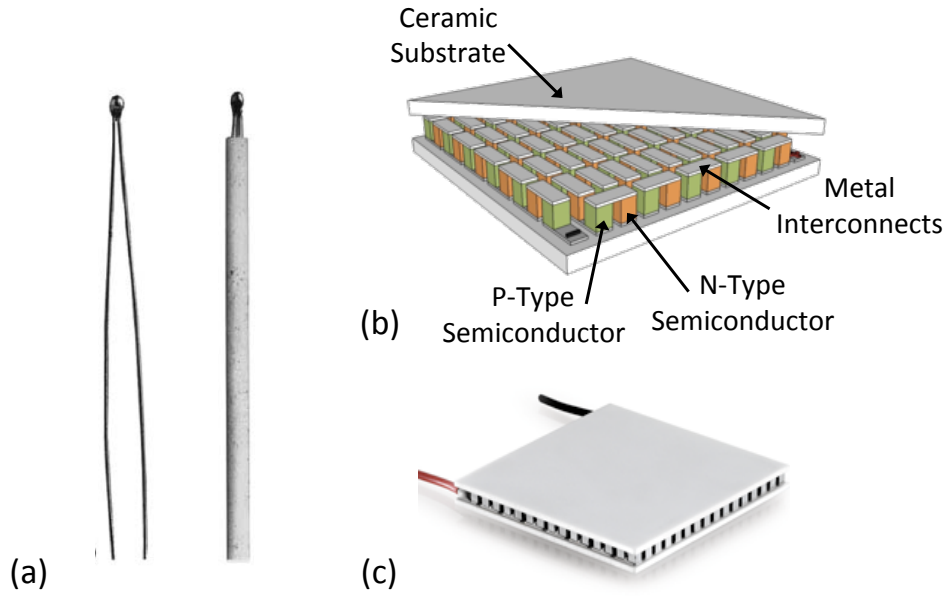

Figure 1.4. (a) Image of conventional metal and metal/alloy thermocouple [15]; (b) schematic of a thermoelectric device; (c) image of a commercially available thermoelectric device [16].

Recent advances in thermoelectric technologies are beginning to meet some of the needs in the growing number of advanced medical devices. While commercial thermoelectric technologies have been available since the 1950's, thermoelectric devices have historically found limited use in biomedical applications. Early uses took advantage of the solid-state heating and cooling

effects for niche applications such as DNA thermal cyclers, medicine cooling bags and medical imaging devices. These are often considered premium applications where the advantages of rapid solid-state heating or cooling outweigh the costs and inefficiencies associated with the state-of-the-art thermoelectric unit. Recent advances in both thermoelectric research and biomedical engineering, however, have drawn renewed interest from the medical community, particularly in its energy harvesting uses. The burgeoning portable electronics industry with its omnipresent goal of low-power consumption and high performance has spawned a new wave of portable and implantable biomedical devices. Consequently, the timing is apt for the convergence of novel thermoelectric technologies with current and future medical devices.

1.3. Solid-state Heating & Cooling for Medical Applications

Thermoelectric heating and cooling utilize the Peltier effect to act as a solid-state heat pump. Also called Peltier devices, thermoelectric heat pumps transfer heat from one side to the other when direct current is applied. State-of-the-art Peltier devices generally have efficiencies around 5-10% of an ideal refrigerator (Carnot cycle). Compared to a conventional compression cycle system with efficiencies around 40-60%, Peltier devices are used when their solid-state nature provides significant advantages. They provide a compact form of reversible and rapid heating or cooling with no moving parts [17]. These unique attributes open the use of Peltier devices to some specific biomedical applications.

Today, the most ubiquitous biomedical uses of thermoelectric devices occur in modern polymerase chain reaction (PCR) thermal cycles for rapid heating and cooling of DNA. Developed in 1983 by Kary Mullis, who subsequently won the Nobel Prize in Chemistry in 1993 for his work, PCR has become a ubiquitous and indispensible method used in medical and biological laboratories for DNA amplification [18]. The process of replicating DNA molecules using PCR requires thermally treating the DNA to three separate set points: (1) denaturation at 94˚C, (2) annealing at 54˚C and (3) extension at 72˚C. These steps are then repeated multiple times with each cycle doubling the amount of DNA [19]. This process naturally lends itself to using solid-state thermoelectric heater/coolers to speed up the thermal cycling time needed for these reactions. The reversibility, fast response and ease of deployment of Peltier devices make them ideal for PCR equipment [20-22]. Thermoelectric manufacturers such as Marlow Industries and Nextreme have successfully commercialized thermoelectric devices in bench top PCR systems using standard Bi_2Te_3-based Peltier devices [23], [24]. Although PCR is a critical application of current thermoelectric devices in the biomedical industry, there have been few alternative uses of thermoelectric devices outside of PCR. It is thus of interest to explore various viable applications for thermoelectric devices.

A potential avenue for wider use of solid-state heating/cooling thermoelectric devices may lie in therapeutic medical applications. Amerigon, one of the more prominent thermoelectric device manufacturers, and its subsidiary, BSST, has explored the use of thermoelectric devices for thermoregulation of cancer patients. Cancer patients undergoing chemotherapy are susceptible to low white blood cell count (neutropenia) [25], infection [26] and low red blood cell count (anemia) [27]. These side effects can lead to temperature sensitivity, leaving the patient feeling cold [28]. Thus, therapeutic products such as temperature controllable blankets or couches using thermoelectrics may potentially help patients cope with the side effects. Amerigon and Mattress, Inc. recently co-developed a thermoelectric heating and cooling mattress called the YuMe

Climate Control Bed, albeit for the luxury mattress market [29]. However, such products can potentially be adapted for therapeutic medical applications. Therapeutic cooling and heating of tissue injuries is also an effective treatment and has been known to reduce the healing time [30]. However, such treatments are traditionally performed with ice or heat packs [31], [32] that are significantly cheaper than thermoelectric devices. There may be an opportunities for solid-state heating or cooling in professional sports therapies. One can perhaps envision a wearable thermoelectric heater/cooler for athletes who require constant and immediate therapy for low-grade tissue injuries, allowing them to return to their activities. Another potential therapeutic application utilizing thermoelectric technology is in therapeutic hypothermia. Therapeutic hypothermia has been shown to be particularly effective for treatment of neonatal encephalopathy (brain disorders) (Figure 1.5) [33], [34] and patient neuroprotection following cardiac arrest [35], [36]. The current method of treatment utilizes water blankets, vests or wraps. While this method dates back to the 1950's, it is still the most prevalent method for noninvasive patient cooling. Nonetheless, water blankets possess certain drawbacks, such as electrical hazards from fluid leakage [37], which might open opportunities for solid-state cooling. Several cases have been reported of cooling blankets causing significant burns to patients [38]. Precise temperature control and response is also frequently another issue with water blankets, resulting in temperature overshoot and delayed compensation. Thus, therapeutic heating and cooling applications may perhaps find potential adoption of thermoelectric technologies if certain traits such as flexibility/conformability, improved coefficient of performance (COP) and lower cost are met by future technologies.

Figure 1.5. An infant being treated for hypoxia (lack of oxygen at birth) with a state-of-the-art cooling blanket. Cooling blankets allow for treatment of newborns that show signs of brain damage and are at risk of developing various cognitive disorders (courtesy of Melissa P.).

Another potentially promising application of thermoelectric cooling and heating is its use in portable biomedical systems. With the future of healthcare focused on portability and on-site care, the field of Biological Micro-electromechanical systems (BioMEMS) has rapidly grown during the last decade [39]. Advancements in micro-engineering adapted from the semiconductor

industry have opened the possibility of scaling laboratory-based systems such as PCR, electrophoresis, single molecular detection and disease diagnosis among many others [40-42]. By utilizing MEMS techniques to make portable laboratory devices, commonly called "lab-on-a-chip" or micro-total analytical system (μTAS), such systems can be fabricated using low-cost and scalable methods while providing device portability and consuming less reagents. The total market size of microarrays and lab-on-a-chip systems was approximately $2.6 billion in 2009 and is expected to annually grow by 17.7%, reaching $5.9 billion in 2014 [43]. Some of these lab-on-a-chip processes such as micro-PCR, a "scaled-down" version of traditional PCR, also require rapid thermal cycling. The portable nature of such devices would require rapidly controllable heating and cooling techniques that can potentially be provided from MEMS-scale thermoelectric devices. While the applications of thermoelectrics to lab-on-a-chip devices are limited to a few specific processes, the expected growth in the field might make it an attractive market for MEMS and micro-scale thermoelectric heating and cooling.

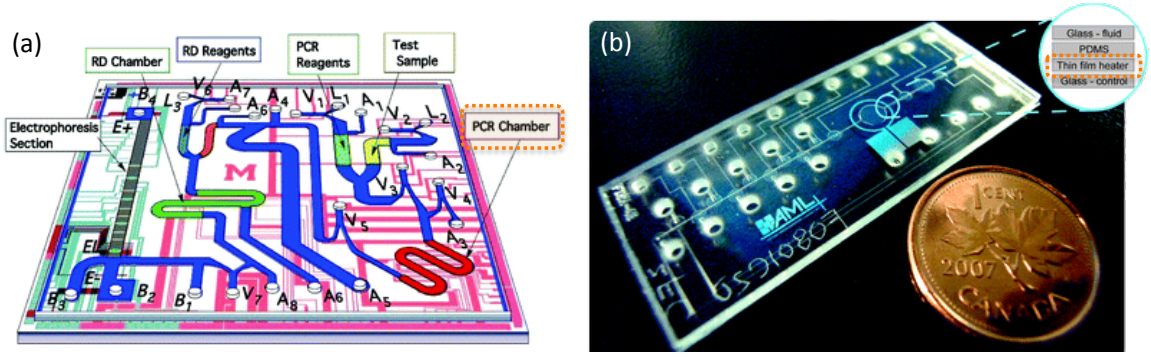

Figure 1.6. Examples of fully integrated lab-on-chip devices: (a) a microfluidic device for influenza and other genetics analyses [44] (reproduced by permission of The Royal Society of Chemistry) and (b) an integrated microfluidic chip for chromosome enumeration using fluorescence in situ hybridization [45] (reproduced by permission of The Royal Society of Chemistry). The thermal reactions within the chips (highlighted) can potentially utilize small-scale thermoelectric heater/coolers.

1.4. Thermoelectric Energy Harvesting for Biomedical Devices

The history of medical diagnostics and treatments can be traced back millenniums to the ancient Egyptians and Greeks. With extraordinary advances in research and enabling technologies, modern medicine has come a long way from the clinical observations of Hippocrates. As diagnostic tools continuously evolve and improve, they tend towards miniaturization and mobility. Continuous patient physiological monitoring can now be performed outside the clinical environment, providing physicians with more thorough information. Life-supporting medical devices have transformed from bulky and invasive machines to portable implantable devices, freeing patients from the direness of permanent hospitalization. Mobility inevitably requires portable energy solutions, a role currently filled by energy storage technologies such as batteries. As it becomes clear that progress in energy research does not follow Moore's law, a multitude of energy harvesting approaches may eventually allow energy research to keep up.

Approximately 80% of the metabolic energy generated in the human body is lost to low-grade heat for thermoregulation [46]. In order to maintain the core body temperature of approximately 37˚C, our bodies constantly generate heat while simultaneously taking active steps dissipating the heat to prevent overheating (such as fever) [47-49]. The heat is eventually lost through conduction, convection, radiation and evaporation, making it the most abundant source of energy from the body [50]. The human body dissipates approximately 100 W of power at rest from thermoregulation [51], [52]. While the heat emitted from the body is readily available, the quality of the heat is too low for any conventional heat engines to harvest [51]. Thermoelectric devices, acting as solid-state power generators from temperature differences [17], may be suitable for harvesting the low quality heat emitted from the body. This recovered energy can potentially provide power for a new wave of diagnostic and medical tools.

Thermoelectric energy harvesting in the biomedical realm can be divided into two sets of applications: (1) wearable and (2) implantable applications. This section will discuss developments and ongoing research in both sets of applications while focusing on the aspects of thermoelectric device design and integration.

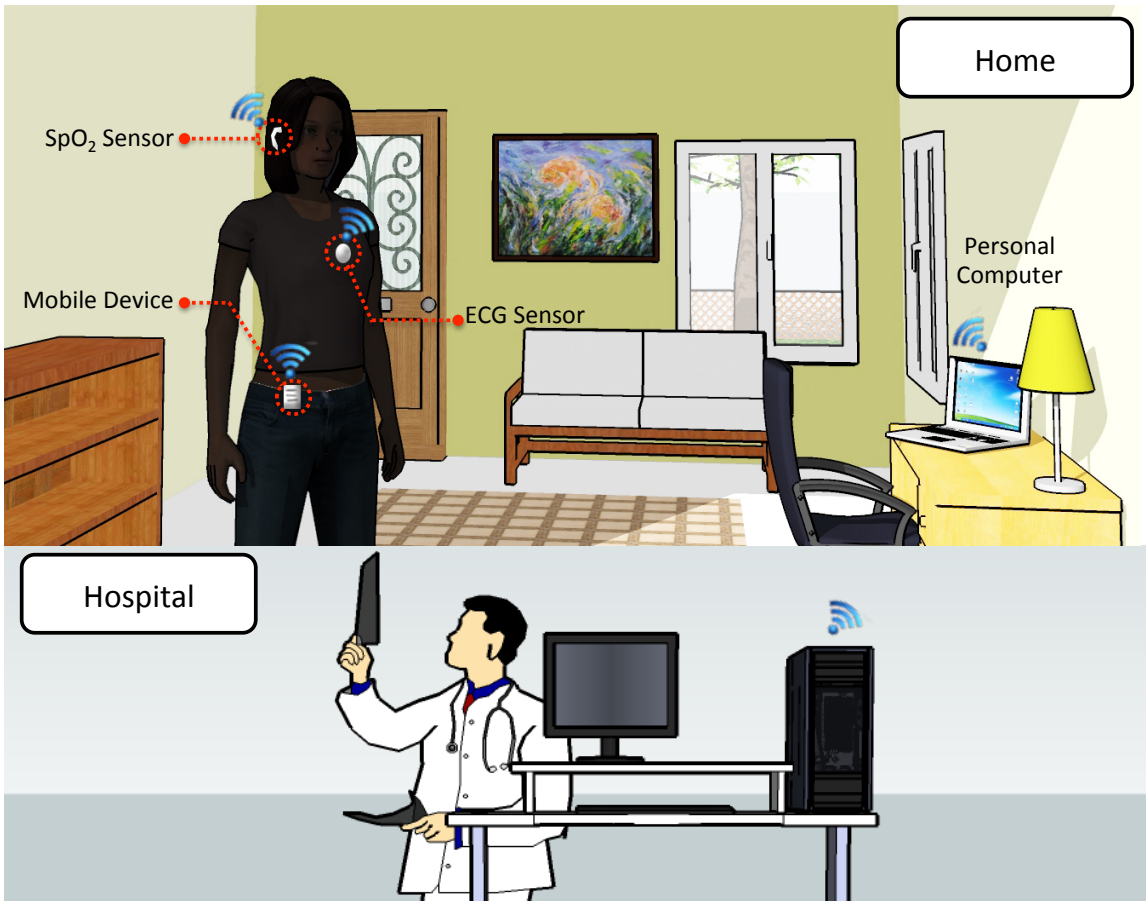

Figure 1.7. An illustration of a wireless physiological monitoring system, also frequently called a Body Sensor Network (BSN) (Courtesy of Dan Chapman).

1.4.2. Wearable Applications

The increasing demand for low-cost and personalized wireless physiological diagnostic tools has increased research efforts in wireless body sensor networks (BSN's) and mobile health (mHealth). Figure 1.7 illustrates an example of a wireless physiological monitoring system. These applications can include long-term (24/7) monitoring of the local/regional events in tissue or organs under investigation and personalized home health care. These tools can be applied to monitoring of patients with chronic diseases, hospitalized patients or the elderly [53]. New generations of medical diagnostic "smart" probes often require high sampling rates resulting in high-energy consumption which has ultimately limited device lifetimes. Due to power constraints, there is often a trade-off between sensor resolution/sampling rate and device usability lifetime. Thermoelectric generators (TEG's) can provide a method to increase the energy storage capacity in BSN's by harnessing thermal gradients between the body and ambient environments. The power and voltage requirements of today's micro-electronic systems have significantly diminished to match the power output of TEG's at low temperature differences (between 5 and 20 K). Studies have suggested that a constant power source exceeding 100 $\mu W/cm^2$ at 1 V is an ideal energy harvester for practical wearable sensor networks [6], [12], [54-57]. Some state-of-the-art ultra-low power radios have reported power consumptions <10μW with transmit/receive ranges of up to 10m [12] [58]. Advancements in TE materials and device fabrication technology have only recently been able to meet some of the power and voltage requirements of the radios and sensors within a constrained device footprint. It is thus important to understand the remote physiological monitoring systems and their applications to provide insight into the design and feasibility of wearable TEG's.

1.4.2.1. *Wearable Biomedical Sensors*

Wearable biomedical sensors typically require wide deployment on various parts of a patient's body with electrical leads from each sensor. As a result, entanglement of electrical wiring becomes an issue while the patient's mobility is limited to the connected instrument. BSN's allow such sensors to "cut the cord". Table 1 shows a list of various common physiological sensors and their clinical applications. These sensors are crucial for monitoring patient vital signs both within and outside the clinical environment. Although these sensors have a diverse range of clinical applications extending far beyond the scope of this chapter, only the two most salient types of sensors will be discussed: biopotential sensors and pulse oximeters.

Sensors that benefit most from BSN's are the family of biopotential sensors that include electroencephalography (EEG) for measuring neural activity at the scalp, electrocardiography (ECG or EKG) for measuring cardiac activity and electromyography (EMG) for recording electrical activity of the muscles [59]. These types of sensors are particularly important to remote physiological monitoring of patients at home, first responders and military personnel [53], [60-63]. Although these biopotential sensors have different diagnostic purposes, they share similar principles of operation to measure electric potentials on the surface of living tissue. An electrochemical transducer is used to measure the ionic current flow in the body to detect muscle contractions and nervous stimuli. Because the current flow in the body is due to ion flow, the electrode must act as a transducer between the ionic transport and electrical current. This is accomplished by first placing an electrolyte "jelly" solution (typically containing Cl^- ions) on the

surface of the tissue, followed by the transducer (typically an Ag-AgCl electrode). The non-contacting side of the electrode is connected to an electrical wire [59]. The surface recording electrode can be used to measure many different biopotential signals. The amplitude of these low electrical signals varies from 10 μV to 1 mV and the frequency can vary from 50 Hz to 1000 Hz. While signal amplification and noise reduction are required due to the low signals from the biopotential sensors, state-of-the-art electronics have reduced the power requirements to <60 μW [6].

Beyond biopotential sensors, pulse oximeters are another crucial measurement device for monitoring patient vital signs. Pulse oximeters non-invasively monitor patient pulse and blood oxygen saturation (SpO_2) levels by measuring the ratio of visible red light to infrared light absorption at the fingertip. Unlike biopotential electrodes, pulse oximeters require additional power for the LED. While commercial pulse oximeters consume 20-60 mW of power, research has shown that lower sampling rates with novel algorithms can lower the power consumption by 10-40X without loss of accuracy [64].

Table 1.1. List of common wearable sensors and some of their clinical applications.

Sensor	Measurement Function	Clinical Application
Electroencephalography (EEG)	Electrical activity of the scalp	Epilepsy diagnosis, sleep disorder studies, loss of consciousness, dementia
Electrocardiography (ECG)	Electrical activity of the heart	Heart related diseases such as arrhythmias, coronary artery disease and tachycardia
Electromyography (EMG)	Electrical activity of the muscle	Detection of neuromuscular diseases, kinesiology and motor control disorders
Pulse oximeters	Oxygen saturation in the blood	Patient monitoring during intensive care, surgical operation, postoperative recovery and emergency room
Ambulatory blood pressure monitor	Continuous blood pressure monitoring	Detection of hypertension (high blood pressure) and hypotension (low blood pressure)
Thermistor or thermocouple	Skin temperature	Neonatal temperature monitoring; diabetic foot ulceration [Armstrong], Infectious diseases, fever
Accelerometer	Patient movement and orientation	Impact and fall detection in elderly patients

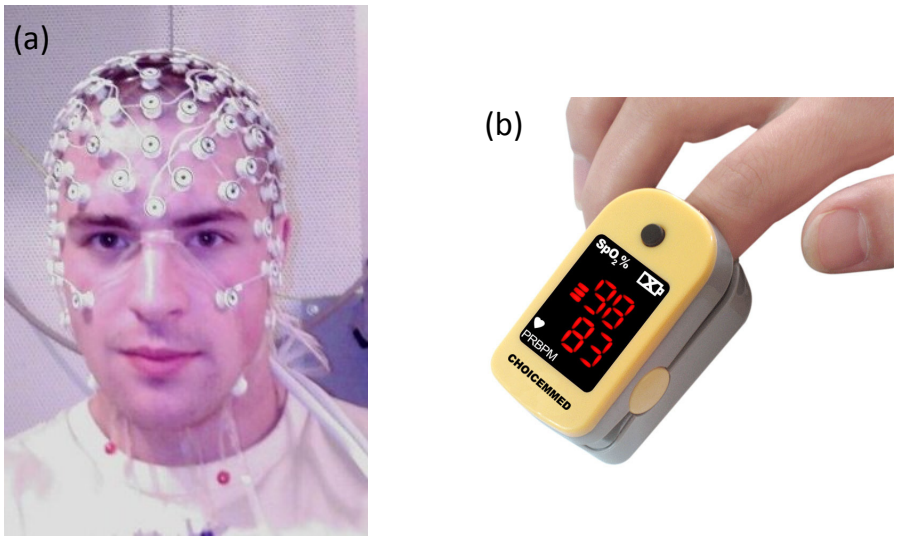

Figure 1.8. Image of (a) a patient outfitted with an EEG cap with each individual electrode is wired to an instrument for data collection, and (b) a digital pulse oximeter for measuring patient pulse and blood oxygen saturation.

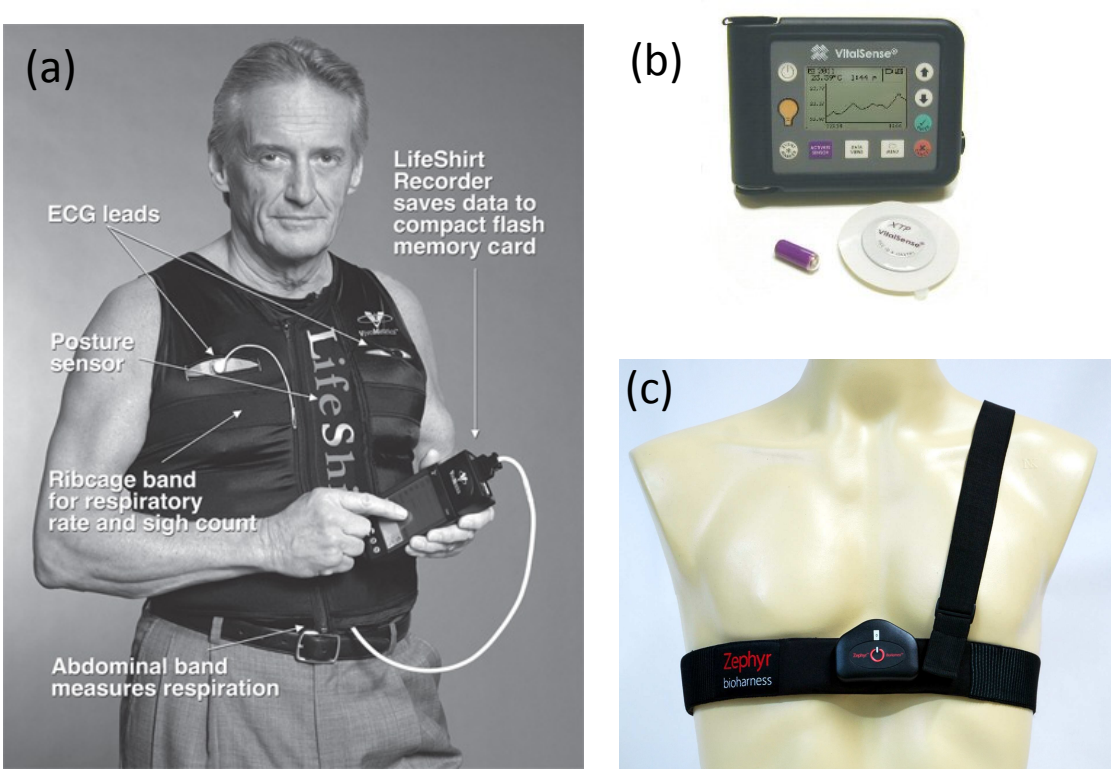

Figure 1.9. (a) Image of the Vivometrics Lifeshirt. The system is a garment that continuously collects patient vital signs for remote physiological monitoring [65]. (b) Image of the Philips Respironics VitalSense which consists of a portable data logger and monitor (top), self-adhesive temperature patches (bottom right) and an ingestible thermometer (bottom left) (courtesy of Philips Respironics) [66]. (c) Image of the Zephyr Bioharness which straps to the body and monitors the user's heart rate and breathing while wirelessly relaying the data via Bluetooth [67] (courtesy of Lyle Reilly).

1.4.2.2. *Remote Physiological Monitoring Systems*

While there are currently very few commercially available remote physiological monitoring systems, some have already entered the market. The LifeShirt by VivoMetrics was among the first commercially available fully integrated wearable physiological sensor system for remote patient monitoring. The LifeShirt (Figure 1.9) is a wearable vest with ECG sensors, respiratory sensors, accelerometers, pulse oximeters, galvanic skin response measurement sensors, blood pressure monitor, microphone and an electronic diary all integrated into Bluetooth capable system [65]. Philips-Respironics has also developed a wirelessly integrated physiological monitoring platform called VitalSense. The modular system allows for a variety of wireless and wearable sensors to transmit data to a portable data logger and monitor. It currently supports measurement of core body temperature, heart rate, respiration rate and skin temperature [66], [68]. Appendix A describes some experiments performed with the VitalSense system to monitor skin temperature changes. A variety of other systems, currently available, include the HealthVest (SmartLife Technologies) [60], [69], Equivital (Bio-Lynx Scientific Equipment, Inc.) [70] and Bioharness (Zephyr) [67], [71]. While all systems utilize similar sensors for remote physiological monitoring, the wireless technology may perhaps vary based on the achievable power reduction of the radios. There is ultimately a trade-off between battery life (<10 days) and sampling rate due to power consumption of the radio and processor. Despite the commercial availability of BSN's and remote physiological systems, issues related to system integration, sensor miniaturization, low-power circuitry design, wireless communication protocols and signal processing are currently being investigated [53]. Energy harvesting from wearable TEGs can enable future BSN technologies by providing a constant power source.

1.4.2.3. *Design of Wearable TEG's*

A wearable BSN system typically consists of the biomedical sensors, a signal amplifier, a microcontroller for processing data, and a power source such as a battery and a wireless radio to transmit the data to a computer or mobile device [53], [54], [62], [72]. The total power consumption is ultimately a function of the duty cycle (data acquisition and transmission frequency) and the sensor resolution. Since most of the wearable sensors listed in Table 1 function by providing low voltage signals (100's of μV), the power consumption of the sensor is quite low and is only limited to the signal amplification. The radio's average power consumption ultimately is the predominant power draw and becomes the limiting factor for the lifetime of the wireless sensor [55], [58]. While a higher sampling rate may allow for finer data resolution, it can significantly shorten the lifetime of the sensor. Torfs et al demonstrated an autonomous wearable EEG with average power requirements of 0.6 mW to 1.4 mW for sampling rates of 128 Hz to 512 Hz, respectively [6]. The choice of the sampling rate is thus very application dependent and system designers must frequently make tradeoffs between the battery capacity (weight), battery life and sampling rate [72]. While significant research is currently ongoing to reduce the average power consumption of wireless radio to <10 μW [12], [58], there is inevitably a lower limit. Since the power output of the TEG and the power consumption of the radio are subject to significant environmental variability, a TEG is not likely to replace a battery. It can instead be used to supplement the existing power source to extend the lifetime of the battery and sensor.

Because the available temperature difference between the human body and the ambient environment is quite low (0-20˚C), it is crucial for the wearable TEG to be optimized to maximize power output within a small areal footprint (1-2cm2). While a TEG is not likely to produce >1mW of power without being significantly large, a target power output of 100μW/cm2 is ideal to sufficiently power most wireless applications. Another requirement for BSN's is the minimum 1V output from the TEG for power electronics [73]. While state-of-the-art power electronics are capable of accepting input voltages as low as 20mV by exploiting DC-DC converters, these converters have fairly low conversion efficiencies (<50%) [74]. These inefficiencies subsequently outweigh the benefits associated with providing an already inefficient energy conversion system. In order to achieve a 1V matched load output, the TEG would require high-density arrays of elements, achievable by recent advances in MEMS based TEGs [75-78].

When designing TEGs for wearable applications, it is important to consider the thermal resistance matching of the TEG to the human body [55], [79]. Proper matching of the high thermal resistance of the TEG to the high thermal resistance of the human body provides a maximum temperature difference across the generator. The thermal resistance model of a wearable TEG is shown in Figure 1.10. Leonov et al demonstrated that by matching the thermal resistance of the TEG, R_{TEG}, with the ambient environment, it can be shown as:

$$R_{TEG} = \frac{(R_{body} + R_{sink})R_{air,0}}{2(R_{body} + R_{sink}) + R_{air,0}} \tag{2.1}$$

Where R_{body} is the thermal resistance of the human body at the TEG location, R_{sink} is the thermal resistance of the heat sink from convection and radiation and $R_{air,0}$ is the thermal resistance of the TEG if all the thermoelectric elements were removed and replaced with the surrounding insulator (usually air) [79], [80]. The thermal resistance of the generator can thus be designed based on the total resistance of the elements, $R_{elements}$, and the resistance of the empty space around the elements, R_{space}, such that $R_{TEG} = R_{elements}R_{space}/(R_{elements} + R_{space})$.

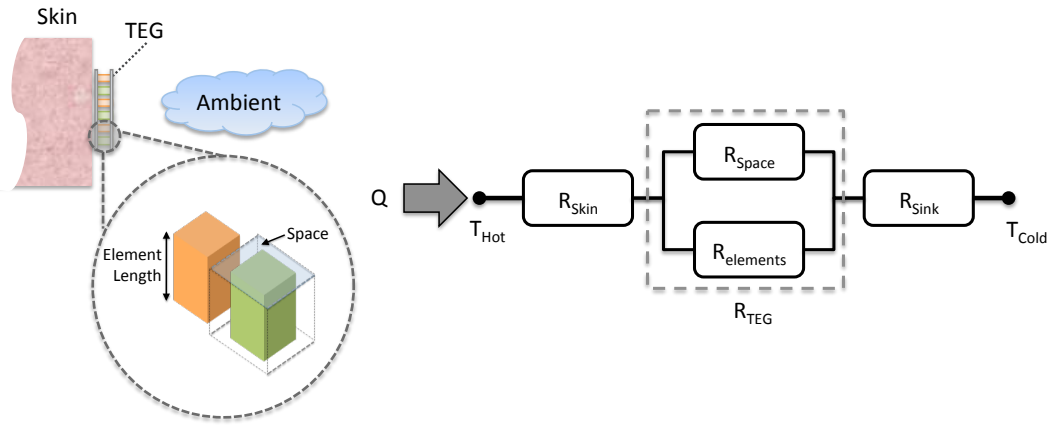

Figure 1.10. Schematic and thermal circuit of a wearable TEG. (Adapted from [80])

The skin thermal resistances can vary significantly depending on location and environment, and as a result, it is difficult to measure with accuracy. Measured values of thermal resistances can also vary based on the TEG and the heat sink used (such as fins), thus changing the local heat flow. It is also important for the design of the TEG to not significantly change the heat flow of the body to the point of discomfort. Table 2 shows some thermal resistance measurements at

various locations and ambient conditions using a 3 cm x 3 cm x 3 cm TEG developed by Leonov et al [79].

Table 1.2. Thermal resistance measurements measured at various body locations [79].

Body Location	Ambient Temperature	Thermal Resistance
Trunk	23˚C	200-800 cm^2K/W
Outer Wrist	22.7˚C	440 cm^2K/W
Inner Wrist (Radial Artery)	22.7˚C	120-150 cm^2K/W
Forehead	21.5-24.7˚C	156-380 cm^2K/W

While heat from the human body is capable of providing power to a wearable TEG in the range of 300 $\mu W/cm^2$ – 1 mW/cm^2, such conditions would result in noticeable discomfort and a cold sensation to the user. Thus, studies have suggested that a practical average power output for a wearable TEG using state-of-the-art TE materials with ZT = 1 is approximately 30$\mu W/cm^2$ [73]. Advances in TE materials to improve the power factor can ultimately improve this figure.

Another strategy to improve the power density of a wearable TEGs is through placement on exothermic regions of the body. Although this may limit the sensor application of the TEG, specific regions of the body may provide higher temperature differences across the generator. There has recently been a growing interest in the research of brown adipose tissue (or brown fat) in adults. In contrast to white adipose tissue, the abundantly found fat in mammals, brown fat is mostly found in infants and hibernating mammals [81]. Since its primary function is to generate heat, it helps maintain warmth and provides heat regulation in newborns and animals. Brown fat was traditionally believed to disappear in adults, but recent studies using positron emission tomography have shown that it is still present in the upper chest and neck of adults [82]. While the implications of these studies are focused on the metabolic effects of brown fat, its exothermic nature suggests the availability of potential "hot-spots" on the body. Such "hot-spots" may be utilized for optimal placement of wearable TEGs, providing more heat flow and power output. Future studies can potentially help understanding the applicability of brown fat to wearable TEGs.

1.4.3. Implantable Applications

Perhaps the earliest investigation of implantable thermoelectric generators surfaced during the late 1960's when zinc-mercury batteries were still the standard power sources for implantable pacemakers. The low energy densities of the zinc-mercury cells frequently limited the device life to <20 months and required patients to frequently undergo surgery to replace the cells [4], [83]. To solve this problem, Medtronic, currently one of the largest implantable medical device manufacturers in the world, and Alcatel jointly designed a nuclear-powered pacemaker consisting of a Plutonium-238 (Pu-238) radioisotope and a thermoelectric generator. The Pu-238, which has a half-life of approximately 85 years, radiated the container walls to provide a constant heat source, while the thermoelectric generator converted the heat to electrical energy for the pacemaker [4], [83], [84]. Figure 1.11 shows an image of the radioisotope TEG and pacemaker manufactured by Alcatel and Medtronic [85]. In 1970, the first radioisotope TEG

powered pacemaker was implanted in a human. Even accounting for the degradation of the radioisotope and the TEG, the pacemaker still functions in patients after more than 35 years from its production [86], [87].

Although the longevity of radioisotope TEG's proved it to be an excellent source of energy for pacemakers, the potential exposure to radiation and toxicity of plutonium was ostensibly a primary concern for physicians and patients. Plutonium is among one of the most toxic and fatal materials known to humans and can spontaneously burst in to flames when exposed to air. Extreme precaution was taken into the shielding design and engineering to prevent exposure of the plutonium and limit the amount of radiation to only 100mrem per year [83]. The average annual background dose for Americans is approximately 360mrem [88] while the standard occupational dose limits for one year is 5000mrem [89]. In 155 cases of implanted radioisotope TEG's, the frequency of malignant tumors was deemed to be no different than the standard population [90].

During the mid-1970's, radioisotope TEG powered pacemakers began to lose favor to lithium batteries which had calculated life-times of approximately 10 years. Physicians decided that it was more appropriate for patients to be updated with newer devices every 10 years instead of using devices with older technologies. Presumably, the inherent risks of plutonium were also reasons for switching to lithium-based batteries. Implants of radioisotope TEG pacemakers stopped in mid 1980's as lithium cells became the predominant power source for implantable medical devices [83], [90].

Figure 1.11. Image of an implantable pacemaker with a radioisotope TEG as the power source [85]. The size of the pacemaker is about as large as a pack of cigarettes, which is much larger than today's pacemakers [91].

Lithium-based primary batteries have become the standard power sources for today's implantable medical devices. Their prevalence in the medical device industry has been attributed to their high energy density and high voltage, allowing single cells to last >10 years with excellent stability and performance [10]. However, rapid developments in the biomedical device industry have begun to expose some limitations in today's lithium chemistries. Higher power and

energy requirements from new devices inevitably shorten the lifespan of the implanted lithium primary batteries, requiring frequent surgeries on patients to replace them. This provides an unnecessary strain on patients as any surgical procedure includes additional risks and hazards. In fact, some devices such as implantable deep-brain neurological stimulators used for the treatment of Parkinson's disease [92], [93], chronic headaches [94] and depression [95], require replacement of batteries every few months [94]. This results in significant scarring of the patient's skin near the collarbone where the battery is placed, creating additional stress for an already distressed patient. Some larger devices such as implantable ventricular assist devices (VAD), also known as implantable mechanical heart pumps, require more power than is possible for implantation. Once thought as a temporary device for patients awaiting heart transplants, implantable VAD's are becoming more prevalent among patients with heart failures. They provide patients with a life-supporting solution without the complications associated with transplants such as infection or organ rejection [96], [97]. However, to supply sufficient power to VAD's, a cable from the device connects to a control unit and large wearable battery packs through a small hole in the abdomen (Figure 1.12) [97]. The cable extruding out of the abdomen is coated in a biomaterial to allow tissue to heal around it without infection. Since the risk of a depleted battery is life threatening, patients must constantly worry about the battery life and many carry extra batteries for back-up [98].

It is thus important to explore alternative strategies to powering implantable devices by either extending the lifetime of batteries or providing perpetual power to such devices. This opens a niche for new thermoelectric generators to harvest waste heat from the body for implantable applications.

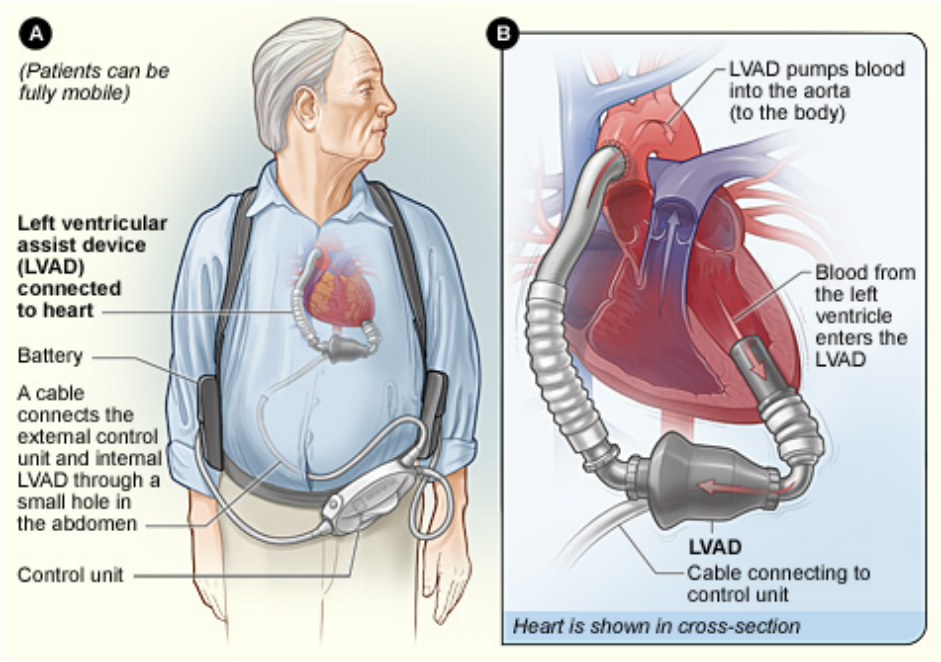

Figure 1.12. Schematic of an implantable left ventricular assist device (LVAD) [97].

1.5. Chapter Conclusion

1. While medical research continues to create novel biomedical devices, there is a growing concern for the usable lifetime of such devices. The increasing power demands of new technologies continue to exceed the energy supplied from primary batteries. The limitations of current energy storage solutions present challenges for widespread use of some medical technologies.
2. The "graying" of the western world and other cultures will require technologies for "aging at home" rather than hospitalization. Simultaneously, the growing cost of healthcare will drive new home healthcare solutions to low-risk conditions for the elderly. Novel home healthcare solutions will inevitably require long-term power sources with minimal user intervention.
3. There are currently more implantable medical devices being used than ever before, with the best example being the implantable cardiac pacemaker. The growing number of life-supporting electronics means an urgent need for self-powered devices to reduce risky surgical procedures for patients.
4. Thermal energy harvesting from the body may extend the use of biomedical devices beyond the lifetime of batteries. Thermoelectric energy generators are an excellent proposition for both wearable home healthcare solutions and implantable medical devices because of their solid-state nature, proven stability and energy harvesting efficiency from low-grade heat.
5. While technological advancements in energy harvesting face equally difficult challenges as energy storage devices, advancements in research and engineering will provide solutions to ultimately perpetuate the lifespan of medical devices.

Chapter References

[1] W. Greatbatch and C. F. Holmes, "History of implantable devices," *IEEE Engineering in Medicine and Biology Magazine*, vol. 10, no. 3, pp. 38–41, 49, 1991.

[2] E. L. Schneider and J. M. Guralnik, "The Aging of America," *JAMA: The Journal of the American Medical Association*, vol. 263, no. 17, pp. 2335–2340, May. 1990.

[3] Ben Gruber, "First Wi-Fi pacemaker in US gives patient freedom," *Reuters*, 10-Aug.-2009. [Online]. [Accessed: 08-Nov.-2011].

[4] V. Parsonnet, "Power Sources for Implantable Cardiac Pacemakers," *Chest*, vol. 61, no. 2, pp. 165–173, Feb. 1972.

[5] J. M. Donelan, Q. Li, V. Naing, J. A. Hoffer, D. J. Weber, and A. D. Kuo, "Biomechanical Energy Harvesting: Generating Electricity During Walking with Minimal User Effort," *Science*, vol. 319, no. 5864, pp. 807–810, Feb. 2008.

[6] T. Torfs et al., "Wearable Autonomous Wireless Electro-encephalography System Fully Powered by Human Body Heat," *IEEE Sensors 2008*, pp. 1269–1272, 2008.

[7] R. Yang, Y. Qin, C. Li, G. Zhu, and Z. L. Wang, "Converting Biomechanical Energy into Electricity by a Muscle-Movement-Driven Nanogenerator," *Nano Letters*, vol. 9, no. 3, pp. 1201–1205, Mar. 2009.

[8] Z. Li, G. Zhu, R. Yang, A. C. Wang, and Z. L. Wang, "Muscle-Driven In Vivo Nanogenerator," *Advanced Materials*, vol. 22, no. 23, pp. 2534–2537, May. 2010.
[9] N. S. Shenck and J. A. Paradiso, "Energy scavenging with shoe-mounted piezoelectrics," *IEEE Micro*, vol. 21, no. 3, pp. 30–42, 2001.
[10] C. L. Schmidt and P. M. Skarstad, "The future of lithium and lithium-ion batteries in implantable medical devices," *Journal of Power Sources*, vol. 97, pp. 742–746, 2001.
[11] J. H. Schulman et al., "Battery Powered BION FES Network," *Proceedings of the 26th Annual International Conference of the IEEE EMBS*, pp. 4283–4286, 2004.
[12] C. C. Ho et al., "Technologies for an Autonomous Wireless Home Healthcare System," *Sixth International Workshop on Wearable and Implantable Body Sensor Networks, 2009 (BSN 2009)*, pp. 29–34, 2009.
[13] D. K. C. MacDonald, *Thermoelectricity: an introduction to the principles*. New York: Wiley, 1962.
[14] J. S. Dugdale, *The Electrical Properties of Disordered Metals*. Cambridge: Cambridge University Press, 1995.
[15] D. M. Rowe, "General Principles and Basic Considerations," in *Thermoelectrics Handbook: Macro to Nano*, no. 1, D. M. Rowe, Ed. Boca Raton, FL: CRC Press, 2006.
[16] "Ferrotec Thermoelectric Products," *thermal.ferrotec.com*. [Online]. Available: http://thermal.ferrotec.com/thermal-home/. [Accessed: 16-Sep.-2011].
[17] F. J. DiSalvo, "Thermoelectric Cooling and Power Generation," *Science*, no. 285, pp. 703–706, 1999.
[18] J. M. S. Bartlett, D. Stirling, J. M. S. Bartlett, and D. Stirling, "PCR Protocols," vol. 226, New Jersey: Humana Press, 2003, pp. 3–6.
[19] J. Sambrook and D. Russell, *Molecular Cloning: A Laboratory Manual*, 3rd ed. Cold Spring Harbor, NY: Cold Spring Harbor Laboratory Press, 2001.
[20] L. E. Bell, "Cooling, Heating, Generating Power, and Recovering Waste Heat with Thermoelectric Systems," *Science*, vol. 321, no. 5895, pp. 1457–1461, Sep. 2008.
[21] T. Pogfai, K. Wong-ek, S. Mongpraneet, A. Wisitsoraat, and A. Tuantranont, "Low Cost and Portable PCR Thermoelectric Cycle," *International Journal of Applied Biomedical Engineering*, vol. 1, pp. 41–45, 2008.
[22] J. Kim, J. Lee, S. Seong, S. Cha, S. Lee, and J. Kim, "Fabrication and characterization of a PDMS–glass hybrid continuous-flow PCR chip," *Biochemical Engineering Journal*, vol. 29, pp. 91–97, 2006.
[23] Marlow Industries, Inc., "PCR | Marlow Industries," *http://www.marlow.com/applications/medical/pcr.html*. [Online]. Available: http://www.marlow.com/applications/medical/pcr.html. [Accessed: May-2011].
[24] Nextreme Thermal Solutions, Inc., "Polymerase Chain Reaction Process (PCR)," *http://www.nextreme.com/pages/temp_control/apps/pcr.shtml*. [Online]. Available: http://www.nextreme.com/pages/temp_control/apps/pcr.shtml. [Accessed: 07-Apr.-2011].
[25] J. Crawford, D. C. Dale, and G. H. Lyman, "Chemotherapy-induced neutropenia," *Cancer*, vol. 100, no. 2, pp. 228–237, 2004.
[26] M. Golant, T. Altman, and C. Martin, "Managing Cancer Side Effects to Improve Quality of Life: A Cancer Psychoeducation Program," *Cancer Nursing*, vol. 26, no. 1, pp. 37–44, 2003.
[27] J. E. Groopman and L. M. Itri, "Chemotherapy-Induced Anemia in Adults: Incidence

and Treatment," *Journal of the National Cancer Institute*, vol. 91, no. 19, pp. 1616–1634, Oct. 1999.
[28] C. D. Kowal and J. R. Bertino, "Possible Benefits of Hyperthermia to Chemotherapy," *Cancer Research*, vol. 39, pp. 2285–2289, Jun. 1979.
[29] "Amerigon Signs 3-Year Agreement Providing Mattress Firm, Inc. Rights to Market Luxury Heated/Cooled Mattress Line," *DailyFinance*, 01-Sep.-2010. [Online]. Available: http://www.dailyfinance.com/rtn/pr/amerigon-signs-3-year-agreement-providing-mattress-firm-inc-rights-to-market-luxury-heated-cooled-mattress-line/rfid362993075/?channel=pf&icid=sphere_copyright. [Accessed: 23-May-2011].
[30] D. A. McLean, "The use of cold and superficial heat in the treatment of soft tissue injuries," *British Journal of Sports Medicine*, vol. 23, no. 1, pp. 53–54, 1989.
[31] C. Bleakley, S. McDonough, and D. MacAuley, "The Use of Ice in the Treatment of Acute Soft-Tissue Injury: A Systematic Review of Randomized Controlled Trials," *American Journal of Sports Medicine*, vol. 32, no. 1, pp. 251–261, Jan. 2004.
[32] J. W. Myrer, G. Measom, E. Durrant, and G. W. Fellingham, "Cold- and Hot-Pack Contrast Therapy: Subcutaneous and Intramuscular Temperature Change," *Journal of Athletic Training*, vol. 32, no. 3, p. 238, Sep. 1997.
[33] A. D. Edwards et al., "Neurological outcomes at 18 months of age after moderate hypothermia for perinatal hypoxic ischaemic encephalopathy: synthesis and meta-analysis of trial data," *BMJ*, vol. 340, no. 9, pp. c363–c363, Feb. 2010.
[34] M. Rutherford et al., "Assessment of brain tissue injury after moderate hypothermia in neonates with hypoxic–ischaemic encephalopathy: a nested substudy of a randomised controlled trial," *The Lancet Neurology*, vol. 9, no. 1, pp. 39–45, Jan. 2010.
[35] M. Oddo, M.-D. Schaller, F. Feihl, V. Ribordy, L. Liaudet, and M. D. Eisner, "From evidence to clinical practice: Effective implementation of therapeutic hypothermia to improve patient outcome after cardiac arrest," *Critical Care Medicine*, vol. 34, no. 7, pp. 1865–1873, Jul. 2006.
[36] S. A. Bernard et al., "Treatment of Comatose Survivors of Out-of-Hospital Cardiac Arrest with Induced Hypothermia," *New England Journal of Medicine*, vol. 246, no. 8, pp. 557–563, Feb. 2002.
[37] M. Holden and M. B. F. Makic, "Clinically Induced Hypothermia: Why Chill Your Patient?," *AACN Advanced Critical Care*, vol. 17, no. 2, pp. 125–132, 2006.
[38] "MAUDE Adverse Event Report 965037: Medivance Arctic Sun," *U.S. Food and Drug Administration*, 05-Dec.-2005. [Online]. Available: http://www.accessdata.fda.gov/scripts/cdrh/cfdocs/cfmaude/detail.cfm?mdrfoi__id=965037. [Accessed: 23-May-2011].
[39] A. C. R. Grayson et al., "A BioMEMS Review: MEMS Technology for Physiologically Integrated Devices," *Proceedings of the IEEE*, vol. 92, no. 1, pp. 6–21, Jan. 2004.
[40] D. R. Reyes, D. Iossifidis, P.-A. Auroux, and A. Manz, "Micro Total Analysis Systems. 1. Introduction, Theory, and Technology," *Analytical Chemistry*, vol. 74, no. 12, pp. 2623–2636, Jun. 2002.
[41] P.-A. Auroux, D. Iossifidis, D. R. Reyes, and A. Manz, "Micro Total Analysis Systems. 2. Analytical Standard Operations and Applications," *Anal. Chem.*, vol. 74, no. 12, pp. 2637–2652, Jun. 2002.
[42] T. Vilkner, D. Janasek, and A. Manz, "Micro Total Analysis Systems. Recent Developments - Analytical Chemistry (ACS Publications)," *Anal. Chem.*, vol. 76, no.

12, pp. 3373–3385, Jun. 2004.
[43] J. Bergin, *Global Biochip Markets*. BCC Research, 2010.
[44] R. Pal et al., "An integrated microfluidic device for influenza and other genetic analyses," *Lab on a Chip*, vol. 5, no. 10, pp. 1024–1032, 2005.
[45] V. J. Sieben, C. S. Debes-Marun, L. M. Pilarski, and C. J. Backhouse, "An integrated microfluidic chip for chromosome enumeration using fluorescence in situ hybridization," *Lab on a Chip*, vol. 8, no. 12, pp. 2151–2156, 2008.
[46] F. H. Martini, "Muscle Tissue," in *Fundamentals of Anatomy & Physiology*, 5th ed. no. 10, Upper Saddle River, NJ: Prentice Hall, 2001.
[47] J. D. Hardy, "The Physical Laws of Heat Loss from the Human Body," *Proceedings of the National Academy of Sciences of the United States of America*, vol. 23, no. 12, p. 631, Dec. 1937.
[48] J. D. Hardy and E. F. DuBois, "Regulation of Heat Loss from the Human Body," *Proceedings of the National Academy of Sciences of the United States of America*, vol. 23, no. 12, p. 624, Dec. 1937.
[49] P. A. Mackowiak, S. S. Wasserman, and M. M. Levine, "A Critical Appraisal of 98.6°F, the Upper Limit of the Normal Body Temperature, and Other Legacies of Carl Reinhold August Wunderlich," *Journal of the American Medical Association*, vol. 268, no. 12, pp. 1578–1580, Sep. 1992.
[50] T. K. Eto and B. Rubinsky, "Bioheat Transfer," in *Introduction to Bioengineering*, no. 5, S. A. Berger, W. Goldsmith, and E. R. Lewis, Eds. Oxford University Press, 2000.
[51] T. Starner, "Human-powered wearable computing," *IBM Systems Journal*, vol. 35, pp. 618–629, 1996.
[52] H. Bottner, J. Nurnus, and A. Schubert, "Miniaturized Thermoelectric Converters," in *Thermoelectrics Handbook: Macro to Nano*, no. 46, D. M. Rowe, Ed. Boca Raton, FL: CRC Press, 2006.
[53] O. Aziz, B. Lo, A. Darzi, and G.-Z. Yang, "Introduction," in *Body Sensor Networks*, no. 1, G.-Z. Yang, Ed. London: Springer, 2006, pp. 1–39.
[54] J. Rabaey, F. Burghardt, D. Steingart, M. Seeman, and P. K. Wright, "Energy Harvesting - A Systems Perspective," *Electron Devices Meeting, 2007*, pp. 363–366, 2007.
[55] P. Mitcheson, "Energy harvesting for human wearable and implantable bio-sensors," *32nd Annual International Conference of the IEEE EMBS*, pp. 3432–3436, 2010.
[56] J. Penders et al., "Power optimization in Body Sensor Networks: the case of an Autonomous Wireless EMG sensor powered by PV-cells," in *32nd Annual International Conference of the IEEE EMBS*, 2010, pp. 2017–2020.
[57] T. Torfs, V. Leonov, C. V. Hoof, and B. Gyselinckx, "Body-Heat Powered Autonomous Pulse Oximeter," *IEEE Sensors 2006*, pp. 427–430, 2006.
[58] E. Yeatman and P. Mitcheson, "Energy Scavenging," in *Body Sensor Networks*, no. 6, G.-Z. Yang, Ed. London: Springer London, 2006, pp. 183–217.
[59] M. R. Neuman, "Biopotential Electrodes," in *The Biomedical Engineering Handbook*, 2nd ed. no. 48, J. D. Bronzino, Ed. Boca Raton, FL: CRC Press, 2000.
[60] B. McCarthy, S. Varakliotis, C. Edwards, and U. Roedig, *Deploying Wireless Sensor Networking Technology in a Rescue Team Context*, vol. 6511, no. 4. Berlin, Heidelberg: Springer Berlin Heidelberg, 2010, pp. 37–48.
[61] D. G. Carey, L. A. Schwarz, G. J. Pliego, and R. L. Ramond, "Respiratory Rate Is a Valid and Reliable Marker for the Anaerobic Threshold: Implications for Measuring

Change in Fitness," *Journal of Sports Science and Medicine*, vol. 4, pp. 482–488, 2005.
[62] E. Jovanov, D. Raskovic, A. O. Lords, P. Cox, R. Adhami, and F. Andrasik, "Synchronized Physiological Monitoring Using a Distributed Wireless Intelligent Sensor System," in *Proceedings of the 25th Annual International Conference of the IEEE Engineering in Medicine and Biology Society*, 2003, vol. 2, pp. 1368–1371.
[63] R. W. Hoyt, J. Reifman, T. S. Coster, and M. J. Buller, "Combat Medical Informatics: Present and Future," *Proceedings of the AMIA Symposium*, p. 335, 2002.
[64] P. K. Baheti and H. Garudadri, "An Ultra Low Power Pulse Oximeter Sensor Based on Compressed Sensing," *Sixth International Workshop on Wearable and Implantable Body Sensor Networks, 2009 (BSN 2009)*, pp. 144–148, 2009.
[65] K. J. Heilman and S. W. Porges, "Accuracy of the LifeShirt® (Vivometrics) in the detection of cardiac rhythms," *Biological Psychology*, vol. 75, no. 3, pp. 300–305, Jul. 2007.
[66] Philips-Respironics, "VitalSense Integrated Physiological Monitor," *http://vitalsense.respironics.com/*. [Online]. Available: http://vitalsense.respironics.com/. [Accessed: 23-May-2011].
[67] Zephyr Technology Corporation, "BioHarness BT," *http://www.zephyr-technology.com/bioharness-bt*. [Online]. Available: http://www.zephyr-technology.com/bioharness-bt. [Accessed: 23-May-2011].
[68] J. E. McKenzie and D. W. Osgood, "Validation of a new telemetric core temperature monitor," *Journal of Thermal Biology*, vol. 29, pp. 605–611, 2004.
[69] Smartlife, "SmartLife HealthVest®," *http://www.smartlifetech.com/technology/Health-Vest-/*. [Online]. Available: http://www.smartlifetech.com/technology/Health-Vest-/. [Accessed: 23-May-2011].
[70] Bio-Lynx Scientific Equipment, Inc, "Equivital Wireless Physiological Monitor," *http://www.bio-lynx.com/Equivital/Equivital.htm*. [Online]. Available: http://www.bio-lynx.com/Equivital/Equivital.htm. [Accessed: May-2011].
[71] S. Bardzell, J. Bardzell, and T. Pace, "Understanding Affective Interaction: Emotion, Engagement, and Internet Videos," in *3rd International Conference on Affective Computing and Intelligent Interaction and Workshops (ACII 2009)*, 2009, pp. 1–8.
[72] C. Otto, A. Milenkovic, C. Sanders, and E. Javanov, "System Architecture of a Wireless Body Area Sensor Network for Ubiquitous Health Monitoring," *Journal of Mobile Multimedia*, vol. 1, no. 4, pp. 307–326, Jan. 2006.
[73] V. Leonov and R. J. M. Vullers, "Wearable Thermoelectric Generators for Body-Powered Devices," *Journal of Electronic Materials*, vol. 38, no. 7, pp. 1491–1498, 2009.
[74] E. Carlson, K. Strunz, and B. Otis, "20mV Input Boost Converter for Thermoelectric Energy Harvesting," *2009 Symposium on VLSI Circuits Digest of Technical Papers*, 2009.
[75] W. Glatz, E. Schwyter, L. Durrer, and C. Hierold, "Bi_2Te_3-Based Flexible Micro Thermoelectric Generator With Optimized Design," *Journal of Microelectromechanical Systems*, vol. 18, no. 3, pp. 763–772, Jun. 2009.
[76] M. Strasser, R. Aigner, C. Lauterbach, and T. Sturm, "Micromachined CMOS thermoelectric generators as on-chip power supply," *Sensors & Actuators: A. Physical*, vol. 114, pp. 362–370, 2004.
[77] J. Xie, C. Lee, M.-F. Wang, Y. Liu, and H. Feng, "Characterization of heavily doped polysilicon films for CMOS-MEMS thermoelectric power generators," *Journal of*

Micromechanics and Microengineering, vol. 19, p. 125029, Nov. 2009.
[78] G. Min, "Thermoelectric Module Design Theories," in *Thermoelectrics Handbook: Macro to Nano*, no. 11, D. M. Rowe, Ed. Boca Raton, FL: CRC Press, 2006.
[79] V. Leonov, Chris Van Hoof, and R. J. M. Vullers, "Thermoelectric and Hybrid Generators in Wearable Devices and Clothes," in *2009 Body Sensor Networks*, Berkeley, CA, 2009, pp. 195–200.
[80] V. Leonov, "Thermal Shunts in Thermoelectric Energy Scavengers," *Journal of Electronic Materials*, vol. 38, no. 7, pp. 1483–1490, Jan. 2009.
[81] S. Gesta, Y.-H. Tseng, and C. R. Kahn, "Developmental Origin of Fat: Tracking Obesity to Its Source," *Cell*, vol. 131, pp. 242–256, Oct. 2007.
[82] S. Kajimura et al., "Initiation of myoblast to brown fat switch by a PRDM16-C/EBP-β transcriptional complex," *Nature*, vol. 460, no. 7259, pp. 1154–1158, Jul. 2009.
[83] D. Prutchi, "Nuclear Pacemakers," *home.comcast.net/~dprutchi/nuclear_pacemakers.pdf*, 2005. [Online]. Available: http://home.comcast.net/~dprutchi/nuclear_pacemakers.pdf. [Accessed: May-2011].
[84] J. J. M. W. J. R. Fred N Huffman and J. C. Norman, "Radioisotope Powered Cardiac Pacemakers," *Cardiovascular Diseases*, vol. 1, no. 1, p. 52, Jan. 1974.
[85] "Assembling Bodies - Prosthetics - Pacemaker," *http://maa.cam.ac.uk/assemblingbodies/exhibition/extended/prosthetics/85/*. [Online]. Available: http://maa.cam.ac.uk/assemblingbodies/exhibition/extended/prosthetics/85/. [Accessed: 23-May-2011].
[86] V. Parsonnet, J. Driller, D. Cook, and S. A. Rizvi, "Thirty-One Years of Clinical Experience with 'Nuclear-Powered' Pacemakers," *Pacing and Clinical Electrophysiology*, vol. 29, no. 2, pp. 195–200, Feb. 2006.
[87] V. Parsonnet, "A Lifetime Pacemaker Revisited," *The New England Journal of Medicine*, vol. 357, no. 25, pp. 2638–2639, Dec. 2007.
[88] J. Peterson, M. MacDonell, L. Haroun, and F. Manotte, *Radiological and Chemical Fact Sheets to Support Health Risk Analyses for Contaminated Areas*. Argonne National Laboratory, 2007.
[89] *Instruction Concerning Risks From Occupational Radiation Exposure*. 1966.
[90] V. Parsonnet, A. D. Berstein, and G. Y. Perry, "The nuclear pacemaker: Is renewed interest warranted?," *The American Journal of Cardiology*, vol. 66, no. 10, pp. 837–842, Oct. 1990.
[91] J. Best, "Atomic Energy Control Board sets stringer ruels for nuclear pacemakers," *CMA Journal*, vol. 110, p. 239, Jan. 1974.
[92] R. Kumar et al., "Double-blind evaluation of subthalamic nucleus deep brain stimulation in advanced Parkinson's disease," *Neurology*, vol. 51, no. 3, pp. 850–855, Sep. 1998.
[93] M. C. Rodriguez-Oroz et al., "Bilateral deep brain stimulation in Parkinson's disease: a multicentre study with 4 years follow-up," *Brain*, vol. 125, no. 10, pp. 2240–2249, Jun. 2005.
[94] D. Magis, M. Allena, M. Bolla, V. De Pasqua, J.-M. Remacle, and J. Schoenen, "Occipital nerve stimulation for drug-resistant chronic cluster headache: a prospective pilot study," *The Lancet Neurology*, vol. 6, pp. 314–321, Apr. 2007.
[95] H. S. Mayberg et al., "Deep Brain Stimulation for Treatment-Resistant Depression," *Neuron*, vol. 45, pp. 651–660, Mar. 2005.
[96] S. Maybaum et al., "Cardiac Improvement During Mechanical Circulatory Support: A

Prospective Multicenter Study of the LVAD Working Group," *Circulation*, vol. 115, no. 19, pp. 2497–2505, May. 2007.

[97] "Ventricular assist device (VAD), Heart Pump," *http://www.nhlbi.nih.gov/health/dci/Diseases/vad/vad_what.html*. [Online]. Available: http://www.nhlbi.nih.gov/health/dci/Diseases/vad/vad_what.html. [Accessed: 23-May-2011].

[98] D. Grady, "A Heart Pump Ticks Down, and a Stranger Steps In to Help," *The New York Times*, 09-Aug.-2010.

Chapter 2

Thermoelectric Generator Design

2.1. Overview

With the need for extended energy sources for implantable medical devices, thermoelectric energy generators (TEG's) provide a potential solution to the growing power consumption of medical devices. However, for TEG's to be effective energy harvesters, device design must be investigated to optimize power generation. This chapter will introduce some basic concepts of TEG's, followed by heat transfer modeling to find the available thermal energy from the human body. Finally, device designs will be proposed for implantable TEG's to maximize thermoelectric power generation.

2.2. Operating Principles of Thermoelectric Energy Generators

Thermoelectric energy generators (TEG's) function based on the Seebeck effect. When a temperature gradient is applied across two dissimilar materials connected electronically in series and thermally in parallel, an open circuit voltage can be measured. Commercially available thermocouples utilize the Seebeck effect to measure temperature based on the open-circuit voltage output. Similarly, traditional thermoelectric devices utilize arrays of couples consisting of doped semiconductor elements arranged electronically in series and thermally in parallel. Additionally, when a voltage potential is applied across the device, the Peltier effect causes a temperature gradient to occur across the device [1], [2]. Figure 2.1 shows a schematic of a typical thermoelectric device.

Efficient devices should consist of materials with high Seebeck coefficients (α) to provide significant voltages, high electrical conductivities (σ) to allow for electron transport, and low thermal conductivity (λ) to minimize heat losses. A dimensionless figure of merit (ZT) is commonly used to assess the effectiveness of the thermoelectric material, and is written as

$$ZT = \frac{\alpha^2 \sigma}{\lambda} T \tag{2.1}$$

where T is the average temperature across the material. Typical ZT values for proven thermoelectric materials such as bismuth telluride (Bi_2Te_3) based alloys are around 1 at room temperature [1], [3]. A more in-depth discussion of thermoelectric materials will be presented in Chapter 4. For thermoelectric devices to be suitable for low power electronics, they must be able to provide a minimum potential of 0.5 V [4]. The open circuit voltage of generators is written as

$$V_{OC} = m\alpha\Delta T_g \tag{2.2}$$

where m is the number of couples, α is the Seebeck coefficient, and ΔTg is the temperature drop across the generator. Since maximum power occurs at matched load resistance, the closed circuit voltage at maximum power is half the open circuit voltage [5]. Power output of a thermoelectric generator takes a more complicated form, but can be approximated as,

$$Power \propto \frac{m^2 \alpha^2 \sigma}{\lambda^2} \Delta T_g^2 \tag{2.3}$$

The power output of a thermoelectric generator is thus primarily a function of the material properties, the number of couples and the temperature applied across the generator. The fundamental equations described in this section will serve as a platform for the design of generators for implantable medical applications.

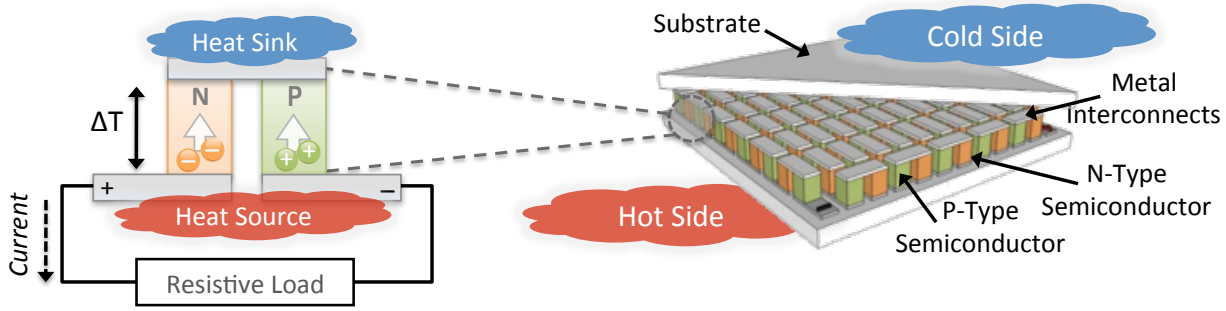

Figure 2.1. Schematic of a thermoelectric device.

2.3. Thermoelectric Generators for Implantable Medical Devices

While lithium-based cells are today's standard source of energy for implantable medical devices (IMD's), their limited improvement in energy and power densities over the last few decades, along with the increased sophistication and power requirements of IMD's has renewed interest in alternative power sources. Advancements in thermoelectric materials and manufacturing methods might allow the use of TEG's in the human body without the apparent risks of radiation from and exposure to radioisotopes.

In designing thermoelectric generators for implantable medical devices, it is important to first understand the power and usage requirements. Typical power requirements for implantable medical devices range from 30 μW to 100 μW. Table 2.1 shows a list of common implantable medical devices, along with their typical power requirements [6-8]. Application and power constraints require careful device design to maximize power output from thermoelectric devices.

Design optimization is required due to the limited availability of temperature gradients within the human body.

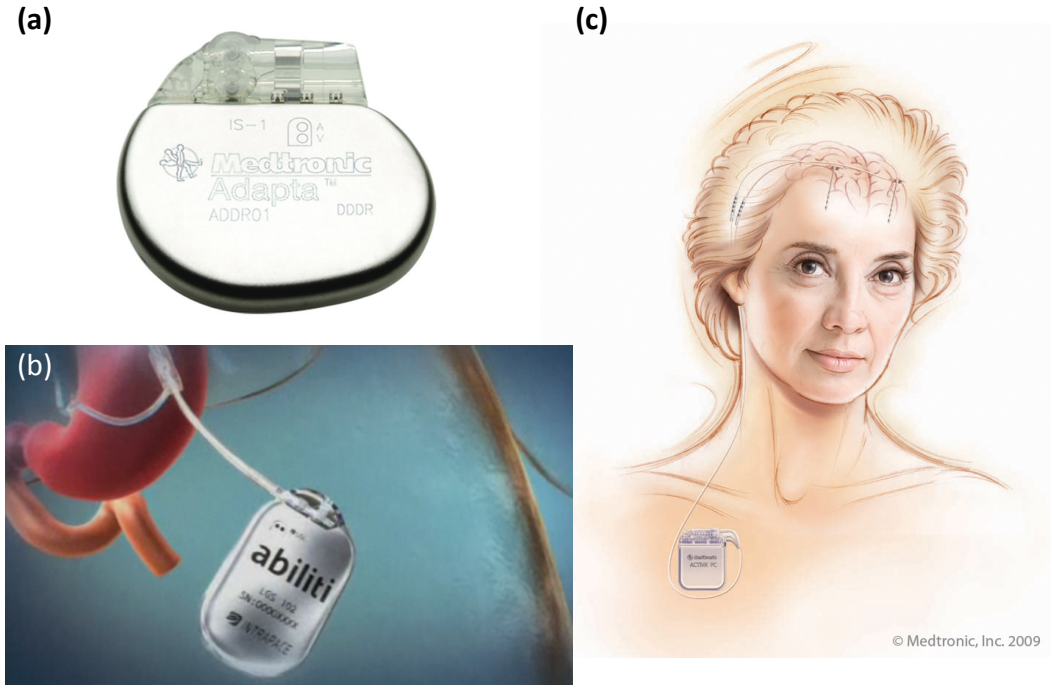

Figure 2.2. Images of (a) an implantable pacemaker (courtesy of Meditronic, Inc.), (b) an implantable gastric stimulator for weight loss (courtesy of IntraPace, Inc.), and (c) a deep brain neurological stimulator (courtesy of Medtronic, Inc.).

Table 2.1. Typical power requirements of common implantable medical devices [6-8].

Implanted Device	Applications	Typical Power Requirement
Cardiac pacemaker	Conduction disorders	30-100 µW
Cardiac defibrillator	Ventricular Tachycardia	30-100 µW (Idle)
Neurological stimulator	Essential tremor	30 µW to several mW
Drug pump	Spasticity	100 µW – 2 mW
Cochlear implant	Auditory assistance	Up to 10 mW
Glucose monitor	Diabetes care	>10 µW

2.3.1. Bioheat Transfer Modeling

While device design and materials can be optimized to increase device performance, the power output ultimately depends on the available temperature differences within the application as seen in Equation 2.3. Since the human thermoregulatory system maintains the core body temperature at approximately 37˚C, temperature differences are only readily available near the surface of the skin where heat is emitted to the ambient environment. The tissue near the skin surface can be modeled as 3 layers consisting of the muscle, fat and epidermis (skin). Previous studies have

shown a 1-5 K temperature difference is available in the fat layer [8]. These temperature differences vary significantly depending upon body location, ambient environments and physical activities. These conditions can be analyzed to determine optimal thermoelectric device placement. Temperature differences near the skin surface can be calculated using the 1-Dimensional tissue model based on the Pennes Bio-heat equation,

$$\rho_t c_t \frac{\partial T_t}{\partial t} = \nabla(k_t \nabla T_t) + \ddot{q}'''_{met} + \omega \rho_b c_b (T_a - T_v) \tag{2.4}$$

where ρ_t is the tissue density, c_t is the tissue heat capacity, T_t is tissue temperature in Kelvin, k_t is the tissue thermal conductivity, $\ddot{q}'''_{met}$ is the metabolic heat generation rate, ω is the blood perfusion rate, ρ_b is the blood density, c_b is the blood heat capacity, T_a is the deep body arterial temperature (310 K, the core body temperature) and T_v is the venous temperature (the skin temperature) [9]. Under steady state conditions, temperature differences are available within the fat layer of the human body due to its the low thermal conductivity. Figure 2.3 shows a schematic of the model and the resulting temperature profile near the skin surface. The temperature gradient in the fat layer is primarily a function of the blood perfusion rate, convective heat transfer coefficient near the skin, and the skin temperature. A computational analysis of several common muscles of the body can be used to determine the various temperature differences within the body. Table 2.2 shows the common material properties of the body and heat transfer coefficients established by Eto & Rubinsky [9]. The other parameters used in the analysis included $\ddot{q}'''_{met}$= 420 W/m^3 and ω = 0.0005 s^{-1} [8], [9]. Coupling the values shown in Table 2.3 with muscle and fat thickness measurements by Ishida et al [10], temperature differences in the fat region for the average male while rested, walking and running can be modeled using the equation 2.4.

Table 2.2. Material properties & convective heat transfer coefficients used for tissue thermal modeling [9].

Material Properties			
Material	**Thermal Conductivity**	**Density**	**Heat Capacity**
Muscle	0.7-1.0 W/m-K	1070 kg/m^3	3471 J/kg-K
Fat	0.1-0.4 W/m-K	937 kg/m^3	3258 J/kg-K
Skin	0.5-2.8 W/m-K	-	-
Blood	0.51-0.53 W/m-K	1060 kg/m^3	3889 J/kg-K
Convective Heat Transfer Coefficients			
Condition	**Equation**	**Notes**	
Seated	h = 8.3u$^{0.6}$ W/m^2-K	u = air velocity (m/s)	
Walking/Running	h = 8.6u$^{0.53}$ W/m^2-K	u = moving speed (m/s)	

Analysis suggests that the maximum temperature differences are found within the abdomen and the subscapular (upper back) region with typical differences between 1-2 K at resting state. In all cases, running, and the consequent exposure to higher convective effects from wind, resulted in higher temperature differences in all parts of the body, with a maximum difference of 4.75 K in

the abdomen (Figure 2.4). The temperature difference appears to be proportional to fat thickness, as seen in Figure 2.5, and is due to the lower thermal conductivity of fat.

This analysis suggests that a 1-5 K temperature gradient is feasible under normal conditions only in high fat thickness regions of the body. These results are also only valid in the case where the thermal resistance of the implanted device matches that of the fat layer to limit any thermal discomfort. Experimental work in human thermometry may provide empirical values for the temperature differences. While current methods for measuring sub-dermal tissue temperatures involve invasive methods (such as needle temperature probes), some newer non-invasive techniques, such a microwave thermometry, are becoming available (see Appendix B).

Table 2.3. Calculated temperature differences in the fat layer of the body in various locations.

Site	Muscle Thickness	Fat Thickness	Rested ΔT	Walking ΔT	Running ΔT
Abdomen	16.34 mm	14.8 mm	1.73 K	3.8 K	4.75 K
Biceps	34.6 mm	3.33 mm	0.45 K	1.22 K	1.7 K
Calf-posterior	65.36 mm	4.93 mm	0.65 K	1.74 K	2.4 K
Chest	33.45 mm	7.26 mm	0.94 K	2.37 K	3.18 K
Forearm	26.04 mm	3.24 mm	0.44 K	1.16 K	1.63 K
Hamstring	69.29 mm	6.97 mm	0.91 K	2.32 K	3.14 K
Lumbar	37 mm	6.54 mm	0.85 K	2.18 K	2.96 K
Quadriceps	54.54 mm	6.42 mm	0.82 K	2.12 K	2.89 K
Subscapular	23.74 mm	8.4 mm	1.06 K	2.6 K	3.44 K
Suprapatellar	29.42 mm	6.23 mm	0.81 K	2.08 K	2.81 K
Triceps	41.84 mm	5.92 mm	0.78 K	2.02 K	2.75 K

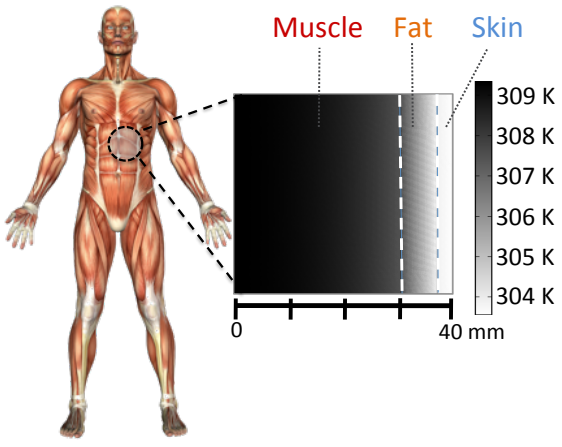

Figure 2.3. Modeled tissue temperature profile near the skin's surface.

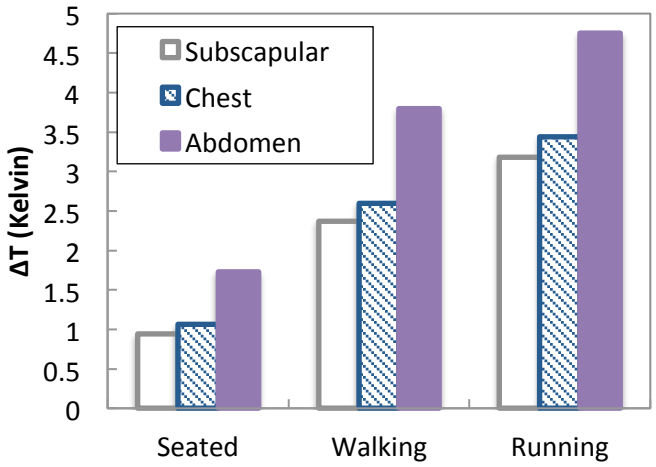

Figure 2.4. Peak temperature differences in the fat layer during various physical activities.

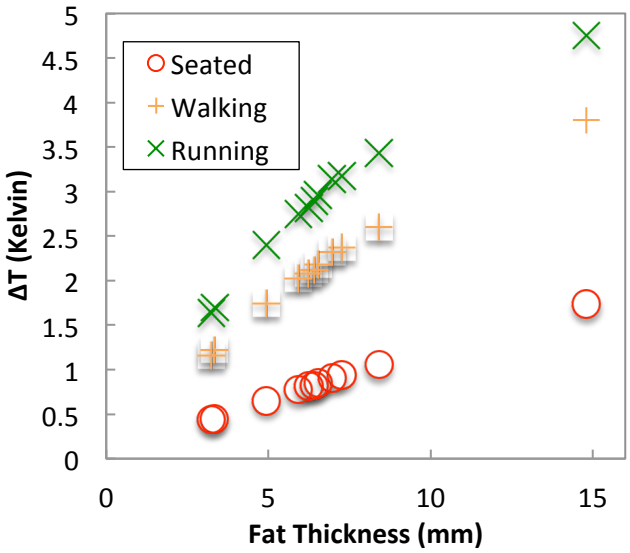

Figure 2.5. Temperature differences in the fat layer as a function of fat thickness.

2.3.2. Thermoelectric Generator Design

In the case of an implantable biomedical device with a 100 μW and 1 V requirement, the open circuit voltage output of a thermoelectric device scales with the number of couples in a device for a given temperature difference. Figure 2.6 demonstrates the relationship between voltage output and power output with the number of couples and device area, respectively. Using Equation 3.2, state-of-the-art Bi_2Te_3 based materials will require approximately 1000 couples to achieve 1 V at a $\Delta T = 5$ K. While the power output also scales with the number of couples, the power density (power output per device area) is independent of the number of couples. The power output ultimately depends on the total device area, the element spacing, element length and material properties [11]. With the goal of minimizing the total device footprint, the minimum

device area for a 100 µW output at ΔT = 5 K is approximately 1.3 cm^2 under ideal conditions. The need for a large number couples within a small footprint requires high-density arrays of thermoelectric elements for a generator.

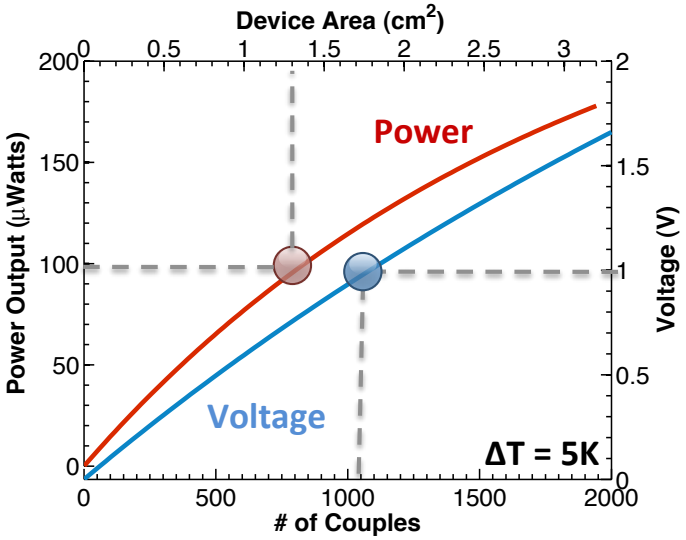

Figure 2.6. Power output of a thermoelectric device as a function of device area (red) and voltage output as a function of the number of couples (blue) for a temperature difference of 5 K.

Because the available thermal gradients across the fat layer are typically below 5 K, thermoelectric devices need to be optimized to take advantage of the total available energy. Figure 2.7a shows the percentage of maximum power output for a thermoelectric device as a function of percent device occupation across the fat layer. Because the temperature difference is across the fat layer, the temperature difference available to a generator is proportional to its element length. This suggests that thin-film TEGs, typically limited to element sizes of <60 µm [12], are not capable of producing sufficient power in the fat layer due to the limited temperature difference available. While modern thermoelectric devices fabricated using conventional methods (such as hot-pressing) are capable of producing longer elements to occupy more of the fat layer, such techniques are incapable of producing high-density arrays within a small footprint. Thus, ideal implantable TEGs will require high aspect ratios to span across the entire fat layer. There are, however, limited available technologies for fabricating such devices. An alternative implementation method is to stack multiple devices to span across the entire fat thickness. Figure 2.7b shows the percentage of maximum power output as a function of the number of TEG stacks assuming devices with 500 µm thick insulators. While the performance of both MEMS and traditional thermoelectric generators can be improved, thermal losses between the devices dominate with an increasing number of stacks. Thus, an optimal TEG still requires high aspect ratio elements.

The previously discussed requirements indicate that in order to maximize the power output of a thermoelectric device within the fat layer, a device requires high-density and high aspect ratio arrays of thermoelectric elements within a small footprint. While this can be difficult to fabricate using traditional 3-dimensional device design, non-traditional planar devices are capable of achieving such dimensions. The planar device can be fabricated on a flexible substrate which allows for a roll-based device to achieve the high density arrays. The use of a substrate for the planar device provides structural support for the high aspect ratio pillars.

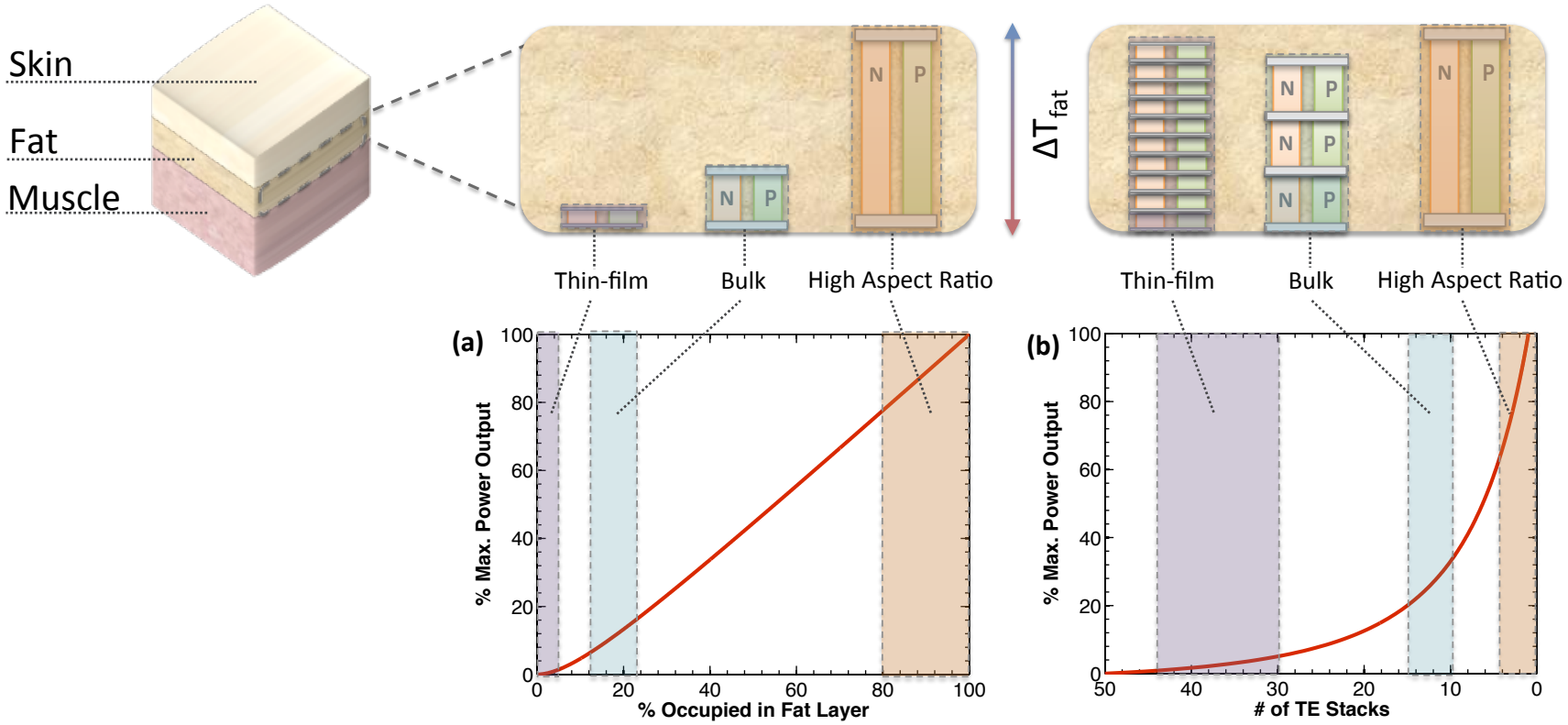

Figure 2.7. Schematic demonstrating various TEG fabrication technologies placed in the fat layer. (a) The percentage of maximum power output as a function of TEG element occupation in the fat layer. (b) The percentage of maximum power output as a function of number of TE stacks to occupy the entire fat layer. Since the power output of a thermoelectric device depends on the temperature difference across the device, the largest temperature difference occurs when the device occupies the entire fat layer. In the case when multiple devices are stacked across the fat layer, the power output is still higher for high aspect ratio devices due to interfacial thermal losses between the devices.

Figure 2.8 depicts and summarizes the two different device designs with regards to their fabrication. While traditional device designs utilize established manufacturing technologies, they are limited to low-density arrays with low aspect ratios. Due to the 3-dimensional nature of such designs, thermoelectric device fabrication is very labor intensive and most commercial manufacturers still use pick and place methods. Manufacturers are only now exploring advanced robotic methods for placing the individual elements. Figure 2.8b shows a planar design where the individual elements are laid onto a flexible substrate that can be rolled together. As a result, the direction of heat flow for the device is parallel to the substrate. By laying the elements on a substrate, structural support is provided for high aspect ratio elements. Rolling of the device allows for high element packing, thus resulting in high-density arrays. Such devices designs can be utilized to fulfill the requirements of implantable TEG's. The planar design can also utilize much more scalable thick and thin-film fabrication methods. Some previous works have explored the planar device design using different fabrication techniques [13], [14]. The next chapter will discuss manufacturing of thermoelectric devices in further detail.

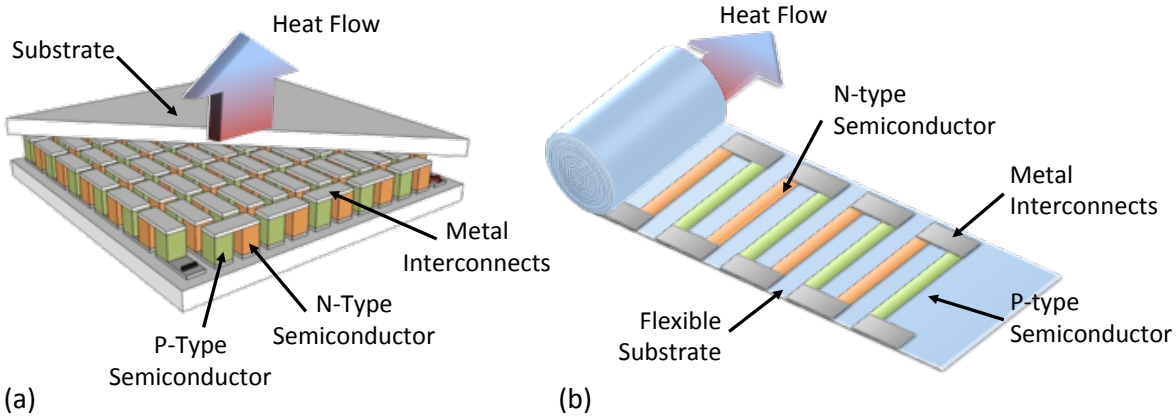

Figure 2.8. Schematic demonstrating (a) traditional thermoelectric device designs and (b) planar device designs.

2.4. Chapter Conclusion

1. Common implantable medical devices have average power requirements ranging between 10 µW to several mW with average power consumptions around 100 µW [6-8].
2. Because the human body naturally maintains its core body temperature, the optimal location of TEG's can be found in the fat layer. Bioheat Tranfer modeling shows that temperature differences between 1 and 5 K can be found within the fat layer depending on the local fat thickness and convective conditions. The largest temperature difference is found in high fat thickness regions (such as the abdomen) in high convection environments.
3. In order for a state-of-the-art TEG to achieve a 100 µW output at 1 V [4], [6-8] for a 5 K temperature difference, at least 1000 couples need to fit within a 1.3 cm^2 footprint. This suggests a need for high-density array TEG devices.

4. For TEG's to be effective in the fat layer, elements must span across the fat layer to capture the largest temperature difference. This requires high aspect ratio thermoelectric elements in high-density arrays for sufficient power generation.
5. The requirements of implantable TEG's can be achieved using planar device designs that will require non-traditional fabrication methods. The next chapter will explore a printed fabrication technique for manufacturing planar TEG's.

Chapter References

[1] D. M. Rowe, "General Principles and Basic Considerations," in *Thermoelectrics Handbook: Macro to Nano*, no. 1, D. M. Rowe, Ed. Boca Raton, FL: CRC Press, 2006.

[2] F. J. DiSalvo, "Thermoelectric Cooling and Power Generation," *Science*, no. 285, pp. 703–706, 1999.

[3] G. J. Snyder and E. S. Toberer, "Complex thermoelectric materials," *Nature Materials*, vol. 7, pp. 105–114, Feb. 2008.

[4] N. M. Pletcher, S. Gambini, and J. Rabaey, "A 52 μW Wake-Up Receiver With -72 dBm Sensitivity Using an Uncertain-IF Architecture," *Solid-State Circuits, IEEE Journal of*, vol. 44, no. 1, pp. 269–280, 2009.

[5] M. Strasser, R. Aigner, C. Lauterbach, and T. Sturm, "Micromachined CMOS thermoelectric generators as on-chip power supply," *Sensors & Actuators: A. Physical*, vol. 114, pp. 362–370, 2004.

[6] C. L. Schmidt and P. M. Skarstad, "The future of lithium and lithium-ion batteries in implantable medical devices," *Journal of Power Sources*, vol. 97, pp. 742–746, 2001.

[7] J. H. Schulman et al., "Battery Powered BION FES Network," *Proceedings of the 26th Annual International Conference of the IEEE EMBS*, pp. 4283–4286, 2004.

[8] Y. Yang, X.-J. Wei, and J. Liu, "Suitability of a thermoelectric power generator for implantable medical electronic devices," *Journal of Physics D: Applied Physics*, vol. 40, pp. 5790–5800, 2007.

[9] T. K. Eto and B. Rubinsky, "Bioheat Transfer," in *Introduction to Bioengineering*, no. 5, S. A. Berger, W. Goldsmith, and E. R. Lewis, Eds. Oxford University Press, 2000.

[10] Y. Ishida, J. F. Carroll, M. L. Pollock, J. E. Graves, and S. H. Leggett, "Reliability of B-mode ultrasound for the measurement of body fat and muscle thickness," *American Journal of Human Biology*, vol. 4, no. 4, pp. 511–520, 1992.

[11] G. Min, "Thermoelectric Module Design Theories," in *Thermoelectrics Handbook: Macro to Nano*, no. 11, D. M. Rowe, Ed. Boca Raton, FL: CRC Press, 2006.

[12] H. Bottner, J. Nurnus, and A. Schubert, "Miniaturized Thermoelectric Converters," in *Thermoelectrics Handbook: Macro to Nano*, no. 46, D. M. Rowe, Ed. Boca Raton, FL: CRC Press, 2006.

[13] J. Weber, K. Potje-Kamloth, F. Haase, P. Detemple, F. Volklein, and T. Doll, "Coin-size coiled-up polymer foil thermoelectric power generator for wearable electronics," *Sensors and Actuators A*, vol. 132, pp. 325–330, 2006.

[14] W. Glatz, S. Muntwyler, and C. Hierold, "Optimization and fabrication of thick flexible polymer based micro thermoelectric generator," *Sensors & Actuators: A. Physical*, vol. 132, pp. 337–345, 2006.

Chapter 3

Thermoelectric Device Manufacturing

3.1. Overview

In the previous chapter, planar designs of thermoelectric generators (TEG's) were proposed for use in implantable medical applications. However, given the lack of manufacturing methods for effectively fabricating planar designs, alternative fabrication techniques must be explored. In this section, thermoelectric device manufacturing will briefly be reviewed. A dispenser printing technique will then be introduced as a method for manufacturing planar TEG's. The prototyping dispenser printer used in this work will be discussed and analyzed to understand the experimental variables of dispenser printing. The results in this chapter will ultimately serve to develop effective printing methods for fabricating planar TEG's.

3.2. Thermoelectric Device Fabrication

Traditional thermoelectric manufacturing technologies have typically been developed around both device designs and materials characteristics. Because ideal thermoelectric materials are typically semiconductors, bulk materials synthesis methods such as melting, extrusion and dicing are today's preferred techniques. These batch-process methods are similar to those used in silicon manufacturing, which have proven scalability as demonstrated by the semiconductor industry. However, complications arise when converting diced wafers into completed thermoelectric modules such as the one shown in Figure 3.1a. Since thermoelectric modules require placement of alternating n-type and p-type semiconductor elements, positioning of the individual elements becomes difficult and labor-intensive. Additionally, the structural nature of the traditional module design and the limits of dicing tools do not allow for high aspect ratio elements. The device packing densities when using bulk elements also become increasingly low due to physical limitations of pick and place methods [1], [2].

Recent research has begun to focus on alternative technologies for manufacturing thermoelectric modules. Advancements in thin and thick-film deposition methods have garnered some renewed

attention due to new potential applications and even physical phenomena at the nano-scale [1], [3-6]. These film-based deposition methods allow for fabrication of both traditional and alternative geometries, such as the planar design shown in Figure 3.1b, with proven scalability. These methods can also produce high-density arrays of thermoelectric elements at the micro-scale, creating attractive opportunities for small-scale thermoelectric generation. The use of a planar design allows for high aspect ratio elements unachievable using bulk methods. Table 3.1 summarizes the different available thermoelectric manufacturing technologies.

While both thin and thick-film methods provide similar advantages over bulk technologies, thick-film methods create less materials waste (due to the additive process) and utilize less energy (no vacuum processing) than thin-film techniques. These advantages makes thick-film techniques a clear technological choice for fabrication of planar high aspect ratio and high density array TEG's.

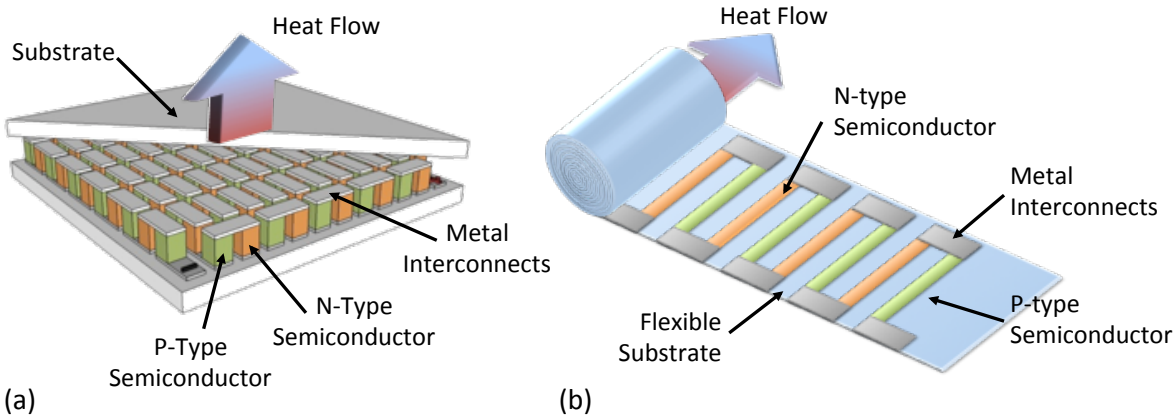

Figure 3.1. Schematics illustrating (a) a traditional 3 dimensional thermoelectric module design and (b) a planar thermoelectric design on a flexible substrate.

Table 3.1. Attributes of available thermoelectric manufacturing technologies [1], [4], [7].

Technology	Examples	Manufacturing Process	Scalability	Aspect Ratio	Energy Use	Packing Density
Thin Film (<60 µm)	Evaporation, Sputtering	Subtractive	High	High	High	High
Thick Film (60 µm – 300µm)	Electrodeposition, Printing	Additive	High	High	Med.	High
Bulk (> 300 µm)	Hot Press, Extrusion, Dicing	Additive	Med.-Low	Low	High	Low

3.3. Manufacturing of Planar Thermoelectric Generators

As described in the previous chapter, the planar design in Figure 3.1b meets the requirements of TEG's for implantable medical applications. Figure 3.2 describes a proposed manufacturing method for prototyping planar TEG's using printed thick-film techniques. By starting with a

flexible substrate, metal interconnects can first be deposited, followed by the individual elements of the TEG. The deposited materials can be processed and rolled into a TEG. This proposed concept allows for TEG fabrication in a 4-step process that can be scaled to various printed manufacturing methods such as screen-printing or flexography. A promising direct-write printing technique has been developed to additively create microscale generators as depicted in Figure 3.2. Direct writing is an alternative method for fabricating thick film structures. It is a simple and flexible additive deposition method for patterning materials at ambient and room temperature conditions [8]. The process energy input and waste generated are both reduced substantially compared to thin-film microfabrication methods [8-10]. Printing techniques, however, involve the use of specially tailored thermoelectric inks that consist of slurry suspensions of active materials in polymer binders and solvents. The next chapter will discuss the development of such inks. Prior to the development of inks, the direct-write dispenser printing method will first be discussed and characterized to understand its capabilities.

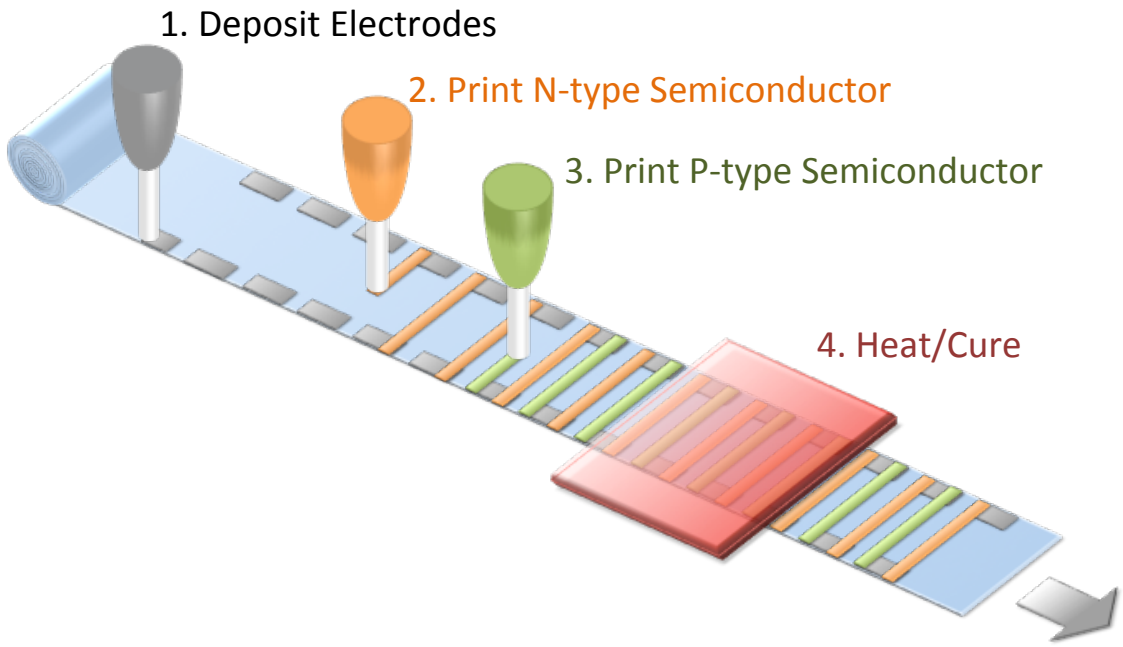

Figure 3.2. Proposed fabrication process for planar TEG's using printed fabrication methods to deposit thermoelectric materials on a flexible substrate.

3.4. Direct-write Dispenser Printing

The prototyping dispenser printer used in this work consists of a 3-axis stage, a pneumatically controlled dispensing syringe head, and a heated vacuum chuck stage. Figure 3.2 shows an image and schematic of the dispenser printer. The printer stages are Newmark Systems NLS4 series stages with 0.03 μm resolution and 5 μm repeatability (based on manufacturer's specifications). The stage controller is a Newmark Systems MSC-M 4-axis stage controller and has 1μm resolution (based on the manufacturer's specifications). Side-view and angled-view cameras are used to image the printer tip relative to the substrate. A top-down camera is used for custom-developed automated software alignment of the dispensing tip. The printer allows for

deposition of inks of a wide range of viscosities from 100-10,000 cP, and is controlled using a Musashi ML-808FX pneumatic controller capable of 20 – 500 kPa output. All equipment is interfaced and controlled through a personal computer running custom Java software. Depending on the inks, typical feature sizes down to 50 µm can be printed with film thicknesses ranging from 10 to 200 µm per pass, depending on a combination of process parameters such as shot pressure, tip size, rheology of the ink, and shot spacing. These parameters are all easily tuned within the automated software and allow for rapid adjustments to the process parameters in real time. Ink viscosity can be tuned by adjusting the amount of solvent/diluent in the mixture (which is removed upon drying), while tip sizes are adjusted by using commercially available disposable plastic and metal syringe tips. These tips are available in sizes ranging from several mm down to 100µm in inner diameter, and smaller tips under 100 µm in inner diameter can be manually pulled from borosilicate glass pipettes. Thermoelectric heater/coolers below the stage allow for heating or cooling of substrate for on-contact drying.

This prototype dispenser printer has been previously used in various other research projects including printed solid-state energy storage devices [11-13], MEMS AC current sensor [14] and MEMS vibrational energy harvesting [15].

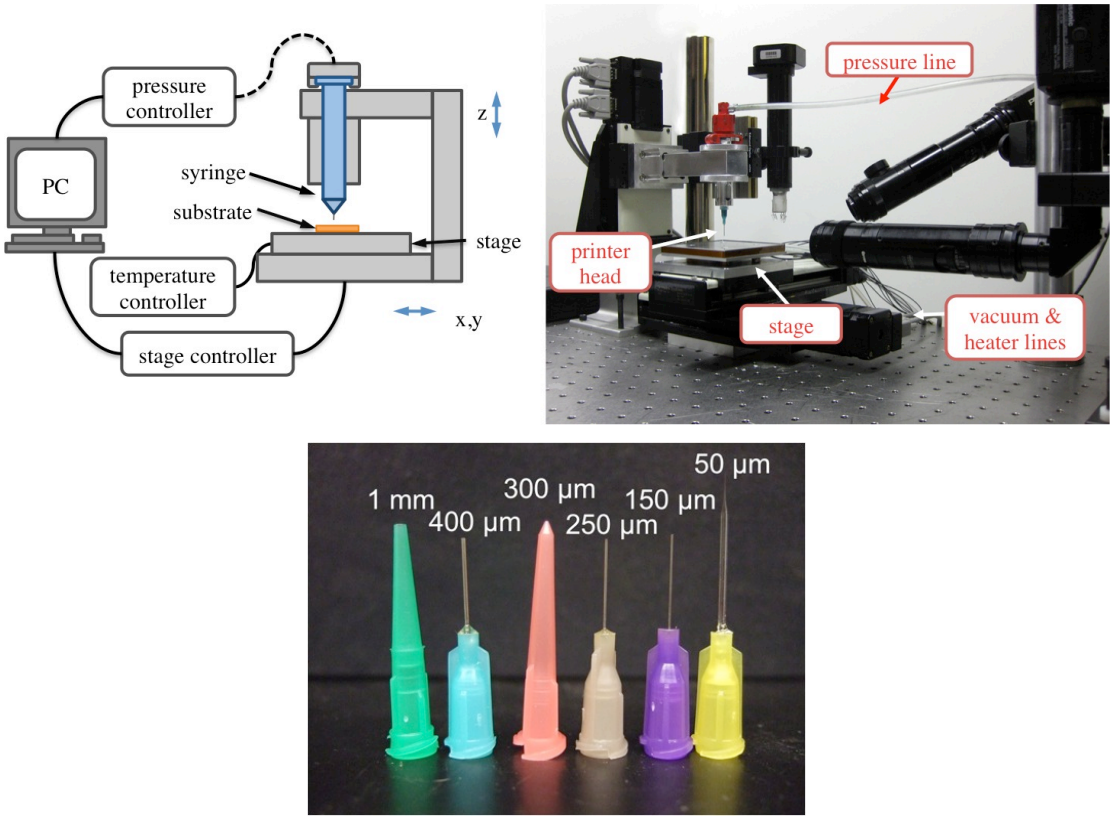

Figure 3.3. Left: schematic of dispenser printer, right: image of the dispenser printer and center: image of various syringe tips [16].

3.4.1. Dispenser Printer Characterization

Since the accuracy and repeatability of dispenser printed features are essential to the fabrication of small-scale devices, printing parameters should be analyzed to understand the printing

processes. In most printing methods, definition of features is typically a function of pixels or dots [8], [17]. In the case of a dispenser printer, printed drops form features such as lines, squares or images (Figure 3.4). Analysis of printed drops can show the effects of the printing parameters on the properties of printed features. Table 3.2 describes various printing parameters of the different processing phases. While a large number of experimental variables are available, only the printer shot height (distance from printer tip to printed surface) and the shot pressure will be examined in detail. These variables were chosen because of their controllability and expected impact on the drop features. Figure 3.5 shows the projected drop cross-sections as a function of the two variables.

Table 3.2. Various key printing process parameters.

Pre-process ➔	Process ➔	Post-process
Ink	Pressure	Temperature
Viscosity	Height	Ambient Pressure
Needle	Shot-spacing	
Substrate		

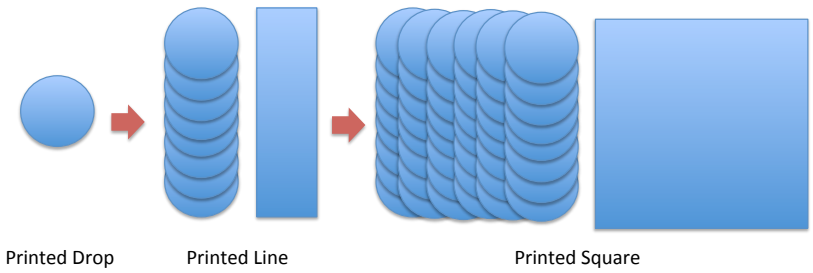

Figure 3.4. Schematic representation of printed features such as drops, lines and squares.

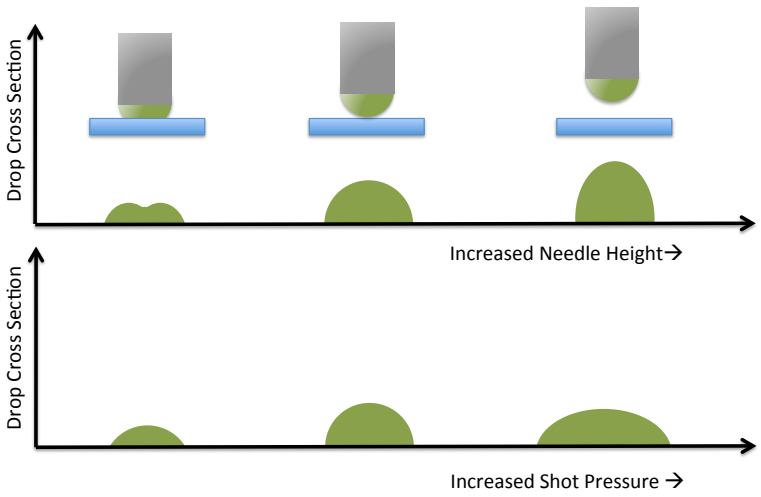

Figure 3.5. Effects on the printed drop cross section as a function of needle/drop height (top) and shot pressure (bottom).

3.4.1.1. *Experimental*

The printed materials chosen for this experiment were epoxy resins. Epoxy resins are a class of thermoset polymers that have proven printability and are commonly used in commercially available electrically conductive adhesives [18]. The epoxy system was formulated using a bisphenol f epoxy resin (EPON 862, Hexion Specialty Chemicals, Inc.) and an anhydride-based hardener (MHHPA, Dixie Chemicals, Inc.). The epoxy-to-hardener equivalent weight ratio was 1:0.85. 2E4MZCN (Sigma-Aldrich, Inc.) was employed as the catalyst in the system. 10-20 wt% of butyl glycidyl ether (Heloxy 61, Hexion Specialty Chemicals, Inc.) was also used in the resin blend as a reactive diluent to adjust the viscosity of the ink to the desired properties. Three different amounts of diluent were used in this study: 0 wt% (high viscosity), 10 wt% (medium viscosity) and 20 wt% (low viscosity). The epoxy was printed from three different sized syringe tips (20, 25 & 30 Gauge) using shot pressures between 20 and 400 kPa and shot heights between 50 and 300 µm. Vacuum between 0.0 and 0.4 kPa was applied to the syringe to prevent overflow of the epoxy. Once the epoxy was printed, it was cured in a convection oven at 150˚C.

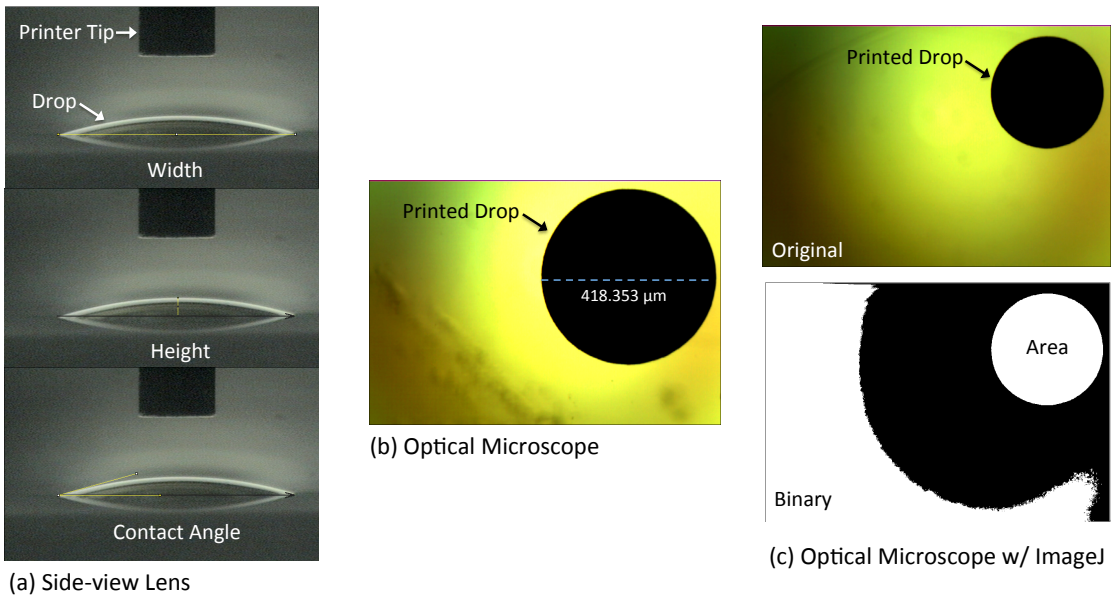

Figure 3.6. Images of the three analysis methodologies used: (a) side-view lens from the dispenser printer, (b) optical microscopy using a pre-calibrated scale and (c) optical microscopy with ImageJ post-process analysis.

3.4.1.2. *Analysis Methodologies*

The drop width, height and contact angle were measured using three optical techniques. The first method used the side-view lens from the dispenser printer. Given the known size of the printer tip, drop measurements were calculated based on the scale of the image. Measurement of contact angles was only performed using the side-view lens. The second methodology involved using an optical microscope (Omano OM-50). Images of the drop were taken from the top and the dimensions were measured using a previously calibrated scale. The final method involved processing the same image from the optical microscope in ImageJ software. After the images

were imported into ImageJ, there were first converted to binary images. Measurements of the drop area and calculations of the average drop diameter were then performed using geometric relationships.

3.4.1.3. *Results & Discussion*

Due to the large number of variables, the most salient results will be discussed in this section. Figures 3.7 and 3.8 demonstrate the effects of printed drop width as a function of shot pressure and shot height, respectively, for the same tip size, vacuum pressure and viscosity. The experiments were performed using the previously described methodologies. In both experiments of printed drop width and shot height, the optical microscope gave the largest values while the side lens gave the lowest values for drop width. The results using optical microscopy with ImageJ post-processing gave the most consistent results that fell between the other methods. Given the potential sources of error for the side lens method (low resolution and vague borders) and the optical microscopy method (user error), the ImageJ method was chosen as the standard methodology for measurements in the following experiments. It should noted from the figures that the drop width is primarily affected by the pressure. However, the drop width is insignificantly affected by the height of the needle (shot height).

Figures 3.9 and 3.10 show the drop height as a function of shot pressure and shot height, respectively. The figures indicate that the drop height is also primarily affected by the pressure and is proportional to an upper limit. The limit exists due to physical restrictions such as adhesion, cohesion or gravitational forces, and can be seen where the graph plateaus in Figure 3.9. Conversely, the shot height has an insignificantly effect on the drop height. Figure 3.9 shows a very slight increase in drop height with increasing shot height, but the subtle changes are most likely insignificant given the limited resolution of measurement.

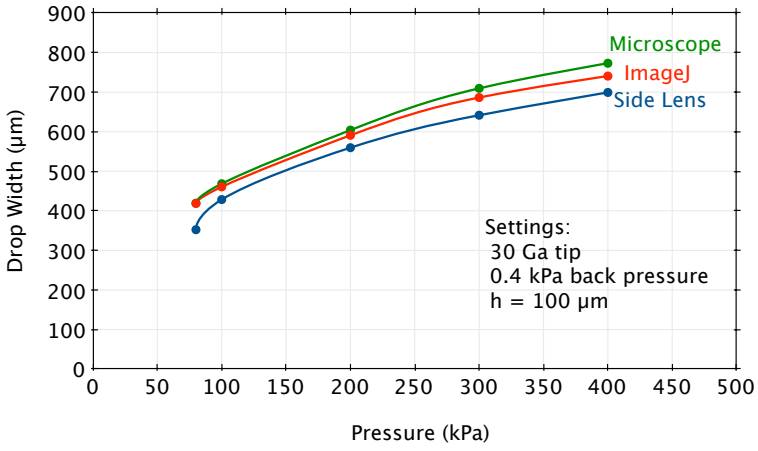

Figure 3.7. Measured printed drop width as a function of shot pressure at a shot height of 100 µm for the high viscosity epoxy. The results analyzed use the three methodologies.

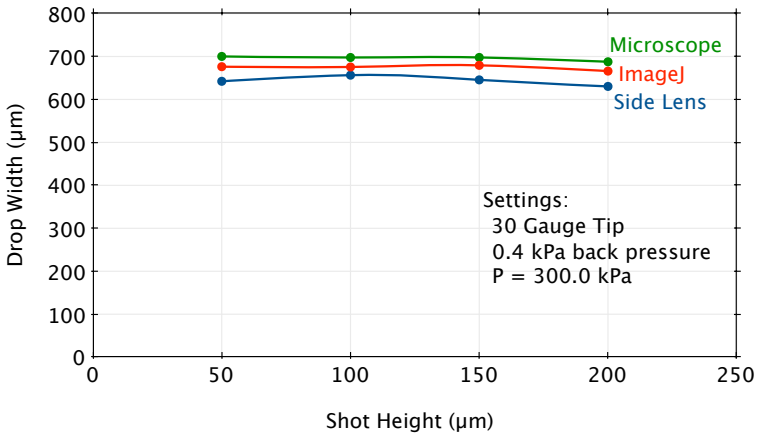

Figure 3.8. Measured printed drop width as a function of shot height at 300 kPa shot pressure for the high viscosity epoxy. The results were analyzed using the three methodologies.

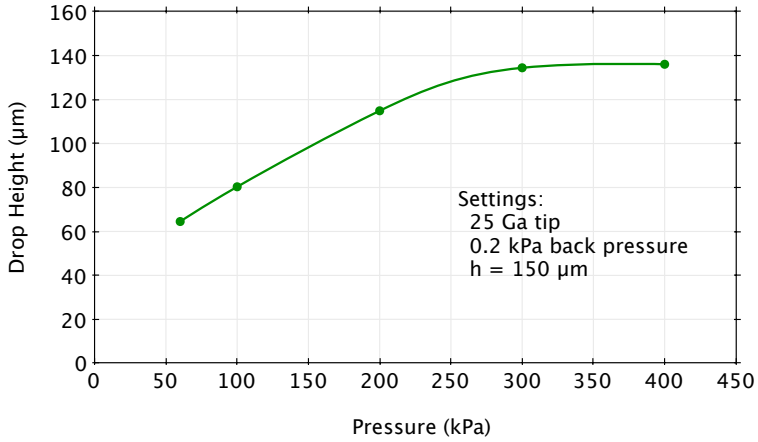

Figure 3.9. Drop height as a function of shot pressure for high viscosity epoxy printed through at 25 Gauge tip at a drop height of 150 µm.

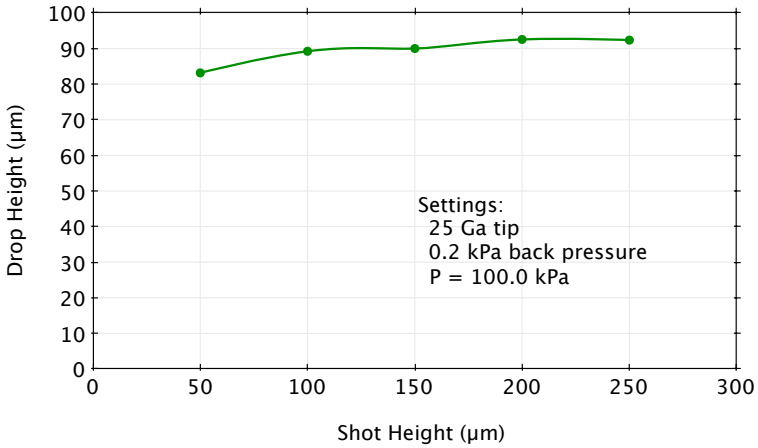

Figure 3.10. Drop height as a function of shot height for high viscosity epoxy printed through a 25 Gauge tip at a fixed shot pressure of 100 kPa.

Figures 3.11 and 3.12 show the contact angle as a function of shot pressure and shot height, respectively, for a low viscosity epoxy. In the case of the low viscosity epoxy, neither the pressure nor the height of the needle affects the contact angle. The low viscosity of the epoxy allows the drop to freely flow to a relaxed state. The final contact angle of the drop is thus most likely affected by the surface interactions between the epoxy and the substrate. Figures 3.13 and 3.14 show the same contact angle measurements for a high viscosity epoxy. The results suggest that both the pressure and the height of the needle define the contact angle. In the case of the high viscosity epoxy, the contact angle is inversely proportional to the pressure and directly proportional to the height of the needle. The inability for the high viscosity epoxy to naturally flow ultimately allows the printer to shape the resulting drop.

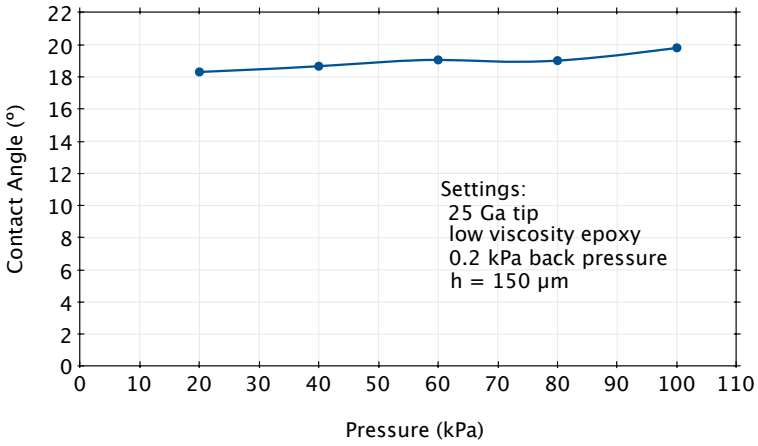

Figure 3.11. Measured contact angle of a low viscosity epoxy drop as a function of shot pressure for a 25 Gauge tip at a fixed drop height of 150 µm.

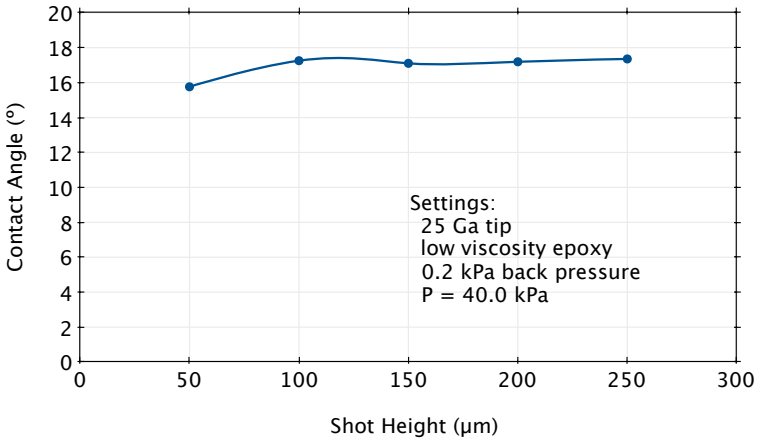

Figure 3.12. Measured contact angle of a low viscosity epoxy drop as a function of shot height for a 25 Gauge tip at a fixed shot pressure of 40 kPa.

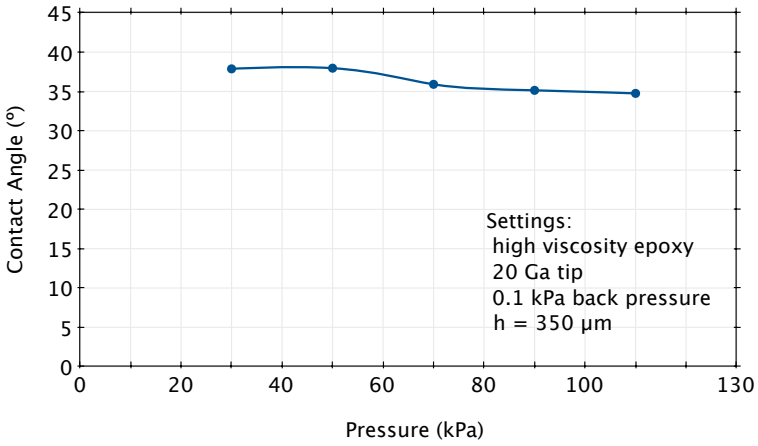

Figure 3.13. Measured contact angle of a high viscosity epoxy drop as a function of shot pressure for a 25 Gauge tip at a fixed drop height of 350 µm.

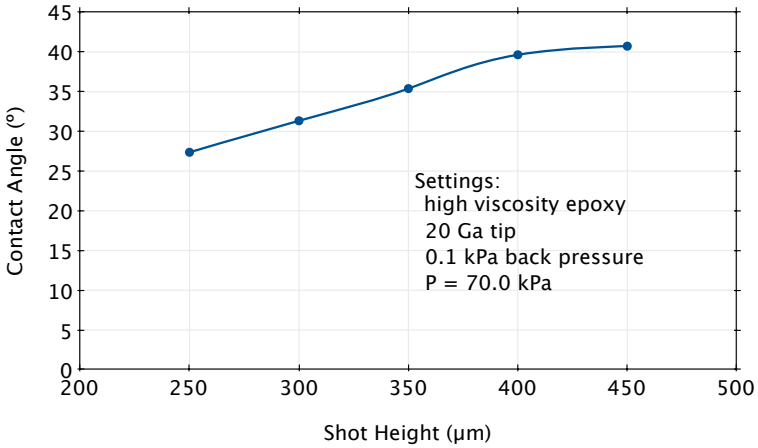

Figure 3.14. Measured contact angle of a high viscosity epoxy drop as a function of shot pressure for a 25 Gauge tip at a fixed drop height of 70 kPa.

Figure 3.15 maps the results of all the experiments and shows the drop height as a function of syringe tip gauge size. The results from all the viscosities, pressures and shot heights are mapped to demonstrate trends in drop height. The data helps visualize the primary variables in controlling the drop height. The importance of the key variables for tuning the drop height is ranked as follows: (1) gauge size, (2) shot pressure and (3) shot height. The range of drop height decreases as the gauge size increases (smaller tip diameter) for all viscosities. The mid and high viscosity epoxies have a much smaller range of drop heights, particularly when using the 30 Gauge syringe tip. This is possibly due to the smaller diameter that restricts the flow of material from the syringe tip. Figure 3.16 maps a similar graph demonstrating the effects of variables on the drop width. The results of the analysis of the printed drop width are similar to that of the drop height. Again, the gauge size is the most important factor affecting the printed drop width, followed by the shot pressure and shot height. It appears that the shot height has the least effect on the printed feature.

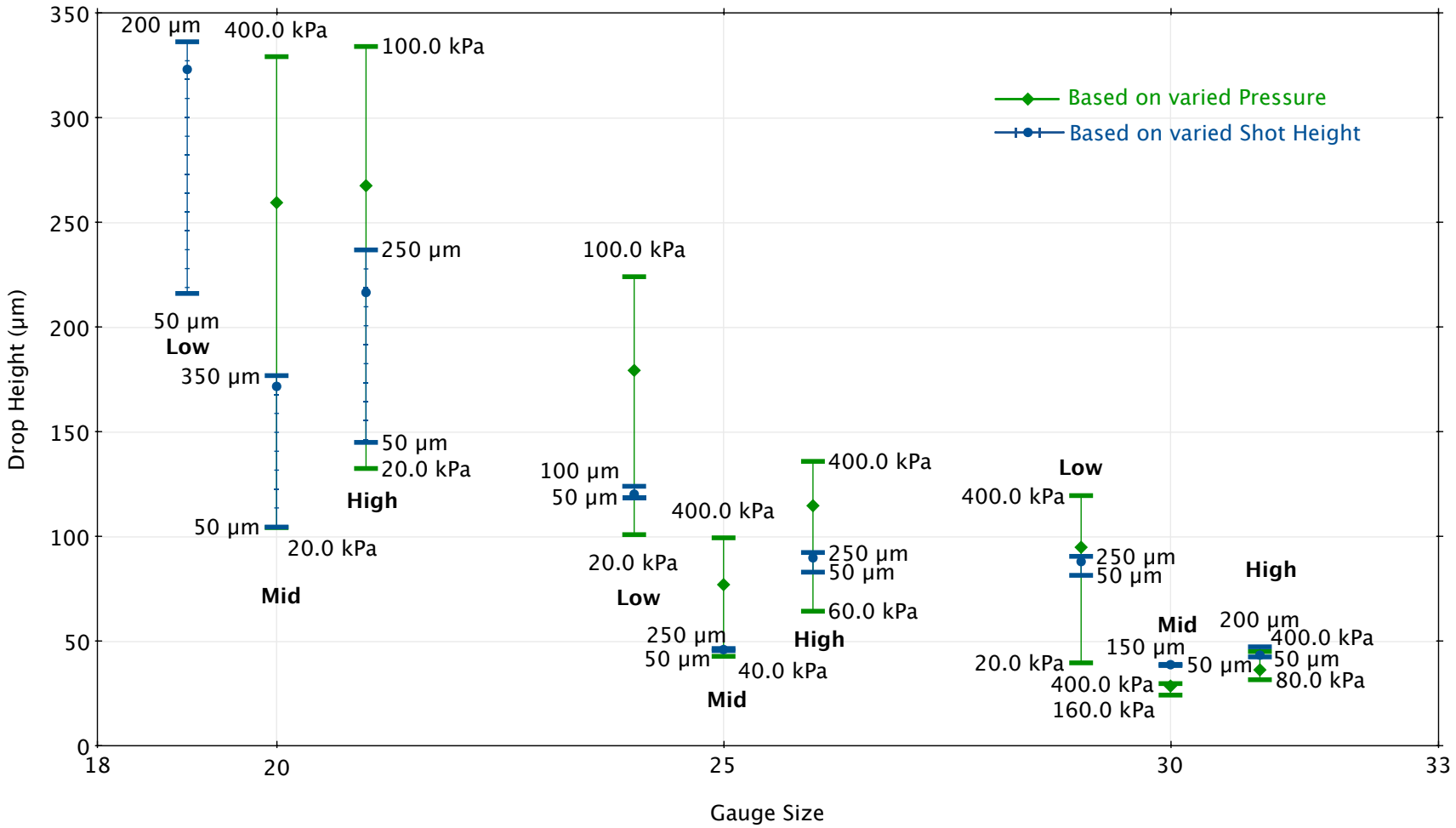

Figure 3.15. Map of drop height as a function of gauge size for the various viscosities, pressures and shot heights. The plotted data aim to demonstrate ranges and trends in drop height with regards to the other variables. The variables for adjusting drop height in order of importance are (1) gauge size, (2) shot pressure and (3) shot height.

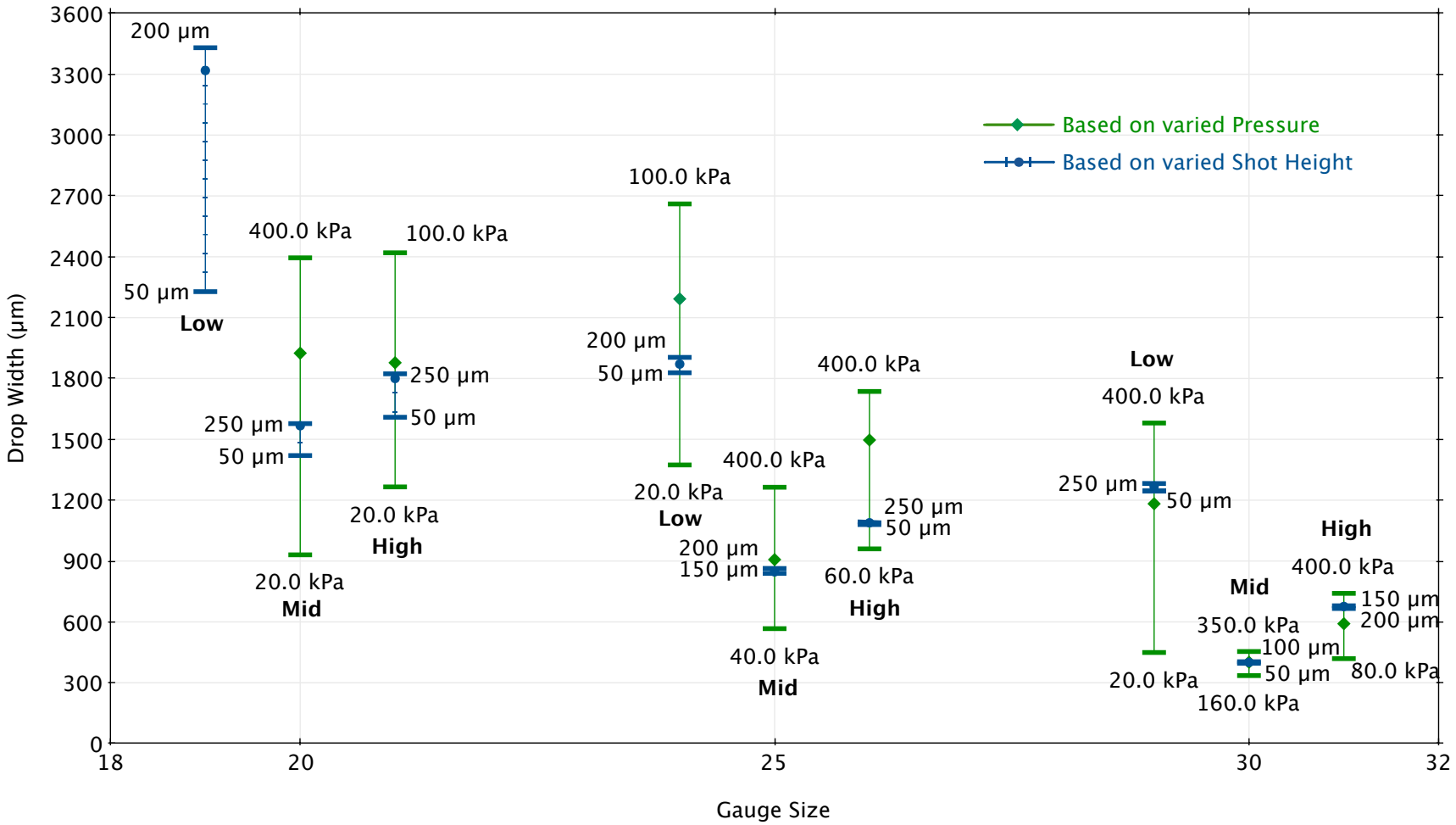

Figure 3.16. Map of drop width as a function of gauge size for the various viscosities, pressures and shot heights. The plotted data again aim to demonstrate ranges and trends in drop height with regards to the other variables. The variables for adjusting drop width in order of importance are (1) gauge size, (2) shot pressure and (3) shot height.

3.5. Chapter Conclusion

1. Traditional 3-dimensional thermoelectric designs lack the geometries and manufacturing scalability that can be found in planar device designs. Planar device designs can utilize various thick-film (60 μm – 300 μm) and thin-film (< 60 μm) manufacturing methods for effectively depositing thermoelectric materials on flexible substrates.
2. A method for fabricating planar TEGs is proposed using dispenser printed techniques. By using a 2 to 3 step printing process, a planar TEG device can be fabricated on a flexible and roll-able substrate to form high-density arrays of high aspect ratio elements.
3. The prototyping dispenser printer used in this work is capable of 1 μm stage accuracy with 5 μm repeatability. The printed features sizes depend on the tip size, which can range from 1 mm to 50 μm.
4. The printing capabilities of the dispenser printer were analyzed to understand the effects of printing variables on feature sizes. The key variables in the dispenser printing process can be categorized by pre-process (ink, viscosity, needle and substrate), process (pressure, shot height and shot spacing) and post-process (temperature and ambient pressure).
5. An epoxy resin was chosen as the ink of study and printed from three different from three different sized syringe tips (20, 25 & 30 Gauge) using shot pressures between 20 and 400 kPa and shot heights between 50 and 300 μm. Vacuum pressure between 0.0 and 0.4 kPa was applied to the syringe to prevent overflow of the epoxy. Once the epoxy was printed, it was cured in a convection oven at 150˚C.
6. While three different optical methods were used to analyze the printed drops, optical microscopy with ImageJ software analysis was found to be the most accurate method. It was found that the printed drop height and width could be adjusted, in order of effectiveness, by the printer tip size, shot pressure and shot height.
7. Further experiments can be performed to understand other variables in dispenser printing including printing speed, accuracy and sample sizes. While the experiments were performed for specifically controlled variables, the resulting trends can be interpreted for different materials systems. The next chapter will introduce thermoelectric materials developed for the described printing method.

Chapter References

[1] H. Bottner, J. Nurnus, and A. Schubert, “Miniaturized Thermoelectric Converters,” in *Thermoelectrics Handbook: Macro to Nano*, no. 46, D. M. Rowe, Ed. Boca Raton, FL: CRC Press, 2006.

[2] W. Glatz, S. Muntwyler, and C. Hierold, “Optimization and fabrication of thick flexible polymer based micro thermoelectric generator,” *Sensors & Actuators: A. Physical*, vol. 132, pp. 337–345, 2006.

[3] G. J. Snyder and E. S. Toberer, “Complex thermoelectric materials,” *Nature Materials*, vol. 7, pp. 105–114, Feb. 2008.
[4] W. Glatz, E. Schwyter, L. Durrer, and C. Hierold, “Bi_2Te_3-Based Flexible Micro Thermoelectric Generator With Optimized Design,” *Journal of Microelectromechanical Systems*, vol. 18, no. 3, pp. 763–772, Jun. 2009.
[5] I. Stark and M. Stordeur, “New Micro Thermoelectric Devices Based On Bismuth Telluride-Type Thin Solid Films,” in *18th International Conference on Thermoelectrics*, 1999, pp. 465–472.
[6] J. Xie, C. Lee, M.-F. Wang, Y. Liu, and H. Feng, “Characterization of heavily doped polysilicon films for CMOS-MEMS thermoelectric power generators,” *Journal of Micromechanics and Microengineering*, vol. 19, p. 125029, Nov. 2009.
[7] S. B. Riffat and X. Ma, “Thermoelectrics: a review of present and potential applications,” *Applied Thermal Engineering*, vol. 23, no. 8, pp. 913–935, Jun. 2003.
[8] K. K. B. Hon, L. Li, and I. M. Hutchings, “Direct writing technology—Advances and developments,” *CIRP Annals - Manufacturing Technology*, vol. 57, pp. 601–620, Nov. 2008.
[9] J. A. Rogers and Z. Bao, “Printed plastic electronics and paperlike displays,” *J. Polym. Sci. Part A: Polym. Chem.*, vol. 40, no. 20, pp. 3327–3334, Sep. 2002.
[10] E. Kunnari, J. Valkama, M. Keskinen, and P. M. ki, “Environmental evaluation of new technology: printed electronics case study,” *Journal of Cleaner Production*, vol. 17, pp. 791–799, 2009.
[11] C. C. Ho, J. W. Evans, and P. K. Wright, “Direct write dispenser printing of a zinc microbattery with an ionic liquid gel electrolyte,” *Journal of Micromechanics and Microengineering*, vol. 20, p. 104009, Oct. 2010.
[12] C. C. Ho, *Dispenser Printed Zinc Microbattery with an Ionic Liquid Gel Electrolyte*, Berkeley, CA: University of California, Berkeley, 2010.
[13] D. Steingart, C. C. Ho, J. Salminen, J. W. Evans, and P. K. Wright, “Dispenser Printing of Solid Polymer-Ionic Liquid Electrolytes for Lithium Ion Cells,” *IEEE Polytronic 2007 Conference*, 2007.
[14] E. S. Leland, P. K. Wright, and R. M. White, “A MEMS AC current sensor for residential and commercial electricity end-use monitoring,” *Journal of Micromechanics and Microengineering*, vol. 19, no. 2009, p. 094018 (6pp), 2009.
[15] L. M. Miller, A. Chen, P. K. Wright, and J. W. Evans, “Resonance Frequency Modification of MEMS Vibration Energy Harvesters using Dispenser-Printed Proof Mass,” in *Proceedings of PowerMEMS 2010*, 2010, vol. 2, pp. 411–414.
[16] P. K. Wright, D. A. Dornfeld, A. Chen, C. C. Ho, and J. W. Evans, “Dispenser Printing for Prototyping Microscale Devices,” in *Transactions of NAMRI/SME*, Kingston, Ontario, Canada, 2010, vol. 38, pp. 555–561.
[17] D. Soltman and V. Subramanian, “Inkjet-Printed Line Morphologies and Temperature Control of the Coffee Ring Effect,” *Langmuir*, vol. 24, no. 5, pp. 2224–2231, Mar. 2008.
[18] Y. Li and C. P. Wong, “Recent advances of conductive adhesives as a lead-free alternative in electronic packaging: Materials, processing, reliability and applications,” *Materials Science & Engineering R*, vol. 51, pp. 1–35, 2006.

Chapter 4

Dispenser Printed Thermoelectric Materials

4.1. Overview

In order to print thermoelectric devices, printable thermoelectric materials must first be developed. Because printed electronic materials are traditionally synthesized as composite materials, printable thermoelectric materials can be developed using established theories and methods. A background on thermoelectric materials will first briefly be introduced. Next, composite materials modeling will be discussed and followed by experimental work on the synthesis of composite thermoelectric materials. Finally, the performance of the materials will be examined with consideration to their applications to printed thermoelectric generators.

4.2. Thermoelectric Materials

The efficiency of thermoelectric materials is conventionally measured by its figure of merit (ZT), which can be written as:

$$ZT = \frac{\alpha^2 \sigma}{\lambda} T \tag{4.1}$$

where α is the Seebeck coefficient, σ is the electrical conductivity, λ is the total thermal conductivity and T is the temperature of operation.

In order to achieve high efficiency thermoelectric materials, ZT needs to be maximized through optimization of the individual material properties. Subsequently, this requires a high Seebeck coefficient, high electrical conductivity and low thermal conductivity. This task becomes complex because of the fundamentally conflicting material properties (i.e. good conductors of electricity are frequently good conductors of heat).

The carrier concentration of a material is essential to the individual materials parameters. A high Seebeck coefficient requires a low concentration of a single carrier type. Thus, insulators and

semiconductors have high Seebeck coefficients. Based on electron transport models [1], [2], the Seebeck coefficient of metals or degenerate semiconductors can be approximated as:

$$\alpha = \frac{8\pi^2 k_B^2}{3eh^2} m^* T \left(\frac{\pi}{3n}\right)^{2/3} \tag{4.2}$$

where k_B is the Boltzmann constant, e is the electron charge, h is Planck's constant, n is the carrier concentration, m^* is the effective mass of the carrier and T is the temperature.

The electrical conductivity can be described as:

$$\sigma = \frac{1}{\rho} = ne\mu \tag{4.3}$$

where ρ is the electrical resistivity and μ is the carrier mobility.

Equations (4.2) and (4.3) suggest a conflicting relationship between a high Seebeck coefficient and a high electrical conductivity as a function of n. Figure 4.1 demonstrates the balance between the two properties to ultimately maximize the power factor ($\alpha^2\sigma$). The power factor is typically optimized through doping of narrow-band semiconductor materials to adjust the carrier concentration, with peaks typically between 10^{19} and 10^{21} carriers per cm^3 [2], [3].

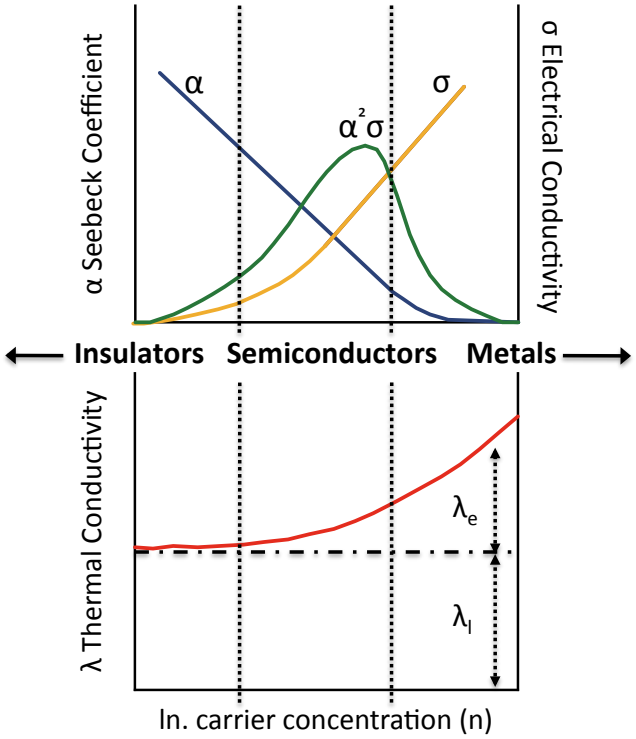

Figure 4.1. Thermoelectric material properties as a function of carrier concentration. Adapted from [4].

Additional materials choices to maximize the ZT are complicated when considering the total thermal conductivity, which can be expressed as:

$$\lambda = \lambda_e + \lambda_l \tag{4.4}$$

where λ_e is the electronic thermal conductivity and λ_l is the lattice thermal conductivity. The electronic thermal conductivity results from electrons and holes transporting heat, and is directly related to the electrical conductivity through the Wiedemann-Franz law:

$$\lambda_e = L\sigma T = ne\mu LT \tag{4.5}$$

where L is the Lorenz factor for free electrons [5], [6]. This results in conflicting material properties since high electrical conductivities and low thermal conductivities are desirable for high *ZT* materials. Thus, high power factors of the heavily doped semiconductors in conjunction with their relatively low lattice thermal conductivities ultimately give the largest *ZT* [3].

Figure 4.2 shows the *ZT,* for various temperatures of the state-of-the-art thermoelectric materials. Decades of research and development have established Bi_2Te_3-based alloys as the most ubiquitous thermoelectric materials for near room-temperature applications. First investigated in the 1950's [7], [8] as promising thermoelectric materials, Bi_2Te_3 and its alloys are still the predominant thermoelectric materials today [2], [3], [9]. However, recent advances over the last decade in low-dimensional nanostructured materials have begun to demonstrate materials with *ZT*>1 [2], [9-11]. While these developments have only recently emerged from various research institutions, the potential for their future adoption in commercial technologies is promising. Given the wide availability of Bi_2Te_3 and Sb_2Te_3 materials and their high *ZT*'s (~1) near room temperature, they are ideal candidates for the development of printable composite thermoelectric materials.

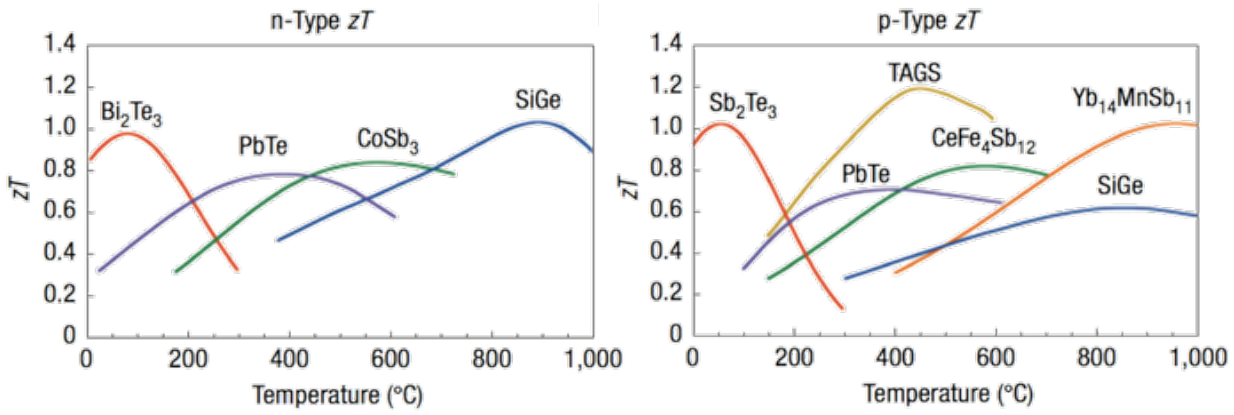

Figure 4.2. Figure of merit (ZT) of n-type (left) and p-type (right) state-of-the-art thermoelectric materials as a function of operating temperature [2].

4.3. Printable Composite Materials

In order to fabricate thermoelectric devices using printed methods, printable thermoelectric materials must first be developed. Printed materials typically consist of active particles suspended in an uncured polymer matrix. The composite system becomes an "ink" which can be deposited using various printing techniques and finally cured or dried. The active particles consist of various conductive inorganic materials, while the polymer matrix acts as a binder and is typically an epoxy and thermoplastic [12-15]. Methods for synthesizing polymer composites have been well established in the electronics industry for printed circuit boards (PCB) and thermal interface materials (TIM) [15-20]. A similar approach can thus be used for developing

printable thermoelectric materials with active thermoelectric particles (such as Bi_2Te_3 or Sb_2Te_3) dispersed in a polymer matrix. Figure 4.3 demonstrates a representation of thermoelectric composite ink used for dispenser printing.

Since the printed thermoelectric material consists of two distinct components, the effective material properties of the printed material will be a function of the constitutive elements. It is thus of interest to investigate composite theories to predict the expected material properties. Among the thermoelectric material properties, effective media theories for electrical conductivity and thermal conductivity, which are well-established in literature, will be explored [15], [16], [18], [20]. The complex nature of the Seebeck coefficients in composite systems will be empirically examined in section 5.4.

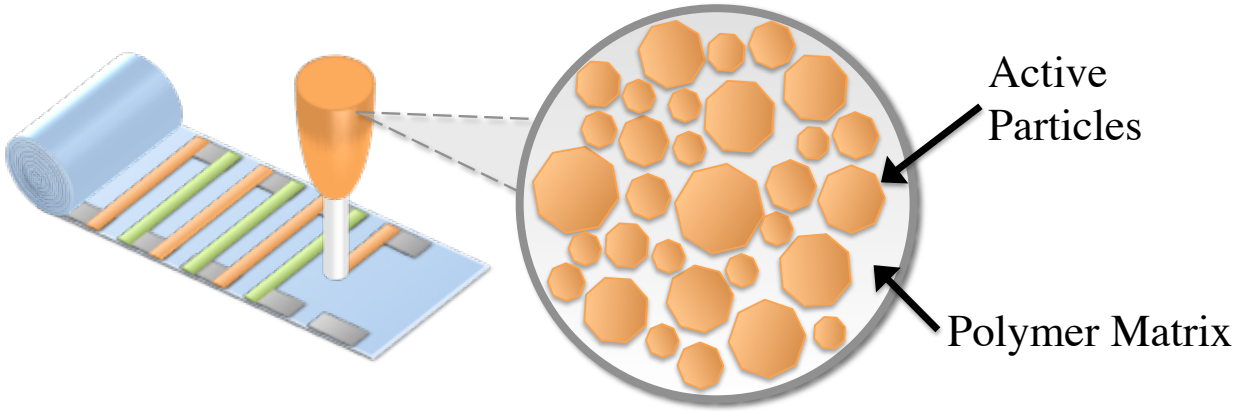

Figure 4.3. Schematic representation of the thermoelectric composite ink used for dispenser printing.

4.3.2. Electrical Conductivity of Composites

In order to model the electrical conductivity of a composite system, various effective media theories for composites can be utilized. Electrically conductive composite materials are widely used in industrial applications as resistors, sensors and transducers. These can include commonly found products such as thermistors, piezoresistors or chemical sensors [21]. This work will not aim to review some of the various composite models for electrical conductivity, but will instead focus on utilizing the available theories for predicting the performance of composite thermoelectric materials. Thorough reviews on composite theory and experimental work can be found in [21-24].

The effective electrical conductivity of a composite (σ_{eff}) can be classically described as a function of the conductivities of the two phases, the conductive particle ($\sigma_{particle}$) and the polymer matrix (σ_{matrix}), and their respective volume fractions ($\phi_{particle}$ and ϕ_{matrix}). Modern theories have evolved to include percolation theories and the Bruggeman effective media theories to simulate effects from the metal-insulator transition phenomenon and asymmetry, respectively [21], [25]. The Bruggeman-general effective media (GEM) theory can be shown as a matched asymptotic expression:

$$\frac{\phi_{matrix}\left(\sigma_{matrix}^{1/t}-\sigma_{eff}^{1/t}\right)}{\sigma_{matrix}^{1/t}+A\sigma_{eff}^{1/t}}+\frac{(1-\phi_{matrix})\left(\sigma_{particle}^{1/t}-\sigma_{eff}^{1/t}\right)}{\sigma_{particle}^{1/t}+A\sigma_{eff}^{1/t}}=0 \tag{4.6}$$

$$= \frac{(1-\phi_{particle})(\rho_{eff}^{1/t} - \rho_{matrix}^{1/t})}{\rho_{eff}^{1/t} + A\rho_{matrix}^{1/t}} + \frac{\phi_{particle}(\rho_{eff}^{1/t} - \rho_{particle}^{1/t})}{\rho_{eff}^{1/t} + A\rho_{particle}^{1/t}}$$

where t is the exponent for percolation equations (typically 1.65-2.0), ρ_{eff}, $\rho_{particle}$ and ρ_{matrix} are the respective resistivities ($\rho = 1/\sigma$) of the composite, particle and matrix, and A is defined as:

$$A = \frac{1-\phi_c}{\phi_c} \tag{4.7}$$

where ϕ_c is the critical percolation volume fraction of the particle (typically ~0.16 for metal-insulator composites).When the $\sigma_{matrix} = 0$ and $\rho_{particle} = 0$, Equation 4.6 can be written as:

$$\sigma_{eff}^{1/t} - \sigma_{particle}^{1/t}\left(1 - \frac{1-\phi_{particle}}{1-\phi_c}\right) = 0 = \rho_{eff}^{1/t} - \rho_{matrix}^{1/t}\left(1 - \frac{\phi_{particle}}{\phi_c}\right) \tag{4.8}$$

which are the classical percolation equations.

Figure 4.4 demonstrates various effective resistivity bounds as a function of particle volume fraction [21]. It is interesting to note that classical theories including the rule of mixtures (Figure 4.4a and 4.4g), Hashin-Shrikman (Figure 4.4b and 4.4f) and GEM (Figure 4.4c and 4.4e) only give an upper and lower bound to the effective resistivity of the composite system. The Bruggeman-GEM theory provides a clearer understanding of the effective resistivity provided a known percolation volume.

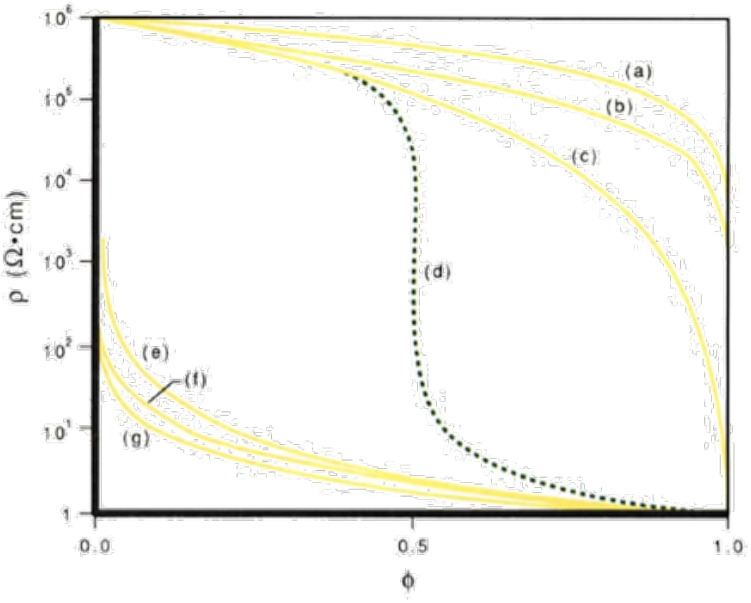

Figure 4.4. Various resistivity bounds for a composite system where $\rho_{matrix} = 10^6$ Ω-cm and $\rho_{particle} = 1$ Ω-cm. The curves represent the effective resistivity of the composite as a function of particle volume fraction using the (a) series addition formula, (b) Hashin-Shrikman upper bound, (c) GEM equation (t = 3, $\phi_c = 1$), (d) Bruggeman-GEM equation (t = 1, $\phi_c = 0.5$), (e) GEM equation (t = 3/2, $\phi_c = 0$), (f) Hashin-Shrikman lower bound and (g) parallel additional formula [21].

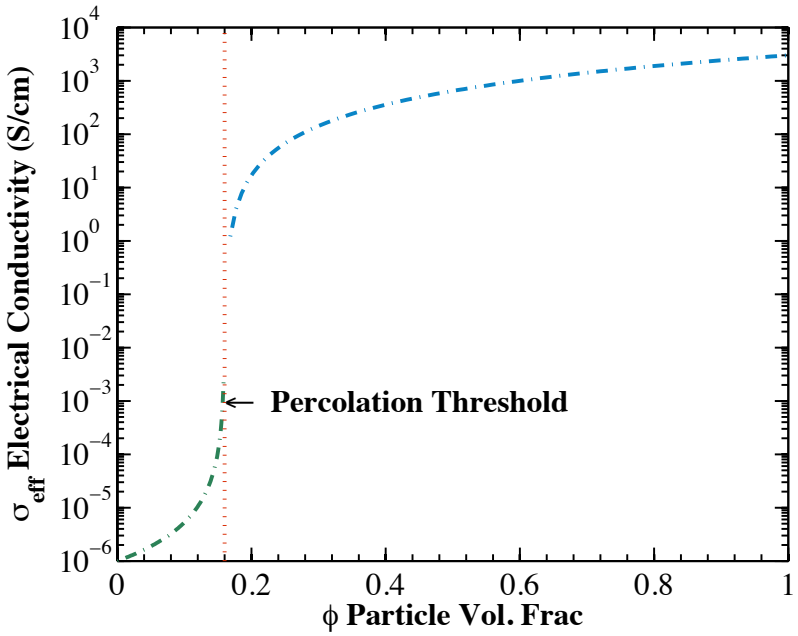

Figure 4.5. Effective electrical conductivity of a composite system consisting of a conductive Bi_2Te_3 particle ($\sigma_{particle}$ = 3000 S/cm) in an insulating epoxy matrix (σ_{matrix} = 10^{-6} S/cm) calculated using the Bruggeman-GEM equation (ϕ_c = 0.16 and t = 1.7).

The effective conductivity of a composite thermoelectric material can thus be estimated using Equation 4.6. Figure 4.5 shows the effective composite electrical conductivity as function of particle volume fraction for system consisting of an insulating polymer (σ_{matrix} = 10^{-6} S/cm) and an active thermoelectric material ($\sigma_{particle}$ = 3000 S/cm for Bi_2Te_3-based alloys). The percolation threshold was assumed to be ~0.16 while the exponent for the percolation equation was assumed to be ~1.7 based on previous empirical studies on thick-film resistors [21]. However, accurate values for ϕ_c and t must ultimately be empirically determined. It should be noted that the Bruggeman-GEM model assumes low particle contact resistance due to sintering at high particle volume fractions. While this assumption is valid for many ceramic and low-temperature sintering metal systems, inter-particle contact resistance can ultimately become a limiting factor in achieving high conductivity systems. Based on the Bruggeman-GEM model, the effective electrical conductivity of the composite system can be expected to be approximately 1 to 2 orders of magnitude lower than the bulk electrical conductivity of the particle once the volume fraction exceed the percolation threshold. The decrease in the electrical conductivity can be attributed to the addition of an electrically insulating polymer in the composite system. While the lower electrical conductivity of the composite will decrease the efficiency of the thermoelectric system, the thermally insulating effects of the polymer can perhaps lower the effective thermal conductivity of the system.

4.3.3. Thermal Conductivity of Composites

Effective thermal conductivity theories and experiments have similarly been well established due to wide use of thermal interface materials (TIM) for microelectronics. In fact, many of the theories on the electrical conductivity of composites directly translate to theories on thermal

conductivity. Conduction theories including the rule of mixtures [20], [26], Maxwell-Garnett equations [27-29] the Bruggeman asymmetric model [30], [31] are valid for modeling effective thermal conductivity. In depth studies on the theories and reviews on the thermal conductivity of composites and TIM's can be found by various authors [18-20], [26-32].

The effective thermal conductivity of a composite (λ_{eff}) can be similarly described as a function of the conductivities of the two phases, the conductive particle ($\lambda_{particle}$) and the polymer matrix (λ_{matrix}), and their respective volume fractions ($\phi_{particle}$ and ϕ_{matrix}). The modified Bruggeman asymmetric model (BAM) including interface resistance between particles has been found to be effective in modeling TIM systems similar to that of the desired thermoelectric composite systems [18]. This can be written as:

$$\left(1-\phi_{particle}\right)^3 = \left(\frac{\lambda_{matrix}}{\lambda_{eff}}\right)^{(1+2a)/(1-a)} \times \left(\frac{\lambda_{eff}-\lambda_{particle}(1-a)}{\lambda_{matrix}-\lambda_{particle}(1-a)}\right)^{3/(1-a)} \tag{4.9}$$

where a is the Biot number defined as:

$$a = \frac{R_b \lambda_{matrix}}{\mathrm{d}} \tag{4.10}$$

where R_b is the interface contact resistance and d is the average particle size. For systems where $\lambda_{particle} >> \lambda_{matrix}$, Equation 5.9 can be simplified to:

$$\frac{\lambda_{matrix}}{\lambda_{eff}} = \frac{1}{\left(1-\phi_{particle}\right)^{3(1-a)/(1+2a)}} \tag{4.11}$$

Studies have found that values for a between 0 and 0.1 match well with experimental work on thermal interface compounds as shown in [18].

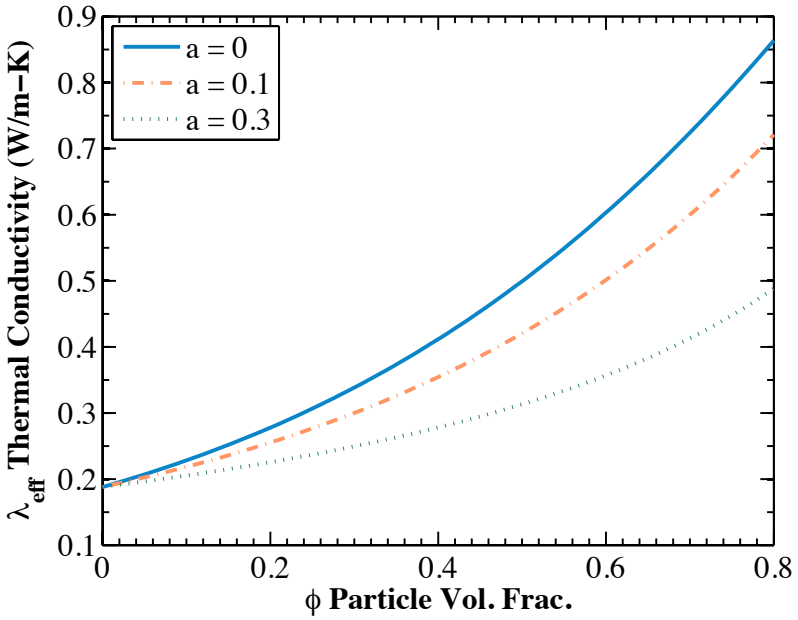

Figure 4.6. Effective thermal conductivity of a composite system consisting of a Bi_2Te_3 particle ($\lambda_{particle}$ = 1.2 W/m-K) in an insulating epoxy matrix (λ_{matrix} = 0.19 W/m-K) calculated using the Bruggeman assymetric model (BAM) for various Biot numbers (a = 0, 0.1 and 0.3).

Using the BAM, Figure 4.6 shows the simulated effective thermal conductivity of a composite thermoelectric system consisting of Bi_2Te_3 particle dispersed in an epoxy matrix as a function of the particle volume fraction for various Biot numbers. At 30 – 40 % particle volume fractions, a range used for similar systems [15], [33-36], the effective thermal conductivity can be estimated between 0.23 – 0.4 W/m-K depending on the Biot number. The low effective thermal conductivity is a result of the thermally insulating characteristics of the polymer, and its application towards the ZT is encouraging. The reduced thermal conductivity can thus offset losses in electrical conductivity to provide a respectable ZT for the effective composite.

4.4. Experimental

4.4.1. Materials Synthesis

The printable thermoelectric materials are composite systems, consisting of active thermoelectric powder (n-type Bi_2Te_3 or p-type Sb_2Te_3 particles) and a polymer binder. Empirical tests have suggested that powders with an average particle size of 10μm produce optimal composite properties [15], [33], [37]. To synthesize such powders, 80-100 mesh Bi_2Te_3 (Merit Technology Group Co., Ltd.) and Sb_2Te_3 (Super Conductor Materials, Inc.) powders were individually placed into 100ml stainless steel jars with 3mm stainless steel balls at a ball-to-powder mass ratio of 10:1. The jars were then placed in a high-energy planetary ball mill (Torrey Hills ND 0.4L) and operated at rotational speeds of 210-280 rpm for 30-180 min. Isopropanol (Sigma Aldrich, Inc.) was used as a process control agent at a 1:1 weight ratio of powder to fluid. All materials preparation and extraction were performed in a dry argon environment at < 0.1 ppm oxygen to prevent the oxidation of materials. The particle size distribution of the powders was confirmed using a Coulter LS-100 particle sizer. The resulting average particle size after ball milling was 10 μm while the particles ranged between 2 μm and 60 μm. Particle density measurements were performed using helium gas pycnometry by Micromeritics Analytical Services to confirm the respective densities of the milled powders (7.6767 g/ml for Bi_2Te_3 and 6.2282 g/ml to Sb_2Te_3).

The polymer binder was an epoxy system formulated using a bisphenol f epoxy resin (EPON 862, Hexion Specialty Chemicals, Inc.) and an anhydride-based hardener (MHHPA, Broadview Technologies, Inc.). The epoxy-to-hardener equivalent weight ratio was 1:0.85. A phosphate-based accelerator (AC-8, Broadview Technologies, Inc.) was employed as the catalyst in the system. 10-20 wt% of butyl glycidyl ether (Heloxy 61, Hexion Specialty Chemicals, Inc.) was added to the resin blend as a reactive diluent to reduce the viscosity of the ink. Low percentages of organic solvents were also used to both extend the shelf-life of the epoxy system and adjust the viscosity for printing. The epoxy system used in this work was particularly chosen for its low viscosity and extended pot-life [15], [33].

80-82 wt% Bi_2Te_3 or Sb_2Te_3 powder and 18-20 wt% epoxy resin were mixed to make inks. The inks were mixed using a vortex mixer and an ultrasonic bath to disperse the particles. The thermoelectric inks were then printed on glass substrates to form 100-200 μm thick films using the dispenser printer. The films were finally cured at either 250°C or 350°C in an argon/vacuum oven for a minimum of 3 hours. Previous studies have described the effects of processing and optimization of these thermoelectric composite inks [38]. Figure 4.8 shows scanning electron microscope (SEM) images of dispenser printed Bi_2Te_3/epoxy composite films cured at 250°C

and Sb_2Te_3/epoxy composite films cured at 350°C. The images suggest that the composite films are uniform and have low porosity. Sb_2Te_3 films cured at 350°C show sintering behavior and its effects on material properties will be discussed later.

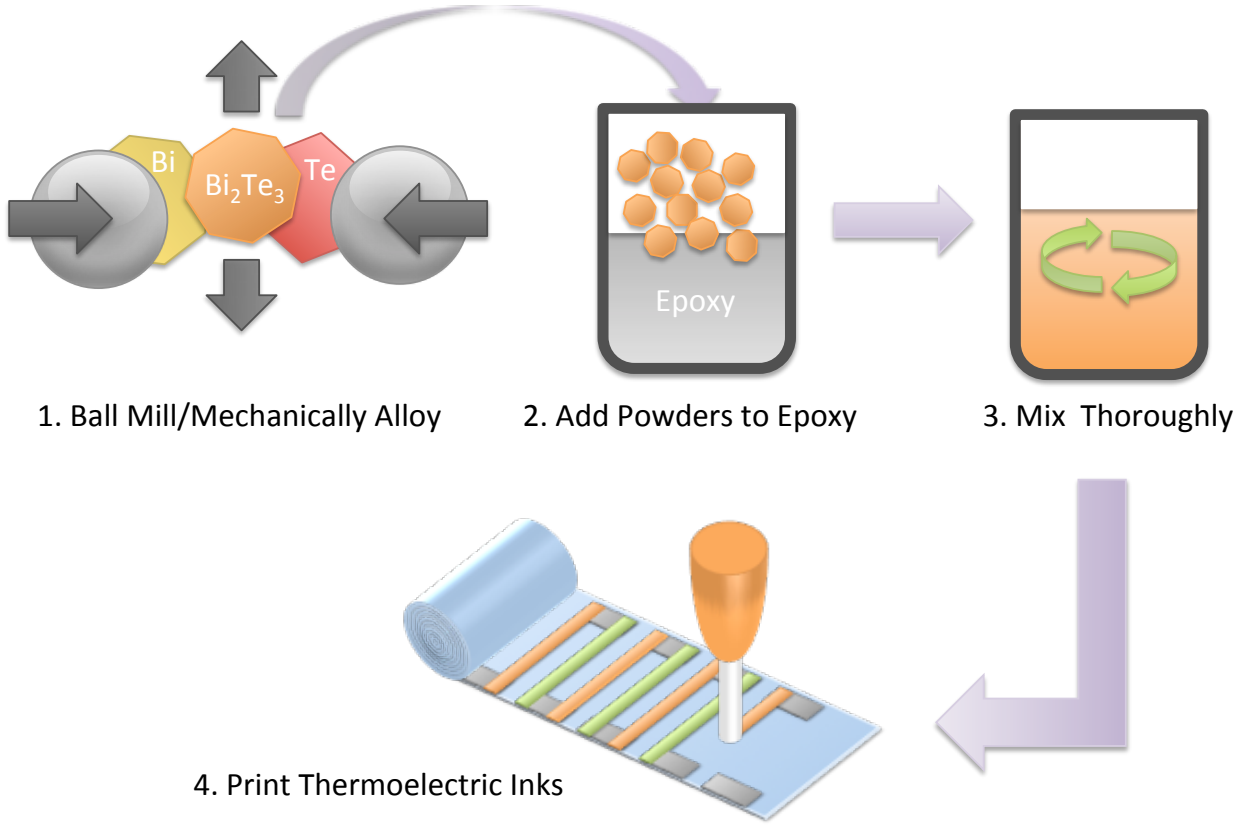

Figure 4.7. Materials synthesis process flow for printable thermoelectric materials. (1) Bulk elemental or semiconductor powders first ball-milled or mechanically alloyed to reduce the average particle size to 10 µm. (2) The powders are next added to an epoxy resin mixture. (3) The slurry or "ink" is thoroughly mixed using a vortex mixer and ultrasonic bath to disperse the particles. (4) The thermoelectric "ink" is printed and cured using various processing parameters.

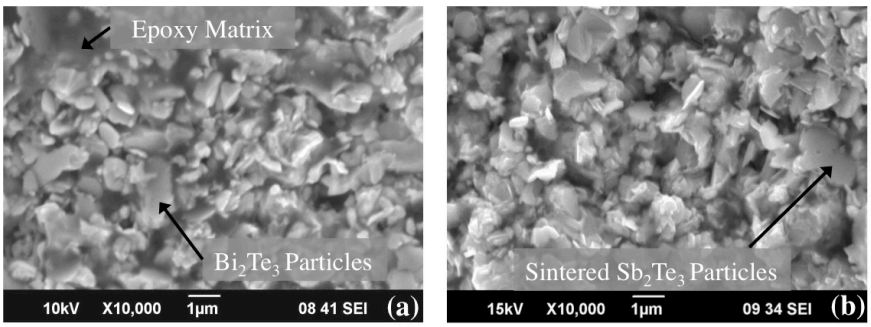

Figure 4.8. Scanning electron microscope images of (a) Bi_2Te_3/epoxy composite film cured at 250°C and (b) Sb_2Te_3/epoxy composite films cured at 350°C.

Bulk samples of the Sb_2Te_3 powders were additionally synthesized using traditional cold-pressing techniques. The as-milled powders were first molded in a pellet and pressed between 2000 – 3000 psi. The pallet was then placed in an Ar furnace where the temperature was increased at a rate of 3°C /min to 465°C. The temperature was next reduced to 350°C and annealed for 4 hrs. Finally, the temperature was reduced down to room temperature at a rate of 3°C /min. The cold-pressed samples were used for comparison of material properties relative to the composite films. Bulk samples of Bi_2Te_3 from the stock batch were used as the reference material for the n-type composite film.

4.4.2. Materials Characterization

A modulated Differential Scanning Calorimeter (DSC, Model 2920, TA Instruments) was used to study the curing profile of the polymer matrix. The onset peak and disintegration temperatures from the exothermic and endothermic diagrams were recorded and analyzed. The morphology of grains and grain boundaries were observed using a scanning electron microscope (JSM-6490 LV).

Electrical conductivity measurements of the printed thermoelectric materials were carried out using the Van der Pauw method to determine the sheet resistance of the materials. Seebeck measurements were performed using a custom Seebeck testing system to determine the voltage output of the material for a given temperature difference (ΔT). Both the electrical conductivity and the Seebeck coefficients of the materials were measured at various temperature set points ranging from room temperature to 150˚C. This allows for materials characterization at temperature ranges of low-grade heat applications. For each temperature set point, up to 70 measurements were taken for each sample. All measurements were taken in a thermally insulated Faraday cage to limit sources of error from the ambient environment. Details of the experimental configuration can be found in Appendix C.

Thermal conductivity measurements were performed using two different bulk thermal conductivity measurement methods. The first method was using an Anter Corp. Model 2021 steady-state thermal conductivity tester. Since measurements of thermal conductivity were limited by the large sample size requirements (24.5 mm x 24.5 mm) of the tester, large composite samples were prepared by first casting the thermoelectric slurries in a Teflon mold followed by a similar curing process in an argon/vacuum oven. The second method of measuring thermal conductivity was performed using a transient plane source (TPS) method with a C-Therm TCi thermal conductivity analyzer. Transient plane source techniques have been proven to be effective for characterization of other composite systems similar to the materials presented in this work [39-42]. To synthesize samples for the transient plane source method, 20 ml scintillation glass vials (Wheaton Industries, Inc.) were first coated with a Teflon spray (Dupont D00110101 Teflon Multi-use Dry, Wax Lubricant). The polymer and active materials were then placed into the vials and thoroughly mixed. Acetone and solvent mixtures (SPI Supplies Silver Paint Thinner) were empirically added to ensure homogenous slurries. The glass vials were then placed on a hot plate at 65˚C for 12-24 hrs with the top exposed to air to evaporate the solvents. The glass vials were then placed in the vacuum/argon oven for curing. After the composite were cured, the glass vial was broken to release the large composite sample for measurement. The resulting composite disk had a diameter of 24 mm and ranged in thicknesses between 3-4 mm. Some surface polishing was performed to flatten the disks for measurement.

4.5. Results & Discussion

As with any composite material system, the effective properties of the composite are a function of all the properties of the individual material properties [43]. It is ultimately desirable to achieve composite properties similar to or exceeding those of the bulk properties of individual materials. However, given that the electrical conductivity and the Seebeck coefficient of the polymer binder are significantly lower than that of the active filler thermoelectric material, the effective properties of the composite system are expected to be less than desirable. To achieve the preferred conductivity of the thermoelectric composite films, both the composite volume fractions and polymer curing temperatures need to be optimized. The shrinkage of the polymer matrix upon curing effectively packs the fillers involved [44]. The curing profile for the epoxy polymer matrix measured by the DSC is shown in Figure 4.9a. An exothermic peak is observed at about 150°C, which is typical for catalyzed epoxy resin system with an anhydride hardener [33]. An endothermic peak at approximately 400°C also suggested the pyrolysis of the epoxy resin. The curing profiles of electrically conductive composites (with 40% volume fraction of particles) were fairly similar to that of the polymer matrix. DSC was also used to study phase changes of Sb_2Te_3 and Bi_2Te_3 ball milled powders (Figure 4.9b). A sharp endothermic peak for Sb_2Te_3 is observed at about 425°C which corresponds to the melting point of Te or a Te rich phase [45]. No endothermic sharp peaks were observed in the DSC curve for the Bi_2Te_3 ball milled powder in the studied temperature range.

XRD studies were also performed on the as received Sb_2Te_3 and Bi_2Te_3 as shown in Figure 4.10. Extra peaks of Te were found in the Sb_2Te_3 suggesting the presence of excess Te in the as received powder [46]. It substantiates the lower melting point of Sb_2Te_3 as shown in DSC of Sb_2Te_3 Figure 4.9b.

In order to optimize the volume fraction of the composites, samples with different ranges of particle volume fractions were synthesized and characterized. Figures 4.11a and 4.11b show the electrical conductivity and Seebeck coefficient of the n-type Bi_2Te_3 composites as a function of particle volume fraction. The electrical conductivity of the composite shows an increasing trend with particle volume fraction beyond the percolation threshold, similar to that of Figure 4.5. However, the electrical conductivity appears to plateau beyond 40% particle loading due to the lack of sintering in the system. Volume fraction loadings >45% were unachievable in the current system due to cracking in the film after curing. The Seebeck coefficient of the composite system is surprisingly consistent between particle volume fractions of 13-45%. There appears to be no dependency between the Seebeck coefficient and the volume fraction at that range. This presents an intriguing finding for thermoelectric polymer-composite systems and the physics of the systems should be further explored.

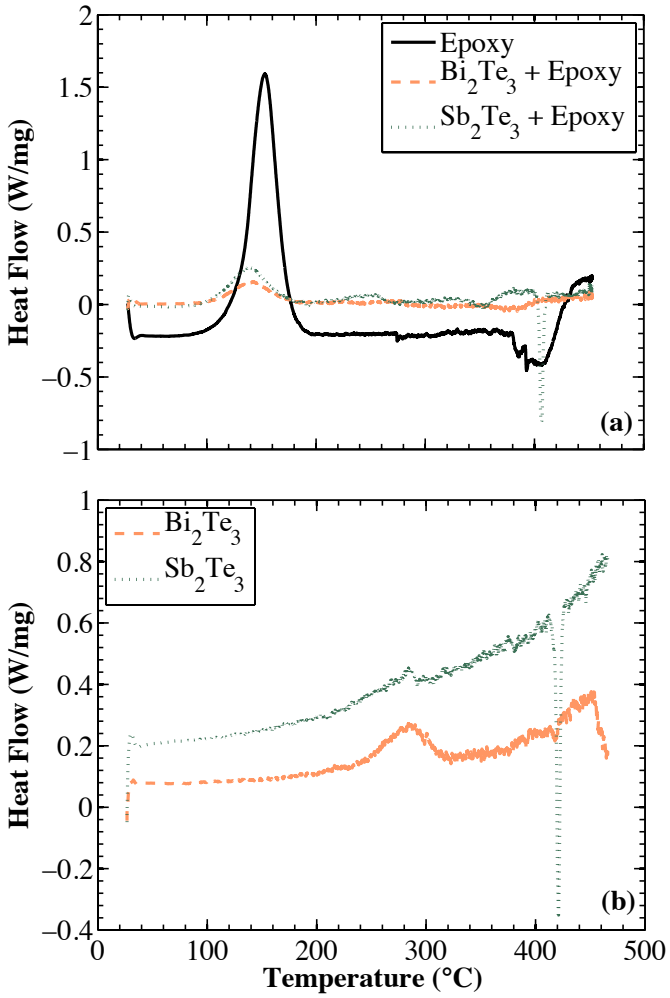

Figure 4.9. Differential Scanning Calorimeter (DSC) measurements of (a) the epoxy polymer and the thermoelectric composites, and (b) ball-milled Sb_2Te_3 and Bi_2Te_3 powders.

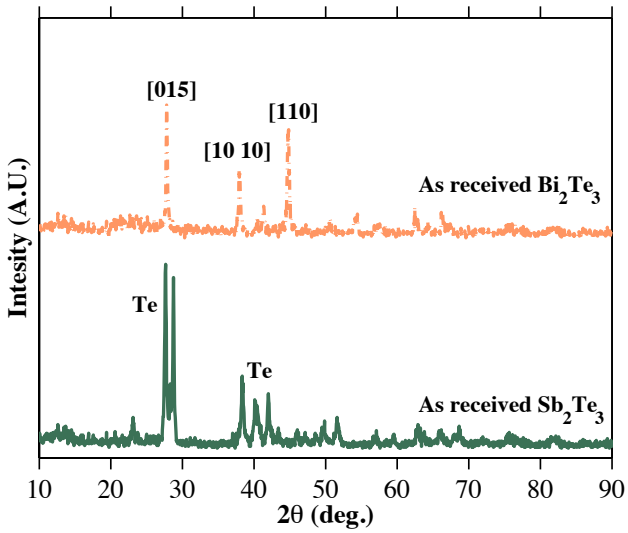

Figure 4.10. X-ray powder diffractions (XRD) of the as-received thermoelectric powders.

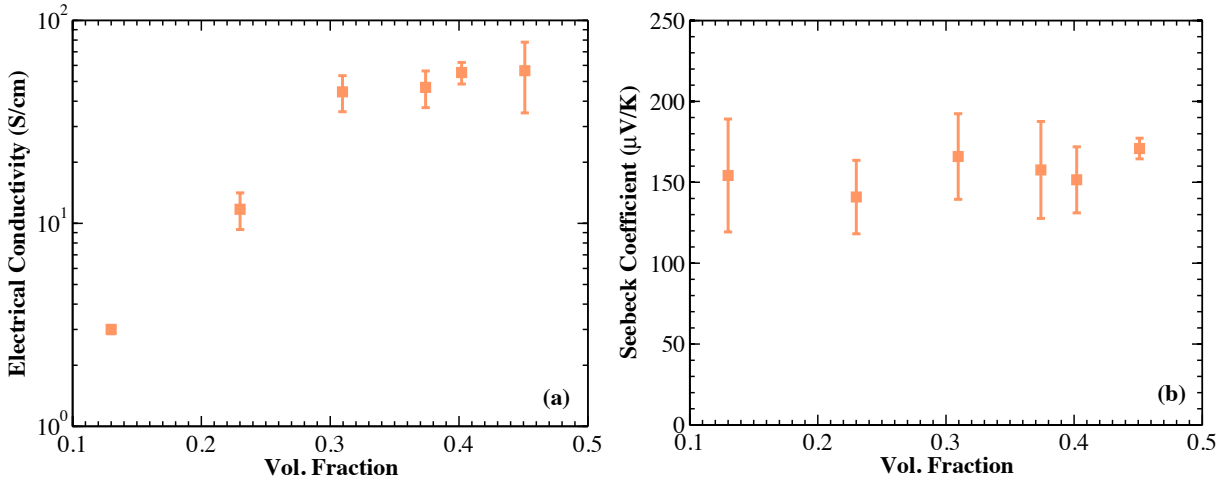

Figure 4.11. Measurements of (a) electrical conductivity and (b) Seebeck coefficient as a function of particle volume fraction for the Bi_2Te_3-based composites.

Since the performance of the composite materials proved to be most consistent at approximately 40% particle volume fraction, the formulation was chosen for further characterization. Figure 4.12 shows the temperature dependence of the thermoelectric composite materials compared to the values of bulk cold-pressed samples. The Seebeck coefficient (α) of the p-type Sb_2Te_3 composite has a peak value of approximately 160 μV/K when cured at 250°C, which is higher than the bulk cold-pressed Sb_2Te_3. However, the electrical conductivity (σ) of the composite system is approximately an order of magnitude less than that of bulk sample. This is due to the insulating characteristics of the polymer. When the p-type Sb_2Te_3 composite is cured at 350°C, the particles sinter as shown by the necking between particles in Figure 4.8b. This allows for better hole transport and increases σ for the composite by an order of magnitude [47]. Nevertheless, this presents a trade-off as α of the p-type composite reduces to 120 μV/K. The resulting power factor ($\alpha^2\sigma$) for the Sb_2Te_3 composite is ultimately higher for a sintered system.

Sintering of the n-type Bi_2Te_3 composite was not achievable because its high temperature sintering requirements exceed the 400°C disintegration temperature of the polymer. When the n-type composites were cured at 350°C a slight improvement in thermoelectric properties could be observed. Due to inconsistencies in the measured material property, the temperature dependent data for n-type Bi_2Te_3 cured at 350˚C are not reported. The α of this composite n-type system is -157 μV/K, comparable to that of the p-type Sb_2Te_3, while the σ of the Bi_2Te_3 composite is almost 2 orders of magnitude lower than bulk due to the insulating polymer in the system.

The temperature dependence of the composite materials suggests that the materials are best suited for near-room temperature applications. Both composite systems show a decreasing trend in performance as the operating temperature increases. These trends in power factor are similar to that of bismuth and antimony telluride based materials [48-51]. Further research involving processing optimization and low-temperature sintering additive can be explored to improve the performance of these composites.

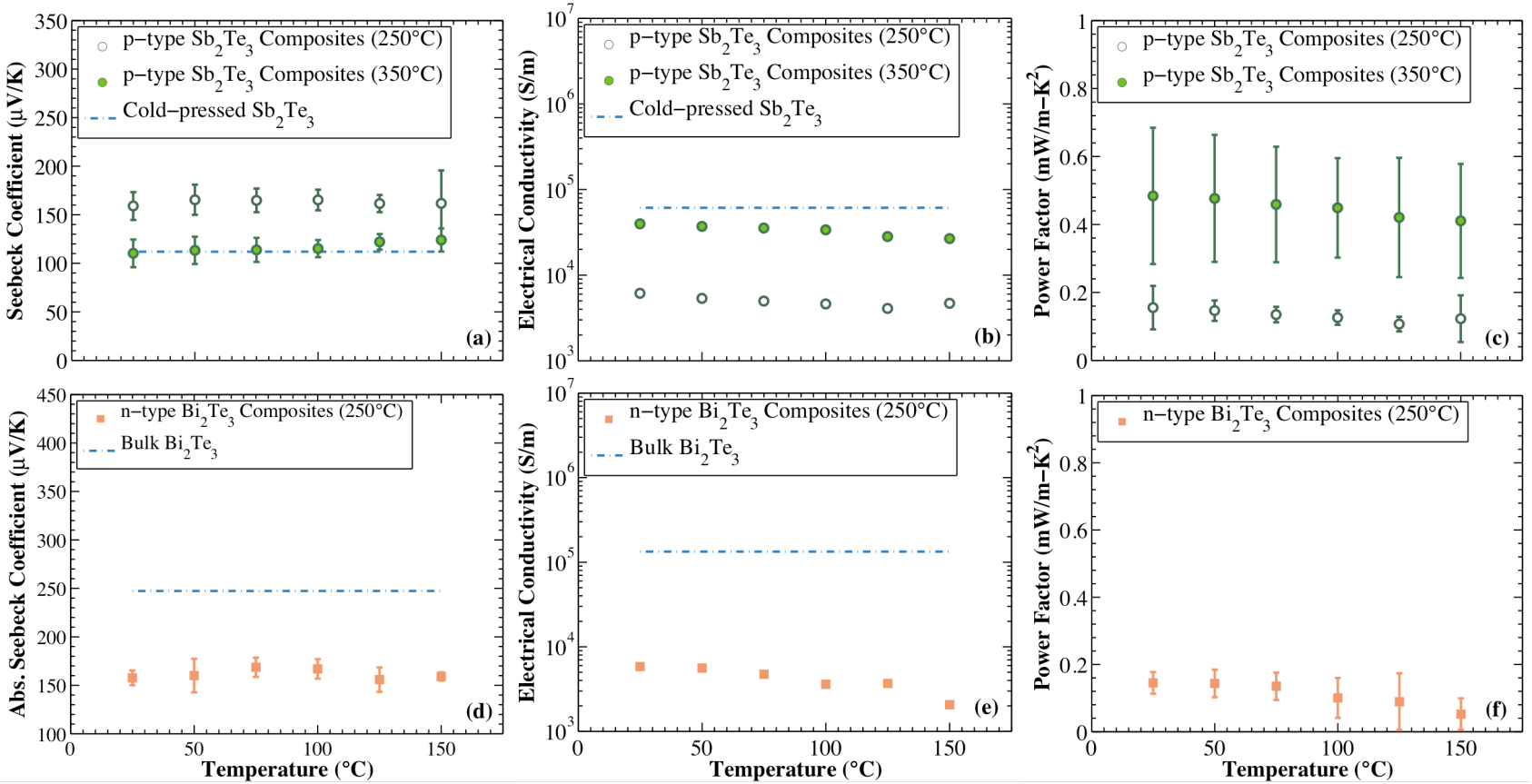

Figure 4.12. Temperature dependence of the (a, d) Seebeck coefficient, (b, e) electrical conductivity and (c, f) power factor for Bi_2Te_3 composites (solid square), Sb_2Te_3 composites cured at 250˚C (clear circle) and 350˚C (solid circle).

Figure 4.12 shows the temperature dependent thermal conductivity of both the p-type Sb_2Te_3 and Bi_2Te_3 composites cured at 250˚C. The measurements in Figure 4.13 were taken using the transient plane source (TPS) method. Measurements taken using the steady state heat flow method are shown in Table 4.1. Results taken from the steady state heat flow technique consistently gave lower values for the thermal conductivity compared to the TPS method. Both the Sb_2Te_3 and Bi_2Te_3 systems exhibit low thermal conductivities due to the insulating effects of the polymer. The thermal conductivities of both systems are lowest at room temperature proving again that they are best suited for near-room temperature applications. The thermal conductivity of the bulk n-type Bi_2Te_3 material is shown in Figure 4.13b for reference as provided by the materials supplier. The resulting temperature dependent dimensionless figures of merit (ZT) for both composite systems are shown in Figure 4.14. The maximum ZT's for both systems are found near room temperature. They are 0.22 and 0.18 for the p-type Sb_2Te_3 and n-type Bi_2Te_3 respectively. The thermal conductivity of p-type Sb_2Te_3 cured at 350°C, however, is slightly higher due to the sintering effects. These effects allow the maximum ZT of the Sb_2Te_3 composite to reach 0.34 with primary improvements form the electrical conductivity of the system.

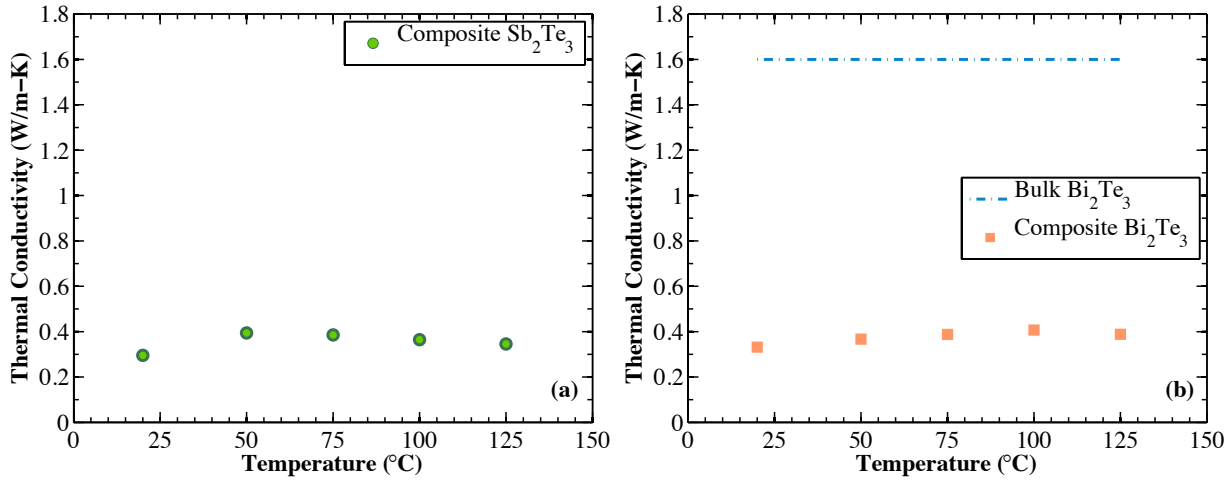

Figure 4.13. Temperature dependent transient plane thermal conductivity measurements of (a) p-type Sb_2Te_3 composites and (b) n-type Bi_2Te_3 composites cured at 250˚C.

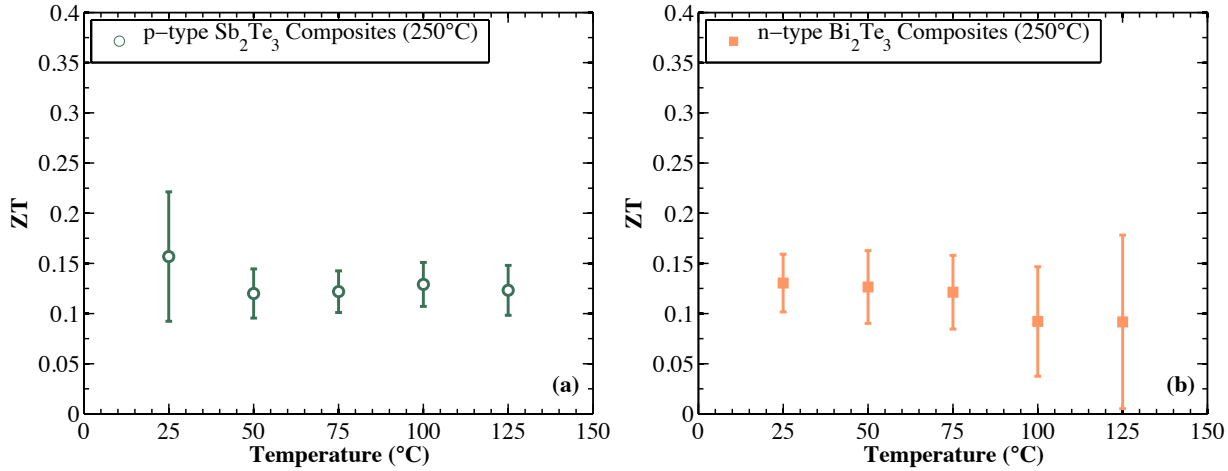

Figure 4.14. Temperature dependent figures of merit (ZT) for (a) p-type Sb_2Te_3 and (b) n-type Bi_2Te_3 composites cured at 250˚C.

Table 4.1. Thermal conductivity and ZT values for composite thermoelectric materials.

Composite Material	Curing Temp.	Thermal Conductivity (W/m-K)	Max. *ZT*
p-type Sb_2Te_3	250°C	0.24 – 0.29 [1]	0.22
p-type Sb_2Te_3	350°C	0.42 [2]	0.34
n-type Bi_2Te_3	250°C	0.24 – 0.33 [1]	0.18

1. Measured using both the transient plane source and steady state heat flow methods.
2. Measured using only the steady state heat flow method.

4.6. Chapter Conclusion

1. In order to dispenser print thermoelectric energy generators, printable thermoelectric materials must be first synthesized. Printed thermoelectric inks consist of active materials dispersed in a polymer binder. Composite theory can be utilized to predict the material properties of the printed inks. While such theories are available for modeling electrical and thermal conductivity, there are limited theories on modeling the effective Seebeck coefficient of printed systems.
2. N-type and p-type composite thermoelectric materials have been successfully developed for fabricating printed thermoelectric devices. The Seebeck coefficients of the composite materials are found to be similar to that of bulk materials while the electrical conductivity of non-sintered composites are approximately one order of magnitude less than that of bulk materials. The use of a polymer binder in the printable system ultimately reduces the thermal conductivity of the printed material.
3. A maximum *ZT* of 0.34 was found for the sintered Sb_2Te_3 system while the non-sintered systems has maximum *ZT*'s of 0.22 and 0.16 for the Sb_2Te_3 and Bi_2Te_3 composites, respectively.
4. While the efficiency of printed thermoelectric composites is not as high as some state of the art materials with $ZT \geq 1$, the results are encouraging. The ease of processing and device fabrication with printed materials provides deployment advantages over such materials. Sintering of particles noticeably improves the electrical conductivity of the system as demonstrated by the p-type Sb_2Te_3 composites.
5. Further materials processing parameters may be able to improve the effective *ZT* of the materials and future work includes various materials optimization. The current material properties are sufficient for fabrication of prototype thermoelectric generators and will be discussed in the next section.

Chapter References

[1] M. Cutler, J. Leavy, and R. Fitzpatrick, "Electronic Transport in Semimetallic Cerium Sulfide," *Physical Review*, vol. 133, no. 4, pp. A1143–A1152, Feb. 1964.

[2] G. J. Snyder and E. S. Toberer, "Complex thermoelectric materials," *Nature Materials*,

vol. 7, pp. 105–114, Feb. 2008.
[3] T. M. Tritt and M. A. Subramanian, “Thermoelectric Materials, Phenomena, and Applications: A Bird's Eye View,” *MRS Bulletin*, vol. 31, no. 3, pp. 188–198, Mar. 2006.
[4] D. M. Rowe, “General Principles and Basic Considerations,” in *Thermoelectrics Handbook: Macro to Nano*, no. 1, D. M. Rowe, Ed. Boca Raton, FL: CRC Press, 2006.
[5] M. Graf, S. K. Yip, J. Sauls, and D. Rainer, “Electronic thermal conductivity and the Wiedemann-Franz law for unconventional superconductors,” *Physical Review B*, vol. 53, no. 22, pp. 15147–15161, Jun. 1996.
[6] G. V. Chester and A. Thellung, “The Law of Wiedemann and Franz,” *Proceedings of the Physical Society*, vol. 77, no. 5, pp. 1005–1013, Dec. 2002.
[7] H. J. Goldsmid and R. W. Douglas, “The use of semiconductors in thermoelectric refrigeration,” *British Journal of Applied Physics*, vol. 5, no. 11, pp. 386–390, 1954.
[8] F. D. Rosi, B. Abeles, and R. V. Jensen, “Materials for thermoelectric refrigeration,” *Journal of Physics and Chemistry of Solids*, vol. 10, no. 2, pp. 191–200, Jul. 1959.
[9] C. J. Vineis, A. Shakouri, A. Majumdar, and M. G. Kanatzidis, “Nanostructured Thermoelectrics: Big Efficiency Gains from Small Features,” *Advanced Materials*, vol. 22, pp. 3970–3980, 2010.
[10] A. Majumdar, “Thermoelectricity in Semiconductor Nanostructures,” *Science*, vol. 303, no. 5659, pp. 777–778, Feb. 2004.
[11] M. S. Dresselhaus et al., “New Directions for Low-Dimensional Thermoelectric Materials,” *Advanced Materials*, vol. 19, no. 8, pp. 1043–1053, Apr. 2007.
[12] K. K. B. Hon, L. Li, and I. M. Hutchings, “Direct writing technology—Advances and developments,” *CIRP Annals - Manufacturing Technology*, vol. 57, pp. 601–620, Nov. 2008.
[13] V. Subramanian et al., “Progress Toward Development of All-Printed RFID Tags: Materials, Processes, and Devices,” *Proceedings of the IEEE*, vol. 93, no. 7, pp. 1330–1338, Jul. 2005.
[14] J. A. Rogers and Z. Bao, “Printed plastic electronics and paperlike displays,” *J. Polym. Sci. Part A: Polym. Chem.*, vol. 40, no. 20, pp. 3327–3334, Sep. 2002.
[15] Y. Li and C. P. Wong, “Recent advances of conductive adhesives as a lead-free alternative in electronic packaging: Materials, processing, reliability and applications,” *Materials Science & Engineering R*, vol. 51, pp. 1–35, 2006.
[16] J. E. Morris and J. Liu, “Electrically Conductive Adhesives: A Research Status Review,” *Micro- and Opto-Electronic Materials and Structures: Physics, Mechanics, Design, Reliability, Packaging*, vol. 20, pp. 527–570, 2007.
[17] S. K. Kang and S. Purushothaman, “Development of conducting adhesive materials for microelectronic applications,” *Journal of Electronic Materials*, vol. 28, no. 11, pp. 1314–1318, Nov. 1999.
[18] R. Prasher, “Thermal Interface Materials: Historical Perspective, Status, and Future Directions,” *Proceedings of the IEEE*, vol. 94, no. 8, 2006.
[19] Farhad Sarvar, D. C. Whalley, and P. P. Conway, “Thermal Interface Materials - A Review of the State of the Art,” in *Proceedings of the 1st IEEE Electronic Systemintegration Technology Conference*, Dresden, Germany, 2006, vol. 2, pp. 1292–1302.
[20] C. P. Wong and R. S. Bollampally, “Thermal conductivity, elastic modulus, and

coefficient of thermal expansion of polymer composites filled with ceramic particles for electronic packaging," *Journal of Applied Polymer Science*, vol. 74, no. 14, pp. 3396–3403, 1999.

[21] D. S. McLachlan, M. Blaszkiewicz, and R. E. Newnham, "Electrical Resistivity of Composites," *Journal of the American Ceramic Society*, vol. 73, no. 8, pp. 2187–2203, 1990.

[22] R. Crossman, "Conductive composites past, present, and future," *Polymer Engineering & Science*, 1985.

[23] M. Clingerman, J. King, and K. Schulz, "Evaluation of electrical conductivity models for conductive polymer composites," *Journal of Applied Polymer Science*, 2002.

[24] S. K. Bhattacharya and A. C. D. Chaklader, "Review on Metal-Filled Plastics. Part 1. Electrical Conductivity," *Polymer-Plastics Technology and Engineering*, vol. 19, no. 1, pp. 21–51, 1982.

[25] P. Delahay and C. W. Tobias, *Advances in Electrochemistry and Electrochemical Engineering, Vol. 2-Electrochemical Engineering*, vol. 2. New York, NY: Interscience Publishers, 1963.

[26] P. E. Phelan and R. C. Niemann, "Effective Thermal Conductivity of a Thin, Randomly Oriented Composite Material," *Journal of Heat Transfer*, vol. 120, no. 4, pp. 971–976, 1998.

[27] C.-W. Nan, R. Birringer, D. R. Clarke, and H. Gleiter, "Effective thermal conductivity of particulate composites with interfacial thermal resistance," *Journal of Applied Physics*, vol. 81, no. 10, p. 6692, 1997.

[28] L. C. Davis and B. E. Artz, "Thermal conductivity of metal-matrix composites," *Journal of Applied Physics*, vol. 77, no. 10, p. 4954, 1995.

[29] J. D. Felske, "Effective thermal conductivity of composite spheres in a continuous medium with contact resistance," *International Journal of Heat and Mass Transfer*, vol. 47, no. 14, pp. 3453–3461, Jul. 2004.

[30] A. Every, Y. Tzou, D. P. H. Hasselman, and R. Raj, "The effect of particle size on the thermal conductivity of ZnS/diamond composites," *Acta Metallurgica et Materialia*, vol. 40, no. 1, pp. 123–129, Jan. 1992.

[31] R. Landauer, "Electrical Conductivity in Inhomogeneous Media," in *AIP Conference Proceedings*, 1978, vol. 40, pp. 2–45.

[32] R. C. Progelhof, J. L. Throne, and R. R. Ruetsch, "Methods for predicting the thermal conductivity of composite systems: A review," *Polymer Engineering & Science*, vol. 16, no. 9, pp. 615–625, Sep. 1976.

[33] D. Lu and C. P. Wong, "A study of contact resistance of conductive adhesives based on anhydride-cured epoxy systems," *Components and Packaging Technologies*, vol. 23, no. 3, pp. 440–446, 2000.

[34] R. Zhang, K.-S. Moon, W. Lin, and C. P. Wong, "Preparation of highly conductive polymer nanocomposites by low temperature sintering of silver nanoparticles," *Journal of Materials Chemistry*, vol. 20, no. 10, p. 2018, 2010.

[35] F. T. Tan, X. L. Qiao, J. G. Chen, and H. Wang, "Effects of coupling agents on the properties of epoxy-based electrically conductive adhesives," *International Journal of Adhesion and Adhesives*, vol. 26, no. 6, pp. 406–413, 2006.

[36] I. Novak, I. Krupa, and I. Chodak, "Analysis of correlation between percolation concentration and elongation at break in filled electroconductive epoxy-based

adhesives," *European Polymer Journal*, vol. 39, no. 3, pp. 585–592, 2003.
[37] A. Chen, M. Koplow, D. Madan, P. K. Wright, and J. W. Evans, "Dispenser Printed Microscale Thermoelectric Generators for Powering Wireless Sensor Networks," in *ASME 2009 International Mechanical Engineering Congress and Exposition*, 2009, vol. 12, pp. 343–352.
[38] D. Madan, A. Chen, P. K. Wright, and J. W. Evans, "Dispenser printed composite thermoelectric thick films for thermoelectric generator applications," *Journal of Applied Physics*, vol. 109, pp. 034804–1–6, 2011.
[39] S. E. Gustafsson, "Transient plane source techniques for thermal conductivity and thermal diffusivity measurements of solid materials," *Review of Scientific Instruments*, vol. 62, no. 3, pp. 797–804, 1990.
[40] J. A. King, R. A. Hauser, A. M. Tomson, I. M. Wescoat, and J. M. Keith, "Synergistic Effects of Carbon Fillers in Thermally Conductive Liquid Crystal Polymer Based Resins," *Journal of Composite*
Materials, vol. 42, no. 1, pp. 91–107, 2008.
[41] R. A. Hauser, J. A. King, R. M. Pagel, and J. M. Keith, "Effects of carbon fillers on the thermal conductivity of highly filled liquid-crystal polymer based resins," *Journal of Applied Polymer Science*, vol. 109, no. 4, pp. 2145–2155, 2008.
[42] J. M. Keith, C. D. Hingst, M. G. Miller, J. A. King, and R. A. Hauser, "Measuring and predicting in-plane thermal conductivity of carbon-filled nylon 6,6 polymer composites ," *Polymer Composites*, vol. 27, no. 1, 2006.
[43] M. N. Miller, "Bounds for Effective Electrical, Thermal, and Magnetic Properties of Heterogeneous Materials," *Journal of Mathematical Physics*, vol. 10, no. 11, p. 1988, 1969.
[44] Lianhua Fan, Bin Su, Jianmin Qu, and C. P. Wong, "Effects of Nano-Sized Particles on Electrical and Thermal Conductivities of Polymer Composites," in *1st IEEE Consumer Communications and Networking Conference*, 2004, pp. 193–199.
[45] B. Legendre, C. Hancheng, S. Bordas, and M. T. Clavaguera-Mora, "Phase diagram of the ternary system Ge-Sb-Te. I. The subternary GeTe-Sb_2Te_3-Te," *Thermochimica Acta*, vol. 78, no. 1, pp. 141–157, Jul. 1984.
[46] M. Zakeri, M. Allahkarami, and G. Kavei, "Low temperature synthesis of nanocrystalline Sb_2Te_3 by mechanical alloying," *Journal of Materials Science*, 2008.
[47] N. Keawprak, Z. Sun, H. Hashimoto, and M. Barsoum, "Effect of sintering temperature on the thermoelectric properties of pulse discharge sintered (BiSb)Te alloy," *Journal of Alloys and Compounds*, vol. 397, no. 1, pp. 236–244, Jul. 2005.
[48] O. Yamashita, S. Tomiyoshi, and K. Makita, "Bismuth telluride compounds with high thermoelectric figures of merit," *Journal of Applied Physics*, vol. 93, no. 1, pp. 368–374, 2003.
[49] O. Yamashita and S. Tomiyoshi, "High performance n-type bismuth telluride with highly stable thermoelectric figure of merit," *Journal of Applied Physics*, vol. 95, no. 11, pp. 6277–6283, 2004.
[50] B. Poudel et al., "High-Thermoelectric Performance of Nanostructured Bismuth Antimony Telluride Bulk Alloys," *Science*, vol. 320, pp. 634–638, 2008.
[51] Y. Ma et al., "Enhanced Thermoelectric Figure-of-Merit in p-Type Nanostructured Bismuth Antimony Tellurium Alloys Made from Elemental Chunks," *Nano Letters*, vol. 8, no. 8, pp. 2580–2584, 2008.

Chapter 5

Dispenser Printed Thermoelectric Generators

5.1. Overview

With the availability of printable thermoelectric materials developed in Chapter 4, thermoelectric energy generators can be fabricated using the dispenser printed methods described in Chapter 3. This chapter will present the fabrication process and testing of dispenser printed thermoelectric generators. The results of the demonstrated prototype will be discussed with regards to its potential applications.

5.2. Device Fabrication

Dispenser printed thermoelectric generators can be fabricated using the printable composite thermoelectric materials developed in the previous chapter. Figure 5.1 shows an envisioned manufacturing process for dispenser-printed planar thermoelectric devices. In this work, each individual step was performed as a batch process with a stationary substrate. Gold metal contacts were first deposited via shadow mask evaporation onto a 50.8 μm thick flexible polyimide substrate. Polyimide is an ideal substrate due to its flexibility, electrical insulation, high temperature tolerance and low thermal conductivity (0.12 W/m-K). Next, the individual n-type and p-type elements were dispenser printed onto the substrate to form lines spanning across the top and bottom contacts. The printed lines were then cured in an argon/vacuum oven at 250°C. Figure 5.2a shows a picture of the printed thermoelectric lines on a flexible polyimide sheet with evaporated contacts. Printed devices were cut out of the polyimide sheet. 24 AWG copper wires were attached to the device using conductive silver epoxy (1901-S, ESL Electroscience) to form electrical connections. Finally, the device was completed by rolling the substrate to form a coil and sealed with polyimide tape. Figure 5.2 shows a 50-couple prototype consisting of elements that were 5 mm x 640 μm x 90 μm with 360 μm element spacing. The element length of 5 mm was chosen for implantable medical applications where the device spans across the fat layer of the tissue.

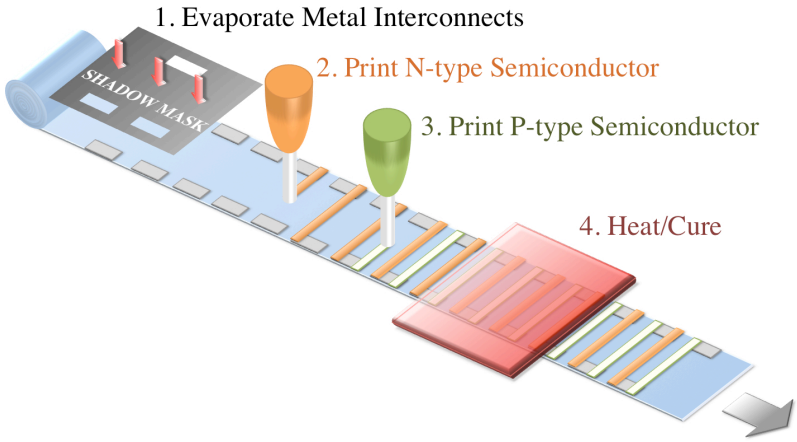

Figure 5.1. Fabrication process for a planer dispenser-printed thermoelectric device.

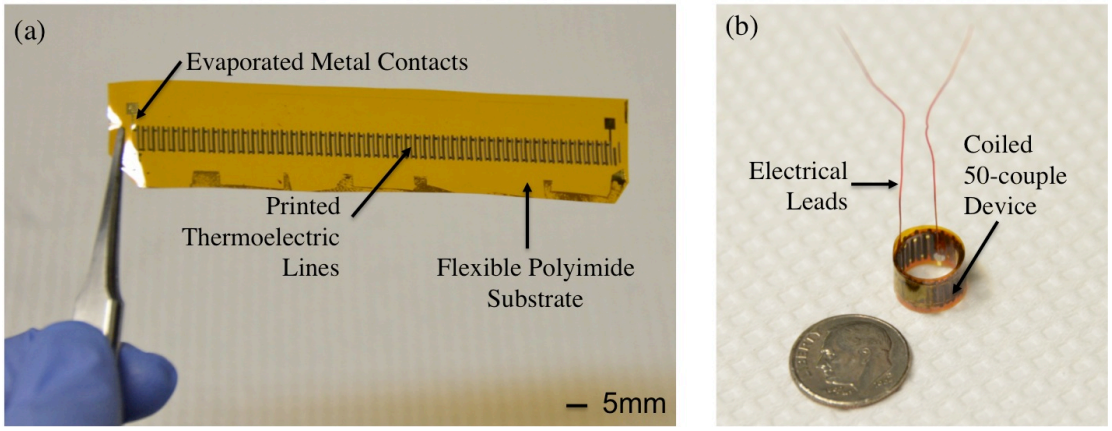

Figure 5.2. Images of (a) printed 50-couple planar thermoelectric device on a flexible polyimide substrate and (b) coiled prototype with electrical connections.

5.3. Experimental Setup

The printed prototype device was tested by placing the device on a heater while carefully monitoring the temperature at both ends of the elements with thermocouples mounted with thermal joint compound (TIM-417, Wakefield Solutions). Once the device reached steady state, the open circuit voltage of the device was measured using a digital multimeter. A variable load resistance was then connected in series with the device and voltage measurements were taken at multiple load resistances. The power was then calculated based on the measured voltage and load resistance at various temperature differences. All testing of the device was performed in an insulated faraday cage to prevent thermal or electric interference from measurement. Figure 5.3 shows an image of the experimental setup for characterizing the device.

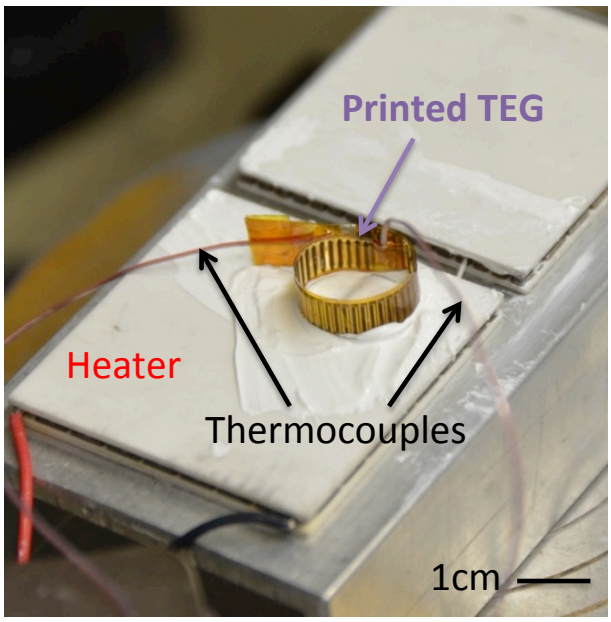

Figure 5.3. Image of the experimental setup for testing the printed TEG. Thermocouples were mounted to the top and bottom of the TEG which was placed on a heater. Various amount of heat was applied while the device was monitored. The open and closed circuit voltage output was measured to characterize the device.

5.4. Prototype Device Characterization

The initial measured device resistance of the prototype was 2.3 kΩ. However, after coiling and packaging, the device resistance increased to 2.55 kΩ. This is likely due to some internal strain in the printed material and the contact interface during coiling [1]. Figure 5.4 shows the power output of the 50-couple prototype measured for ΔT = 10 K at various load resistances. The optimal power output of the device occurs when the load resistance matches the device resistance. The device resistance, however, is higher than the expected resistance calculated from the material properties. The solid line in Figure 5.4 indicates the ideal power output based on the general thermoelectric power model [2-4], while the dashed line indicates the fitted model for the device. The general thermoelectric power model can be described as:

$$P = \frac{\left(m\alpha_{n+p}\Delta T\right)^2}{4R_{gen}} \tag{6.1}$$

where m is the number of couples, α_{n+p} is the Seebeck coefficient of a couple (i.e. sum of the coefficients), ΔT is the temperature difference and R_{gen} is the generator resistance. In the ideal scenario, the generator resistance can be estimated as:

$$R_{gen} = 2m\rho_m \frac{L}{A} \tag{6.2}$$

where ρ_m is the electrical resistivity of the material, L is the element length in the direction of heat flow and A is the cross-sectional area of the element. In the case of the fitted model, R_{gen} was the measured resistance of the generator. The measured data for the prototype closely

matches the fitted model suggesting that the Seebeck voltage output of the device aligns with the measured material properties. Error in the fit can be attributed to temperature oscillations during measurement.

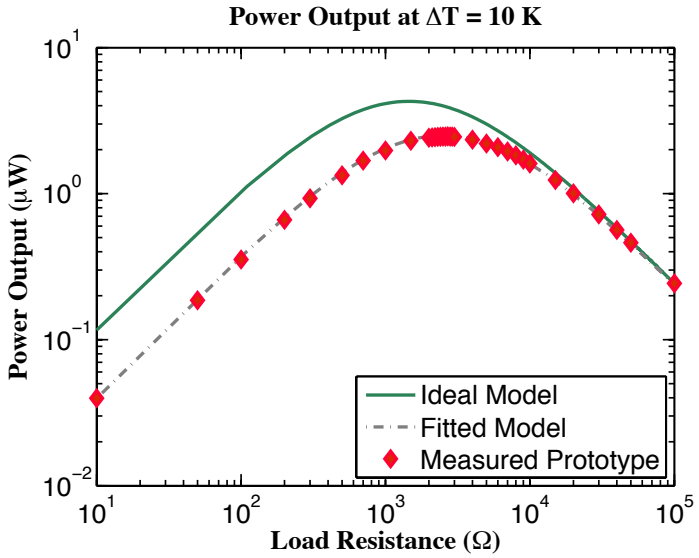

Figure 5.4. Power output of the 50-couple prototype generator as a function of load resistance at a 10 K temperature difference.

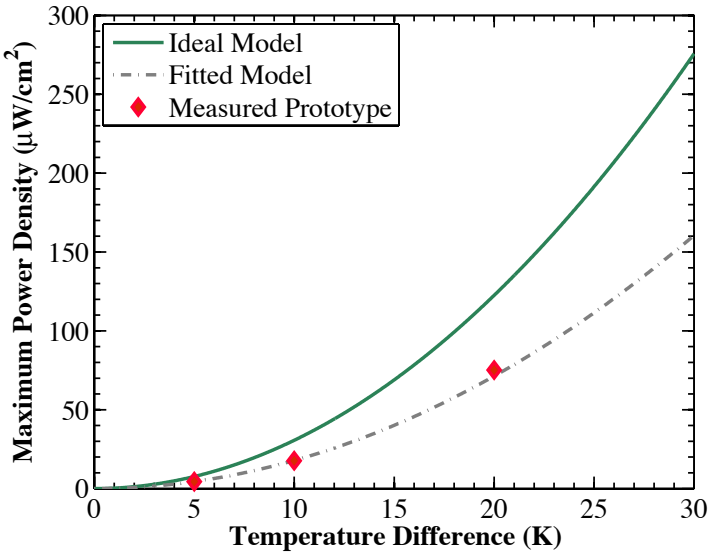

Figure 5.5. Maximum power output at matched load resistance as a function of temperature difference across the generator for the ideal generator model (solid line), the measured prototype (solid diamonds) and the fitted model (dashed line).

Figure 5.5 shows the measured power density of the device as a function of the temperature difference. Maximum power output at matched load resistance was measured at ΔT of 5 K, 10 K and 20 K. The solid line in Figure 5.4 again indicates the ideal model while the dashed line indicates the fitted model based on the equations described above. Figure 5.4 shows the device

characteristic curves for the prototype device at ΔT = 20 K. At matched load resistance, the device produces approximately 10.5 µW at 61.3 µA and 171.6 mV.

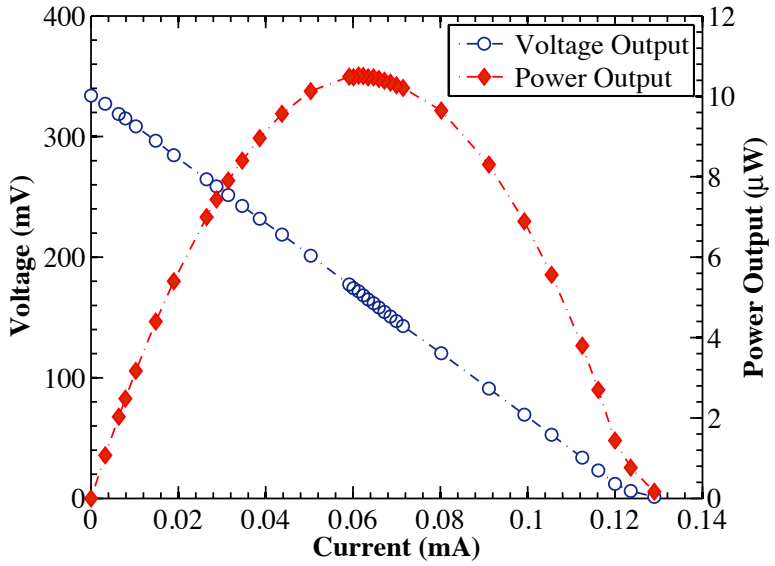

Figure 5.6. Characteristic curve for the 50-couple coiled generator at ΔT = 20 K.

5.5. Discussion

The prototype in this work currently has a less than ideal electrical impedance, which is likely due to the electrical contact resistance between the printed films and metal contacts [5]. Examination of the metal/composite interface may provide solutions to reduce the resistance. Empirical studies have also suggested that the thickness of the metal contacts may affect the device resistance. Various design strategies can potentially alleviate issues with high device resistance.

5.5.1. Flexible Printed Circuit Boards

One potential solution may be to use flexible printed circuit boards (Flex PCB's) as the substrate/electrical interconnects. These consist of copper-clad polyimide typically coated with various metals for corrosion protection. Flex PCB's are also an established and scalable technology that can complement printed fabrication methods. Since Flex PCB's typically use thicker copper interconnects, electrical resistance losses from electrical contacts can be greatly reduced. However, the thicker metal adds interfacial stresses between the printed element and interconnects, resulting in cracking. Careful processing parameters must be chosen to successfully fabricate devices o Flex PCB's.

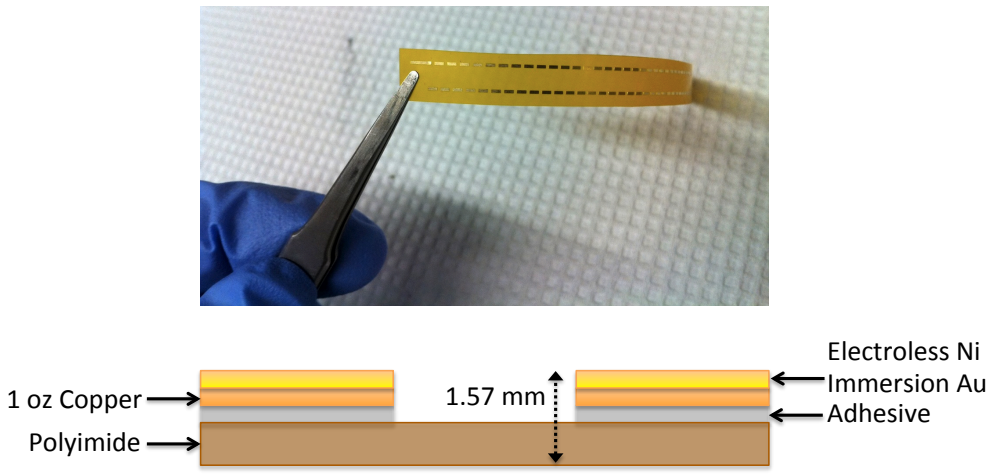

Figure 5.7. Image (top) and schematic (bottom) of a flexible printed circuit board (PCB) substrate designed for a printed thermoelectric device.

5.5.2. Single-element Devices

Another potential method to improve the performance is to utilize a single-element design such that only the higher performing thermoelectric material is used. Figure 5.8 shows a schematic of the single-element device fabricated using printing techniques. Instead of using two dissimilar semiconductor-based materials to form a thermocouple, a p-type thermoelectric ink can form a thermocouple with the metal interconnects. The metal traces then span from the top of one p-type element to the bottom of the next element. By using only the higher performing thermoelectric material, the device performance can be improved since the overall device power factor is higher. Figure 5.9 shows an image of a 20-element prototype fabricated similarly to the process described in section 5.2. A 40-element prototype was also fabricated and is not pictured. Each element in the prototype is a printed p-type Sb_2Te_3 composite with dimensions of 5 mm x 70 µm x 200 µm. The measured device resistance of the 40-element prototype is 870 Ω.

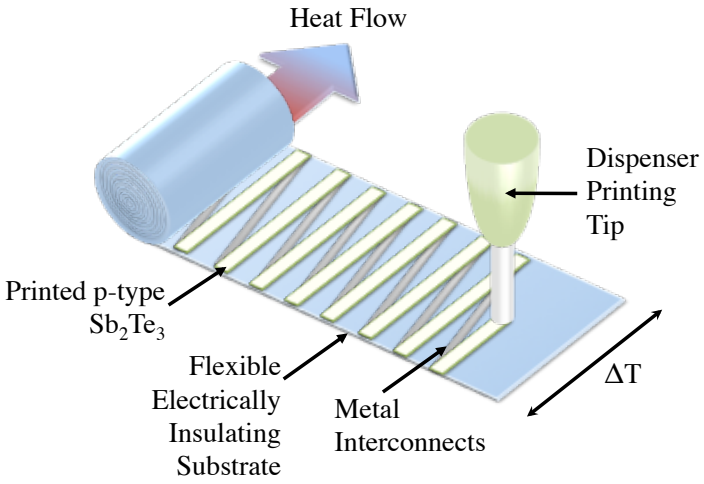

Figure 5.8. Schematic of a dispenser-printed single-element thermoelectric device.

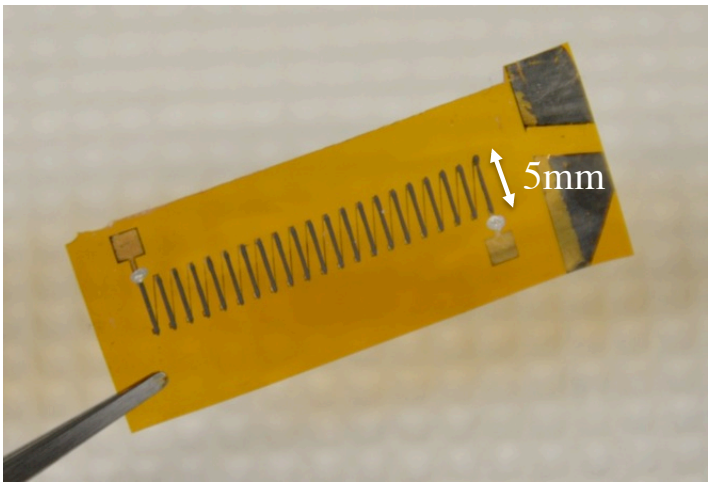

Figure 5.9. Image of a dispenser-printed single-element thermoelectric device consisting of 20 p-type Sb_2Te_3 elements that are 5 mm x 70 µm x 200 µm.

Figure 5.10 shows the performance of the 40-element single-element prototype at various temperature differences. The maximum power occurs at matched load resistance and reaches a peak of approximately 4 µW for a 20 K temperature difference.

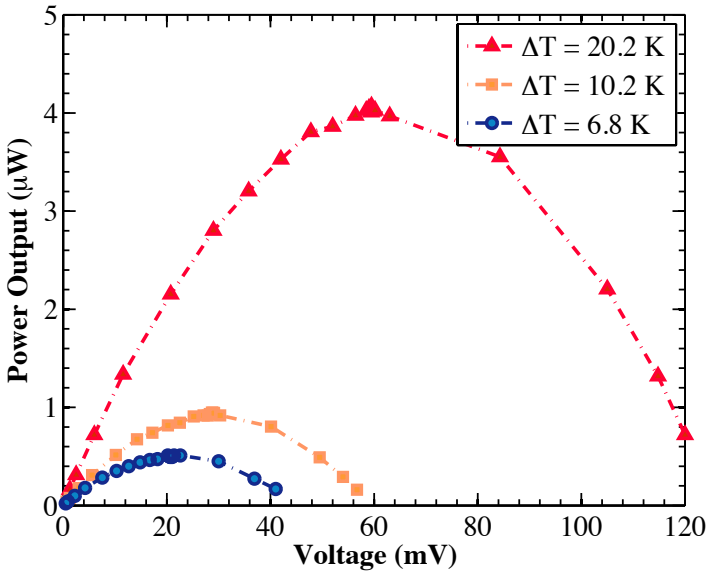

Figure 5.10. Power output performance for a 40-elemenet single-element prototype using printed p-type Sb_2Te_3 materials.

While the use of a single element design can improve the overall device power factor, the improvement come with a trade-off. The use of the metal contact as the complementary element increases the thermal conductivity across the device. This makes is difficult to maintain larger temperature differences across the device without proper thermal design. The single-element design also does not allow for ideal packing of thermoelectric materials to maximize power density. Further work can be performed to optimize the performance of the design.

5.5.3. Parallel Systems

Practical energy harvesting systems require some type of DC-to-DC conversion to step up the voltage between 2-5 V for an energy storage device. Commercially available low-voltage converters are unfortunately designed for low impedance inputs. Because the resistivities of the printed thermoelectric materials typically produce high-resistance thermoelectric devices (1-2 kΩ), low device resistances needed for matching converters (1-20 Ω) are unachievable in the current design. To achieve a lower overall device resistance, the thermoelectric device can be redesigned such that devices are placed in parallel instead of a series configuration. However, lower device resistance comes at the cost of reduced output voltage. A balance must be found to optimize the design for input requirements of step-up converters. Figure 5.11 shows a schematic of a parallel configuration where sets of printed devices in series are placed in parallel using Flex PCB technologies. By connecting each series-set of elements in parallel through backside vias, the overall device resistance can be reduced. This design allows for the same printed fabrication method as described in section 5.2. Future work can explore the use of this design for integrated systems.

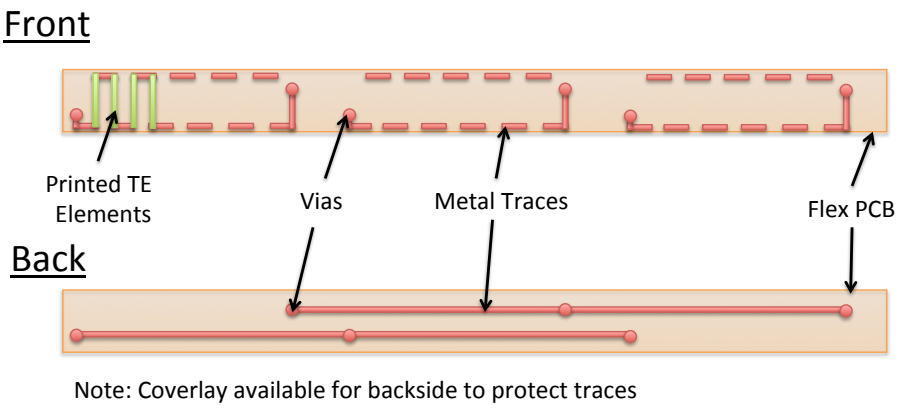

Figure 5.11. Schematic of a parallel thermoelectric device configuration.

5.5.4. Materials Improvement

The total device resistance can also potentially be lowered by curing the materials at 350°C as indicated by materials processing experiments. Thermal expansion and degradation of the substrate and materials, however, must be considered at such temperatures since changes in volume will affect the coiling and packaging of the device.

5.6. Chapter Conclusion

1. The 50-couple prototype presented in this work produced 10.5 µW for a 20 K temperature difference, yielding a cross-sectional areal power density of 75 µW/cm^2. This is well suited to scale for many low-power residential, industrial and medical wireless sensor applications [6-10].

2. The modeling suggests that a device with current material properties is capable achieving a power density of 109 μW/cm^2 at ΔT = 20 K given negligible contact resistance. Thus, optimization of device design, fabrication and materials processing must be further investigated to improve device performance.
3. Further optimization will be particularly important for applications where $\Delta T < 5$ K such as the case for implantable medical devices. It is worth noting that in the case of a planar TEG design, the substrate reduces the effective heat flow through the active material [6], [11]. The choice of a thin and low thermal conductivity substrate, such as the polyimide used in this work, minimizes such losses.
4. Polymer-based systems as printed thermoelectric materials for TEGs can be utilized for low-grade heat (<200˚C) energy generation below the polymer degradation temperature [11]. These applications may include low-grade waste heat recovery [9], wearable electronics [10], [12], [13]or autonomous wireless sensor networks [14], [15].
5. While the TEG shown in this work demonstrates the feasibility of printed planar TEGs, further application design can investigated. However, the versatility of printed fabrication processes allow for rapid customization by varying the printed element length, width and thickness through printing parameters.

Chapter References

[1] D. R. Cairns et al., "Strain-dependent electrical resistance of tin-doped indium oxide on polymer substrates," *Applied Physics Letters*, vol. 76, no. 11, p. 1425, 2000.

[2] W. Glatz, S. Muntwyler, and C. Hierold, "Optimization and fabrication of thick flexible polymer based micro thermoelectric generator," *Sensors & Actuators: A. Physical*, vol. 132, pp. 337–345, 2006.

[3] M. Strasser, R. Aigner, C. Lauterbach, and T. Sturm, "Micromachined CMOS thermoelectric generators as on-chip power supply," *Sensors & Actuators: A. Physical*, vol. 114, pp. 362–370, 2004.

[4] D. M. Rowe and G. Min, "Design theory of thermoelectric modules for electrical power generation," *IEE Proc.-Sci. Meas. Technol.*, vol. 143, 1996.

[5] D. Lu and C. P. Wong, "A study of contact resistance of conductive adhesives based on anhydride-cured epoxy systems," *Components and Packaging Technologies*, vol. 23, no. 3, pp. 440–446, 2000.

[6] N. S. Hudak and G. G. Amatucci, "Small-scale energy harvesting through thermoelectric, vibration, and radiofrequency power conversion," *Journal of Applied Physics*, pp. 1–24, May. 2008.

[7] C. C. Ho et al., "Technologies for an Autonomous Wireless Home Healthcare System," *Sixth International Workshop on Wearable and Implantable Body Sensor Networks, 2009 (BSN 2009)*, pp. 29–34, 2009.

[8] N. M. Pletcher, S. Gambini, and J. Rabaey, "A 52 μW Wake-Up Receiver With -72 dBm Sensitivity Using an Uncertain-IF Architecture," *Solid-State Circuits, IEEE Journal of*, vol. 44, no. 1, pp. 269–280, 2009.

[9] D. M. Rowe, "Review: Thermoelectric Waste Heat Recovery as a Renewable Energy Source," *International Journal of Innovations in Energy Systems and Power*, vol. 1, no.

1, pp. 13–23, 2006.
[10] V. Leonov and R. J. M. Vullers, “Wearable Thermoelectric Generators for Body-Powered Devices,” *Journal of Electronic Materials*, vol. 38, no. 7, pp. 1491–1498, 2009.
[11] J. Weber, K. Potje-Kamloth, F. Haase, P. Detemple, F. Volklein, and T. Doll, “Coin-size coiled-up polymer foil thermoelectric power generator for wearable electronics,” *Sensors and Actuators A*, vol. 132, pp. 325–330, 2006.
[12] T. Torfs, V. Leonov, C. V. Hoof, and B. Gyselinckx, “Body-Heat Powered Autonomous Pulse Oximeter,” *IEEE Sensors 2006*, pp. 427–430, 2006.
[13] T. Torfs et al., “Wearable Autonomous Wireless Electro-encephalography System Fully Powered by Human Body Heat,” *IEEE Sensors 2008*, pp. 1269–1272, 2008.
[14] C. Knight and J. Davidson, “Thermoelectric Energy Harvesting as a Wireless Sensor Node Power Source,” *Proc. of SPIE*, vol. 7643, p. 76431E, 2010.
[15] E. James, “An investigation of self-powered systems for condition monitoring applications,” *Sensors & Actuators: A. Physical*, vol. 110, no. 1, pp. 171–176, Feb. 2004.

Chapter 6

Medical Device Considerations

6.1. Overview

In addition to the materials characteristics and device performance of thermoelectric systems for implantable applications, concerns with device safety are important for biomedical devices. This chapter will briefly discuss the medical device approval process for the class of devices proposed in this work, followed by an examination of the biocompatibility of materials for thermoelectric devices.

6.2. Medical Device Approval

With the ultimate goal of coupling TEG's with wearable and implantable biomedical applications, the biocompatibility of the device materials must be considered. The biocompatibility of wearable systems is of less concern due to the established and well-understood guidelines set by medical regulatory institutions (such as the United State Food and Drug Administration (FDA) or the Competent Authority (CA) of European Union countries). Table 6.2 details the device classification and approval processes established by the FDA [1]. The FDA classifies all medical devices by risk and uses two general approval processes: (1) Pre-Market Approval (PMA) [2] and (2) 510(k) clearance [3]. The PMA approval process is used for new and untested devices, requiring a much lengthier review process (>1 year) while the 510(k) clearance process is a more expedited process (<1 year) [1], [4].

Since most wearable TEG's would either be worn similarly to clothing or mounted with an adhesive (much like a bandage), regulation of such devices would be minimal as long as the device is non-allergenic to the skin. Commercially available remote physiological systems such as the Zephyr Bioharness [5] and the Philips Respironics VitalSense [6] have already received 510(k) clearances. Future applications of wearable TEG devices for remote physiological monitoring would likely go through a similar 510(k) clearance process. In the case of implantible thermoelectric generators, the approval process would be less clear due to the nascency of the

technology. While similarly classed devices such as pacemakers have established safety records, the biocompatibility of the materials are of utmost concern.

Table 6.1. Table 5. U.S. Food and Drug Administration (FDA) classification and approval processes for different types of medical devices [1], [7].

Device Classification	Risk	Clearance	Example
Class I	Minimal	Typically exempt from FDA clearance.	Enemas, crutches, bandages, bedpans
Class II	Moderate	Almost all require regulatory submission. Typically 510(k) clearance.	Condoms, IV's, sutures, inflatable blood pressure cuffs
Class III	High	All require regulatory submission. Typically Premarket approval (PMA).	Implantable pacemakers, blood vessel stents, breast implants
510(k) Clearance			
Demonstrates that a device is "substantially equivalent" to a predicate device (one that has been cleared by the FDA or marketed before 1976)			
Human data are usually not required and the decision is made at the discretion of the FDA. Laboratory testing is almost always a requirement			
Manufacturers may also need to submit a 510(k) if they alter the device			
510(k) devices can only be legally advertised as "cleared" by the FDA			
Premarket Approval (PMA)			
Demonstrates to the FDA that a new or modified device is safe and effective. PMA's have higher standards than is required for 510(k) submissions			
Human use data from a formal clinical study is required in addition to laboratory studies			
Manufacturers have less leeway in modifying PMA devices than for changes to 510(k) devices			
PMA devices can be legally advertised as "PMA-approved" or "FDA-approved"			

6.3. Materials Biocompatibility

The most prevalent health concern is in the biocompatibility of TEG's for implantable medical devices. Implantable medical devices such as the cardiac pacemaker and the implantable cardiac defibrillator have proven long-term stability and biocompatibility [8]. Approximately 600,000 people per year are implanted with cardiac pacemakers worldwide and there are more than 3 million people with implanted pacemakers already [9]. The industry know-how established from the large number of implantable devices provides insight for biocompatible designs of implantable TEGs. In fact, pacemakers powered by radioisotope TEG's implanted during the 1970's are still safely operating in patients today [10], [11], suggesting that the safety and biocompatibility of implantable TEG's have been tested. One concern might be in the

implementation of an implantable TEG in the fat layer. Since the TEG would likely be separate from the implantable device (such as a pacemaker or a deep brain stimulator), electrical wiring may be an issue of concern. However, implantable wiring technologies are already available and currently use blood vessels as channels for electrical wiring.

The primary concern for TEGs may indeed be the toxicity of the thermoelectric materials used, such as bismuth and tellurium based systems in state-of-the-art devices. While bismuth telluride is considered to have relatively low toxicity, its effects must be considered. When inhaled in limited quantity, bismuth telluride has been found to have no adverse health effects with the exception of tellurium breath, which has an odor similar to that of garlic consumption [12]. Bismuth compounds and its salts are known to cause kidney damage. In small doses, damage is usually quite mild, but large doses can be fatal.

Other toxic effects may develop from bismuth compounds such as bodily discomfort, presence of albumin or other proteins in the urine, diarrhea, skin reaction and exodermatitis [13]. Elemental tellurium is considered to have relatively lower toxicity and is converted to dimethyl telluride. Heavy exposure to tellurium, however, results in headache, drowsiness, metallic taste, loss of appetite, nausea, tremors, convulsions, and respiratory arrest [14]. In a year-long study on dogs, rabbits and mice continuously exposed to $15mg/m^3$ of bismuth telluride for 6 hours per day in air and 5 days a week, pulmonary lesions were found in all animals but the effects were considered mild and reversible. Similar studies were replicated with non-adverse physiological effects [12].

Considering the mild but nonetheless toxic effects of the bismuth telluride, caution must be taken when designing the device for implantation. One choice is to consider alternate thermoelectric materials with better biocompatibility. This may be undesirable as bismuth telluride-based compounds are the most efficient existing materials at room temperature. Another option is to enclose the device in a biocompatible material with a relatively low thermal conductivity such as a silicone-based polymer. Ultimately, it is up to the device designers and engineers to make such decisions.

6.4. Chapter Conclusion

1. The FDA medical device approval process can be categorized two general process: Premarket Approval (PMA) and 510(k). The PMA approval process is used for new and untested devices (>1 year) while the 510(k) clearance process is a more expedited process (<1 year).
2. Wearable thermoelectric devices for external physiological monitoring applications would likely follow an expedited 510(k) process due the low health risks involved. The market availability of other wearable physiological systems would further expedite the approval process due to their proven safety.
3. Considering the prevalence of implantable pacemakers, and the historical use of nuclear thermoelectric pacemakers, implantable thermoelectric devices may also follow an expedited 510(k) approval process. However, due to inherent safety concerns of any implantable medical devices, the medical approval process for an implantable TEG in the fat layer of the body would require further studies.

4. While the biocompatibility of thermoelectric materials must also be proven, an analysis of the bismuth-telluride materials suggests only mild toxicity. Proper encapsulation of an implantable thermoelectric device using knowledge established in the biomedical device industry would ultimately allow the successful realization of implantable TEGs.

References

[1] A. V. Kaplan et al., "Medical Device Development: From Prototype to Regulatory Approval," *Circulation*, vol. 109, no. 25, p. 3068, Jun. 2004.

[2] *Code of Federal Regulation - Title 12 Part 814 - Premarket Approval of Medical Devices*. 1986.

[3] *Code of Federal Regulation - Title 12 Part 807 - Establishment Registration and Device Listing for Manufacturers and Initial Importers of Devices*. 1977.

[4] "FDA - Overview of Device Regulation," *http://www.fda.gov/MedicalDevices/DeviceRegulationandGuidance/Overview/default.htm*. [Online]. Available: http://www.fda.gov/MedicalDevices/DeviceRegulationandGuidance/Overview/default.htm. [Accessed: 24-May-2011].

[5] Zephyr Technology Corporation, "BioHarness BT," *http://www.zephyr-technology.com/bioharness-bt*. [Online]. Available: http://www.zephyr-technology.com/bioharness-bt. [Accessed: 23-May-2011].

[6] Philips-Respironics, "VitalSense Integrated Physiological Monitor," *http://vitalsense.respironics.com/*. [Online]. Available: http://vitalsense.respironics.com/. [Accessed: 23-May-2011].

[7] J. Smith and S. Barrett, "What are 510(k) Clearance and Premarket Approval?," *devicewatch.org*. [Online]. Available: http://www.devicewatch.org/reg/reg.shtml. [Accessed: 06-Sep.-2011].

[8] O. Aziz, B. Lo, A. Darzi, and G.-Z. Yang, "Introduction," in *Body Sensor Networks*, no. 1, G.-Z. Yang, Ed. London: Springer, 2006, pp. 1–39.

[9] V. S. Mallela, V. Ilankumaran, and N. S. Rao, "Trends in Cardiac Pacemaker Batteries," *Indian Pacing and Electrophysiology Journal*, vol. 4, no. 4, p. 201, 2004.

[10] V. Parsonnet, "A Lifetime Pacemaker Revisited," *The New England Journal of Medicine*, vol. 357, no. 25, pp. 2638–2639, Dec. 2007.

[11] V. Parsonnet, J. Driller, D. Cook, and S. A. Rizvi, "Thirty-One Years of Clinical Experience with 'Nuclear-Powered' Pacemakers," *Pacing and Clinical Electrophysiology*, vol. 29, no. 2, pp. 195–200, Feb. 2006.

[12] W. N. Rom and S. Markowitz, *Environmental and Occupational Medicine*. Philadelphia, PA: Lippincott Williams and Wilkins, 2006.

[13] N. H. Proctor, G. J. Hathaway, and J. P. Hughes, *Proctor and Hughes' Chemical Hazards of the Workplace*, 5th ed. NY: John Wiley & Sons, 2004.

[14] R. J. Lewis, *Sax's Dangerous Properties of Industrial Materials*, 11th ed. NY: John Wiley & Sons, 2005.

Chapter 7

Future Outlook

7.1. Overview

This work was the first successful demonstration of thermoelectric energy generators manufactured using dispenser printing. Given a temperature difference of 5 K, a power generation of 0.62 μW can be harvested from the 50-couple prototype. With appropriate scaling, an energy density of 4.43 $\mu W/cm^2$ at 5 K, which can be found in the abdomen while running, or 0.18 $\mu W/cm^2\text{-}K^2$ is achievable with the current technology. Therefore, a 2.25 cm^2 thermoelectric device based on the printed thermoelectric technology developed in this work would be capable of powering an implantable medical device such as an implantable glucose sensor (~10 μW).

The successful demonstration of dispenser-printed planar thermoelectric generators opens opportunities for a wide variety of energy harvesting applications. The developing medical and healthcare needs of the world will place demands on more complex diagnostic and treatment technologies that require autonomous power sources. Given the limitations of primary battery systems, thermoelectric generators provide a solid-state solution to alleviate the power demands of current and new technologies. As research on thermoelectric technology and materials continue to progress, the successful realization of thermoelectric generators within medical devices is imminent. This chapter will discuss the impending needs for thermoelectric technologies in healthcare, followed by a discussion of state-of-the-art thermoelectric technologies and their scientific advancements.

7.2. Growing Healthcare Needs

As we live longer lives, an increasingly older population will unavoidably require more medical care [1], [2]. According to the National Institute of Aging, there were approximately 39 million people in the U.S. over the age of 65 in 2008, accounting for just over 13% of the population. This population is expected to almost double to 72 million in 2030, representing 20% of the

population [3]. The growing "gray" population in the US is also reflected in the rest of the world. The United Nations expects that today's 5-22% of old people in all regions around the globe will become 11-34% by 2050 [4]. These numbers depict an ever-growing need for new physiological diagnostic tools for the "gray" population. Considering the dearth of healthcare professionals, remote physiological systems for home healthcare will enable physicians and clinical staff to take care of more patients with less clinical visits. Regulatory mandates on the adoption of electronic healthcare records (EHR's) will only expedite the process of moving healthcare beyond the clinical environment [5]. In fact, multi-national corporations such as GE and Intel have already begun to focus efforts on chronic disease management, telehealth/remote patient monitoring and assistive healthcare [6].

The aging population will not only precipitate a demand for new physiological tools, but also increase the need for long-term implantable medical devices. With more than 3 million pacemakers in patients worldwide and more than 600,000 new pacemakers implanted annually, the number of people with similarly critical life-supporting devices will only increase [7]. As more patients are implanted with medical devices, the risk of surgical operations that are required to replace batteries (every 5-8 years for pacemakers [7]) becomes much higher as the patients become older [8]. These imminent healthcare demands present potential opportunities for small-scale thermoelectric devices to complement both wearable physiological tools and implantable medical devices for the "gray" market.

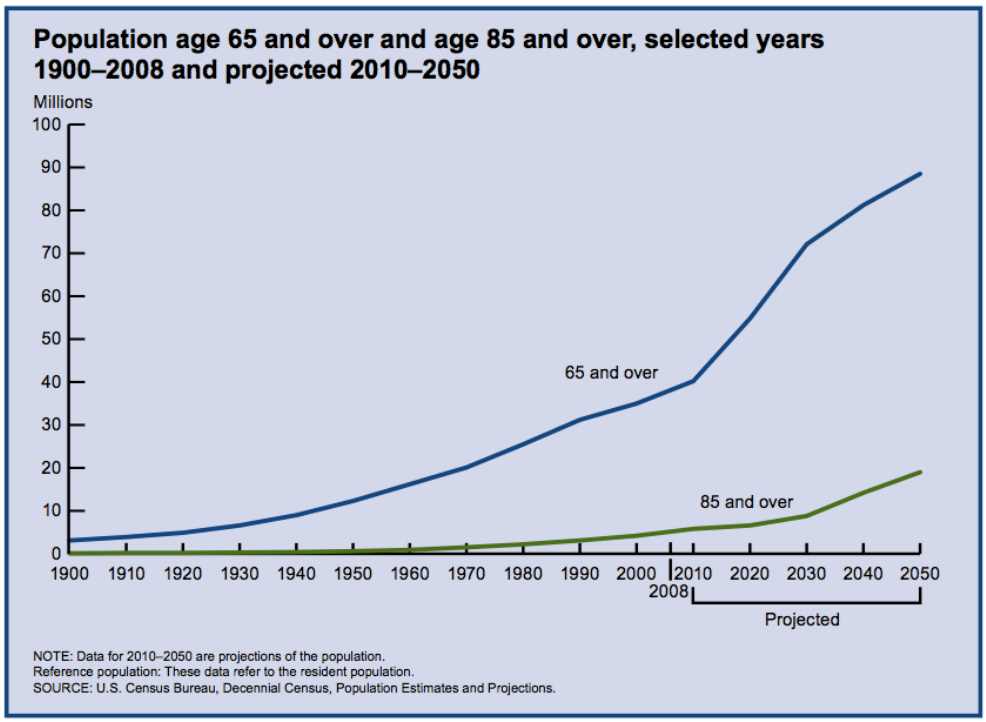

Figure 7.1. Chart indicating the past and projected U.S. population ages of 65 and over and ages 85 and over [3].

7.3. State-of-the-art Thermoelectric Generators

While the current market for thermoelectric devices is disparately spread across various industries, there is growing interest in the use of small-scale thermoelectric generators for wireless sensor applications and medical monitoring. MEMS-scale thermoelectric generators such as those from Micropelt GmbH are becoming commercially available for niche applications [9]. While some of the current MEMS thermoelectric devices are capable of providing small amounts of power to sensors, the thin-film technologies do not allow for conformability, scalability or design modularity provided by printed thick-film methods. Recent discoveries in polymer-based thermoelectric materials are exciting for future prospects of printed thermoelectric systems. New theories and results suggest that organic-inorganic hybrid materials are very promising candidates for efficient thermoelectric materials [10-12]. By using polymer-based materials, potential thermoelectric devices can take advantage of the flexibility and conformability of the polymer. These inherent materials characteristics meet the demands required by device designs for implantable systems. One can also contrive ways of utilizing such technologies as fully wearable thermoelectric garments. Applications can go beyond energy harvesting for physiological monitoring and extend to therapeutic cooling applications.

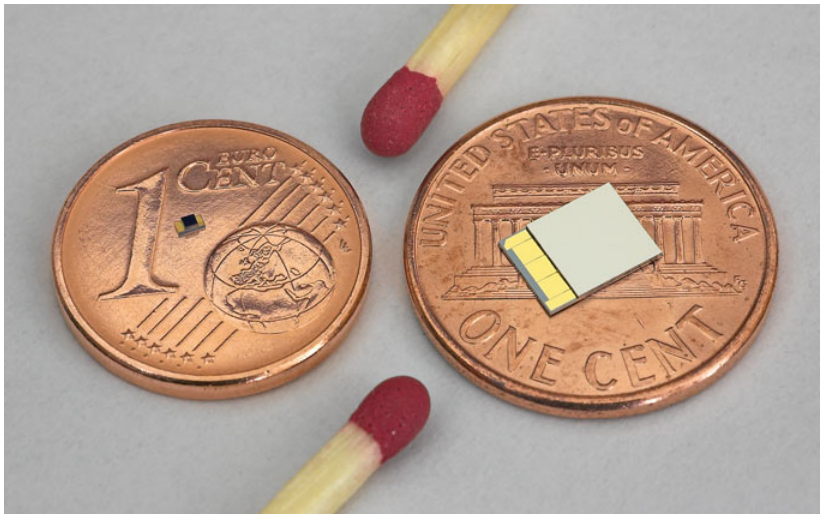

Figure 7.2. Image of a commercially available thin-film MEMS thermoelectric generator by Micropelt GmbH [9].

7.4. Advanced Thermoelectric Materials

As medical devices become more sophisticated, their power requirements continue to exceed the capability of energy storage solutions. The critical enabling technologies still lie in high-performing thermoelectric materials. Although the dimensionless figure of merit (ZT) for thermoelectric materials is still ubiquitously used as the metric of performance, the more important material property is the power factor, $\alpha^2\sigma$, where α is the Seebeck coefficient and σ is the electrical conductivity. The power factor ostensibly plays a larger role in determining the power density of a TEG for low temperature differences on the body.

During the early 1990's, Hicks and Dresselhaus theorized that the individual components of the power factor could be decoupled through quantum confinement of electrons and holes in low-dimensional materials [13], [14]. This galvanized intense research in nanostructured thermoelectric materials for enhanced performance (ZT>1). While enhanced performance materials have now been successfully demonstrated in low-dimensional structures, these materials have benefited from reduced phonon thermal conductivity instead of quantum confinement of electronic carriers [15], [16]. While power factor improvement may still be viewed as a complex challenge, scientists are already theorizing and experimenting with various methods to realize higher power factors [15].

7.5. Future Scenario

One can perhaps envision the future 65-year old patient in 2020 being implanted with a thermoelectric powered cardiac pacemaker with wireless capabilities. Since the heat generated from his body powers the pacemaker, the patient does not have to undergo surgery when s/he turns 75 to replace the battery. The added wireless capability of the pacemaker automatically logs and reports cardiac events to the patient's physician. In the case of aberrant cardiac events, the patient's physician may ask the patient to wear a self-powered physiological monitoring system to track vital signs. All of the patient's data is stored in his or her electronic health record to provide patient history and real-time health diagnostics. This integrated body sensor network will very likely be the future of healthcare in a society that can "age in place" or "age at home". This highly important paradigm shift will support people in the comfort and safety of their own homes, allowing them to stay close to their families. Additionally, they avoid being exposed to hospital environments where risks of staphylococcal and other infections are possible. Such fundamental shifts in healthcare will inevitably reduce the costs of healthcare in both the U.S. and countries around the world.

Chapter References

[1] E. L. Schneider and J. M. Guralnik, "The Aging of America," *JAMA: The Journal of the American Medical Association*, vol. 263, no. 17, pp. 2335–2340, May. 1990.

[2] D. C. Angus, M. A. Kelley, R. J. Schmitz, A. White, and J. Popovich, "Current and Projected Workforce Requirements for Care of the Critically Ill and Patients With Pulmonary Disease: Can We Meet the Requirements of an Aging Population?," *JAMA: The Journal of the American Medical Association*, vol. 284, no. 21, pp. 2762–2770, Dec. 2000.

[3] *Older Americans 2010: Key Indicators of Well-being*. The Federal Interagency Forum on Aging-Related Statistics, 2010.

[4] *World Population Ageing 2009*. United Nations, 2009.

[5] E. W. Ford, N. Menachemi, and M. T. Phillips, "Predicting the Adoption of Electronic Health Records by Physicians: When Will Health Care be Paperless?," *Journal of the American Medical Informatics Association*, vol. 13, no. 1, pp. 106–112, Jan. 2006.

[6] "Fact Sheet: GE, Intel to Form New Healthcare Joint Venture," *download.intel.com/pressroom/pdf/Intel_GE_JV_Fact_Sheet.pdf*, 2010. [Online].

Available: http://download.intel.com/pressroom/pdf/Intel_GE_JV_Fact_Sheet.pdf. [Accessed: May-2011].
[7] M. A. Wood and K. A. Ellenbogen, “Cardiac pacemakers from the patient's perspective,” *Circulation*, vol. 105, pp. 2136–2138, 2002.
[8] W. S. Weintraub, J. M. Craver, C. L. Cohen, E. L. Jones, and R. A. Guyton, “Influence of age on results of coronary artery surgery,” *Circulation*, vol. 85, no. 5, pp. 226–235, 1991.
[9] “Advantages of Thermoelectric Thin Film Devices from Micropelt,” *micropelt.com*. [Online]. Available: http://www.micropelt.com/tech/advantages.php. [Accessed: 20-Sep.-2011].
[10] K. C. See, J. P. Feser, C. E. Chen, A. Majumdar, J. J. Urban, and R. A. Segalman, “Water-Processable Polymer−Nanocrystal Hybrids for Thermoelectrics,” *Nano Letters*, vol. 10, pp. 4664–4667, 2010.
[11] D. Madan, A. Chen, P. K. Wright, and J. W. Evans, “Dispenser printed composite thermoelectric thick films for thermoelectric generator applications,” *Journal of Applied Physics*, vol. 109, pp. 034804–1–6, 2011.
[12] O. Bubnova et al., “Optimization of the thermoelectric figure of merit in the conducting polymer poly(3,4-ethylenedioxythiophene),” *Nature Materials*, vol. 10, pp. 429–433, May. 2011.
[13] L. Hicks and M. S. Dresselhaus, “Effect of quantum-well structures on the thermoelectric figure of merit,” *Physical Review B*, vol. 47, no. 19, pp. 12727–12731, May. 1993.
[14] L. D. Hicks, T. C. Harman, and M. S. Dresselhaus, “Use of quantum‐well superlattices to obtain a high figure of merit from nonconventional thermoelectric materials,” *Applied Physics Letters*, vol. 63, no. 23, pp. 3230–3232, Dec. 1993.
[15] C. J. Vineis, A. Shakouri, A. Majumdar, and M. G. Kanatzidis, “Nanostructured Thermoelectrics: Big Efficiency Gains from Small Features,” *Advanced Materials*, vol. 22, pp. 3970–3980, 2010.
[16] A. Majumdar, “Thermoelectricity in Semiconductor Nanostructures,” *Science*, vol. 303, no. 5659, pp. 777–778, Feb. 2004.

Appendix A

Thermal Monitoring of the Upper Torso with VitalSense Temperature Patches

A.1. Overview

This section discusses experimental analysis of the Mini Mitter/Philips Respironics VitalSense temperature monitoring system. The VitalSense is a body sensor network (BSN) used for monitoring skin temperature for various medical applications. The results of the study provide an insight into the feasibility of using wearable thermoelectric devices to harvest energy from the body.

A.2. Background

The Mini Mitter/Philips Respironics VitalSense is a system used for measuring skin temperature using wireless temperature patches. The user can place the patch on any part of the body and monitor the skin temperature via a wireless receiver. It also has the capability of logging the data for further analysis. The receiver must be placed within 1 meter of the patch for the data to be recorded, and up to 10 patches can be used with one receiver. The temperature patches have a measurement rate of 1 temperature per 15 seconds. Figure A.1 shows an image of the patch and receiver. The temperature patch consists of a temperature sensor, radio and circuitry, all enclosed in a silicone-type material. The sensing side of the patch uses a pressure sensitive adhesive to bond to the measured subject's skin. The temperature patch uses an embedded thermistor to measure the surface temperature. In this report, we perform pilot tests with the device to measure local skin temperature of subjects under various functional activities. The temperature patches are also used to monitor the skin temperature over 24-hour periods to study the effects of skin temperature as a function of ambient temperatures.

Figure A.1. Mini Mitter/Philips Respironics VitalSense Receiver with a temperature patch and capsule.

A.3. Comparative Analysis of Modified VitalSense Patches

Further investigation into the device construction revealed that the thermistor in the VitalSense temperature patch was receded into the printed circuit board ~ 2mm away from the desired sensing surface. This presents some problems in measurement accuracy, as the thermistor does not make any contact with the skin surface, and is in fact, only measuring the encapsulated air above the skin. This would also decrease the sensitivity of the device to transient changes in the skin temperature. Thus, in the following analysis, we attempt to modify the thermistor position to improve its sensitivity and compare it against the unmodified temperature patch.

A.3.1. Testing of Unmodified Temperature Patch

The patch was placed on the inner left arm of the subject as a testing site. First, infrared imaging was used to locate large blood vessels to maximize measurement of temperature variation. Figure A.2 shows both an infrared image of the subject's arm, and the arm with the temperature patch. The patch was then placed on the subject to begin measurement. The subject wore the patch for approximately 24 hours, while logging the data in the receiver. An Extech Datalogger 42270 was also used in conjunction with the VitalSense to monitor the ambient temperature variations. Figure 3 shows a time-lapsed chart of the measurements. It can be noted that the peak temperature during the day were at night while the subject was sleeping. This was likely due to the lower temperatures from the air conditioning, causing the subject to seek warmth under the blankets. Shower temperature also showed a peak due to the hot water used in the shower.

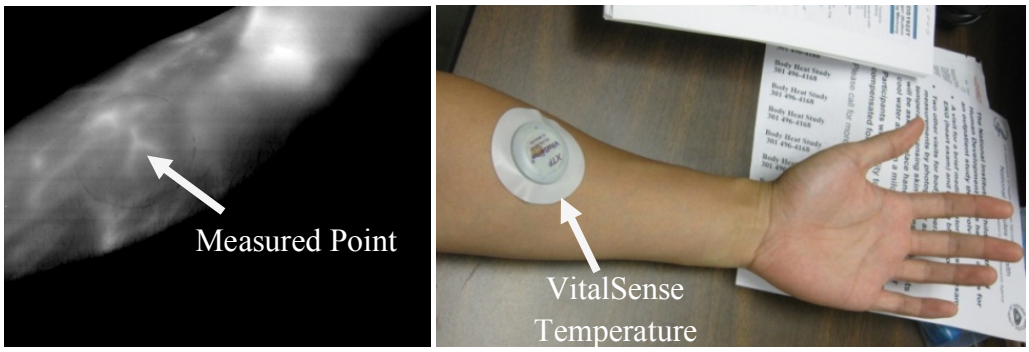

Figure A.2. Infrared image of the subject's arm and image of the subject's arm with a temperature patch

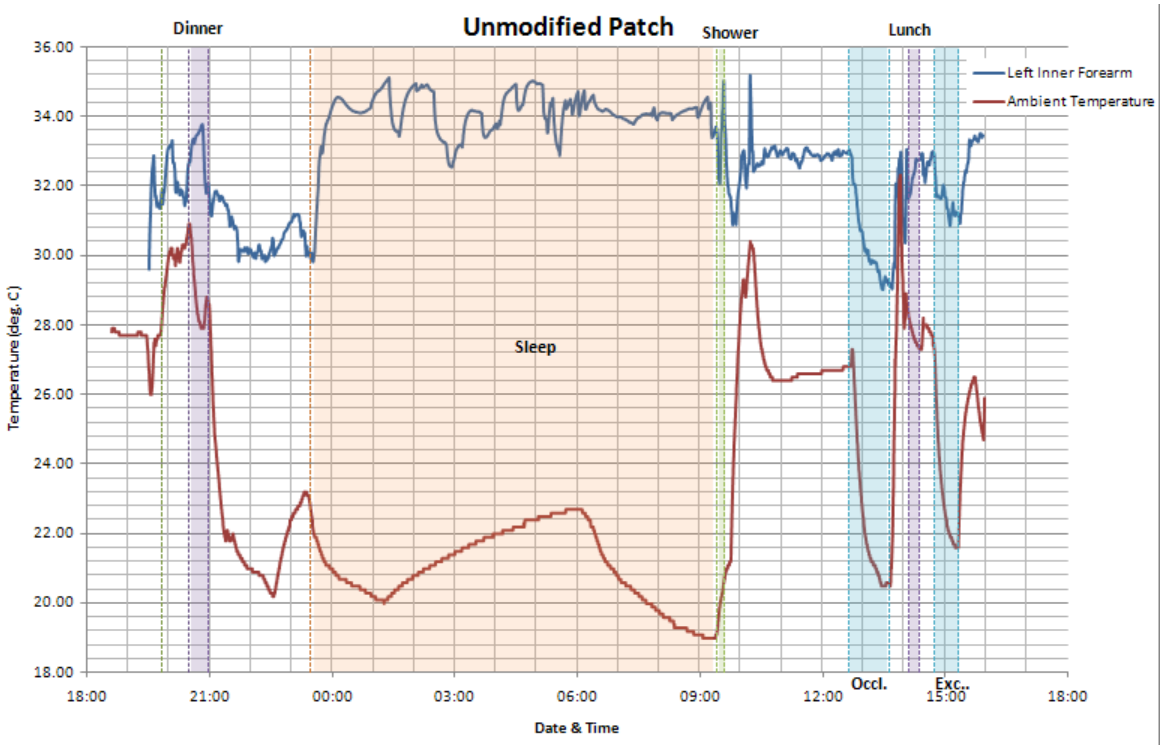

Figure A.3. Time-lapsed chart of measured skin temperature and ambient temperature for a 24hr Period using the unmodified Mini Mitter VitalSense .

To test the sensitivity of the device, two tests were performed. The first was an occlusion test to measure the variation of skin temperature from occlusion of the blood vessels in the arm. A cuff was placed on the upper arm, and was inflated to approximately 220 mm Hg. It was held for 3 minutes to limit blood flow to the forearm. The cuff was finally deflated after 3 minutes and allowed to relax. The second test was an exercise test where the subject performed 20 curls using a 10lb dumbbell. In both tests, the subject was placed in the testing room for 20 minutes prior to the tests to reach steady state. The subject also stayed in the room for 20 minutes after the test to monitor the resulting effects. Figure 4 shows the results of the occlusion test and Figure 5 shows the results of the exercise test.

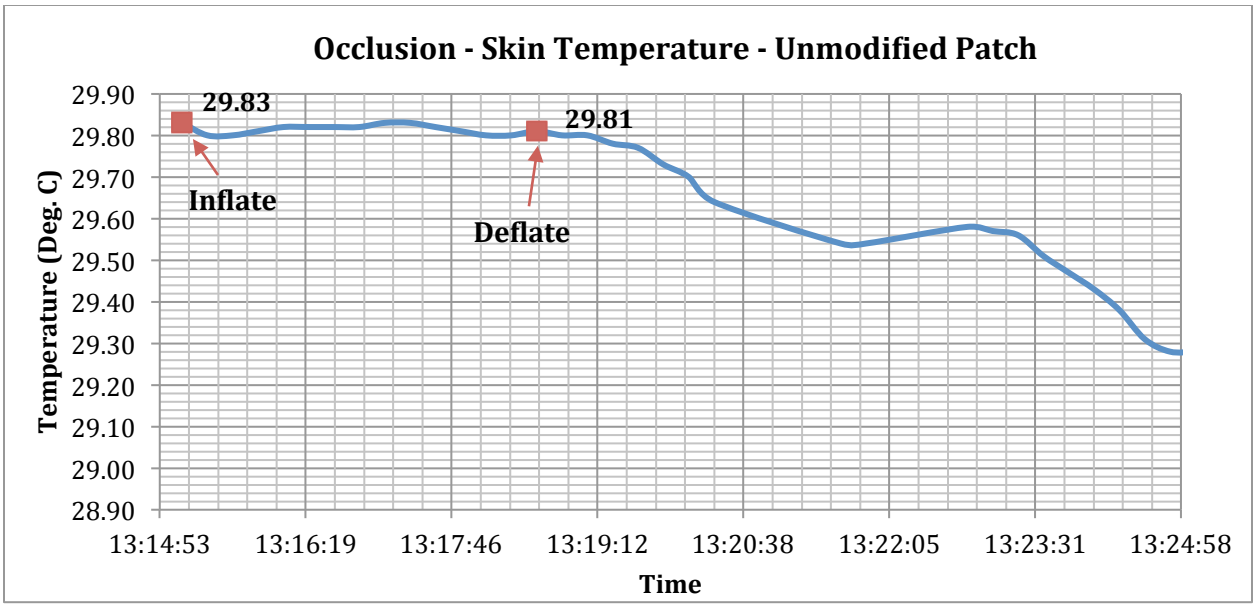

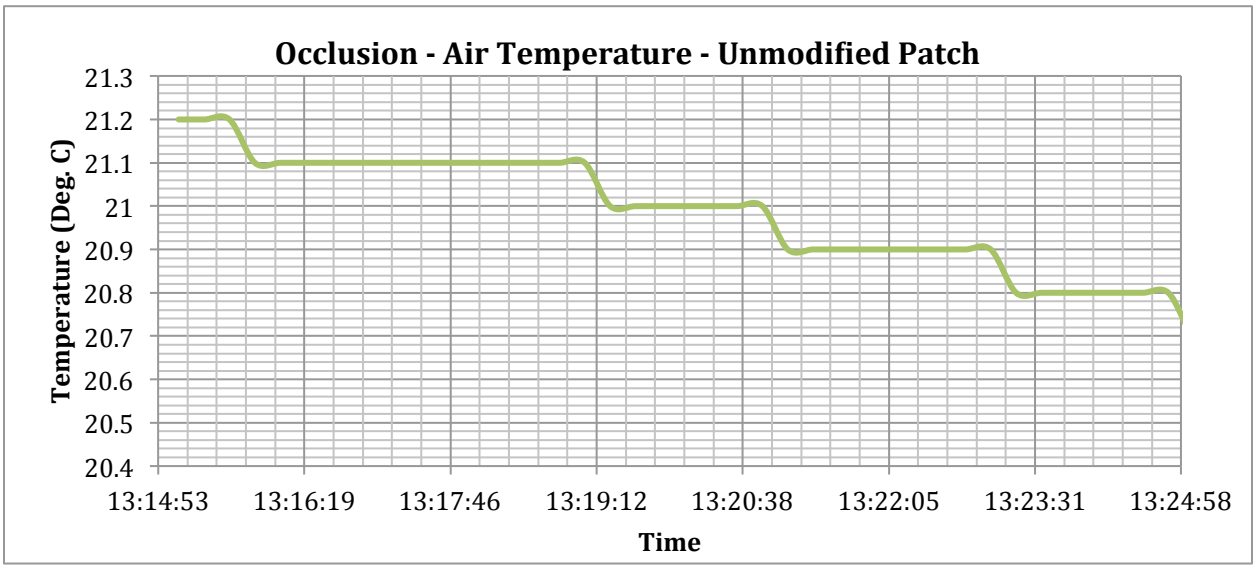

Figure A.4. Skin Temperature and Air Temperature measurements during the occlusion test using the unmodified temperature patch.

During the occlusion test, the skin temperature decreased 0.02°C, and continued to decrease afterwards. While one might expect the temperature to decrease from the lack of blood flow, the variation was not significant, and might have been attributed to the decreasing room temperature. It should be noted that the ambient temperature readings varied slightly, but was within 1°C.

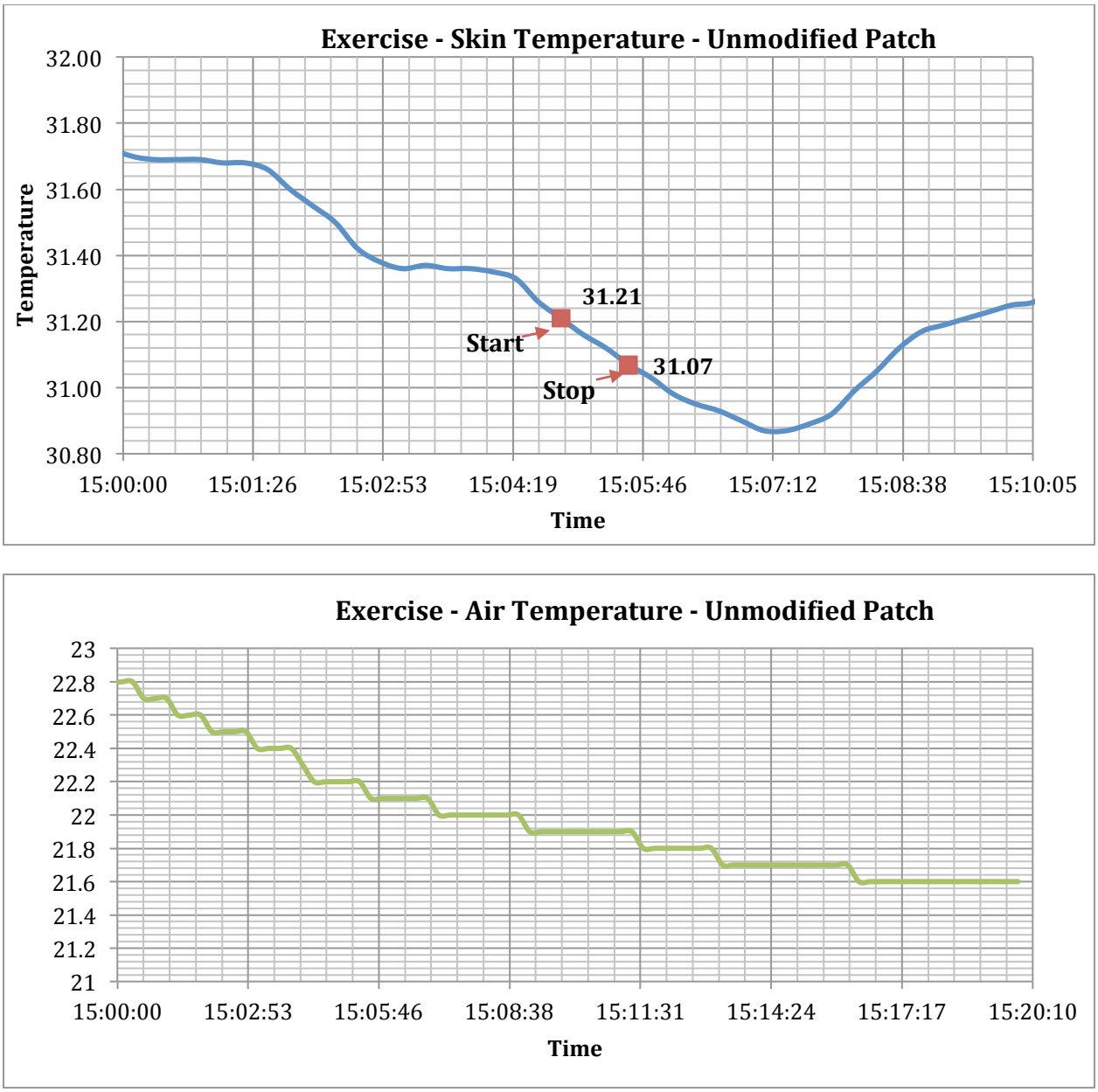

Figure A.5. Skin Temperature and Air Temperature measurements during the exercise test using the unmodified temperature patch.

In the case of the exercise test, the temperature decreased 0.14°C during the exercise, and went as low as 30.87°C before going back up. The decrease in temperature is likely due to some slight occlusion during the curling exercise, while the increasing temperature after the exercise was due to the increase in blood flow to the tissues due to physical activity. The ambient temperature also varied in this test, but was again within a 1°C range.

A.3.2. Modifying the MiniMitter Vitalsense Temperature patch

To improve the sensitivity of the patch, the thermistor needed to make better contact with the sensed surface. Thus, a new temperature patch was modified to allow the thermistor to slightly protrude from the surface of the adhesive side of the patch and make better contact with the skin.

Again, the subject wore the patch for 24 hours to monitor temperature changes, while the temperature logger was also used to measure the ambient temperature. Both the occlusion and exercise tests were performed again. Figure 6 shows the time-lapsed chart of the subject's skin temperature and the ambient temperature for the worn period. There were slightly more peaks and variations in this measurement using the unmodified patch. Again, the peak temperature occurred during the sleeping hours. A sharp temperature drop occurred between 6:20AM and 6:22AM while the subject was on the DC Metro, and walking through the security checkpoint at NIH. It can be hypothesized that the air conditioning was set particularly low in those areas, thus resulting in the same temperature drops in of the skin and the ambient temperatures. Another peak temperature reading occurred at approximately 3:00PM. This occurred when the subject was at the DPSAC office, which filled with many people in a waiting room.

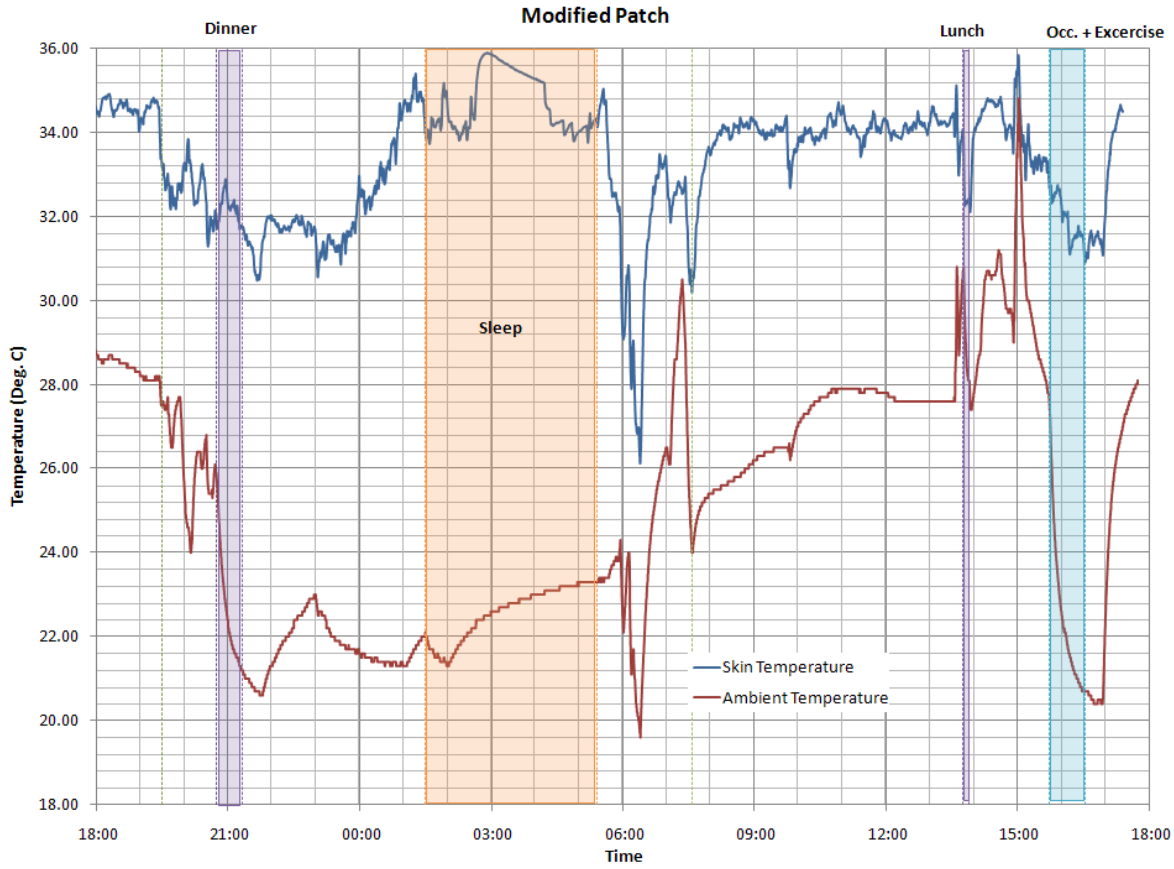

Figure A.6. Time-lapsed chart of measured skin temperature and ambient temperature for a 24hr Period using the modified VitalSense.

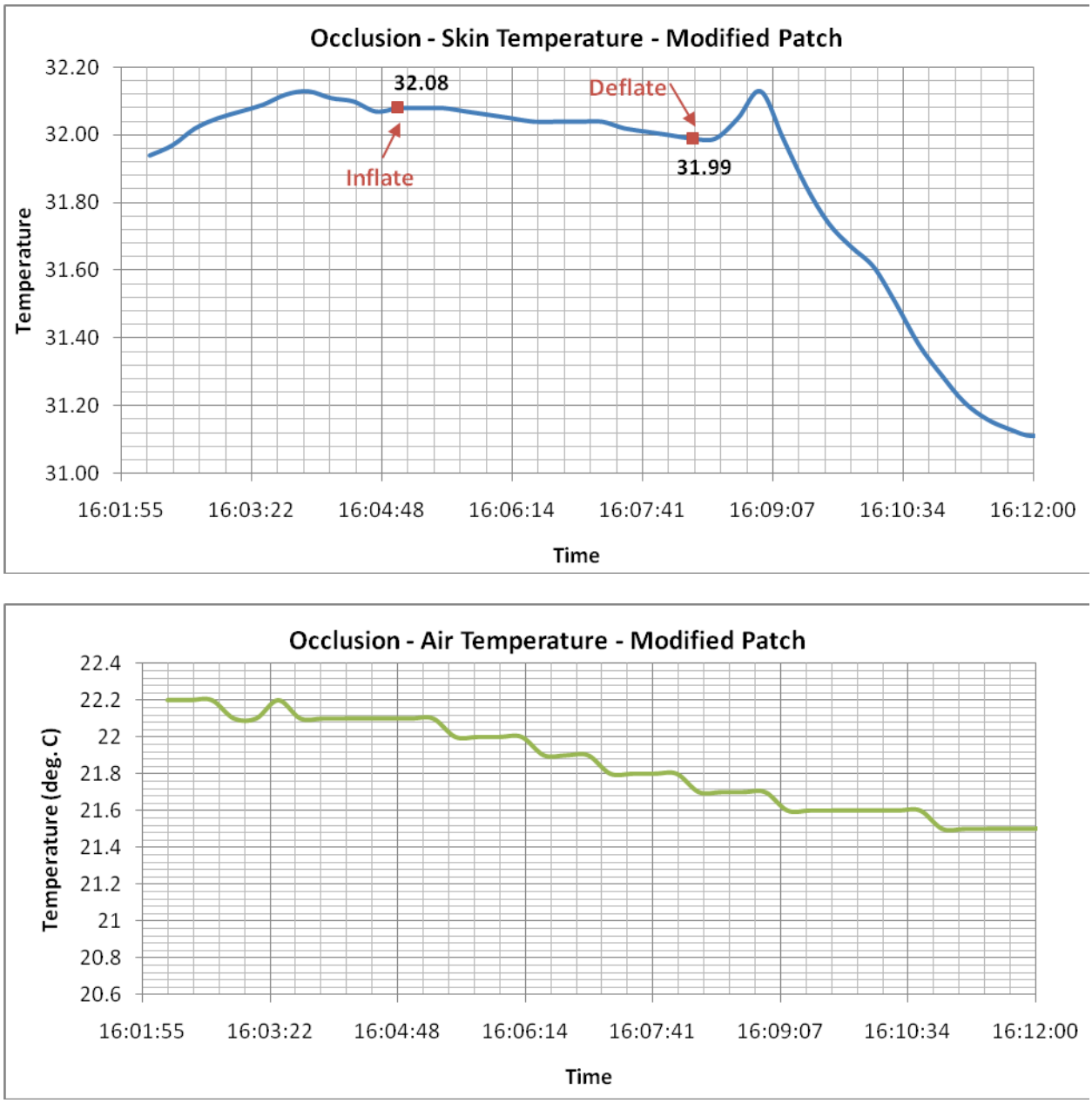

Figure A.7. Skin Temperature and Air Temperature measurements during the occlusion test using the modified temperature patch.

The occlusion test using the modified patch gave more results that correlated with previously shown infrared imaging results. While the temperature decreased 0.09°C during the occlusion, a slight jump in temperature to 32.13°C was measured immediately following cuff deflation, followed by a decrease in temperature. This attributed to a quick rush in blood flow after deflation, returning skin temperature to the baseline temperature. This effect is well known and has been seen in previous studies with infrared imaging. While the room temperature may have varied slightly during the test, the variations were not too significant to vary the results.

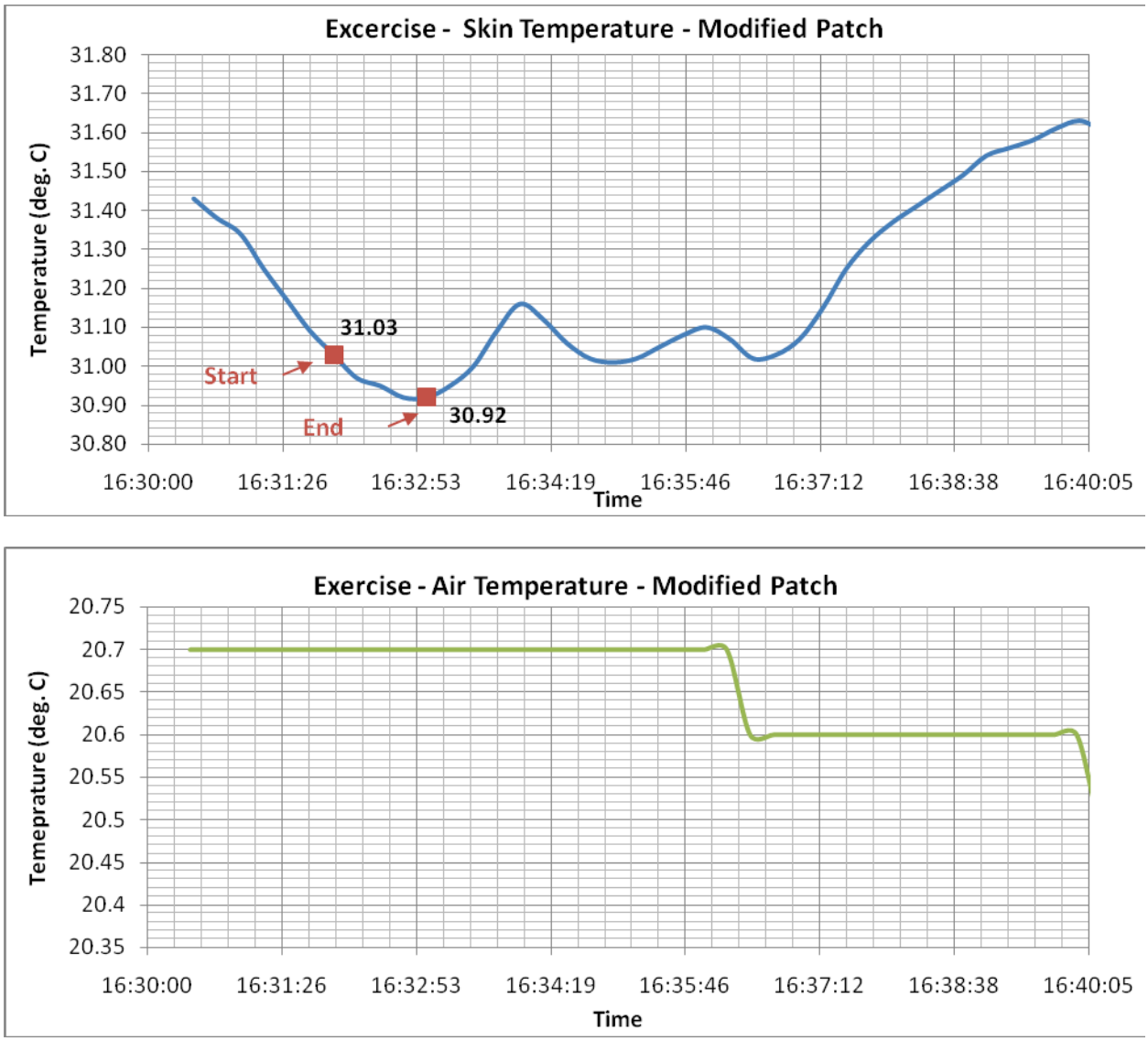

Figure A.8. Skin Temperature and Air Temperature measurements during the exercise test using the modified temperature patch.

This test with the modified patch showed a decrease of 0.89°C in the skin temperature during the exercise, followed by an increase in skin temperature. This result is consistent with known temperature fluctuations during exercise of the forearm. The temperature variations in the ambient temperature were much less than that of previous tests.

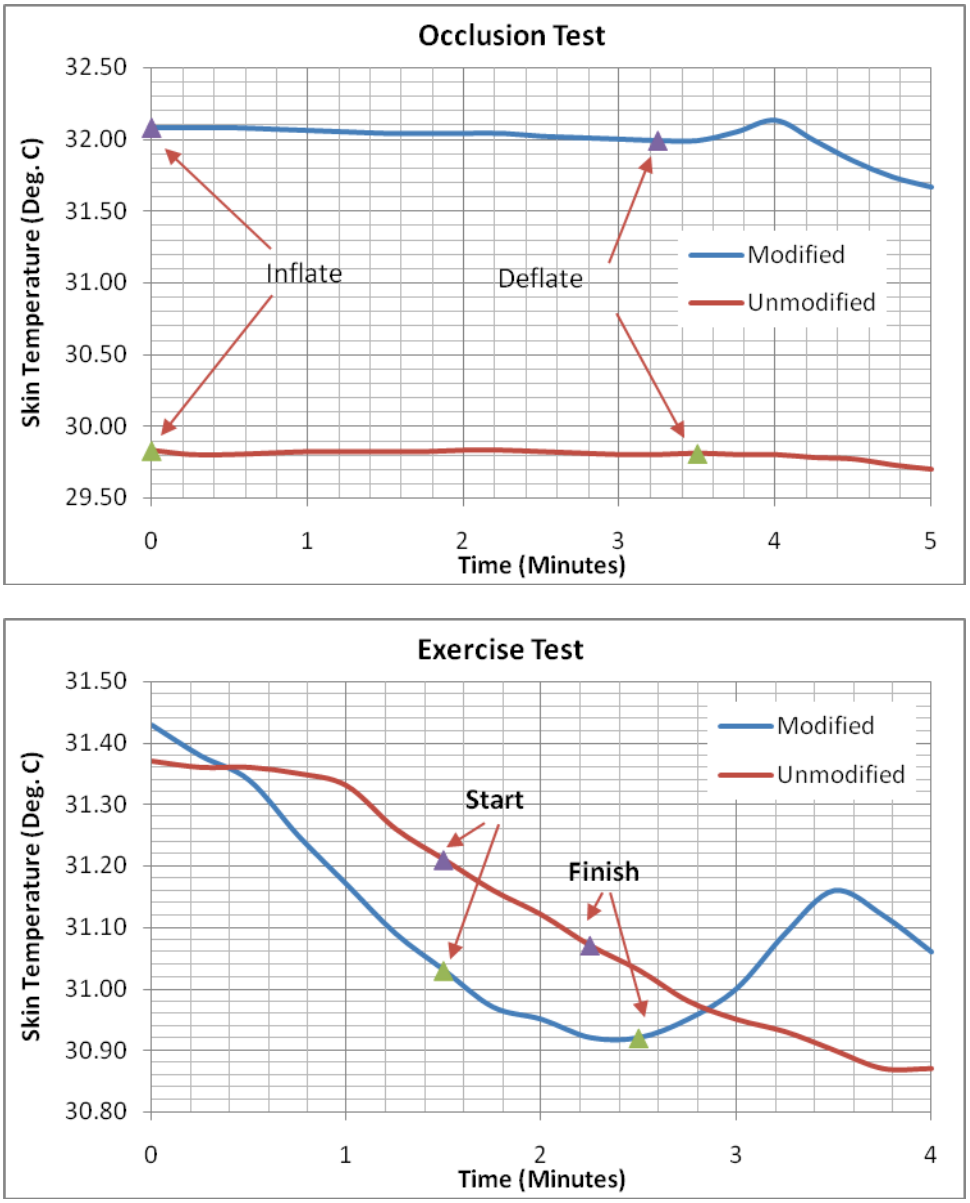

Figure A.9. Comparison of the skin temperature for both the modified and unmodified temperature patches during both the occlusion and exercise test

Wavelet analysis is applied to the de-trended temperature logs of the unmodified/modified thermal patches. First, the trends of two logs were calculated by a second order Savitzky-Golay smoothing filter with 2 minutes time window. The difference between the trend and the original signal was then transformed to the time-frequency domain by continuous Morlet wavelet (6^{th} order, 32 subscales/major scale). Since the patches measured the body temperature every 15 seconds, the highest observable frequency from the wavelet analysis was 0.033Hz according to the sampling theorem.

The following two figures show the temperature logs from 2 patches and the corresponding wavelet spectrum with synchronized time axes. The spectrum of the modified patch reveals more frequency components within the range 0.0095-0.021Hz, which means that the patch is more

sensitive and is able to capture the temperature changes corresponding to the rate of endothelial release of *NO*.

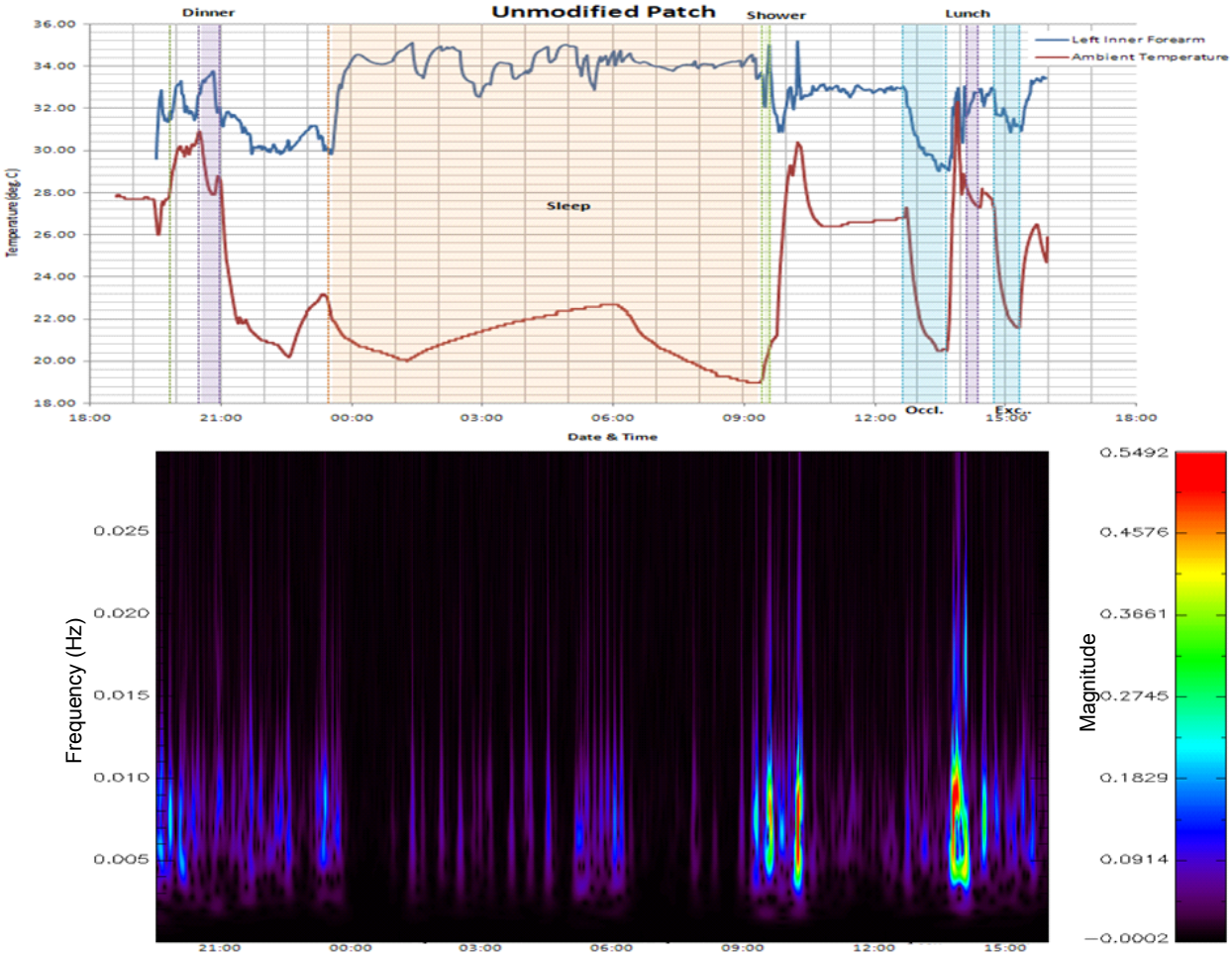

Figure A.10. Wavelet analysis of the unmodified temperature patch

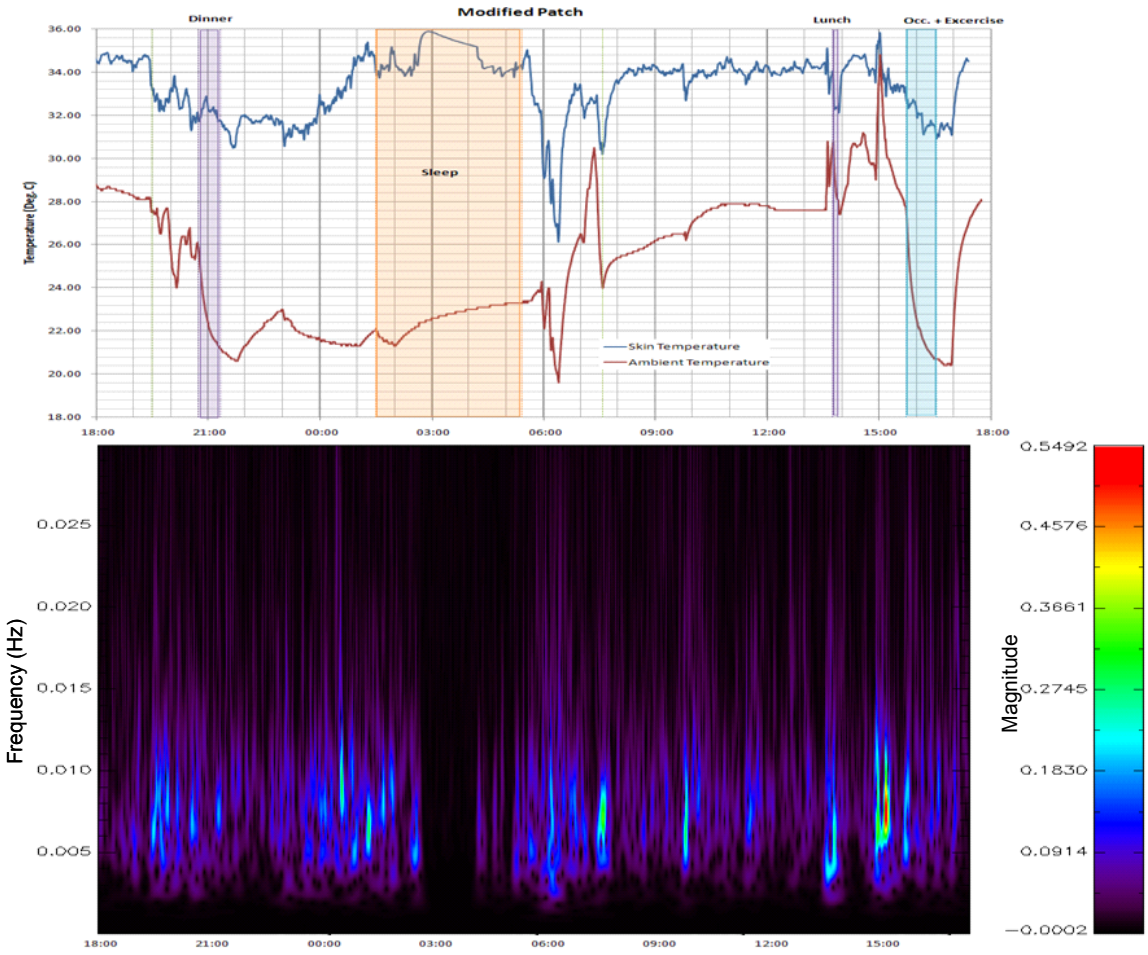

Figure A.11. Wavelet analysis of modified temperature patch

A.3.3. Discussion & Conclusions

Figure A.9 shows the comparison of the two functional tests for both the modified and unmodified patches. The modification of the VitalSense temperature patch appeared to have improved the responsiveness of the temperature patch. The occlusion test using the modified showed more subtle temperature variations during the test this was not seen with the unmodified patch. In particular, a temperature rebound was detected after the cuff was deflated using the modified temperature patch, while the unmodified patch did not show the rebound. This rebound has been shown in previous studies using infrared imaging, and is a result of blood reperfusion after cuff deflation. The discrepancy can also possibly be attributed to the delayed transient response of the unmodified patch. However, since the temperature rebound occurred within a short time-window, the high sampling rate (15s) may have also have affected the results. In the case of the exercise test, the unmodified patch measured the increased skin temperature after a continued drop in temperature. With the modified patch, the skin temperature increased immediately after the exercise was completed. Again, this was possibly attributed to a delayed transient response in the measurement. Thus it might be desirable to use a modified patch for studies involving temperature changes under functional activities. Further studies should be

conducted, however, to better evaluate the response of the modified temperature patch against the unmodified temperature patch. It should be noted that ambient temperature variations, though small, occurred frequently throughout the tests. This may have been due to variations of the ventilation system. The subject was also placed in the room 20 minutes prior to the tests, which did not appear to be a long enough transient time for the temperature patch to reach steady state. The transient time also depends on the human body mass index (BMI). Thus, future tests should require the room temperature to be constantly monitored more than 20 minutes prior to the test. While initial tests proved fairly successful, further testing should be completed to verify the better response of the modified temperature patch.

A.4. Thermal Monitoring of the Neck/Clavicle Areas using Temperature Patches

After initial testing for the temperature patches, further work was performed to monitor the temperatures of the neck/clavicle region. To determine regions-of-interest (ROI) for placement of temperature patches, infrared imaging was first used to note the key "hot spots". The subject first waited in a room at 17°C for 25 minutes with his upper torso exposed to the ambient air. This allowed the subject's body to reach a steady state temperature with respect to the ambient air. This also allowed thermally significant vasculatures to increase blood flow and expose them under infrared imaging. Next, an infrared camera was used to locate the thermally significant vasculature and 3 locations were chosen for monitoring. Figure A.11 shows both an infrared image and photographic image of the subject's upper torso and the corresponding locations chosen for monitoring. The temperature in the room was monitored using a datalogger (Extech Model 42270, USA) for 8 hours before and after the subject entered the room.

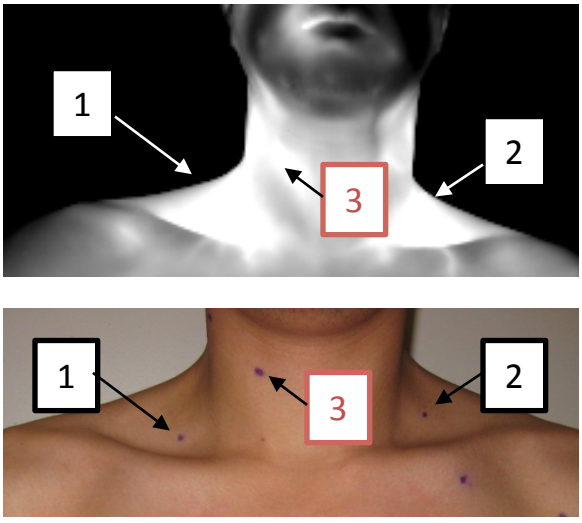

Figure A.12. Infrared image and image of the subject's neck/clavicle and the chosen regions of measurement

The patches were then placed on the subject to begin temperature monitoring and measurement. An A datalogger (Extech Model 42270, USA) was also used in conjunction with the VitalSense to monitor the ambient temperature variations. The regions of measurement were labeled as 1, 2 & 3. Of the three patches, one of the patches (patch 3) was modified as described in the previous section. Since the subject was already wearing a temperature patch for monitoring his inner left arm, the original patch was labeled as patch 0 (modified) as shown in Figure A.13.

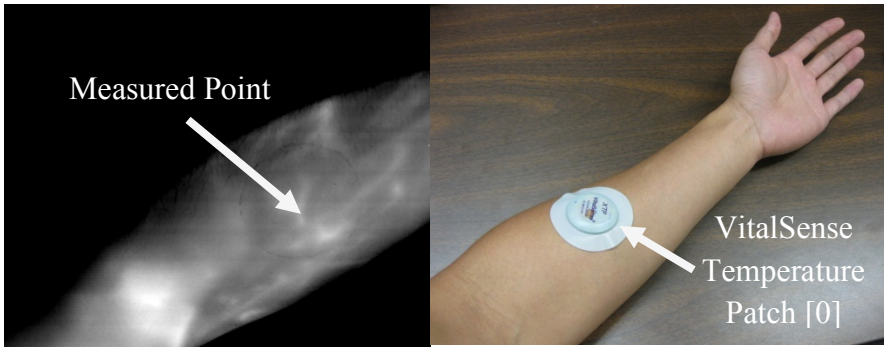

Figure A.13. Infrared image of the subject's forearm and image of the subject's arm with a temperature Patch 0.

Figure A.14 shows the subject's temperatures collected for a 21hr period with 4 patches. The subject's temperature at patches 0, 1 & 3 appeared to peak during the sleeping hours, and was likely due to the cooler temperature in the room, causing the subject to seek warmth under the blankets. The subject also experienced some fairly low temperatures, particularly at patch 0 (inner left arm) during the experiments (14:20-16:10). This was likely due to the cold room (17˚C) of the experiments.

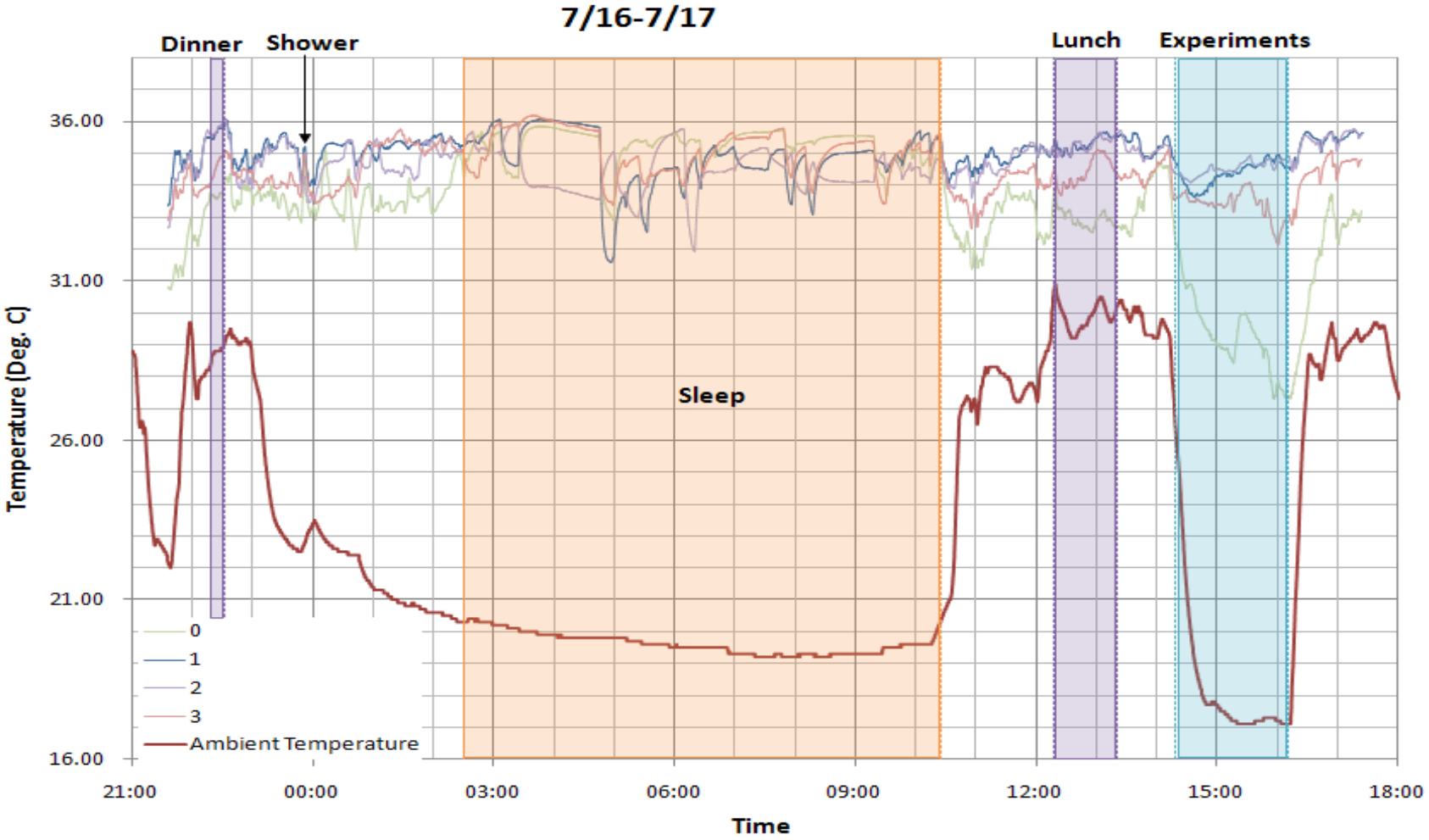

Figure A.14. Time-lapsed chart of measured skin temperature and ambient temperature for a 21hr Period using the Mini Mitter VitalSense.

A.4.1. Experiments to Study Temperature variations under functional activities

To study the effects of temperature variations certain activities, 3 separate tests were performed. All tests were performed in a room at approximately 17°C. The subject entered the room 30 minutes prior to the tests, and rested for 20 minutes after each test to allow the subject's body to reach a baseline temperature.

A.4.1.1. *Total Arm Occlusion*

The first test was an occlusion test to measure the variation of skin temperature from occlusion of the blood vessels in the arm. A cuff was placed on the upper arm, and was inflated to approximately 220 mm Hg. It was held for 3 minutes to limit blood flow to the forearm. The cuff was finally deflated after 3 minutes and the subject was allowed to relax. Figure 14 shows the results of the occlusion test.

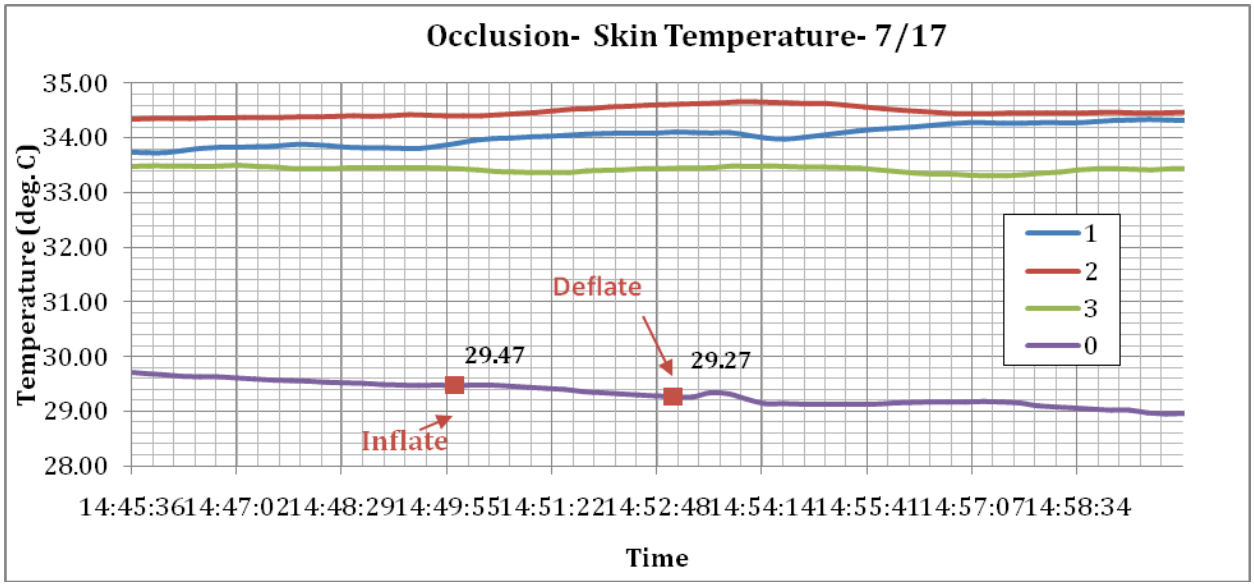

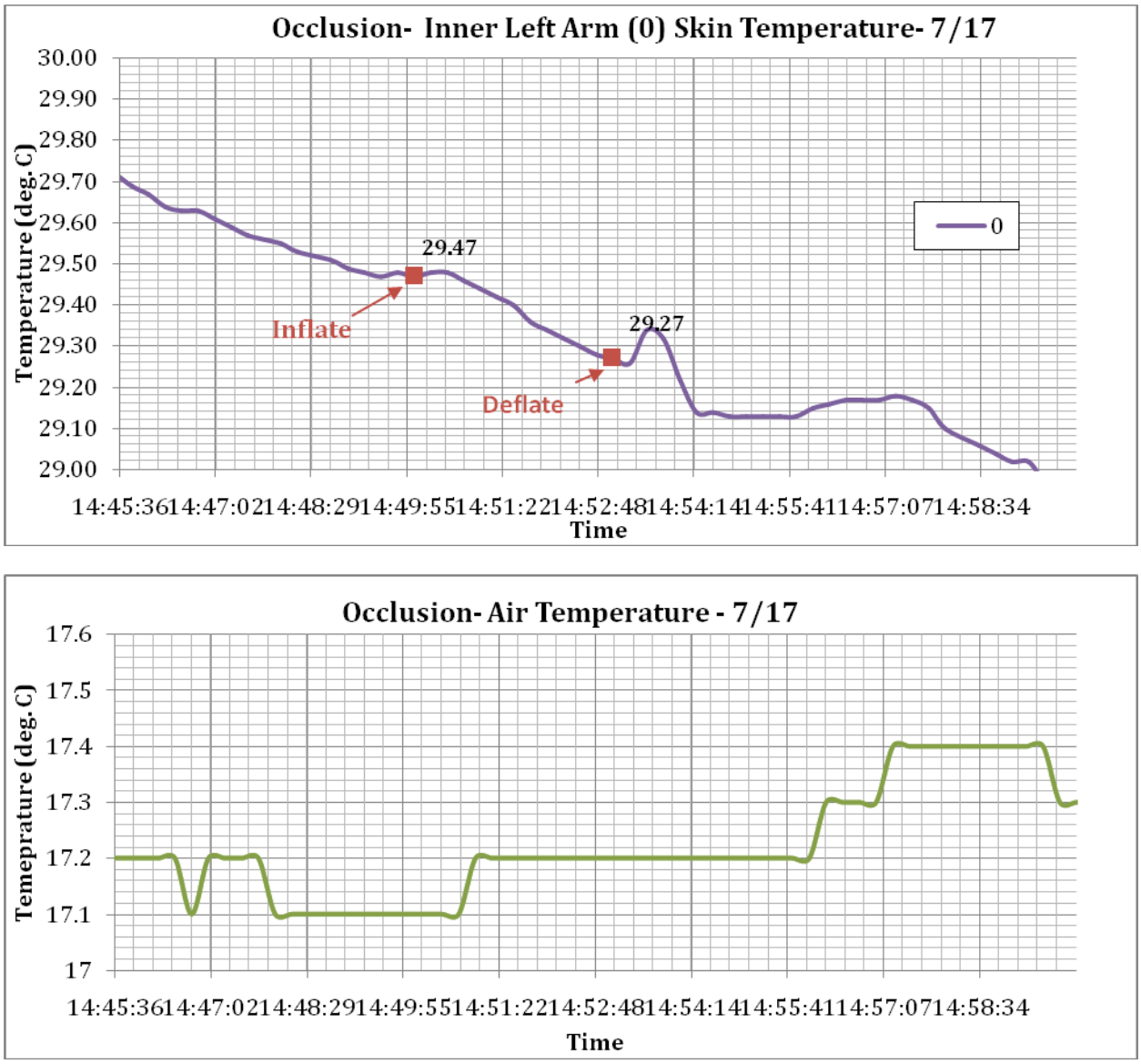

Figure A.15. Skin Temperature and Air Temperature measurements during the occlusion test.

During the occlusion test, the inner left forearm Patch (0) temperature decreased 0.2°C. This was followed by a slight increase in temperature to 29.32°C after the cuff was deflated. Again, this is due to blood reperfusion during the cuff deflation as described earlier. The temperatures of the other patches did not vary significantly during the occlusion test and no trends could be noted during occlusion. It should be noted that the ambient temperature readings varied slightly, but was within 0.5°C.

A.4.1.2. *Exercise Test*

The second test was an exercise test where the subject performed 20 curls using a 10lb dumbbell with his left arm for 1 min. Figure 15 shows the results of the exercise test.

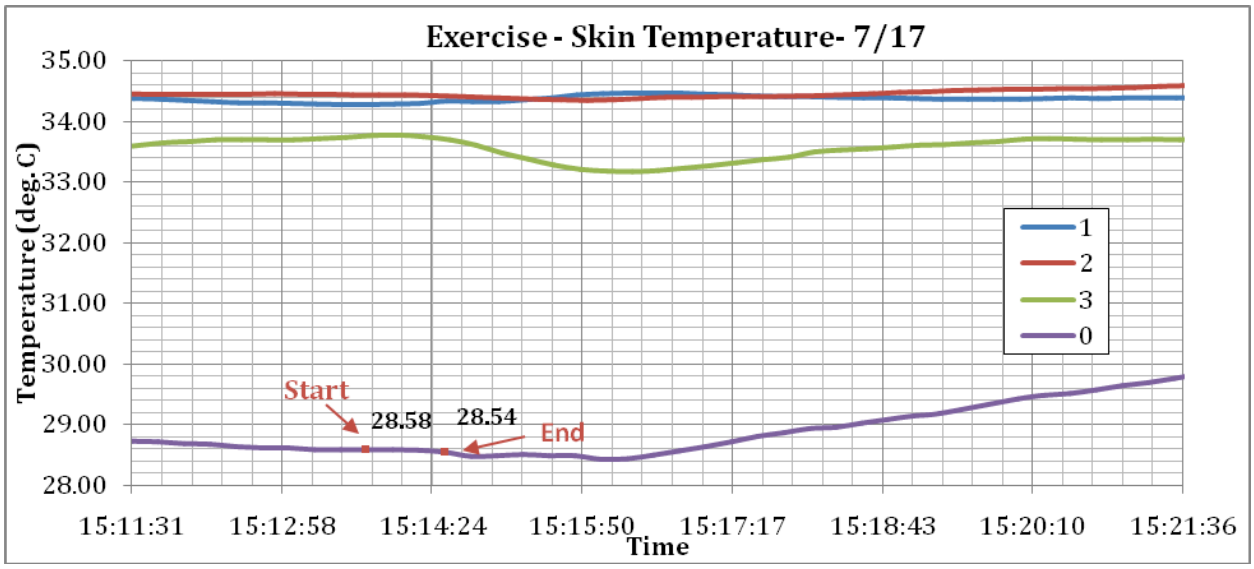

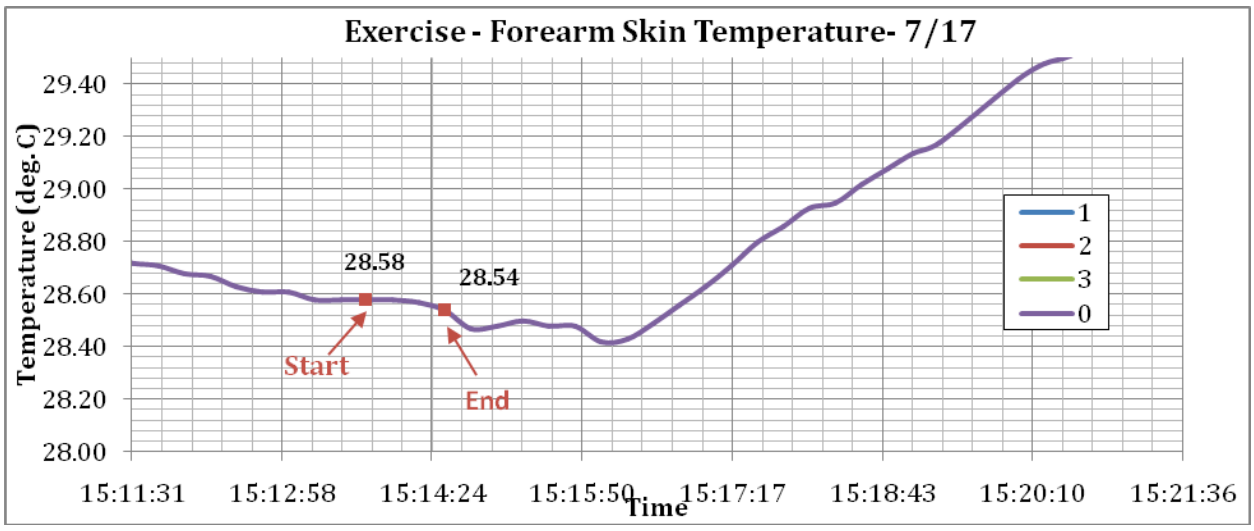

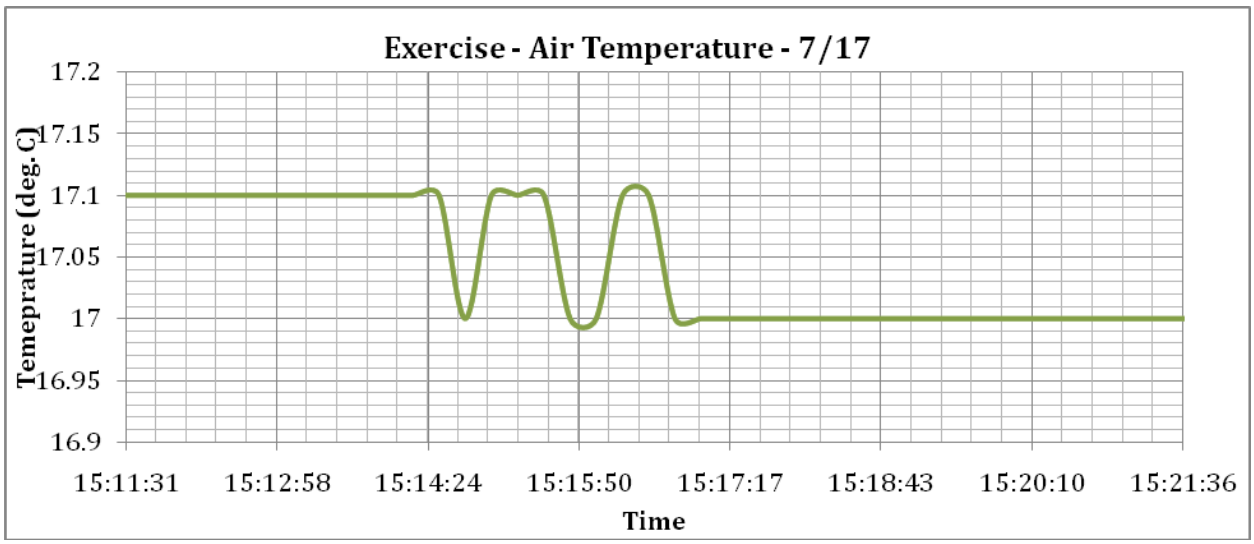

Figure A.16. Skin Temperature (a) and Air Temperature (b) measurements during the exercise test.

In the case of the exercise test, the temperature of the inner left arm (Patch 0) decreased 0.04°C during the exercise, and went as low as 28.43°C before going back up. The decrease in skin temperature is due to the stealing of the blood from skin to muscle. The increasing temperature after the exercise was due thermal conduction of the heat from the muscle to the skin surface. There was also a decrease in temperature of the neck (Patch 3) during the exercise. This might be due to the extra breathing during the activity. The ambient temperature was fairly constant throughout the test and varied only by 0.1°C

A.4.1.3. *Cooling of hands*

Previous studies using infrared imaging have shown the neck/clavicle temperature to increase when a subject's hands are placed in cold water. In this test, the subject placed both his hands individually in separate cold-water baths for 2 minutes. This test was performed to study the brown-fat response in the neck/clavicle region. The initial bath temperature was 6°C while the final bath temperature was 6.5°C. Figure A.16 shows the results of the test.

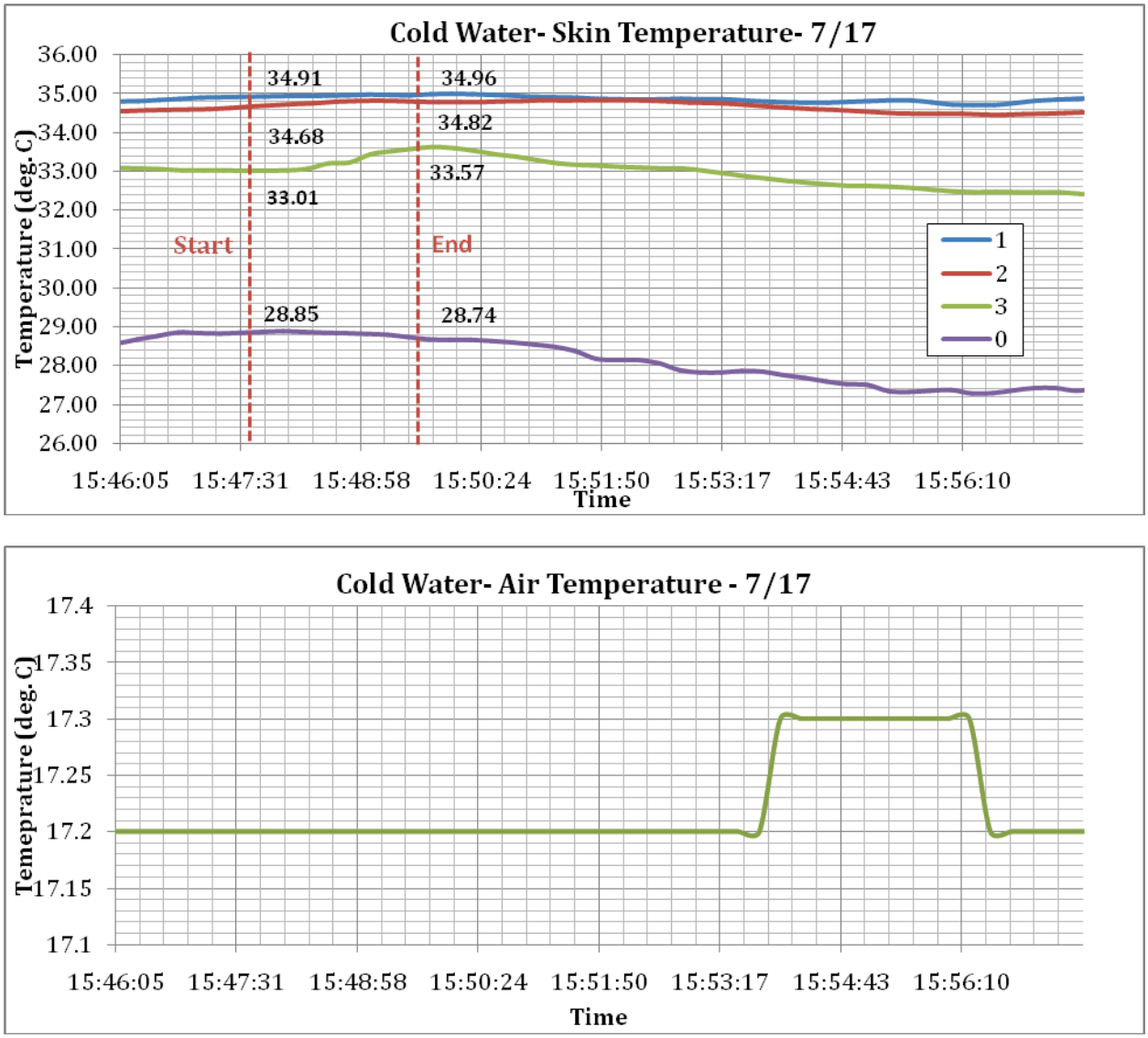

Figure A.17. Skin Temperature and Air Temperature measurements during cold water test.

The cold-water test yielded some interesting results. During the test, the temperature of the inner left forearm (patch 0) decreased. However the temperature of all the other patches in the neck region (1, 2, & 3) all increased during the test.

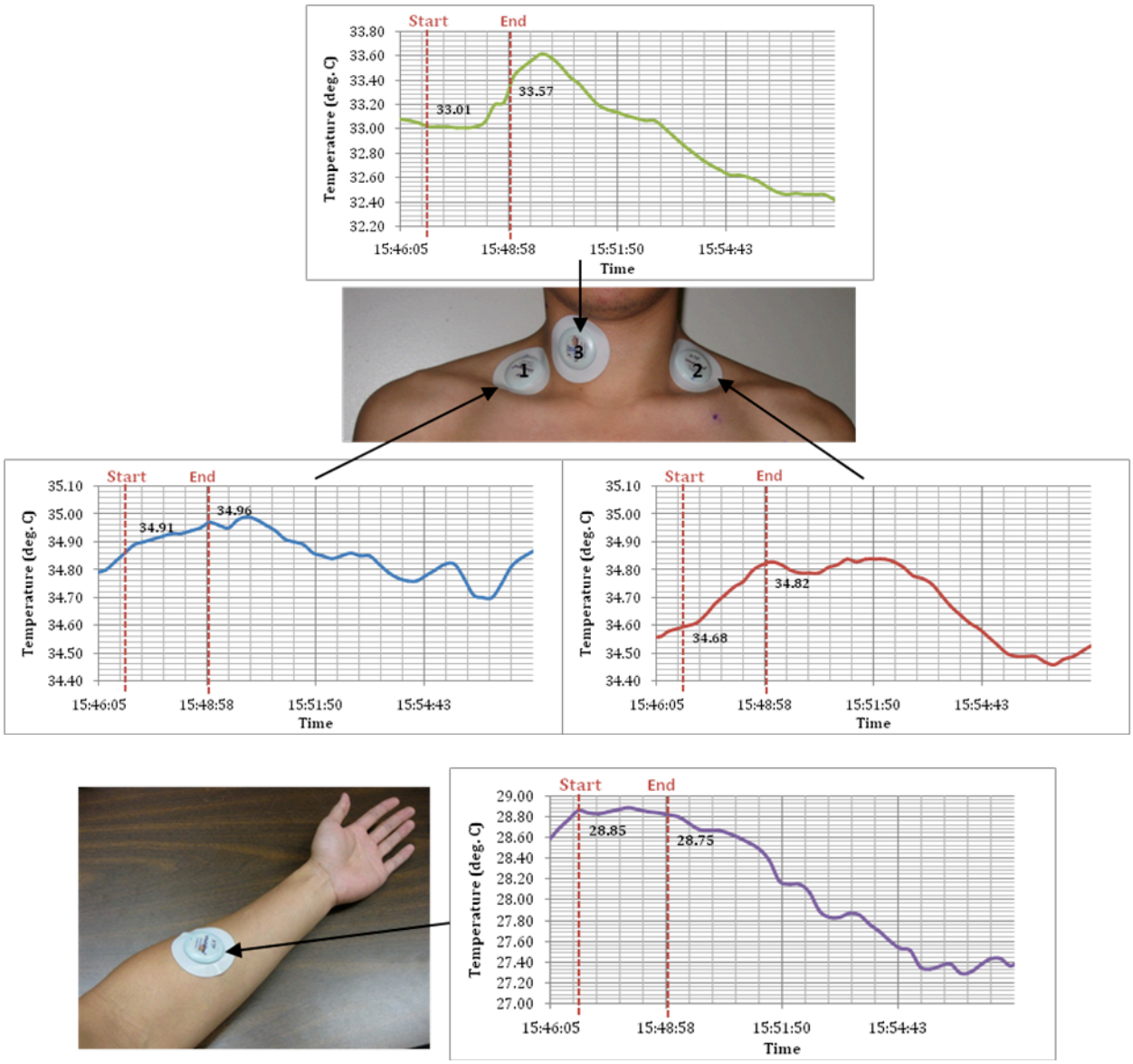

Figure A.18. Individual Patch Temperatures during cooling of hands

A.4.2. Continued Skin Temperature Monitoring of the Neck/Clavicle: 7/17/09 – 7/20/09

The temperature of the upper torso monitored over a period of 3 days (7/17/09 – 7/20/09). The subject wore 4 VitalSense temperature patches as described previously, while carrying a temperature data logger to monitor the ambient temperature. The locations of measurement are shown again in Figures A.17 & A.18.

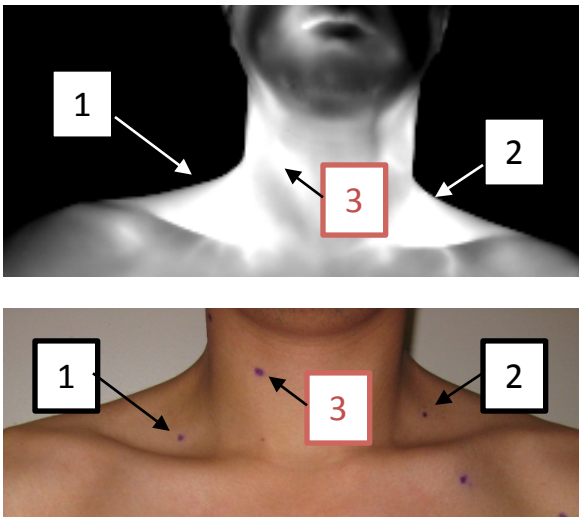

Figure A.19. Infrared image and picture of the subject's neck/clavicle and the chosen regions of measurement

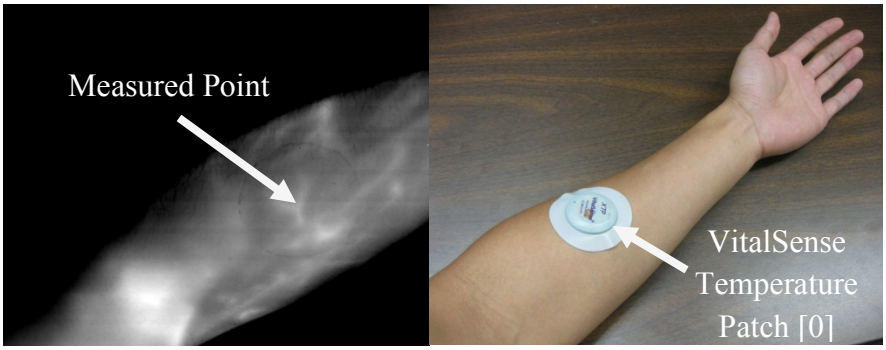

Figure A.20. Infrared image of the subject's arm and image of the subject's arm with a temperature patch

The following figures show the time-lapsed temperature measurements for the 4 patches and surround air over the 3-day period.


7/17-7/18
Dinner
Shower
Sleep
Temperature (Deg. C)
39.00
37.00
35.00
33.00
31.00
29.00
27.00
25.00
23.00
21.00
19.00
18:00
21:00
00:00
03:00
06:00
09:00
12:00
15:00
18:00
Time
1
2
Air Temp.


7/17-7/18
Dinner
Shower
Sleep
Temperature (Deg. C)
37.00
35.00
33.00
31.00
29.00
27.00
25.00
23.00
21.00
19.00
18:00
21:00
00:00
03:00
06:00
09:00
12:00
15:00
18:00
Time
3
0
Air Temp.

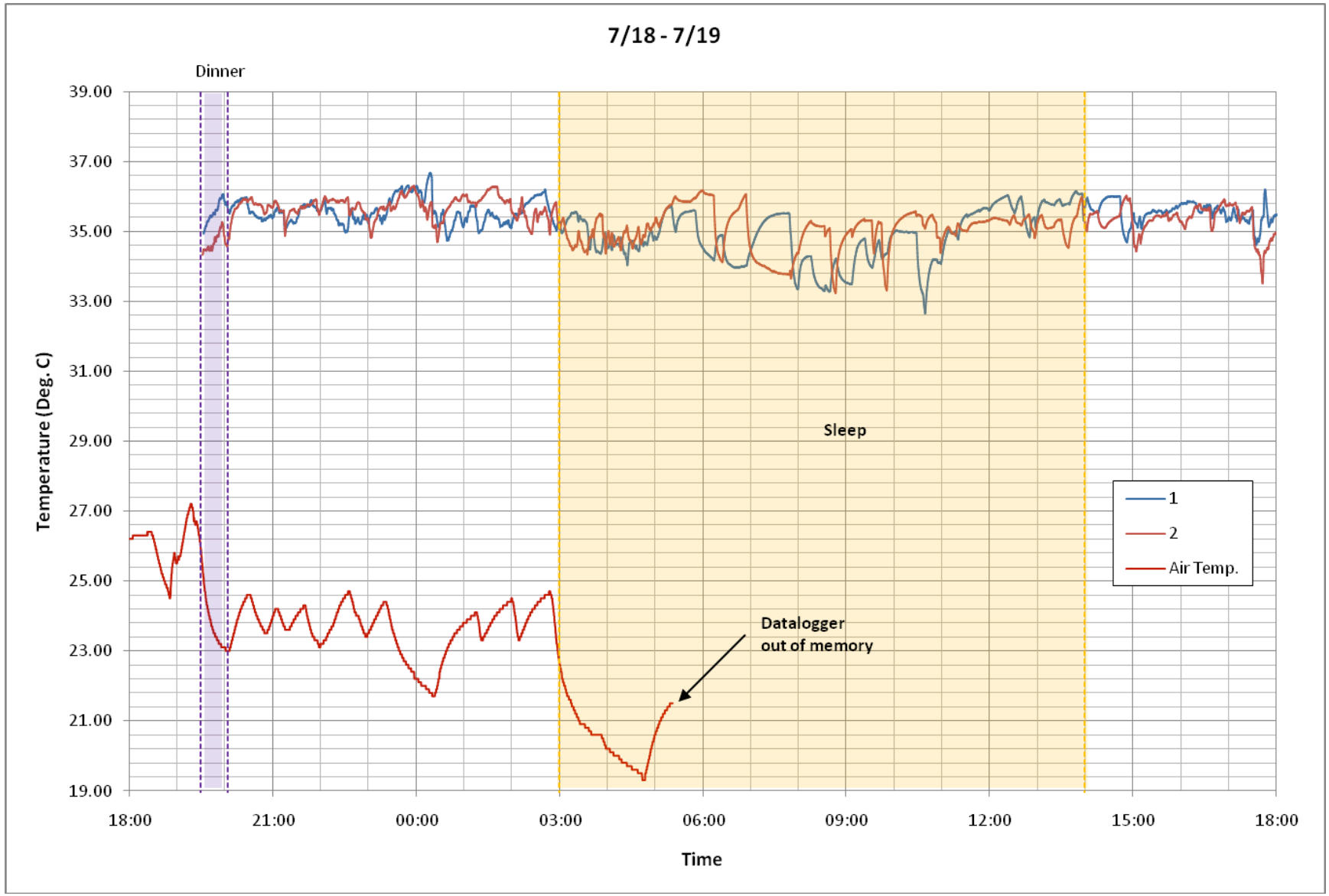
7/18 - 7/19
Dinner
Sleep
Datalogger
out of memory
1
2
Air Temp.
Temperature (Deg. C)
39.00
37.00
35.00
33.00
31.00
29.00
27.00
25.00
23.00
21.00
19.00
18:00
21:00
00:00
03:00
06:00
09:00
12:00
15:00
18:00
Time

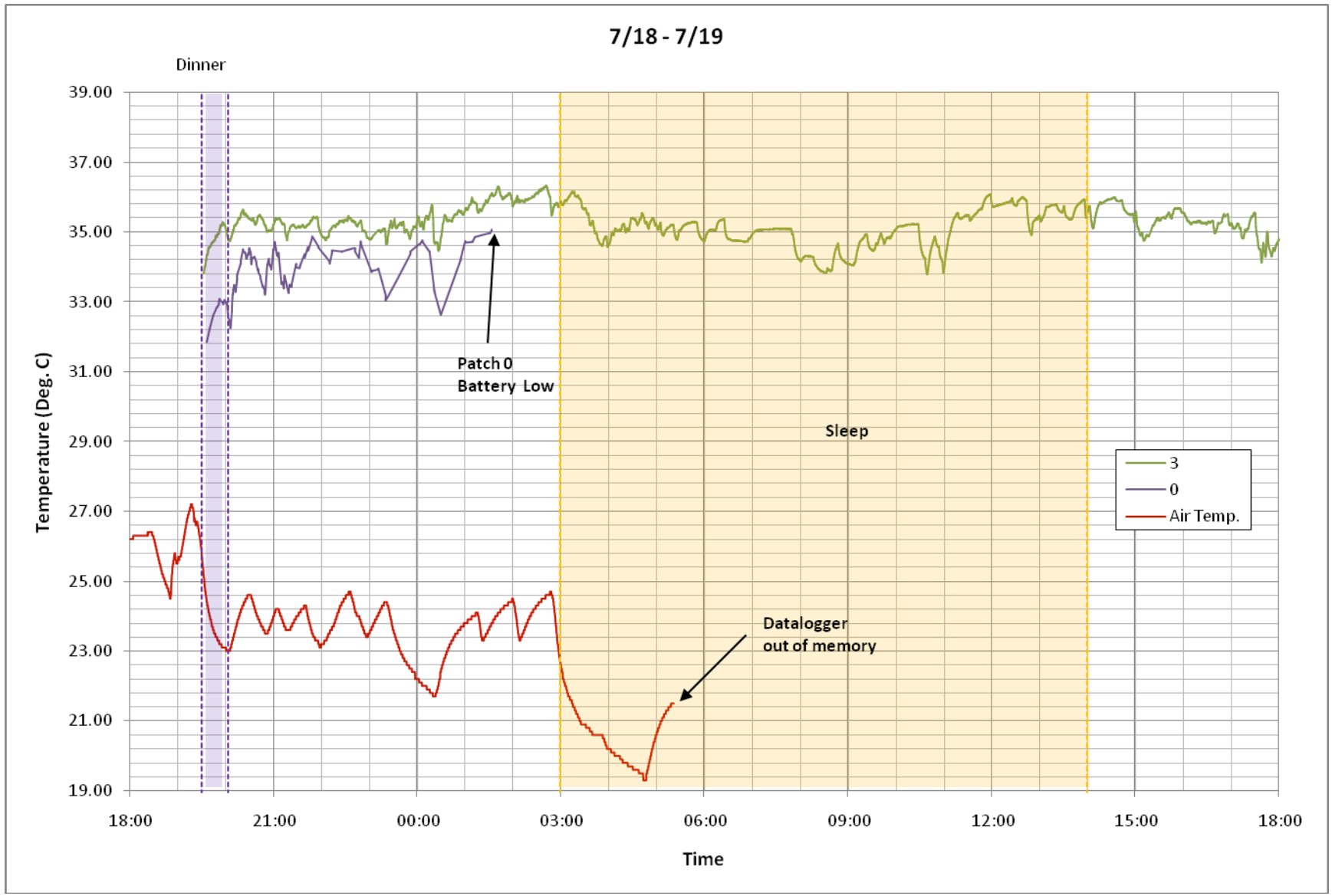
7/18 - 7/19
Dinner
Patch 0
Battery Low
Sleep
Datalogger
out of memory
3
0
Air Temp.
Temperature (Deg. C)
39.00
37.00
35.00
33.00
31.00
29.00
27.00
25.00
23.00
21.00
19.00
18:00
21:00
00:00
03:00
06:00
09:00
12:00
15:00
18:00
Time

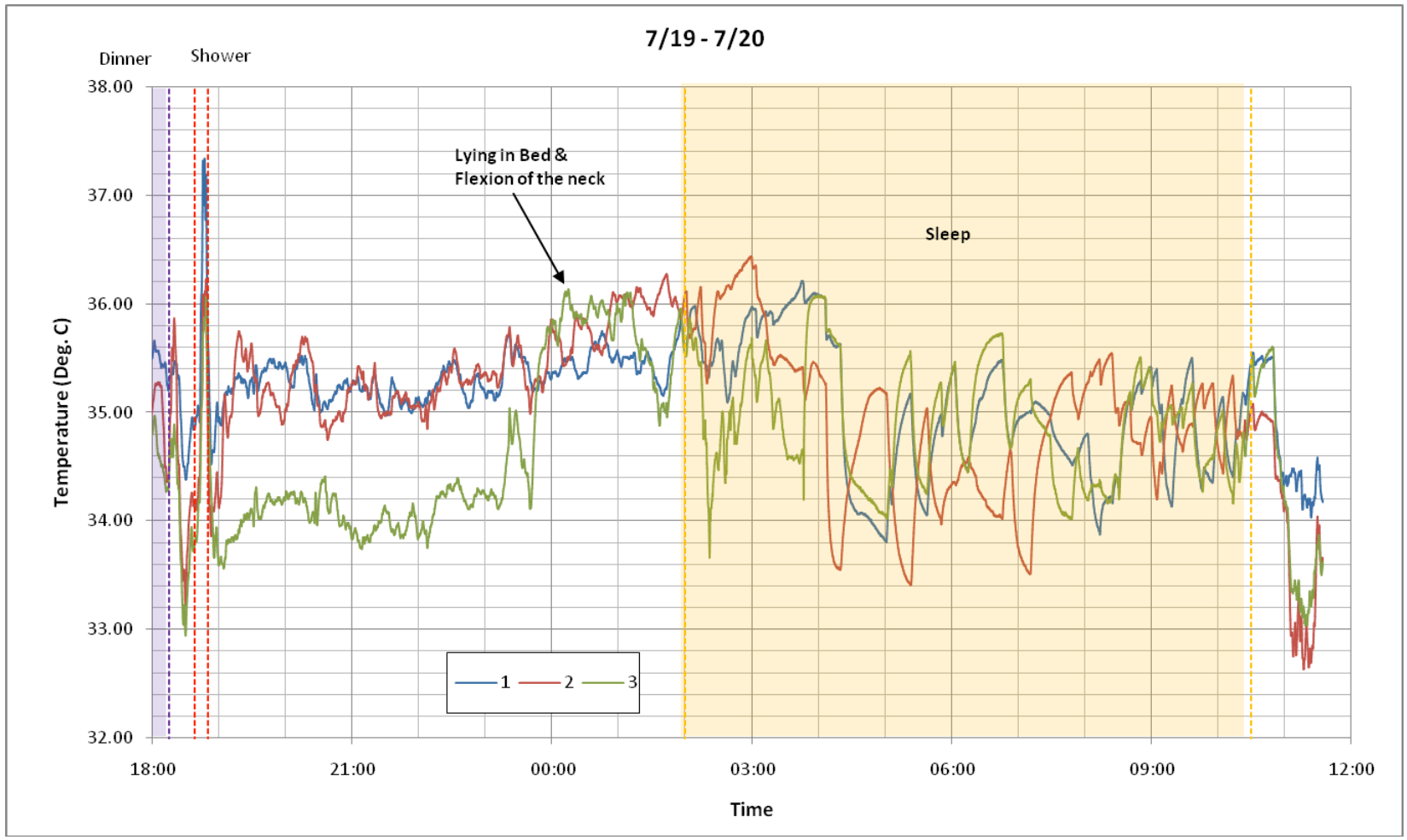

Figure A.21. (a-e). Time-lapsed figures of temperature measurement from 4 temperature patches over a 3 day period. It should be noted that due to limitations in the on-board memory (max. 16,000 data points) of the data-logger, the ambient air temperature was only measured until 5:12 AM on 7/19/2009. Temperature patch 0 (inner left arm) also stopped measuring at 1:33AM on 7/19/2009 when its internal battery was completely drained. This was because temperature patch 0 started measuring data since 7/14/09.

A.4.3. Thermal Monitoring of the Upper Torso using Temperature Patches

Temperature monitoring with the temperature patches was expanded to monitor skin temperature of the upper torso. Again, to determine ROI for placement of temperature patches, infrared imaging was first used to note the key "hot spots". The subject first waited in a room at 20°C with his upper torso exposed to the ambient air. This allowed thermally significant vasculatures to increase blood flow and expose them under infrared imaging. Next, an infrared camera was used to locate the thermally significant vasculature and 9 locations were chosen for monitoring. Figure A.22a shows an infrared image of the subject's upper torso, and Figure A.22b shows the corresponding locations chosen for monitoring. The temperature in the room was monitored using an Extech Datalogger 42270 for 8 hours before and after the subject entered the room.

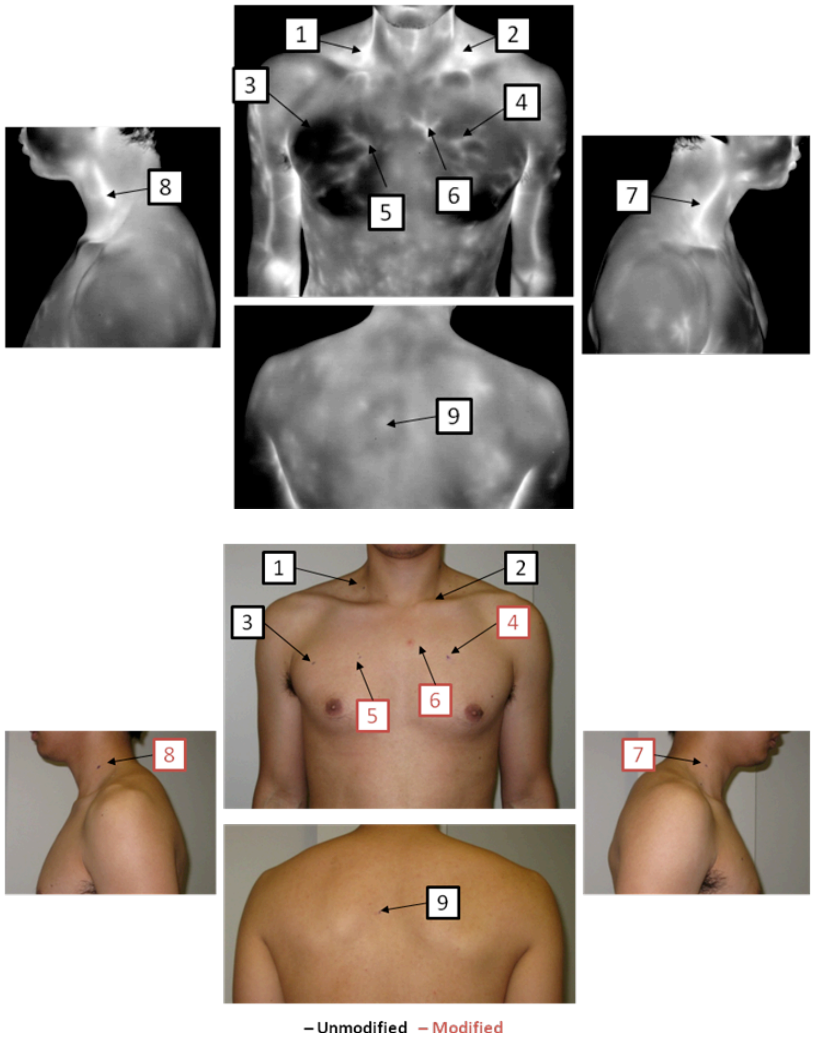

Figure A.22. Figure 23. Infrared image and photographic image of the subject's upper torso and the chosen regions of measurement

The patches were then placed on the subject to begin temperature monitoring and measurement. An Extech Datalogger 42270 was also used in conjunction with the VitalSense to monitor the

ambient temperature variations. Limitations in the availability of temperature patches only allowed us to place 3 temperature patches on the subject. Thus, patches were only placed on locations 1, 2 & 3. Since the subject was already wearing a temperature patch for monitoring his inner left arm, the original patch was labeled as patch 0 as shown in Figure A.20.

Figure A.23 shows the subject's various temperature data for a 24hr period. The subject's temperature appeared to peak during the sleeping hours, and was likely due to the cooler temperature in the room, causing the subject to seek warmth under the blankets. The subject also experienced some fairly low temperature, particularly at patch 0 (inner left arm) during the experiments. This was likely due to the very cold room at which the experiments were performed.

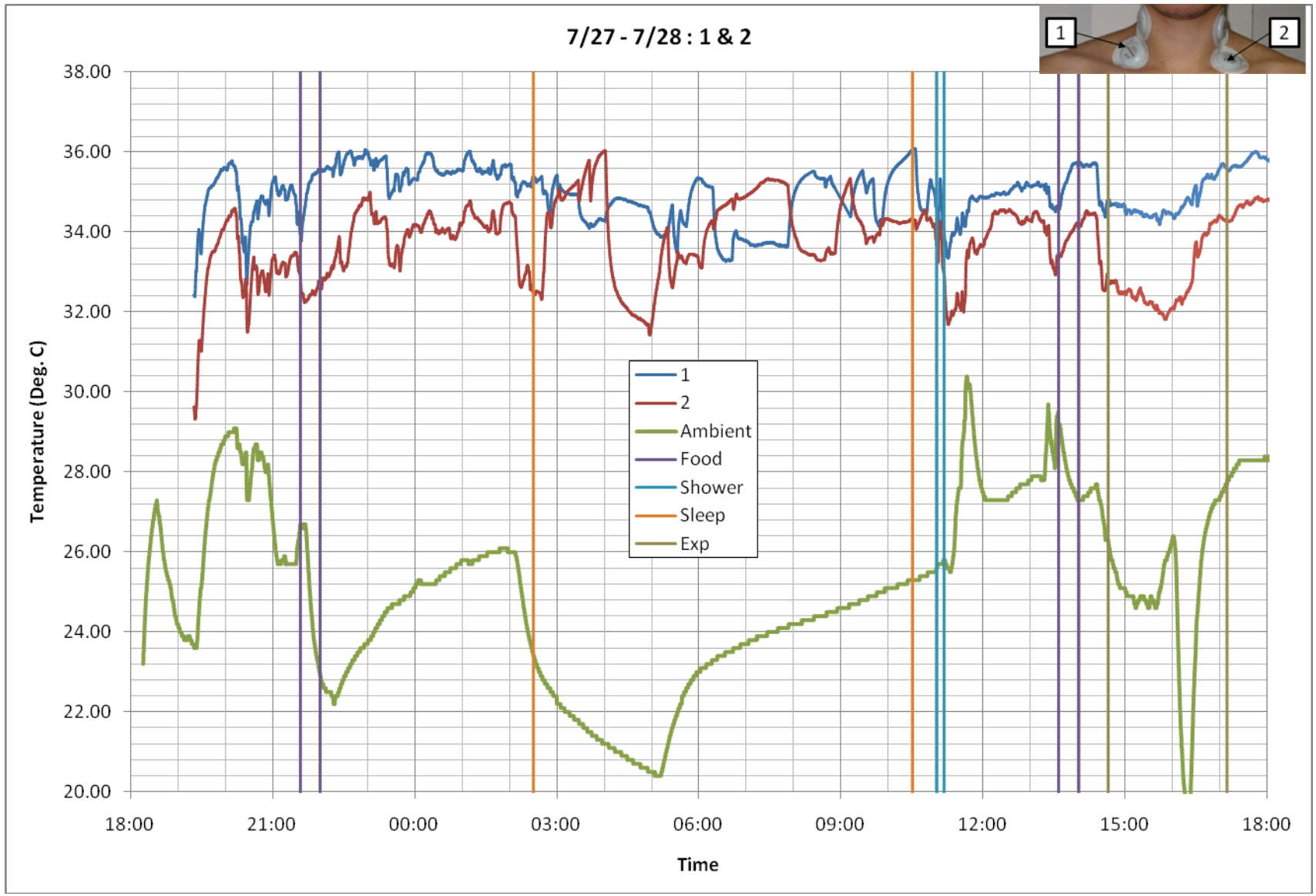
7/27 - 7/28 : 1 & 2
1
2
38.00
36.00
34.00
32.00
30.00
28.00
26.00
24.00
22.00
20.00
Temperature (Deg. C)
18:00
21:00
00:00
03:00
06:00
09:00
12:00
15:00
18:00
Time
1
2
Ambient
Food
Shower
Sleep
Exp


7/27 - 7/28: 3 & 4
3
4
38.00
36.00
34.00
32.00
30.00
28.00
26.00
24.00
22.00
20.00
Temperature (Deg. C)
18:00
21:00
00:00
03:00
06:00
09:00
12:00
15:00
18:00
Time
3
4
Ambient
Food
Shower
Sleep
Exp

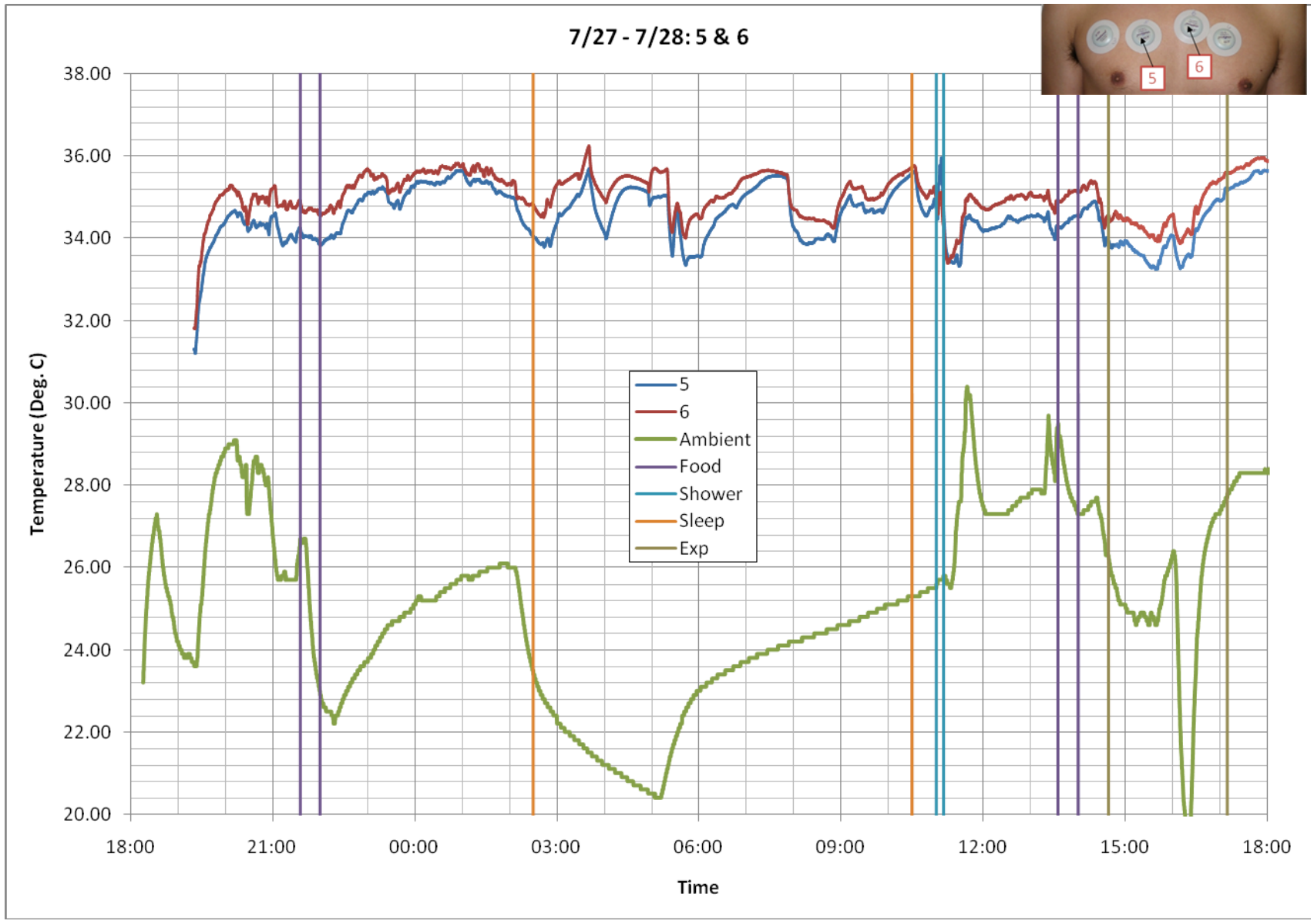
7/27 - 7/28: 5 & 6
5
6
38.00
36.00
34.00
32.00
30.00
28.00
26.00
24.00
22.00
20.00
Temperature (Deg. C)
18:00
21:00
00:00
03:00
06:00
09:00
12:00
15:00
18:00
Time
5
6
Ambient
Food
Shower
Sleep
Exp


7/27 - 7/28: 7 & 8
8
7
38.00
36.00
34.00
32.00
30.00
28.00
26.00
24.00
22.00
20.00
Temperature (Deg. C)
18:00
21:00
00:00
03:00
06:00
09:00
12:00
15:00
18:00
Time
7
8
Ambient
Food
Shower
Sleep
Exp

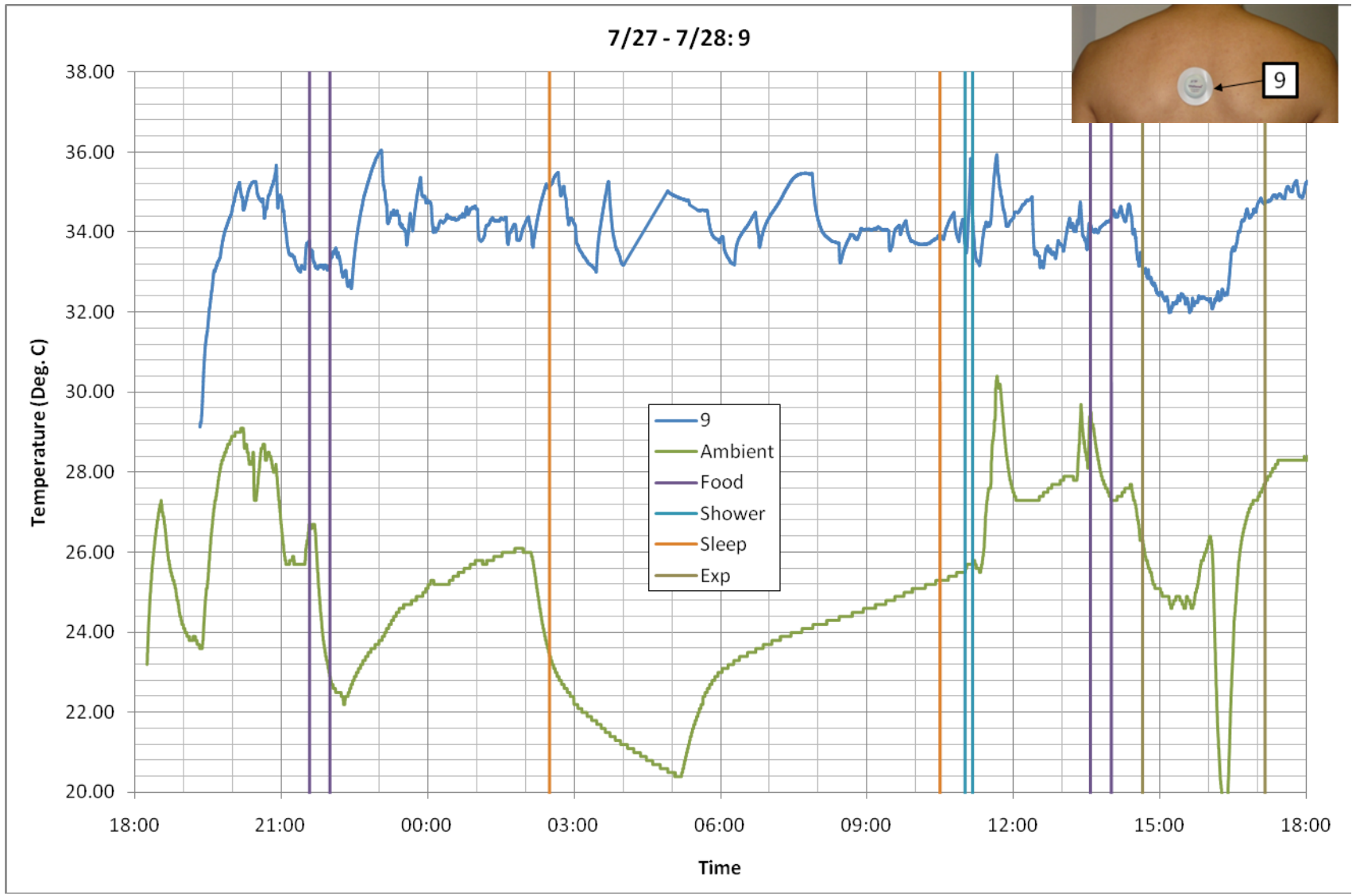

Figure A.23. (a-e). Time-lapsed skin temperature measurements of 9 thermo-patches over a 24hr period

A.4.3.1. *Functional Testing: Cooling of Hands*

To study the effects of the skin temperature under controlled functional tests, the subject cooled his hands in cold water baths as described in previous sections. The subject placed both his hands individually in separate cold water baths for 2 minutes. The initial bath temperature was approximately 7°C. Below are the results of the temperatures during the functional test. The red lines indicate markers for the start and stop of the experiments. The skin temperatures for each point are plotted on the same scale for the test.

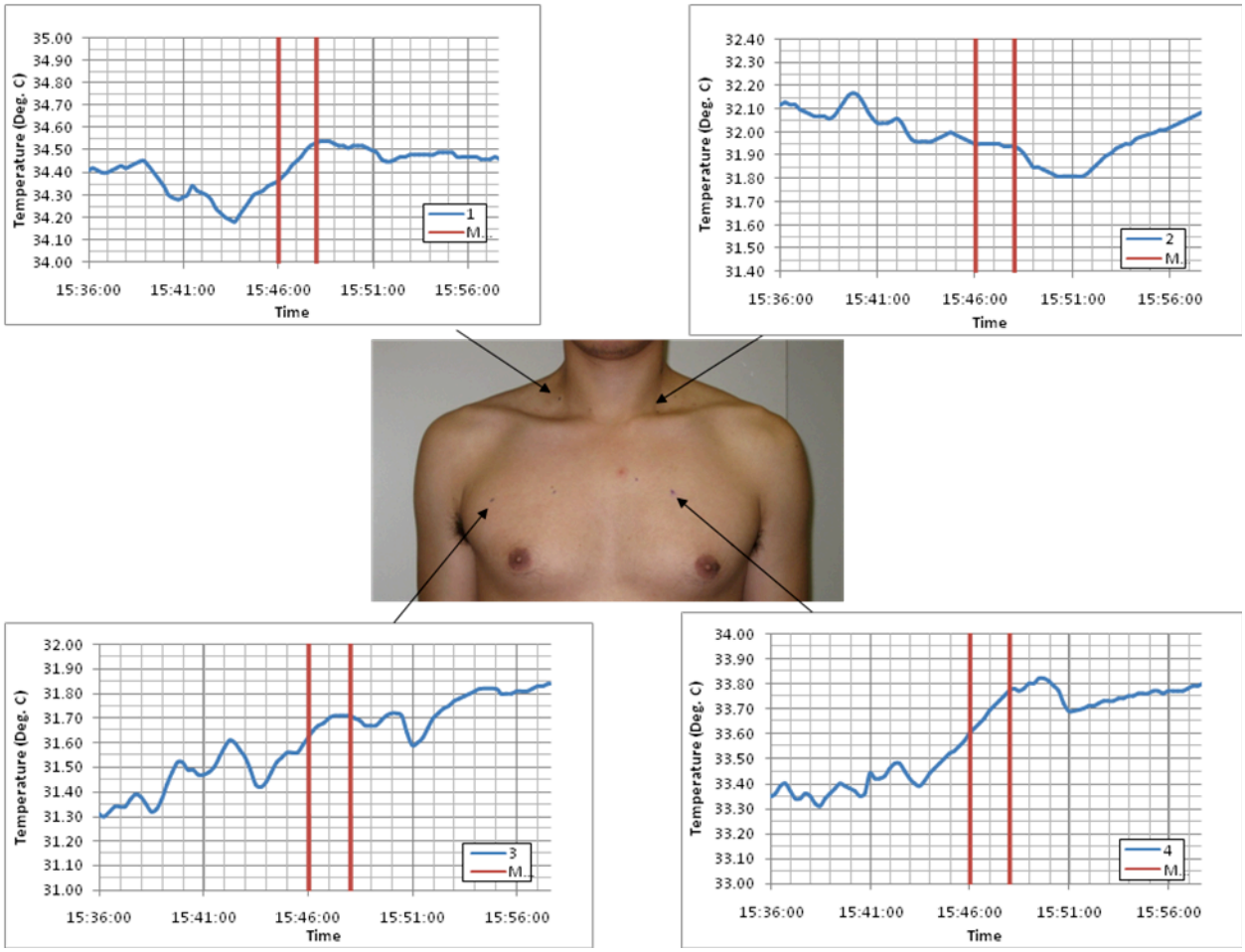

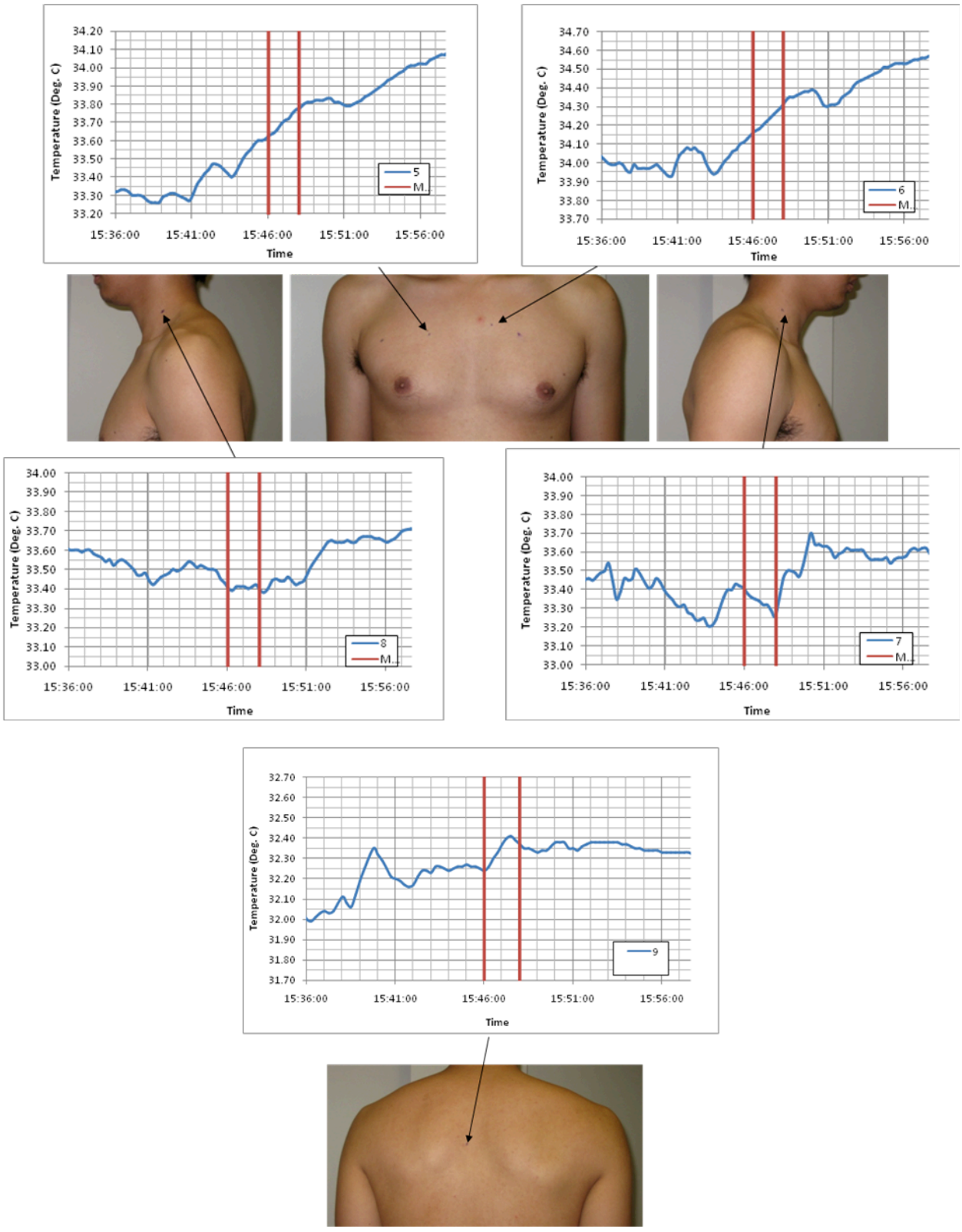

Figure A.24. Skin temperature measurements from the 9 patches during the hand cooling experiment

A.4.4. Continued Thermal Monitoring of the Upper Torso – 7/28/09-7/31/09

The temperature patches described in the previous section were continuously monitored for 24 hours. The images of the patch locations are shown again below for clarity.

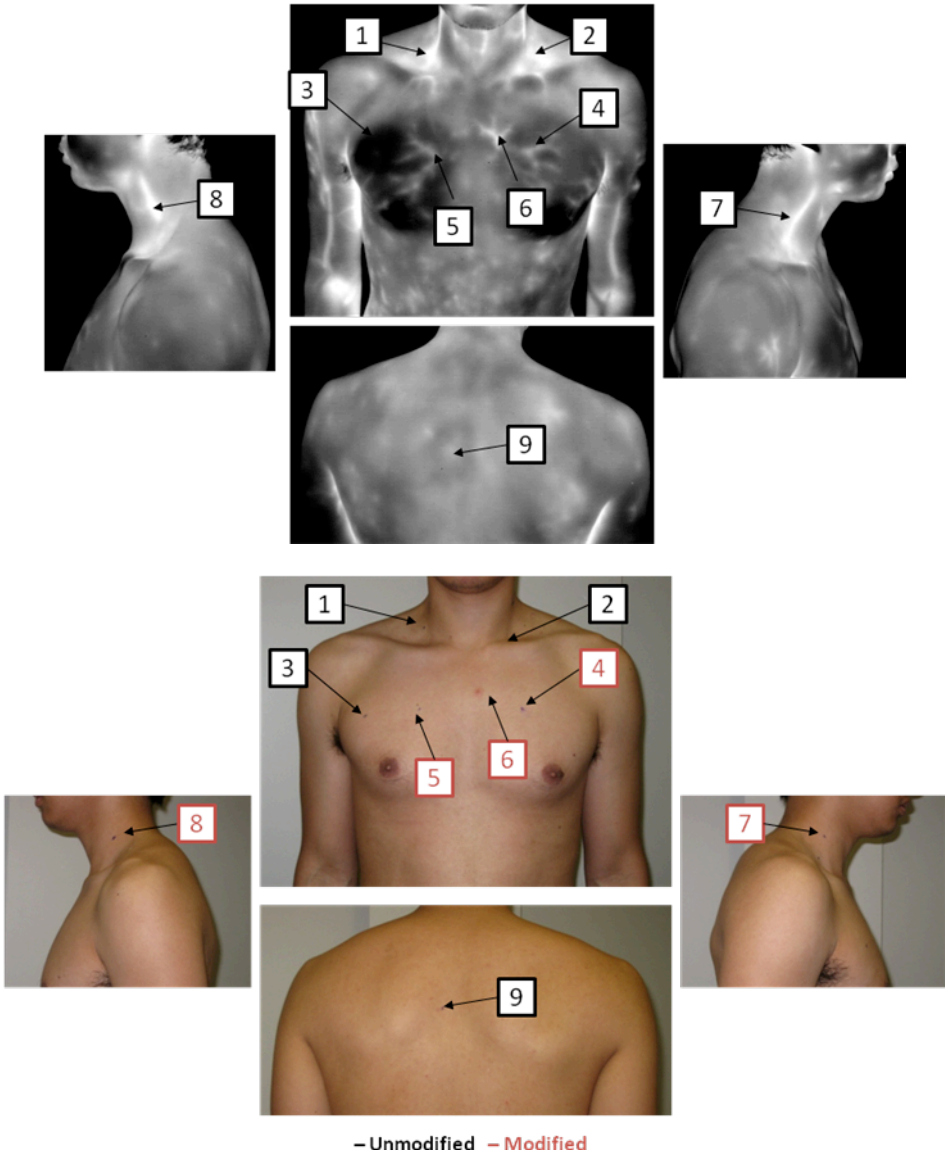

Figure A.25. Figure 26. Infrared image and photographic image of the subject's upper torso and the chosen regions of measurement

1


1
2
7/28 to 7/29: 1&2
Energy Bar
Temperature (Deg. C)
35
30
25
20
18:00
21:00
00:00
03:00
06:00
09:00
12:00
15:00
18:00
Time
1
2
Ambient
Food
Sleep
Shower
Exp

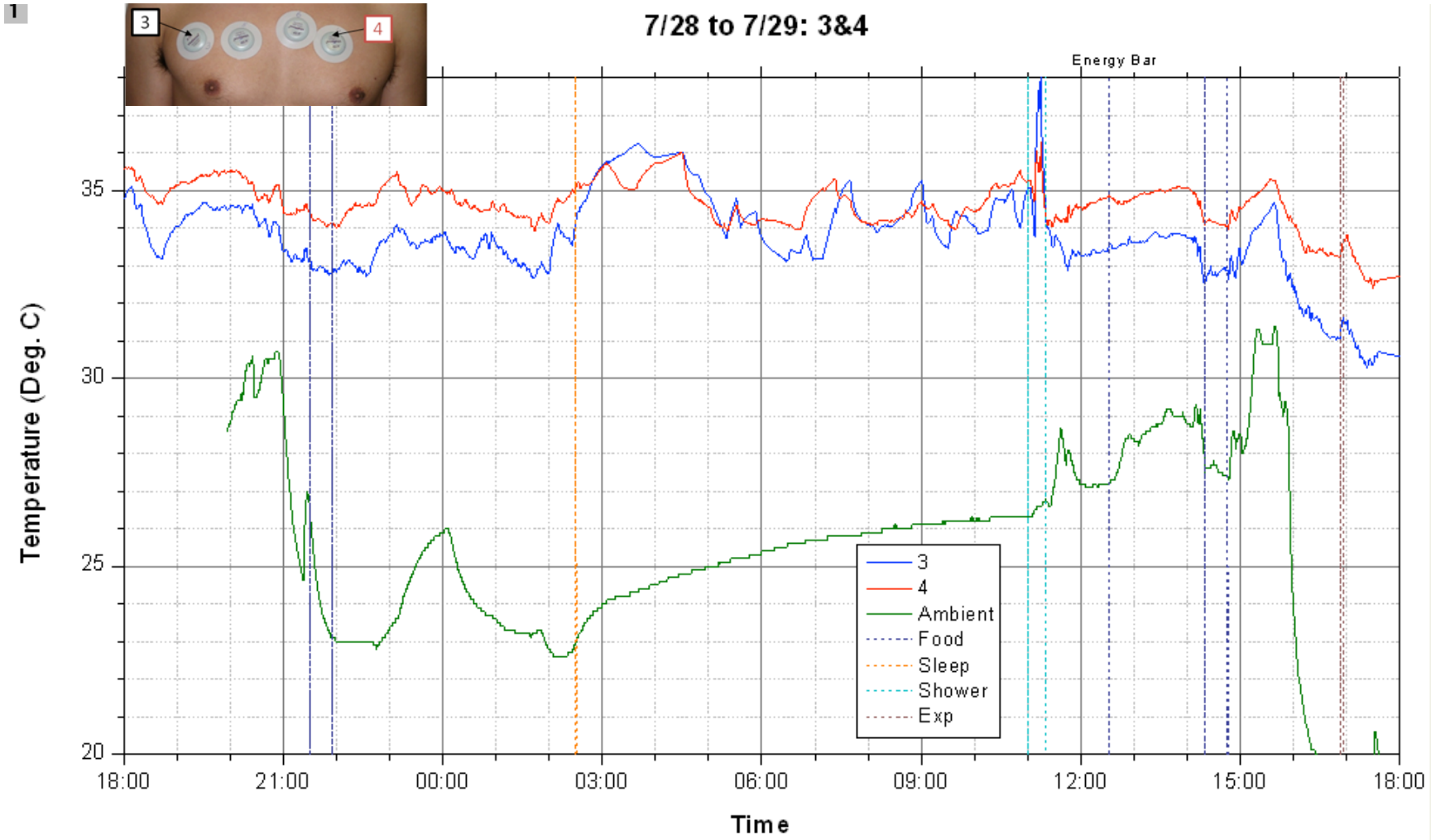
7/28 to 7/29: 3&4
Energy Bar
3
4
Temperature (Deg. C)
35
30
25
20
18:00
21:00
00:00
03:00
06:00
09:00
12:00
15:00
18:00
Time
3
4
Ambient
Food
Sleep
Shower
Exp

1

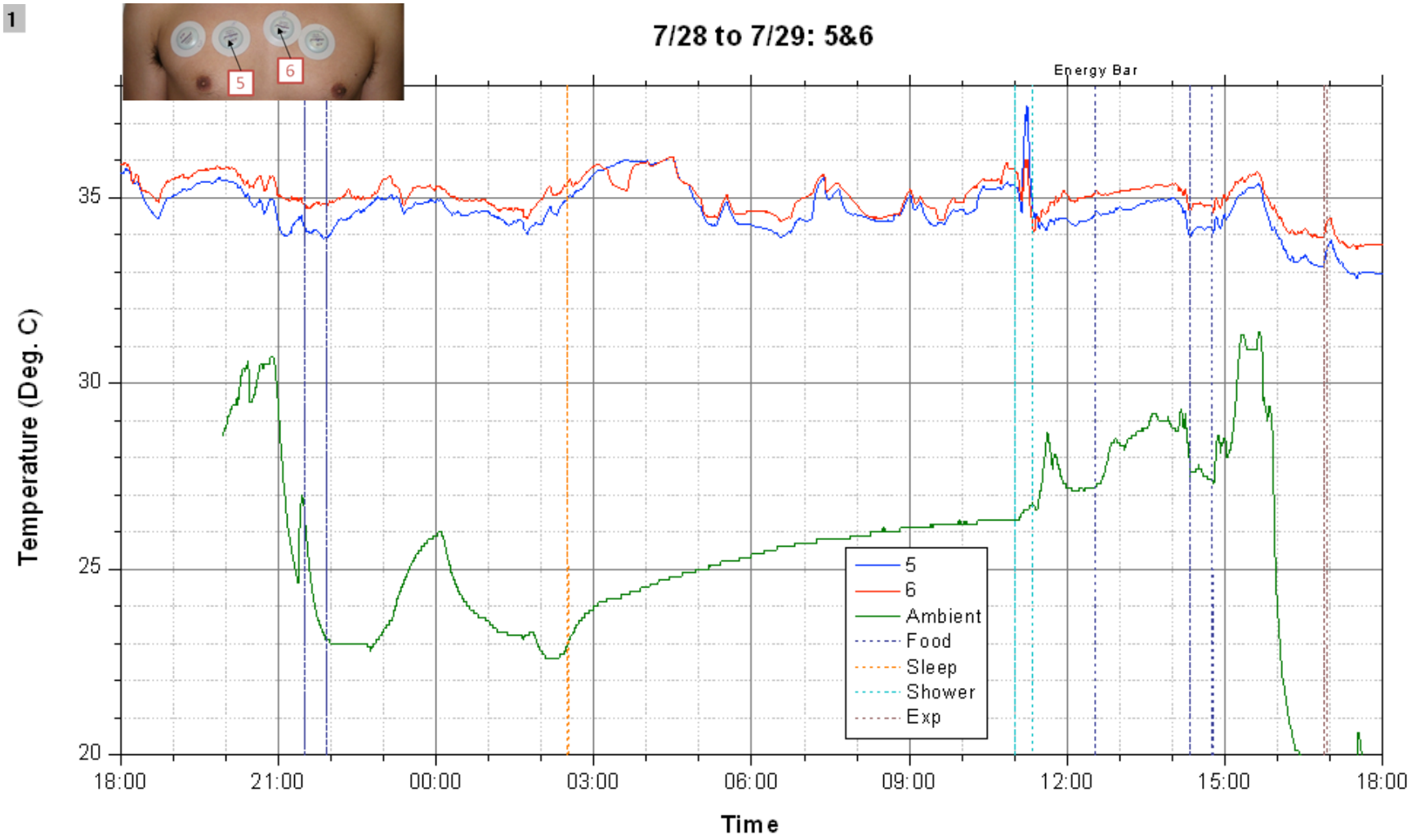
7/28 to 7/29: 5&6
Energy Bar
5
6
Temperature (Deg. C)
35
30
25
20
18:00
21:00
00:00
03:00
06:00
09:00
12:00
15:00
18:00
Time
5
6
Ambient
Food
Sleep
Shower
Exp

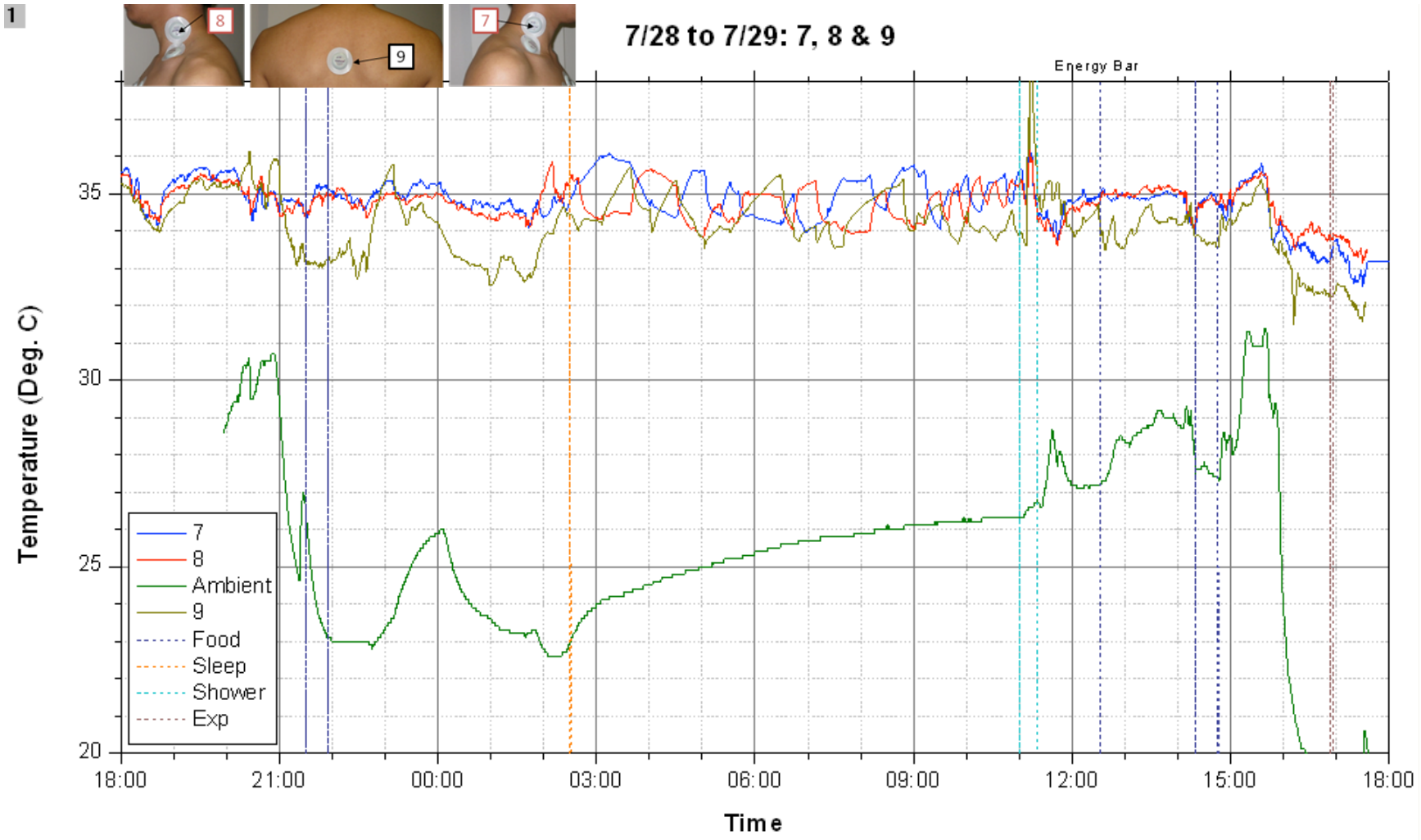

Figure A.26. (a-e). Time-lapsed temperature measurements from the 9 thermo-patches over a 24hr period

A.4.4.1. *Functional Testing: Cooling of Hands*

The functional test for cooling of hands described earlier was performed again on the following day to test repeatability. The subject placed both his hands individually in separate cold water baths for 2 minutes. The initial bath temperature was approximately 9.5°C. The figure below show the results of the temperatures during the functional test. The brown lines indicate markers for the start and stop of the experiments. The skin temperatures for each point are plotted on the same time scale for the test.

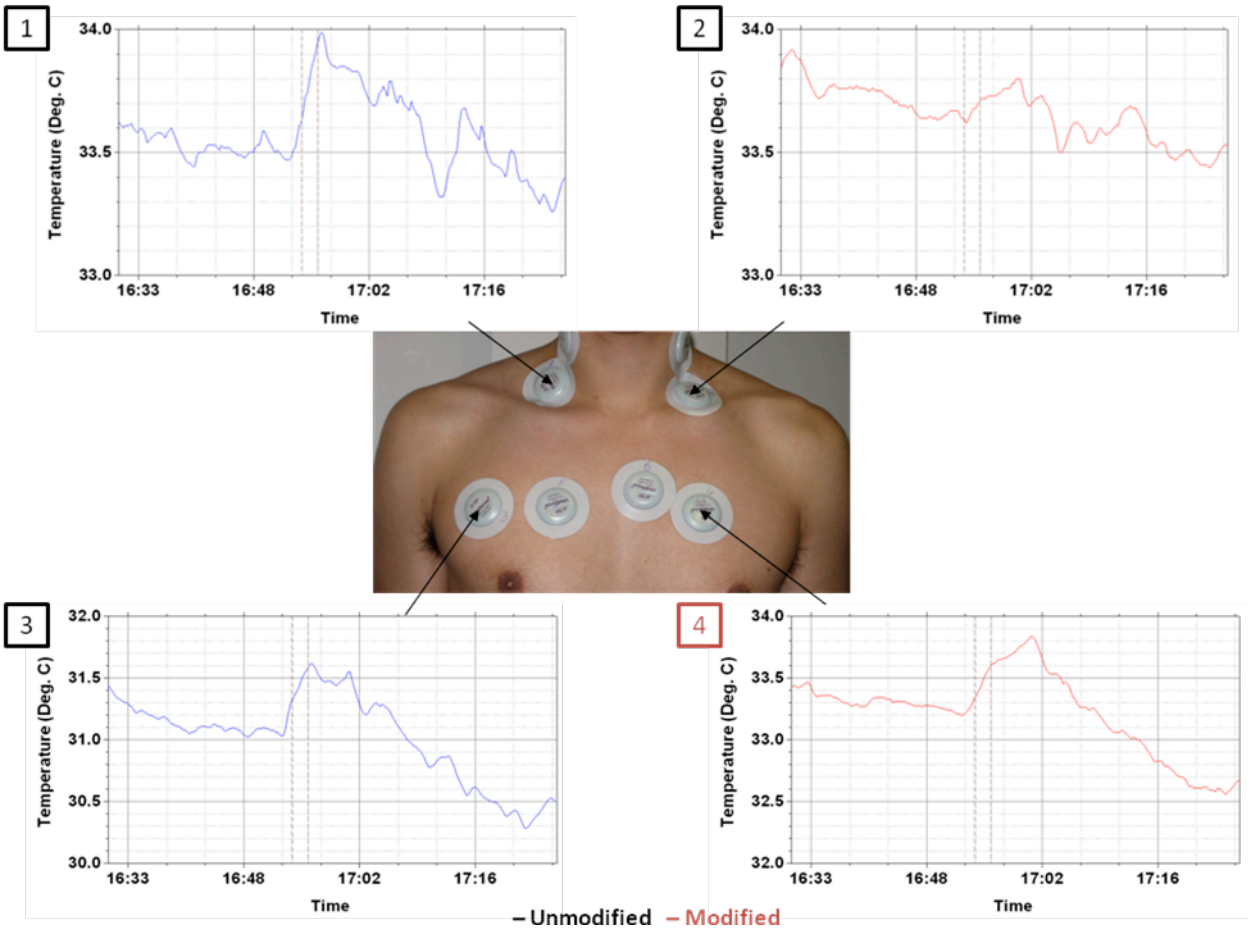

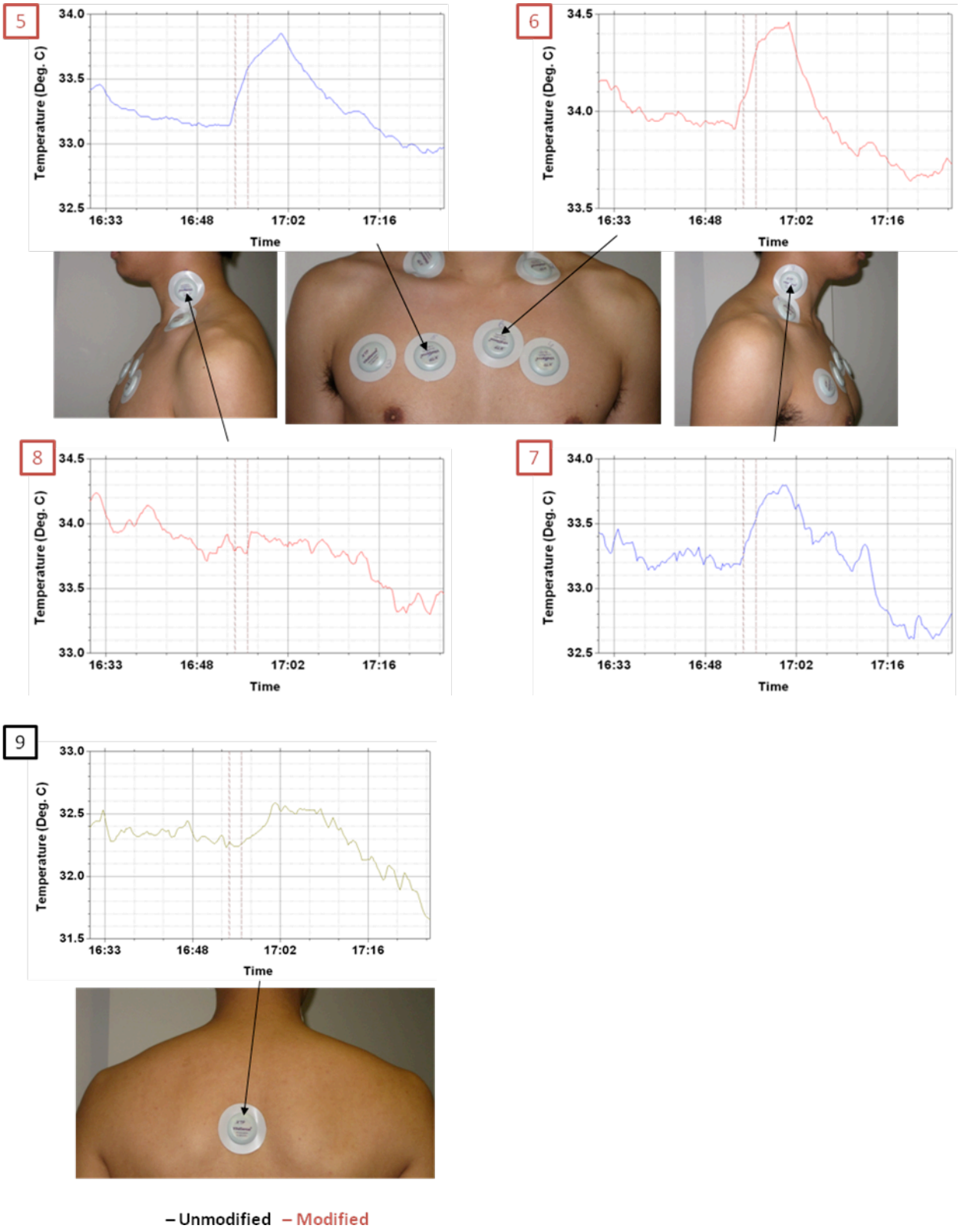

Figure A.27. Skin temperature measurements from the 9 thermo-patches from the repeated hand cooling experiment

A.4.4.2. *Effect of Glucose on Upper Torso Temperature*

To study the effect of glucose on brown fat response, the skin temperature was monitored using both temperature patches and IR imaging. In the first test using the 9 temperature patches, the subject consumed one chocolate PowerBar energy bar (PowerBar Performance: Chocolate, 240 Calories, 2.3 oz) while the 9 thermo-patches were used to monitor the temperatures. The room temperature was 27°C. Figure A.28 show the temperatures of various locations of the body before and after consumption of the energy bar. The dashed vertical line denotes the marker for the time of consumption (<1 min).

In the second test, the subject sat in a cold room (~17°C) while the temperature of his front upper torso was monitored via IR imaging. The subject first sat in the room for a 20-minute baseline measurement. Next, he consumed 6 small chocolate bars (Hershey's Milk Chocolate, 17.5 Calories, 0.13 oz each). The IR camera was directed to the front upper torso of the subject at a distance of ~2 meters, and continued to monitor the temperature of the subject before (20 min) and after (30 min) consumption. The acquisition rate for the IR camera was 2 Hz during the baseline and 0.1 Hz after consumption. The colors of the curves correspond to the colored locations in the infrared image. Figure A.29 shows the IR imaging measurements from the consumption of chocolate.

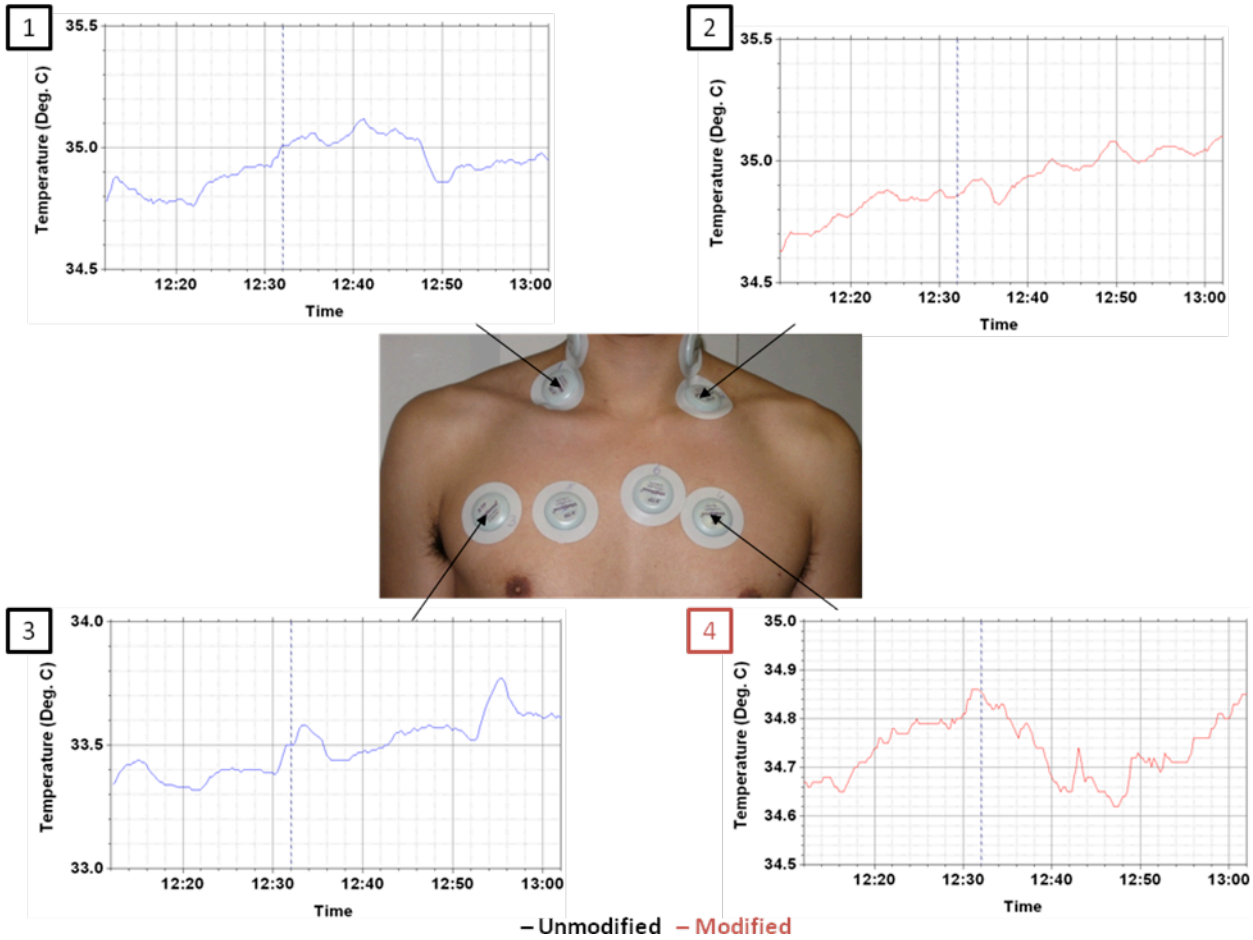

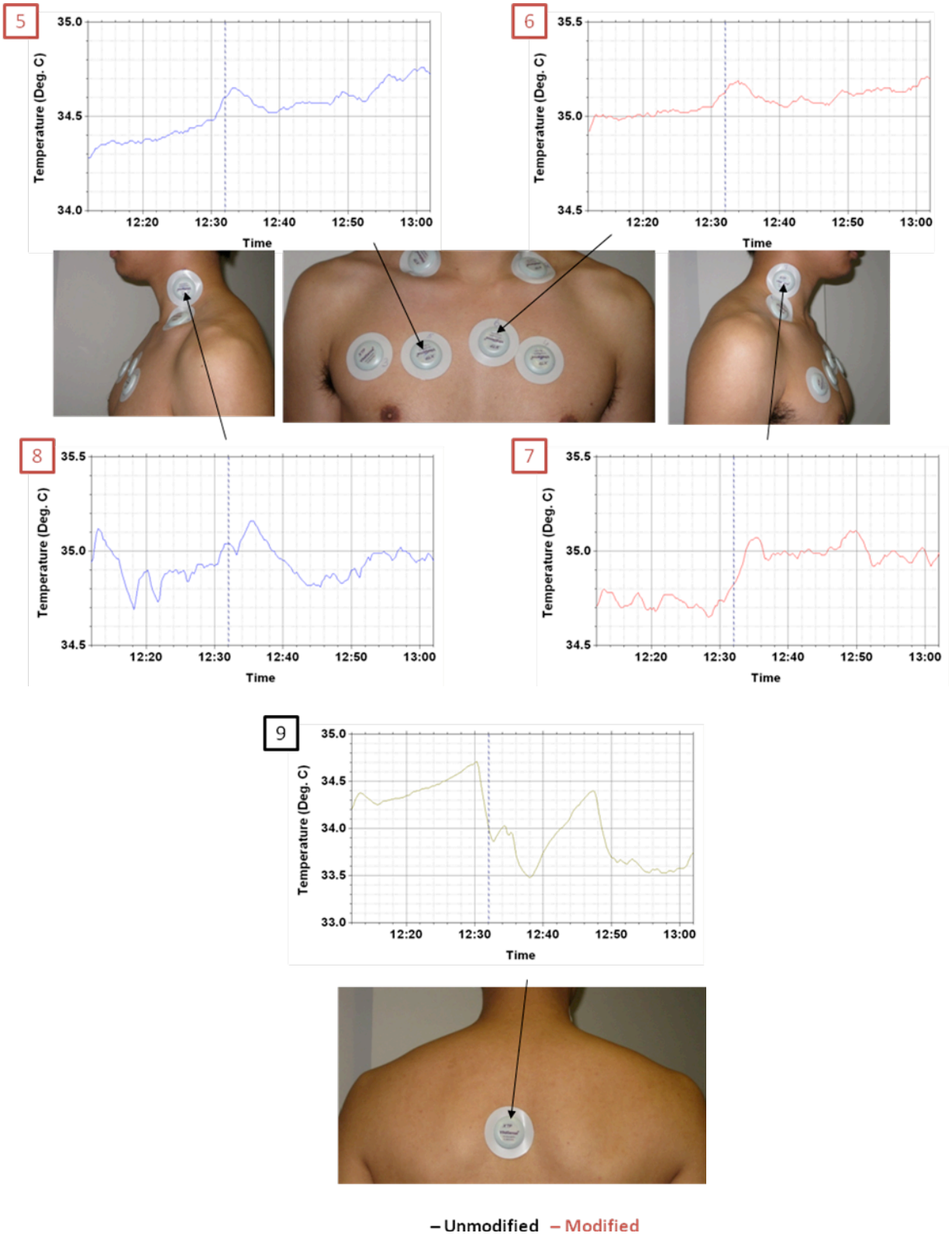

Figure A.28. Temperature measurements using the 9 thermo-patches during consumption of energy bar

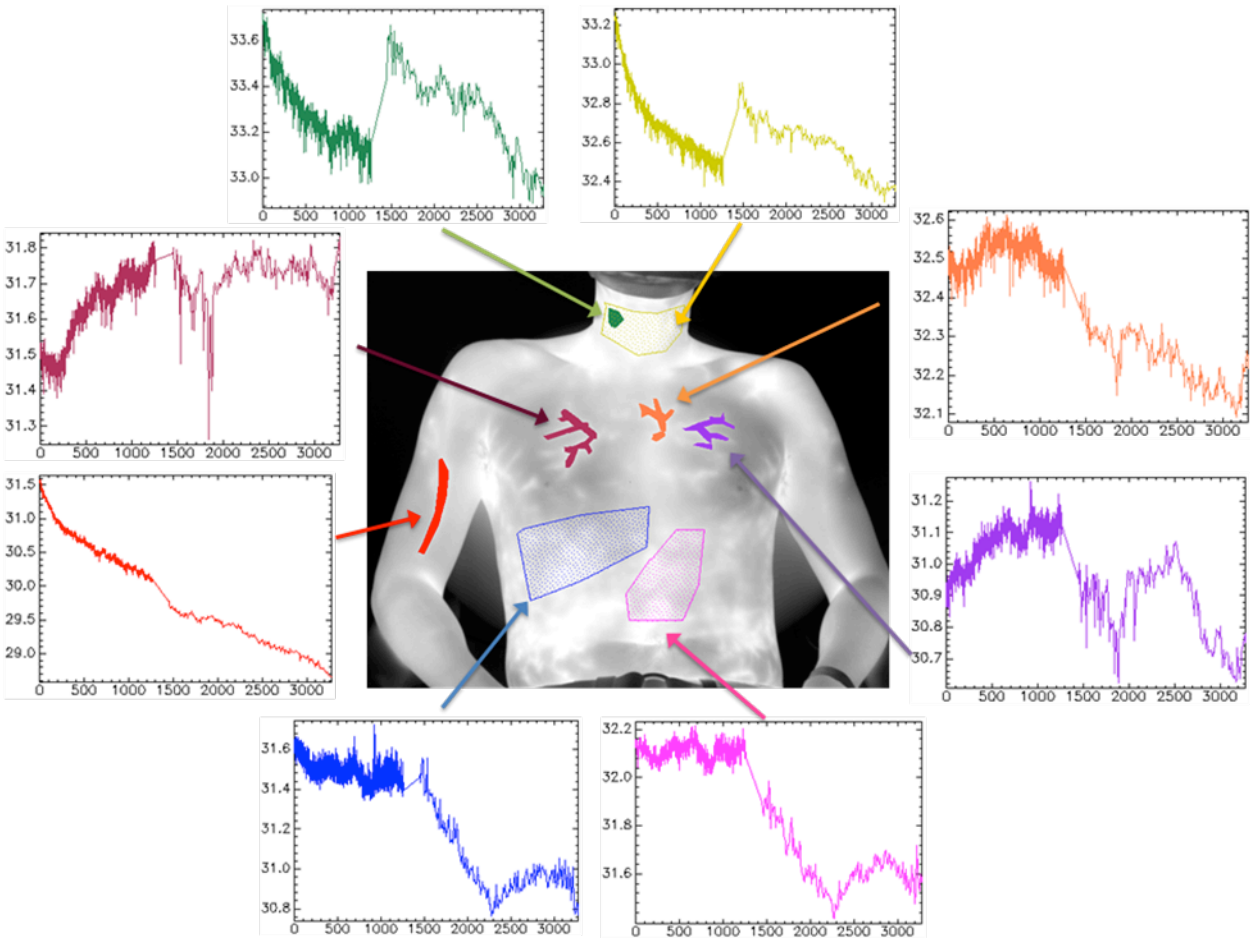

Figure A.29. IR Imaging measurement during consumption of chocolate and individual temperature profiles throughout the body

Appendix B

Passive Microwave Radiometry

B.1. Overview

This section describes some studies performed using passive microwave radiometry to determine its effectiveness in measuring sub-dermal tissue temperatures. Microwave radiometry is an attractive solution for non-invasive deep tissue temperature measurement [1-3]. However, due to the nascence of the technology, studies on its accuracy still need to be confirmed. In this section, pilot tests of the passive microwave radiometry for tissue temperature measurement are shown and discussed.

B.2. Background

To study sub-dermal temperature variations, a passive microwave radiometer (REM-01-RES) [4] was used to measure temperatures of various regions of the body. The passive microwave radiometer (MR) allows for measurement of radiometric temperature changes of living tissue. The device consists of:

(1) Microwave antenna for measuring tissue temperature (T_{rad})

(2) Infrared sensor for measuring skin temperature (T_{ir})

The deep tissue temperature (T_d) is then approximated using the following equation:

$$T_d = \frac{T_{rad} - T_{ir}\kappa}{(1-\kappa)} \tag{B.1}$$

Where κ (weighting coefficient) is assumed as 0.4.

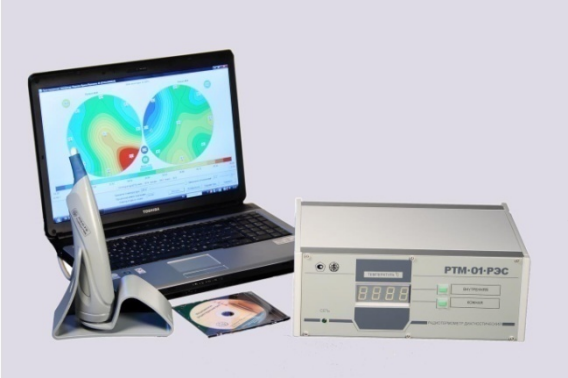

Figure B.1. Picture of the REM-01-RES Microwave Radiometer (RES, Ltd.).

B.3. Pilot Testing of Passive Microwave Radiometry (MR)

To study the reliability of passive microwave thermometry for measurement of radiometric temperature changes in human, 3 separate functional tests were performed to evaluate the device:

(1) Arm Occlusion (n=2, 3 experiments)

(2) Measurement of water temperature in mouth (n=3, 6 experiments)

(3) Clavicle/Neck response from hands cooling (n=2, 4 experiments)

All experiments performed in at 17-18°C room temperatures. The measured data was averaged for 15s intervals to make it comparable to data from the temperature patches (15s sampling rate). All experiments were started after 20 minutes adaptation period with patient reclining in a dental chair.

B.3.1. Pilot Test 1: Total Arm occlusion

In the first pilot test, the temperatures of the volar aspect of the right arms of the subjects (n=2) were monitored for 23 minutes during an arm occlusion test. An inflatable cuff was first placed on the subject's upper right arm. The temperature of the right inner forearm was then measured for a 10-minute baseline measurement. To ensure the stoppage of both arterial and venous blood flow, the cuff was inflated to 240 mm Hg and held for 3 minutes. This was followed by deflation of the cuff, while the temperature of the right inner forearm was measured for another 10 minutes. Figure B.2 shows the experimental setup.

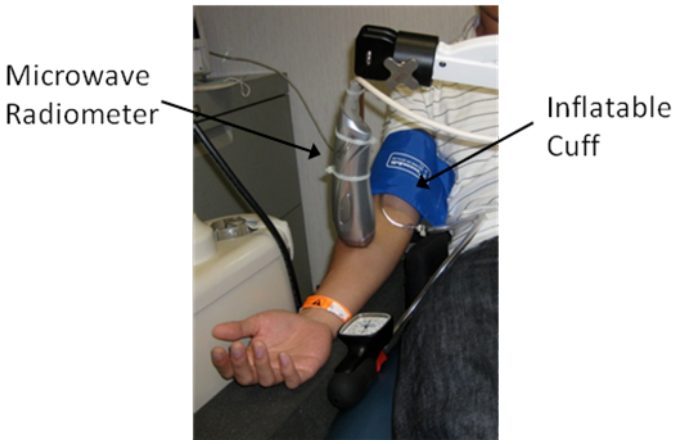

Figure B.2. Picture of the experimental setup for the arm occlusion test.

Figures B.3 & B.4 are the temperature measurements for the two subjects, where

- T_{ir} is the skin temperature measured using the infrared probe on the microwave radiometer
- T_{rad} is the measured radiometric temperature from the device
- T_{deep} is the calculated deep temperature using the values from T_{ir} and T_{rad} as described previously.

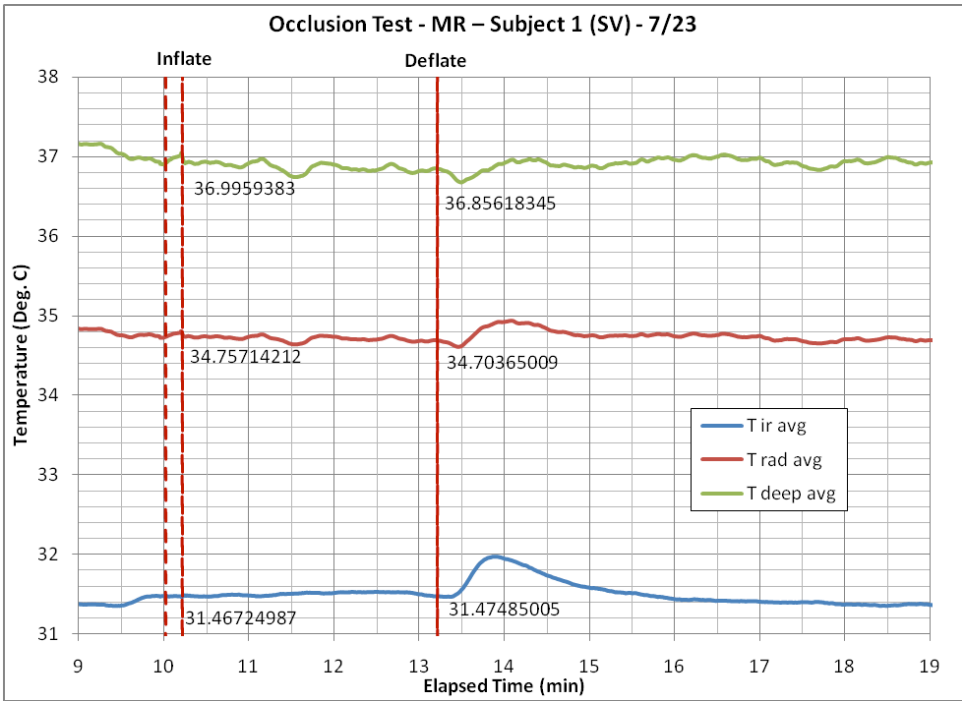

Figure B.3. MR measurements for subject 1 during the arm occlusion test.

No specific trends were found during the total arm occlusion of Subject 1. However, a temperature rebound after the cuff was released occurred, suggesting a reperfusion of blood flow to the skin surface. The lack of trends found during the occlusion may have been due to a leak in the cuff when the pressure dropped from 240 mm Hg to 180 mm Hg during the test. Thus the results suggest that only a partial occlusion occurred during the test.

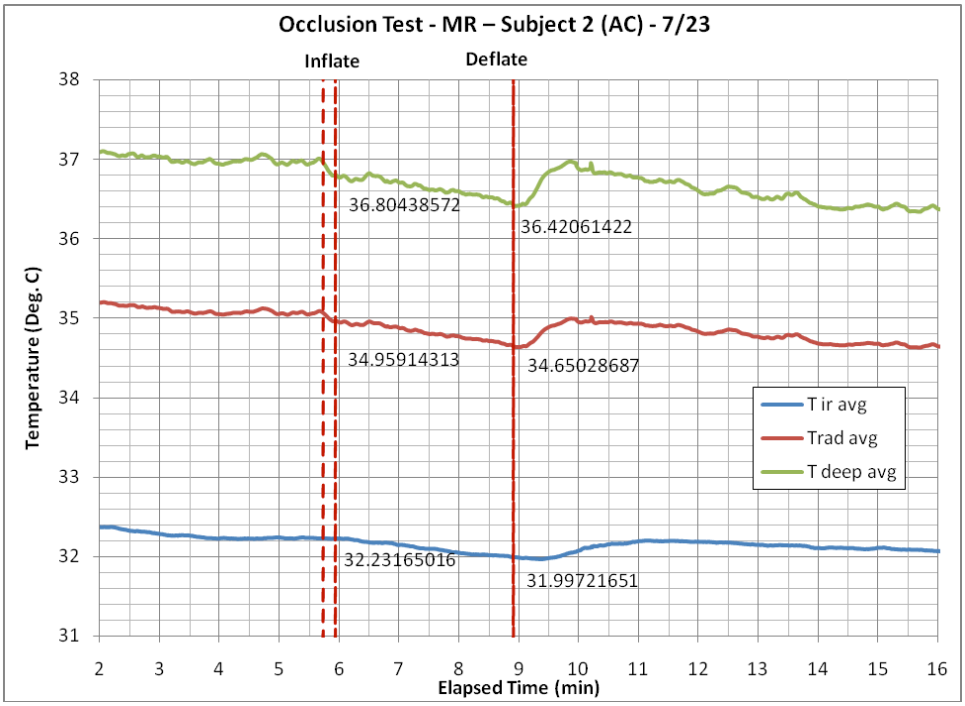

Figure B.4. MR measurements for subject 2 during the arm occlusion test.

A decline in the temperatures during this experiment was clearly seen, followed by a rebound in the temperature after the cuff was deflated.

B.3.2. Pilot test 2: Measuring water Temperature in the mouth through Cheek

In the second pilot test, the temperature of water while held in the mouth of the subject was measured using the microwave radiometer. The microwave radiometer was placed at the right cheek of the subjects (n=3) for 20 minutes during the test. A 5-minute baseline measurement was first conducted. The subject then sipped cold water (7-8°C) and held the water in the right side of his mouth for 5 minutes (Figure 5). The subject then moved the water to the left side of his mouth and held the water for another 5 minutes. Finally, the subject spit out the water and another 5-minute baseline was measured. This test was repeated again using warm water (48°C) Figure 5 shows the image of the experimental setup. Subjects 1, 2 & 3 had cheek thicknesses of approximately 2 cm, 1 cm & 1 cm, respectively.

Figure B.5. Experimental setup for the measurement of water temperature in the mouth

B.3.2.1. *Measurement of the Cold Water temperature in the mouth Through Cheek*

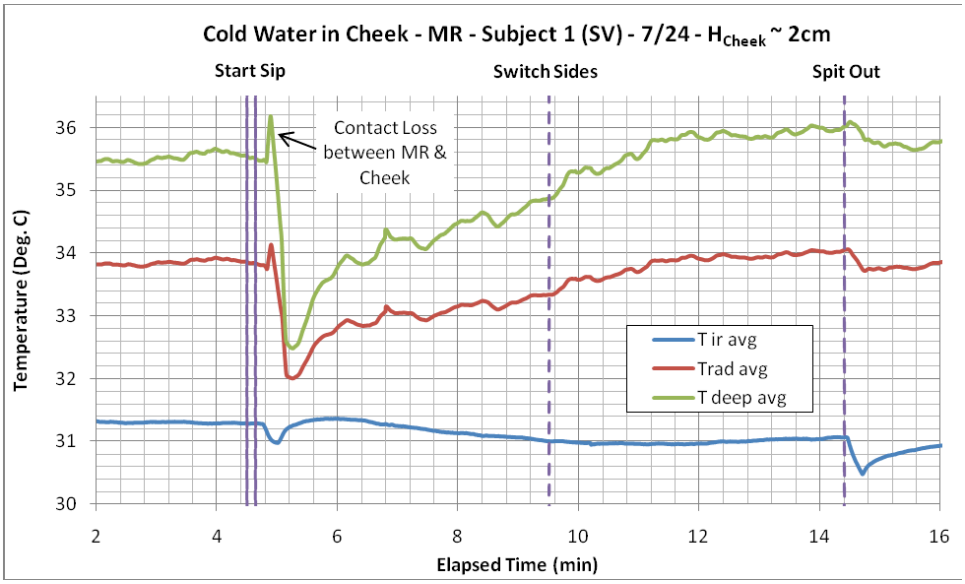

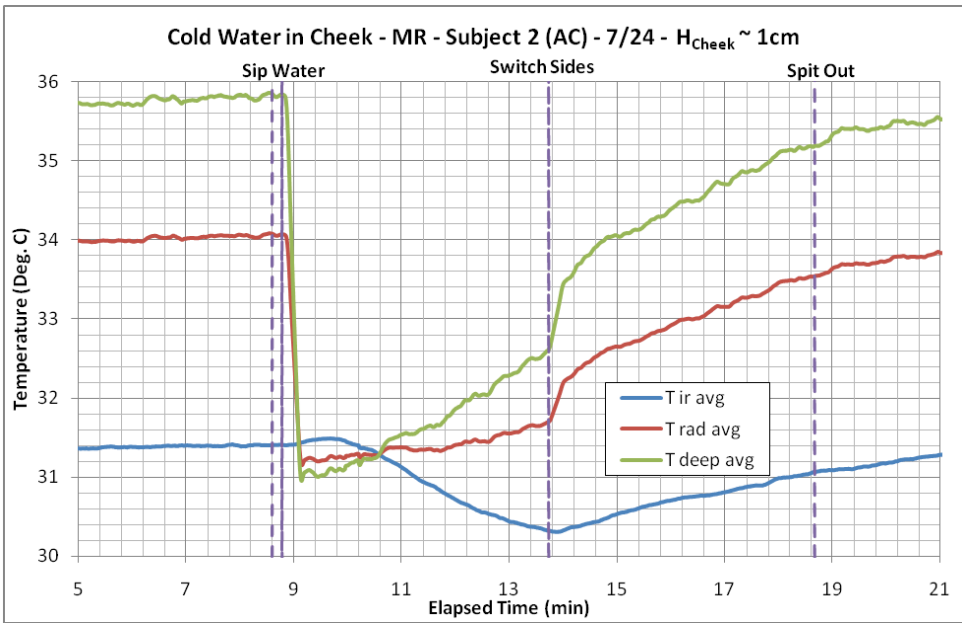

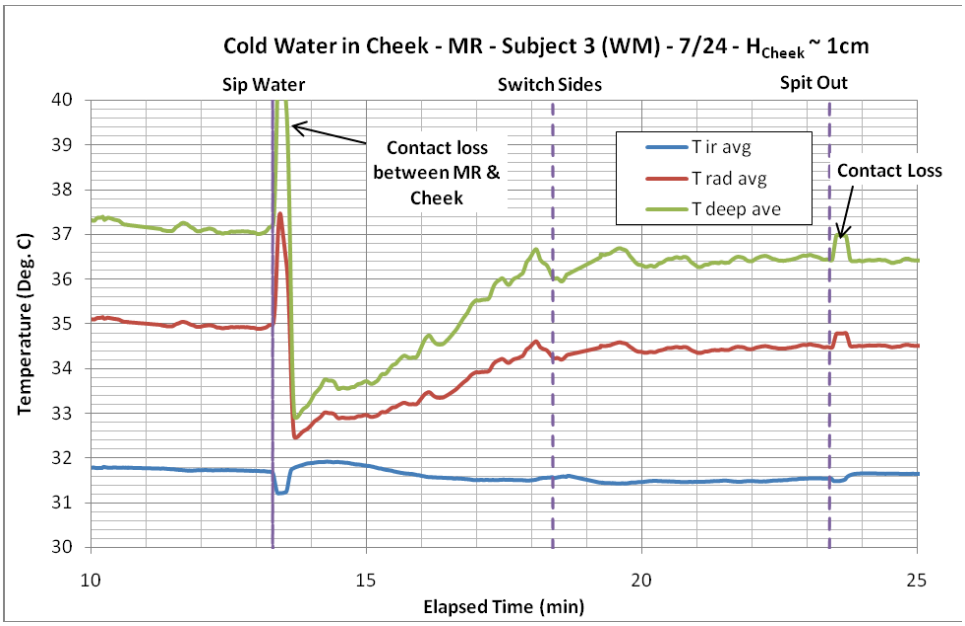

Figure B.6. (a-c) Measured temperature of cold water in cheek of all 3 subjects.

All three subjects' skin temperature (T_{ir}) slowly decreased while the cold water was held in the mouth. The radiometric temperatures (T_{rad}) of the subjects also decreased, but much faster and had a much larger drop in temperature compared to the T_{ir}. The initial decrease in T_{rad} was followed by a slow increase while T_{ir} was still decreasing. This showed that the internal temperature had a much more pronounced temperature drop from the cold water held in the mouth. The data correlates with the general perception that the cold water passively cools the internal temperature of the mouth. As the water begins to heat up, T_{rad} begins to increase towards the baseline temperature. When the subjects moved the water to the left side of their mouth, T_{rad} of the right cheek continued to increase. Subjects had a much more rapid increase when the water was moved from the right cheek to the left cheek, compared to the other two subjects. The magnitude of the temperature decrease varied among subjects and was likely due to various conditions including amount of water sipped, cheek thickness and measurement location.

B.3.2.2. *Measurement of the Warm Water temperature in the mouth Through Cheek*

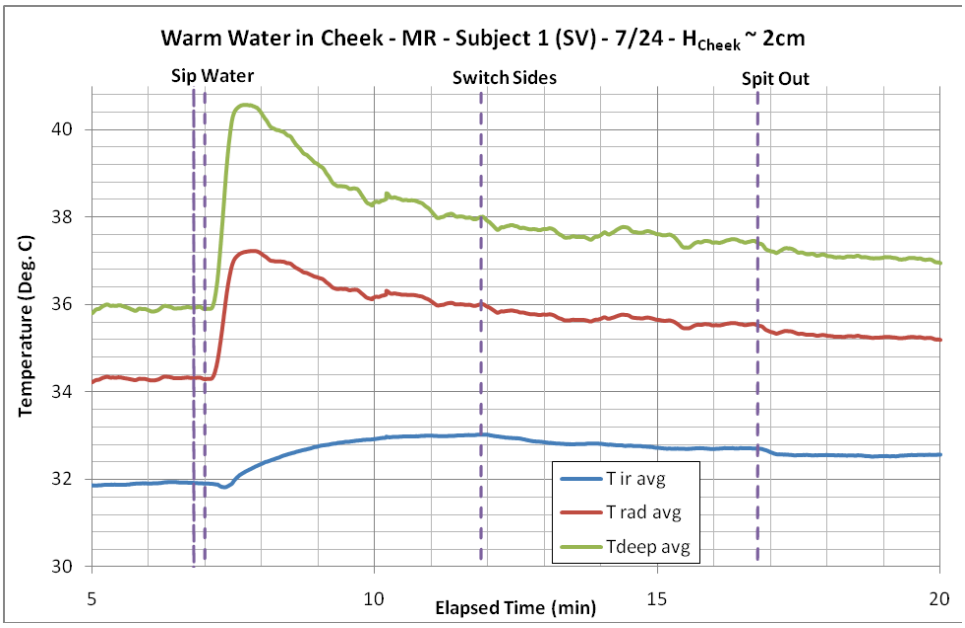

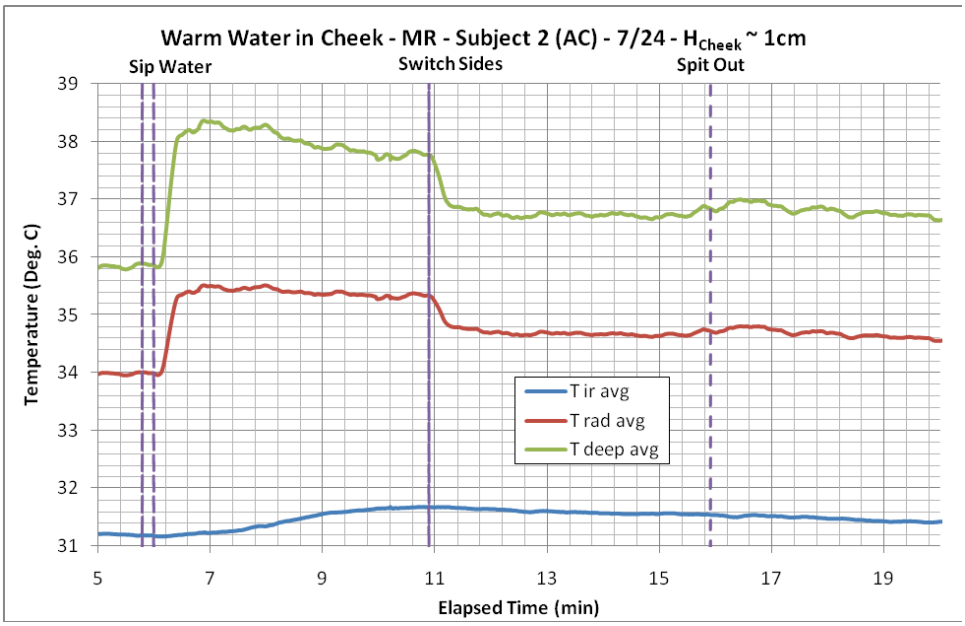

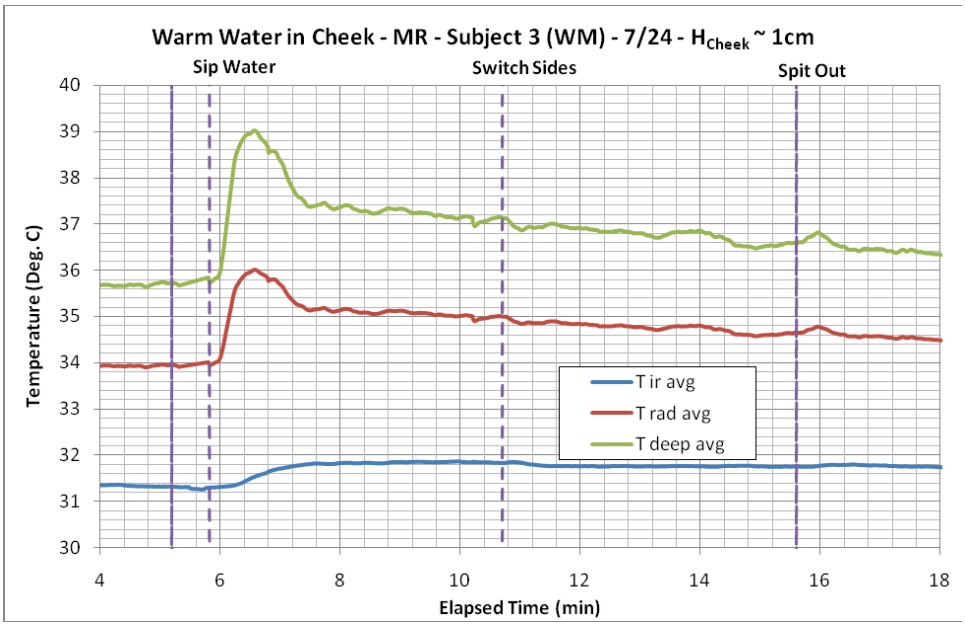

Figure B.7. (a-c) Measured temperature of warm water in cheek of all 3 subjects.

In the case of the warm water test, T_{ir} of all three subjects slowly increased while the warm water was held in the mouth. Similarly to the test using cold water, T_{rad} of all three subjects showed a much higher and faster increase in temperature, followed by a slow decrease while the water was held in the right cheeks of the subjects. Again, this showed that the T_{rad} had a much more pronounced temperature change from the liquid in the mouth. When the subjects moved the water to the left side of their mouth, all temperatures of the subjects' right cheeks continued to decrease. Again, Subject 2 had a faster rate of decrease in temperature when the water was moved from the right side of the mouth to the left side of the mouth. The magnitude of the temperature changes varied among subjects and was likely due to various conditions including amount of water sipped, cheek thickness and measurement location. All collected data were consistent with general perception of water in the mouth during drinking of water.

B.3.3. Pilot test 3: Clavicle/neck temperature – Cooling of Hands

The purpose of the third pilot test was to study the brown-fat response from placing hands in cold water. Previous studies using infrared imaging showed a temperature increase in the neck/clavicle areas when subjects' hands are cooled. In this pilot test, the brown fat response was studied using microwave radiometry. IR imaging was used for the placement of the MR sensor.

The temperature of the clavicle/neck areas was measured using the microwave radiometer while the subjects' hands were placed in cold water. The microwave radiometer measured the right upper-neck of 1 subject and the left clavicle of same subject twice for a period of 22 minutes each. The test began with a 10-minute baseline measurement of the neck/clavicle region. The subject then placed his hands individually into two cold-water baths (~5°C), and held his hands in the baths for 2 minutes. The subject then removed his hands from the baths and quickly dried them using paper towels. The temperature of the neck/clavicle was then measured for another 10 minutes. Figure B.7 shows the image of the experimental setup.

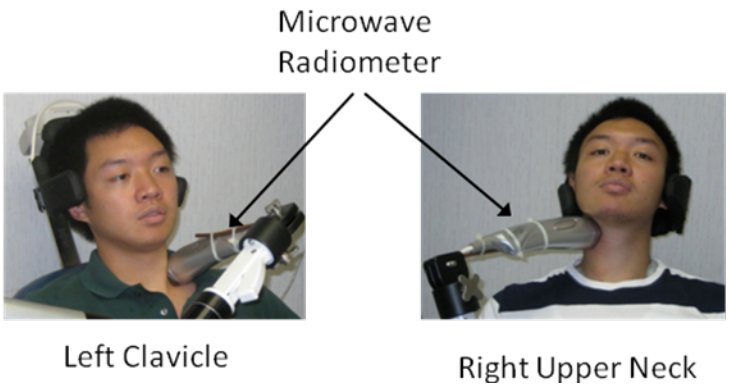

Figure B.8. Experimental setup for the measurement of clavicle/neck response to hands placed in cold water during 2 min.

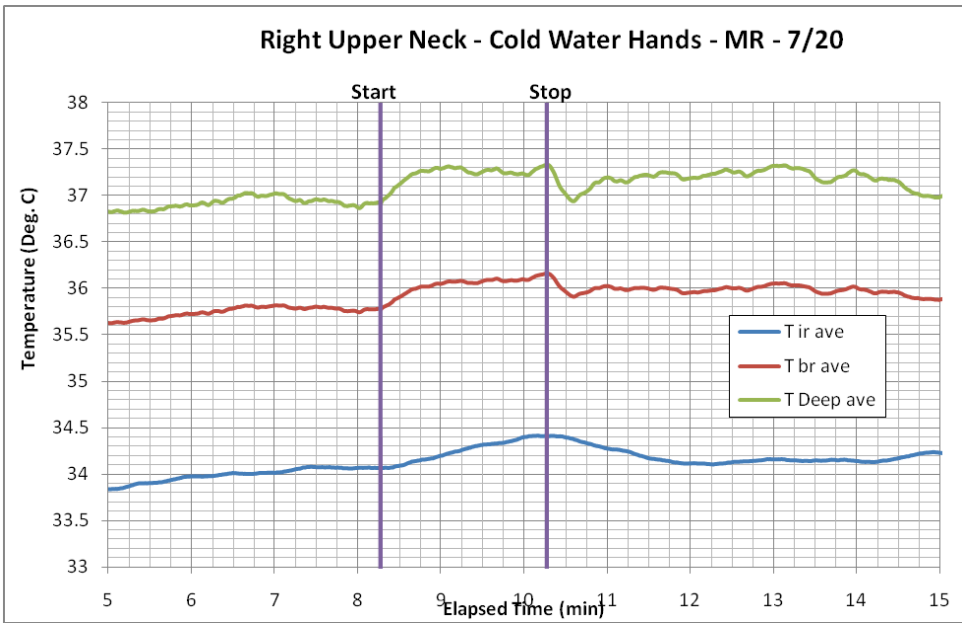

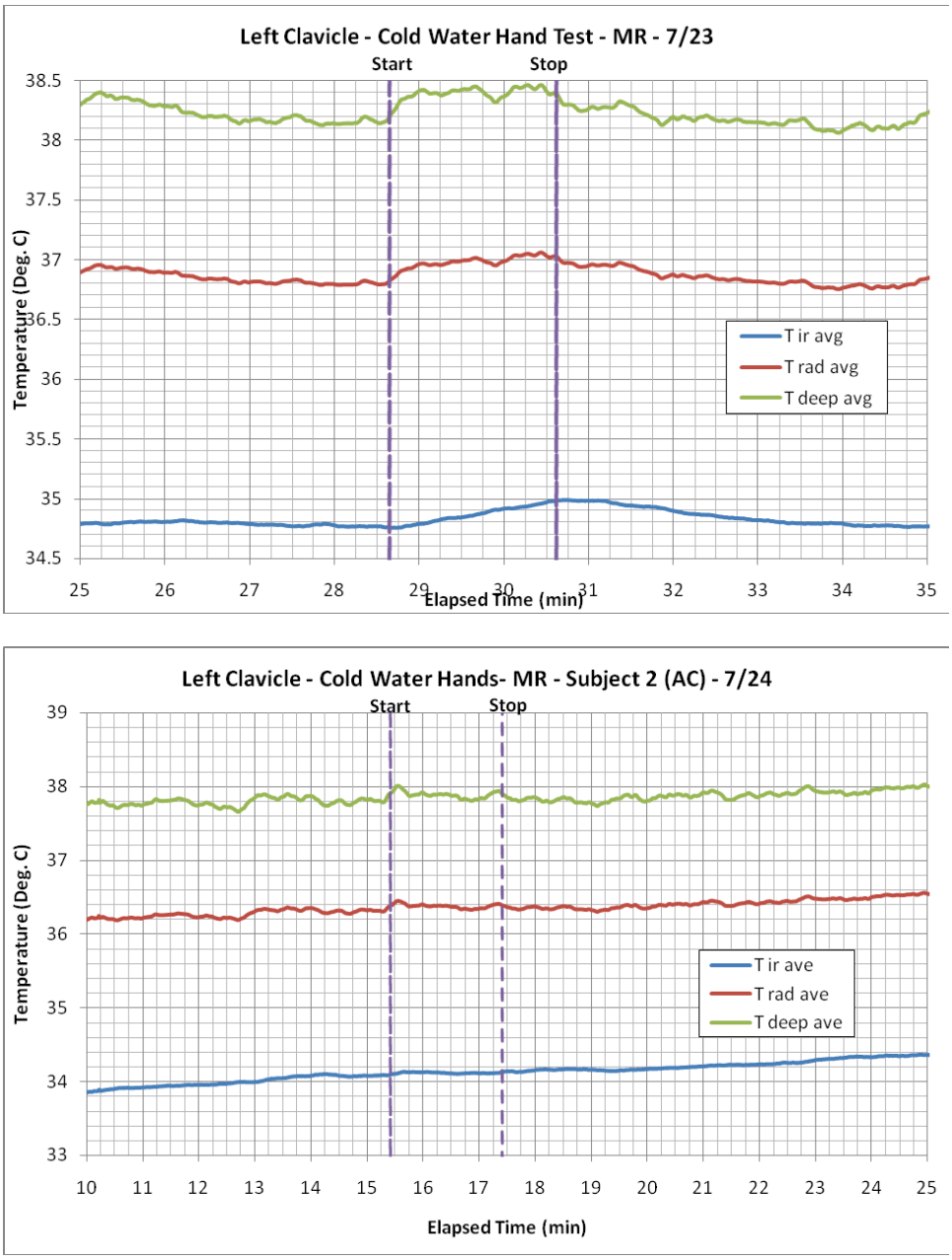

Figure B.9. (a-c) Measured temperature of the clavicle response to hands placed in cold water

The results of this test varied and the brown-fat response from cooling of hands was unclear. In the first test where the temperature of the subject's right upper neck was measured, the skin temperature increased during the cooling of the hands followed by a decrease after the hands were removed from the water baths. The radiometric temperature has a similar increase in temperature, suggesting that the internal temperature was increasing too. In the second test where the left clavicle was measured, the skin temperature increased during the cooling of the hands, and the radiometric temperature also showed a similar increase in temperature. However, in both cases, the temperature changes were not significant and the brown-fat response could not be accurately quantified. The second test was performed again on the different day for repeatability;

however, no response occurred during the final test. Thus, the results of this test proved to a inconclusive in terms of measuring brown fat response, and further work needs to be performed.

B.3.4. Comparison of Microwave radiometry with Thermopatch Measurements

The measured temperatures for two functional tests using the microwave radiometer were compared against temperature measurements using the VitalSense temperature patch. Two of the previously described studies, (1) clavicle/neck temperature response to hands in cold water and (2) arm occlusion, were compared against the measurements on the same subject & locations under similar conditions using the VitalSense temperature modified patch (see Appendix A for description). Since the VitalSense temperature patch measures the skin temperature, it provides a good reference for comparing the measured skin temperature using the infrared probe on the microwave radiometer.

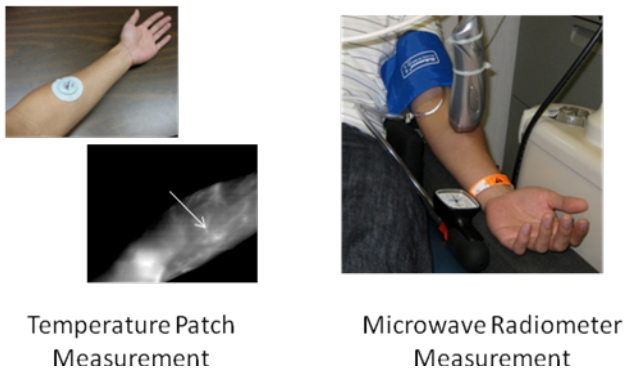

Figure B.10. Experimental setup for comparing the tissue temperature at the inner forearm during occlusion from the temperature patch and microwave radiometer.

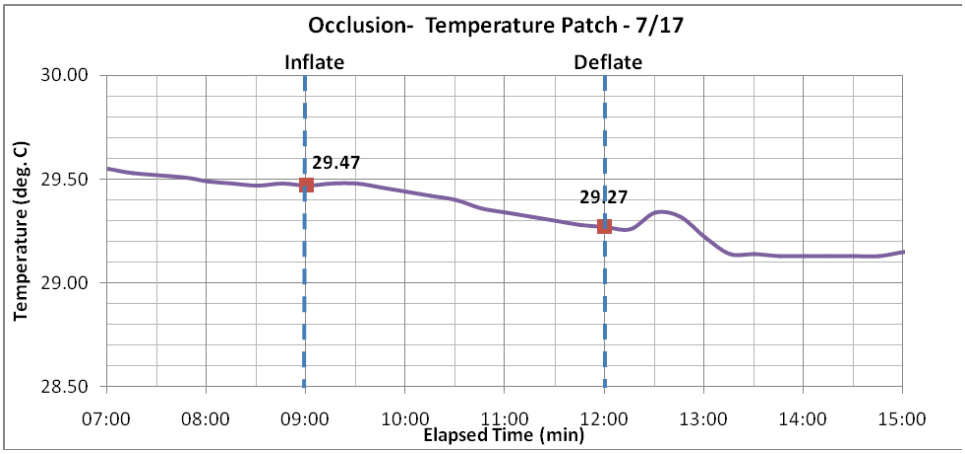

Figure B.11. Skin temperature of the forearm measured with the temperature patch during occlusion.

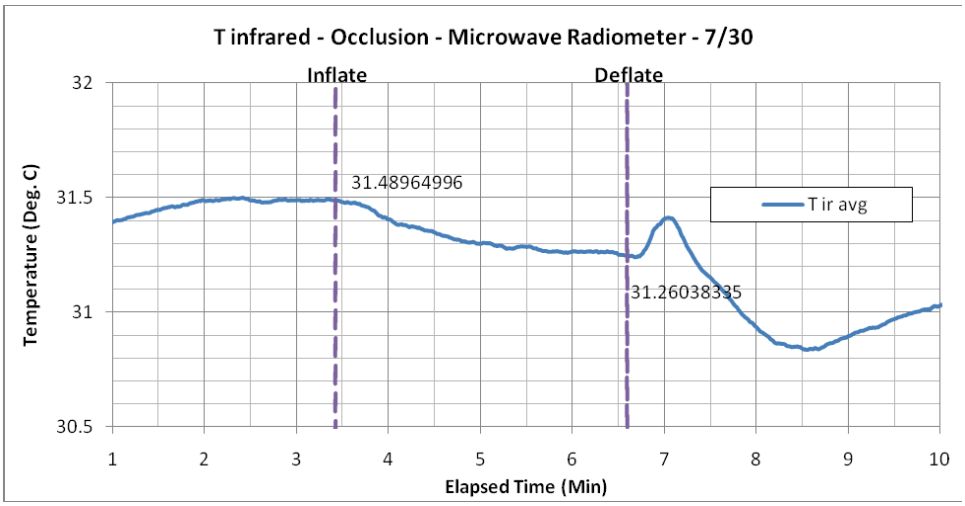

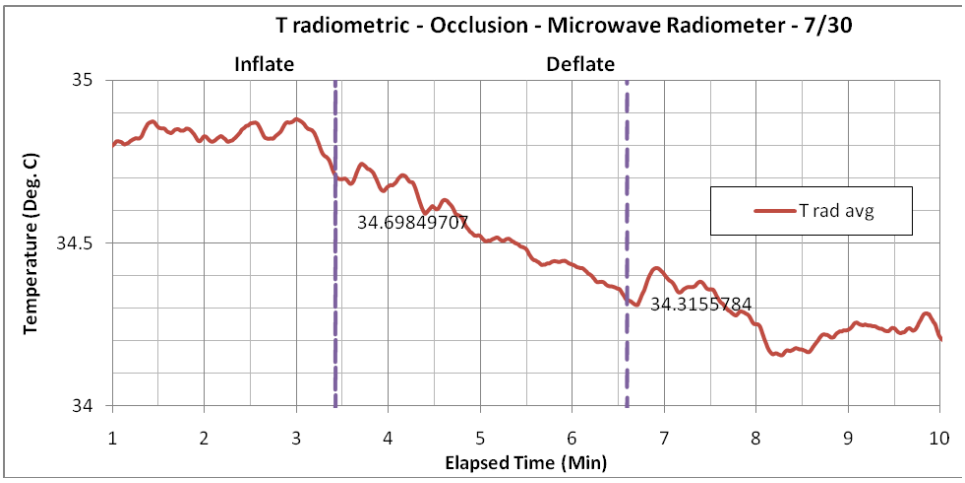

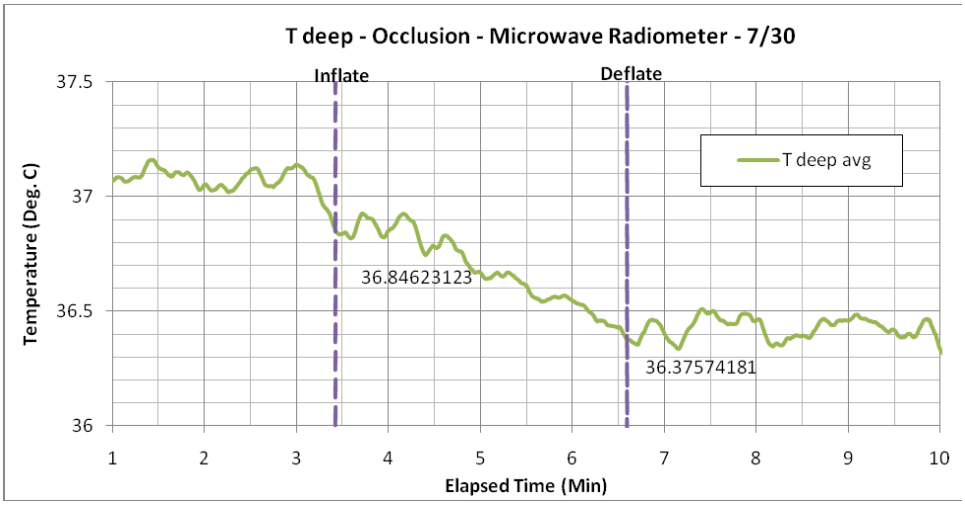

Figure B.12. Infrared, radiometric and deep temperatures of the forearm measured using microwave radiometry during occlusion

The results of the test suggest that the skin temperature during occlusion can be accurately detected using both the temperature patch and the microwave radiometer. The change in skin

temperature was the same in both methods during occlusion. However, a temperature drop after the experiment was more pronounced with the microwave radiometer. The effect may be due to experimental error from movement of the radiometer. Since the patch conforms to the skin, any movement would result in less error. The radiometric and deep tissue temperature show a similar drop in temperature during occlusion. However, these changes in temperature cannot be verified using the temperature patch.

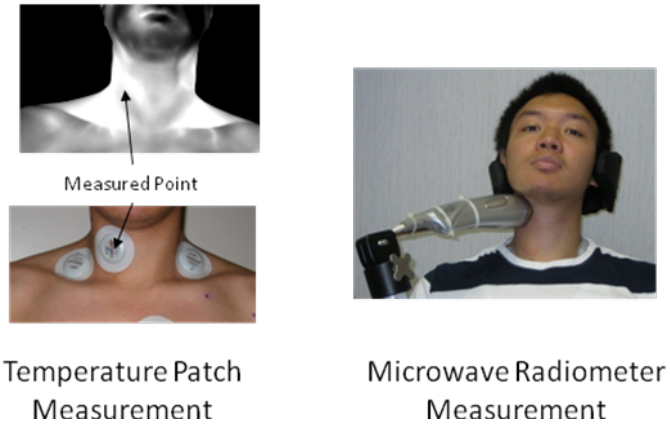

Figure B.13. Experimental setup for comparing the tissue temperature at the clavicle during immersion of hands in cold water from the temperature patch and microwave radiometer.

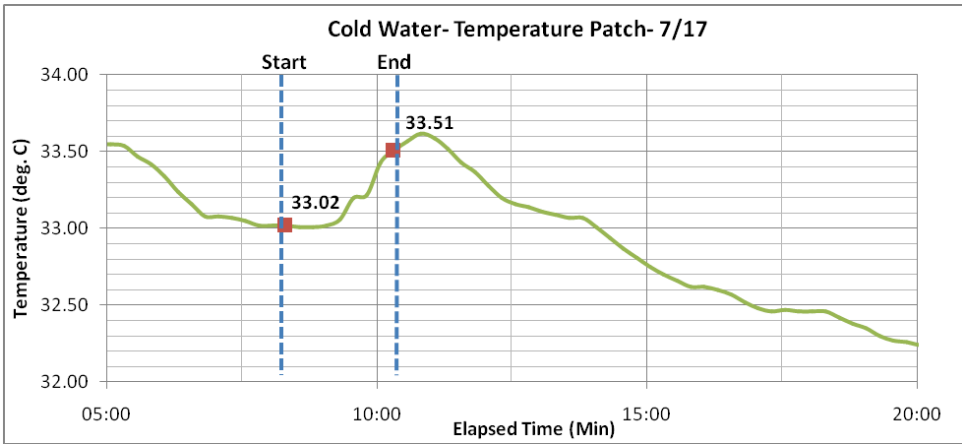

Figure B.14. Skin temperature of the clavicle measured with the temperature patch during immersion of hands in cold water.

Figures B.13 and B.14 show the results from the second functional test. The results from the second functional test were similar to that of the previous test. Skin temperature measurements correlated with each other, during the test. However, a continued decrease in temperature was measured from the temperature patch after the experiment while the microwave radiometer showed a more constant temperature. The results are likely due to localized heating from the microwave radiometer during measurement. However, all three measurements from the microwave radiometer showed a consistent increase in temperature during the experiment.

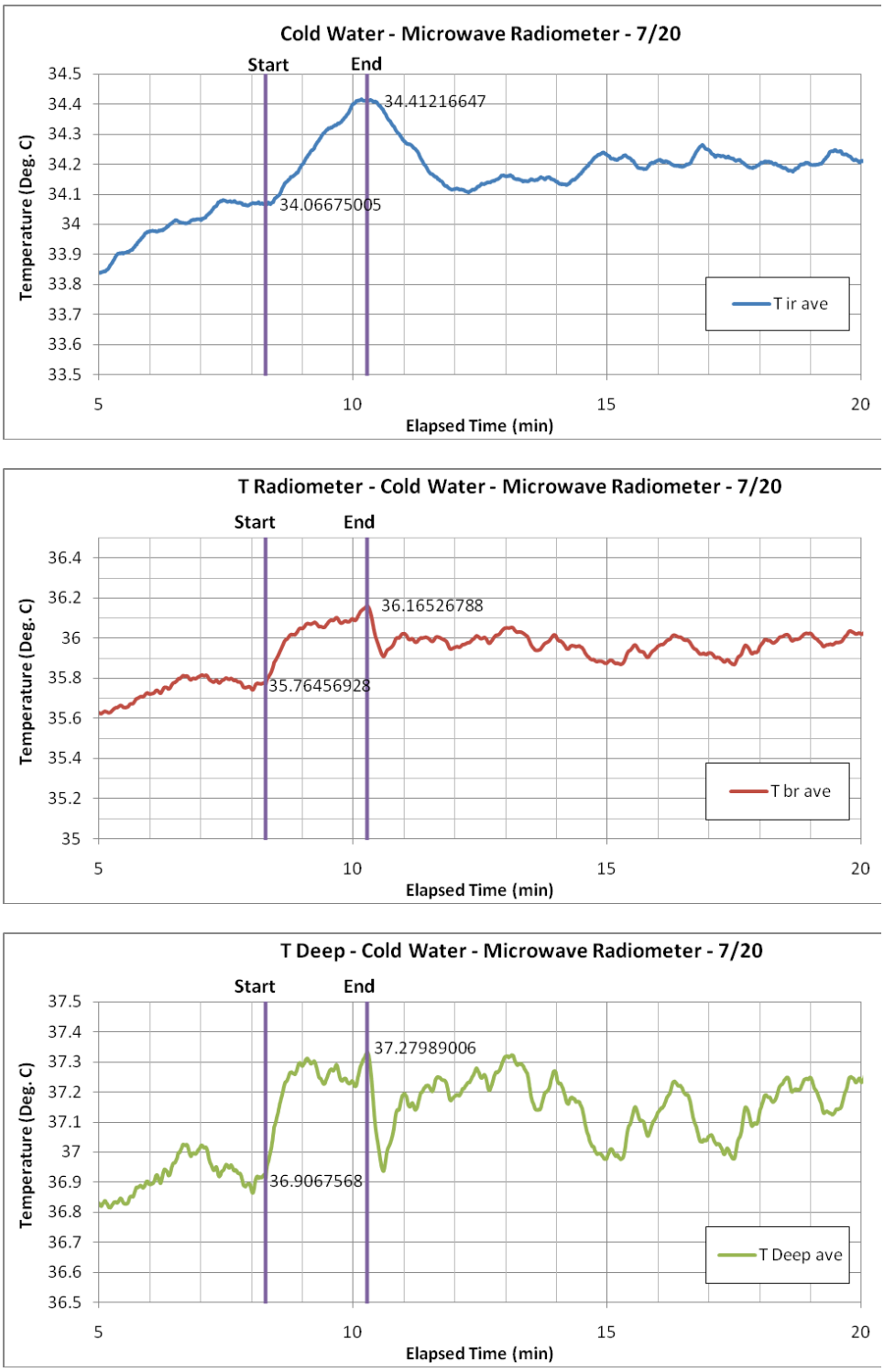

Figure B.15. Infrared, radiometric and deep temperatures of the forearm measured using microwave radiometry during immersion of hands in cold water.

Appendix References

[1] E. A. Cheever and K. R. Foster, “Microwave radiometry in living tissue: what does it measure?,” *Biomedical Engineering*, 1992.

[2] Y. Leroy and B. Bocquet, “Non-invasive microwave radiometry thermometry,” *Physiological measurement*, vol. 19, pp. 127–148, 1998.

[3] B. Enander and G. Larson, “Microwave radiometric measurements of the temperature inside a body,” *Electronics Letters*, vol. 10, no. 15, pp. 317–317, 1974.

[4] “RES, Ltd. Microwave Radiometry,” *resltd.ru*. [Online]. Available: http://www.resltd.ru/eng/radiometry/. [Accessed: 12-Sep.-2011].

Appendix C

Materials Testing & Characterization Tools

C.1. Overview

This section discusses some of the materials testing and characterization tools used for characterizing the printable composite thermoelectric materials.

C.2. Seebeck & Electrical Conductivity Measurement

Seebeck and electrical conductivity measurements were conducted using a custom automated measurement system. Figure C.1 shows the schematic of the measurement system. The setup consists of:

- One (1) Agilent 348970A Multiplexer (DAQ/Switch Unit)
- Two (2) Agilent E3631A Agilent E3631A 80W Triple Output Power Supply (6V, 5A & ±25V, 1A)
- One (1) Hart Scientific 1529 CHUB E-4 Digital Thermometer
- Two (2) Thermoelectric modules (Ferrotec 9501/017/030 B, 11.5mm x 11.5mm, 3.0A max)
- Two (2) Omega T-Type Thermocouples: 5SRTC-TT-T-40-36

This setup allows for simultaneous measurements of the electrical conductivity and Seebeck coefficient of a thermoelectric material at various temperatures.

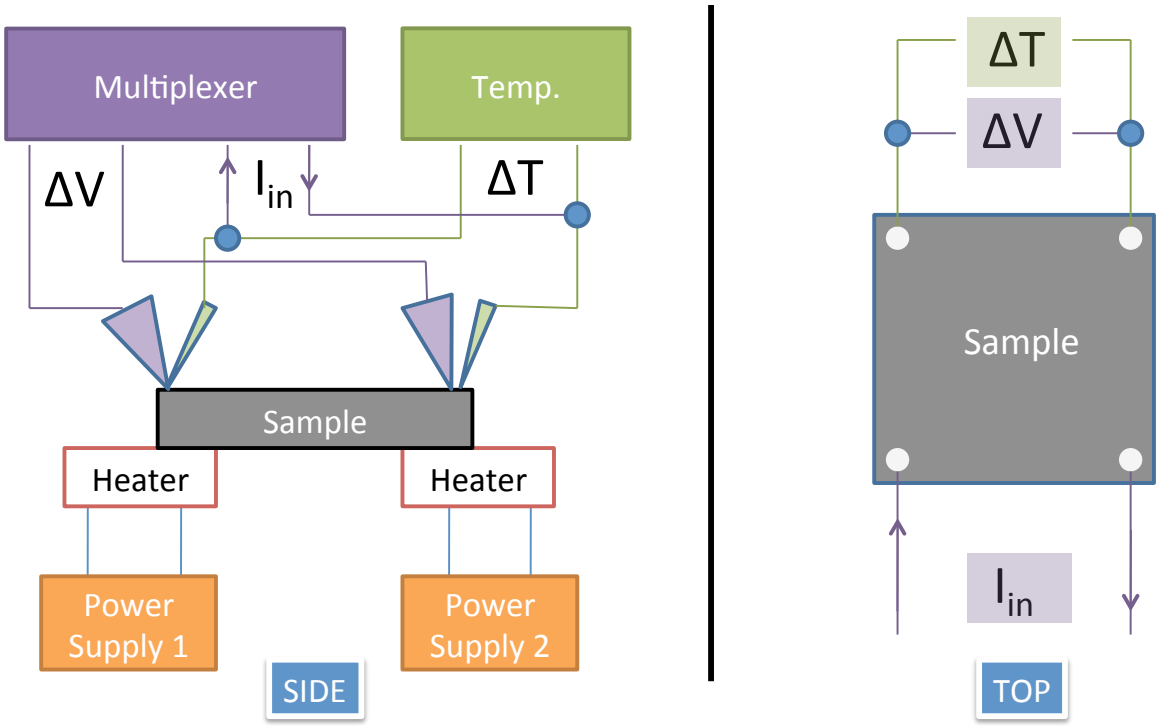

Figure C.1. Schematic of the Seebeck and electrical conductivity measurement system.

To measure the Seebeck coefficient of a thermoelectric material, a sample of the material (typically 7 mm x 7 mm) was placed across two stage-mounted Peltier heater/coolers electrically wired to different power supplies. The Peltiers were then controlled to heat or cool the individual sides. Thermocouples were placed on the corners of the samples (with silver paint as a conduction promoter) to measure both the temperature difference across the sample, and the open circuit voltage resulting from the temperature gradient. T-type thermocouples were used in the measurement to eliminate the additional voltage output from the thermocouple. The entire system is enclosed in a thermally insulated and electrically grounded case to reduce measurement error from noise. The Seebeck coefficient is calculated as,

$$\alpha = \frac{\Delta V_{OC}}{\Delta T} \tag{C.1}$$

where α is the Seebeck coefficient, ΔV_{OC} is the open circuit voltage potential and ΔT is the temperature gradient across the sample. In order to improve the accuracy of the measurement, the ΔV_{OC} is measured 10 times at each ΔT for a total of 6 different temperature differences (-8K, -6K, -4K, 0, +4K, +6K, 8K). These measurements were performed at various average temperature set points to get the temperature dependent properties. The Seebeck coefficient was then calculated by finding the slope of the fitted points. All measurements were automatically taken using custom LabView software. Figure C.2 shows the Seebeck measurements for one set point.

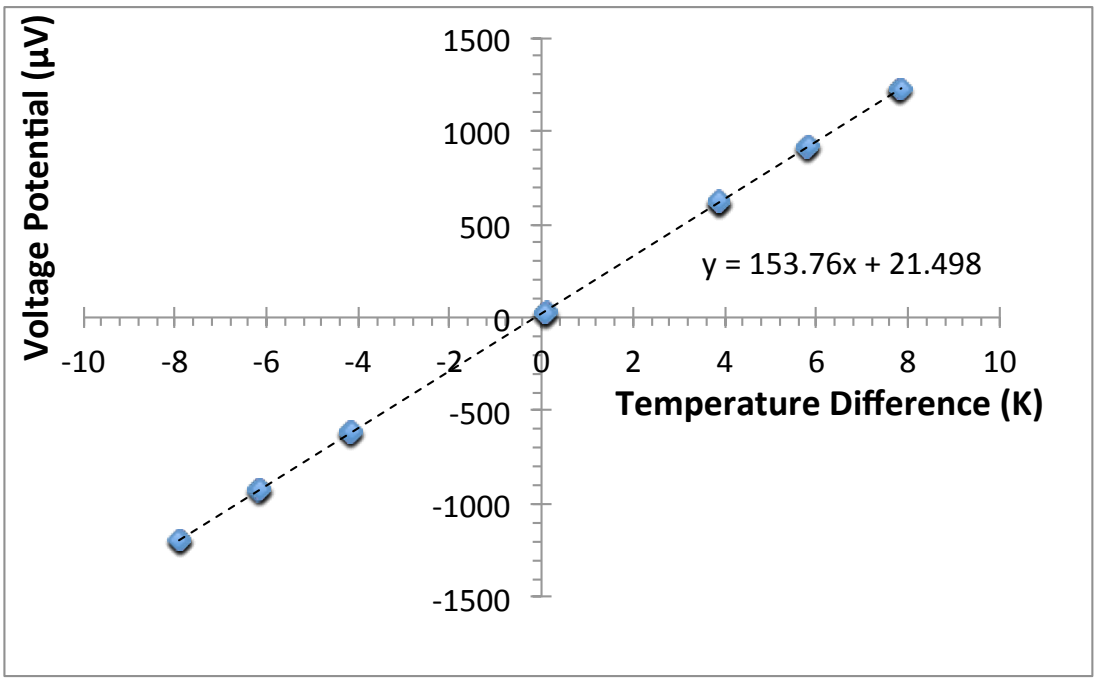

Figure C.2. Measured voltage potential for a sample at various temperature differences for a given temperature set point. The slope of fitted line for the points is the Seebeck coefficient of the sample (in µV/K). Each blue diamond represents 10 measurements.

Electrical conductivity measurements were carried out using van der Pauw's method in the same system. When the sample potential is being measured at $\Delta T = 0$, the digital multiplexer uses the four probes on each corner of the sample to run reciprocal measurements of sheet resistance. Figure C.3 shows the configuration for van der Pauw's method given a square or rectangular sample.

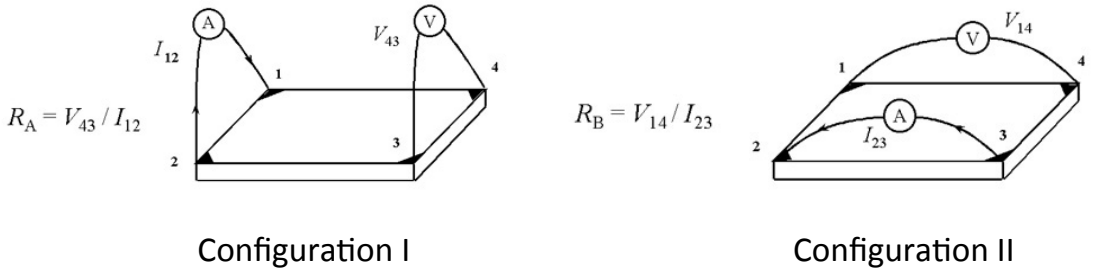

Figure C.3. Resistance measurement configuration for a square sample using van der Pauw's method [1].

The resistance from each configuration can be measured by running current through two adjacent corners while measuring the voltage from the other corners. By utilizing four points, lead resistance error can be minimized. Using Ohm's law, the resistance of the sample can be calculated. The sheet resistance of the sample can then be numerically solved using the van der Pauw's relationship:

$$e^{(-\pi R_A/R_S)} + e^{(-\pi R_B/R_S)} = 1 \qquad \text{(C.2)}$$

Where R_A is the resistance in Configuration I, R_B is the resistance in Configuration II and R_S is the calculated sheet resistance. The resistivity of the material can then be calculated by multiplying the sheet resistance with the thickness of the sample. The accuracy of van der Pauw's method can be improved by taking reversed polarity measurements for R_A and R_B such that

$$R_A = \frac{R_{12,34} + R_{34,21} + R_{21,43} + R_{43,21}}{4}$$
$$R_B = \frac{R_{23,41} + R_{41,23} + R_{32,14} + R_{14,32}}{4} \quad \text{(C.3)}$$

By performing reversed polarity measurements, any thermoelectric potentials from the Seebeck effect can be cancelled out [1]. Figure C.4 shows the Labview graphical user interface for the combined Seebeck and electrical conductivity measurement system.

C.3. Thermal Conductivity Measurement

Two separate thermal conductivity measurement systems were utilized for measuring the composite thermoelectric samples. Both methods required preparations of larger samples than used for the electrical conductivity and Seebeck measurements. Figure C.4 compares the difference in the two measurement methods. While the guarded heat flow method is an established technique for measuring thermal conductivity, it requires a much longer measurement time (due to steady state requirements) and larger sample sizes. Further details of the sample preparation can be found in Chapter 5.4.2.

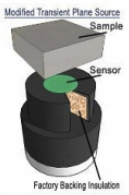

Method	Modified Transient Plane Source	Guarded Heat Flow
Speed	Sec. – Min.	Hours
Sample Prep	Moderate	Moderate
Complexity	Minimal	Minimal
Sample Size	17mm x 17 mm	25 mm. x 25mm
Thickness	~1mm	>1mm

Figure C.4. Comparison of the two thermal conductivity measurement techniques [2].

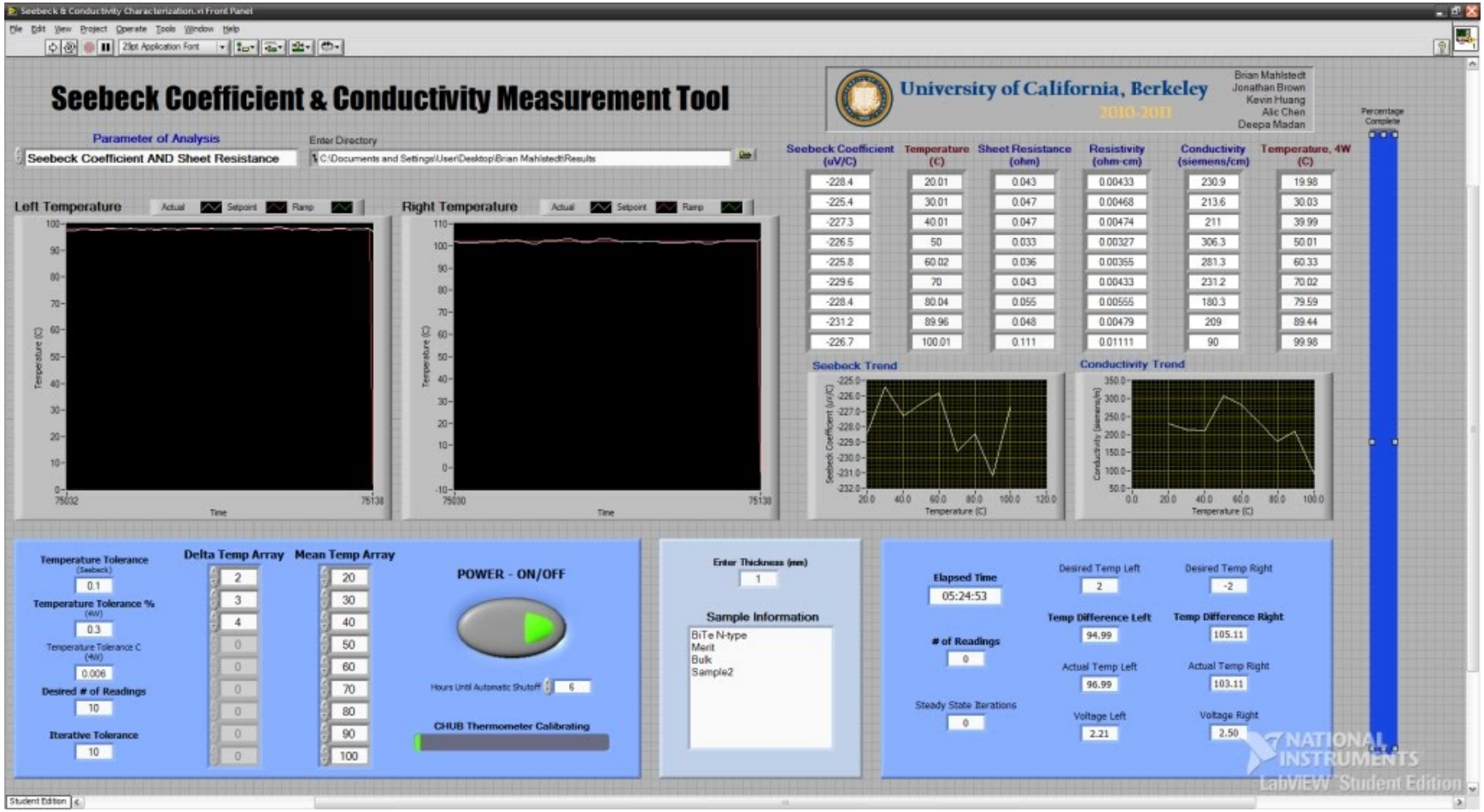

Figure C.5. Labview graphical user interface for the custom Seebeck and electrical conductivity measurement tool. The top left pane shows the current temperatures measured from each thermocouple. The bottom left pane allows for measurement configurations. The results are shown in the top right pane

Appendix References

[1] "III. Resistivity and Hall Effect Measurements," *nist.gov*. [Online]. Available: http://www.nist.gov/pml/semiconductor/hall_resistivity.cfm. [Accessed: 12-Sep.-2011].

[2] "Comparing the Methods - C-Therm - Thermal Conductivity Instruments." [Online]. [Accessed: 14-Sep.-2011].